DOCTOR OF PHILOSOPHY

The Application of CPPs to Improve the Cellular Uptake of a Novel Delivery Vector for use in Directed Enzyme Prodrug Therapy

Anderson, Simon

Award date:
2019

Awarding institution:
Bangor University

The Application of CPPs to Improve the Cellular Uptake of a Novel Delivery Vector for use in Directed Enzyme Prodrug Therapy

A thesis submitted for the degree of

Doctor of Philosophy

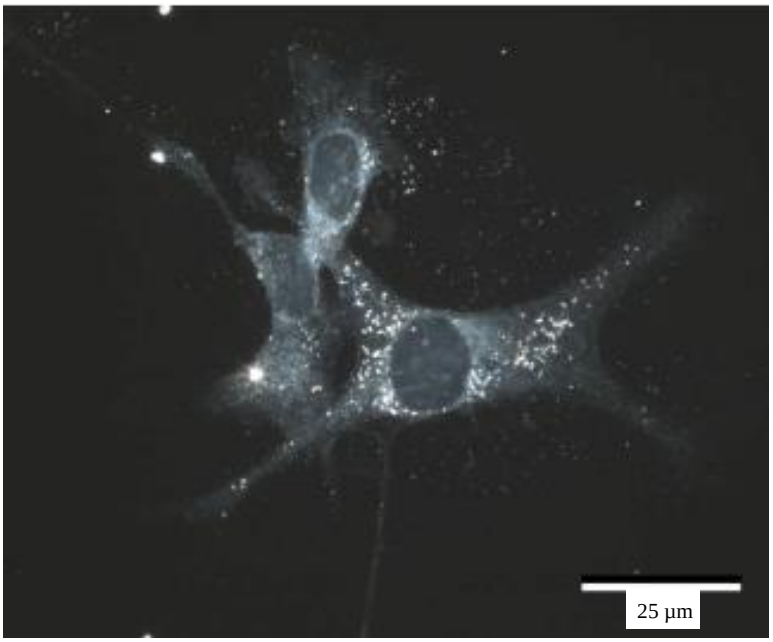

PRIFYSGOL
BANGOR
UNIVERSITY

Prifysgol Bangor • Bangor University

---

by
Simon Derek Anderson

Contents

Covering picture is a Darkfield image of SK-OV-3 cells, the large dark circles are the cell nuclei and the smaller bright areas are intracellular structures.

Abstract

THE APPLICATION OF CPPS TO IMPROVE THE CELLULAR UPTAKE OF A NOVEL DELIVERY VECTOR FOR USE IN DIRECTED ENZYME PRODRUG THERAPY

Cancer is one of the leading world killers, with a higher percentage of cases being diagnosed than ever before. This increase in rate of diagnosis is due to medical improvements, parallel to this needs to be medical improvements for methods to treat cancer patients. The most common and best known method for cancer treatment is chemotherapy, where anti-cancer drugs are administered to the patient in a toxic dose with the aim to kill cancerous cells. However there are side effects due to the toxic dose required in order to cause cell death. One method to overcome this is the use of prodrugs, these are drugs which are not in an active form when administered to the patient and are activated when in the body. Directed enzyme prodrug therapy involves the use of enzymes to activate these prodrugs, these enzymes are attached to a delivery system for direction towards the target site when in the body, where they are intended to activate the prodrug, inducing cell death.

Nanoparticles are considered by many to be the future of science and technology, and already have their place within some aspects of medicine, with the most common being medical imaging. It has already been shown that certain types of enzymes can be genetically manipulated to conjugate to gold nanoparticles, the incorporation of a gold nanoparticle with a superparamagnetic core such as Fe_3O_4 would allow for these enzymes to be directed through the body to a target site. However once reaching the target site the biggest challenge remains, and that is trying to introduce a foreign body into a cell, which usually have mechanisms in place to prevent this or destroy foreign objects that are able to enter the cell. Cell penetrating peptides, commonly referred to as CPPs, offer a way to deliver various objects into cells leaving the cargo intact to allow for medical cargo delivery.

This project outlines a novel synthesis method for coating Fe_3O_4 nanoparticles with gold, the purification, characterization and stability of these nanoparticles in various mediums. The nanoparticles produced have an average size of 50 nm, and are stable in a range of mediums. Following this a genetically modified enzyme has been successfully conjugated onto this nanoparticle and tested for its ability to cause cell death in cancer cells, and compared with nanoparticle:enzyme:CPP conjugates. The results from these trials show that the conjugate without the cell penetrating peptide is able to cause cell death, however the level of cell death is increased when a CPP is used, indicating a successful improvement in cellular uptake.

Acknowledgements

First and foremost I would like to thank my supervisor Dr Chris Gwenin for all his support and enthusiasm during my PhD as well as for his help keeping me focussed on the aims of this project. I also wish to thank all the members of the ARCH research team for their support in advancing the project. Thanks also to my research committee Dr Leigh Jones and Professor Mike Beckett for their input during my committee meetings.

I would also like to offer my thanks to the KESS II funding body, and to my company partner Perpetuus Carbon especially Dr Guido Drago and for his input into my project during our meetings.

Finally I would like to thank my friends and family for their support and words of encouragement during my time studying, in particular Miss Emma Thompson for her patience and giving me something else to talk about other than nanoparticles and nitroreductases.

Chapter 1:

Introduction

1.0 Introduction

1.1 Cancer

1.1.1 Cancer; a brief background

Cancer is one of the biggest global killers each year, second only to cardiovascular disease, with there being 9.6 million deaths attributed to cancer in 2018,[1] and Cancer Research UK estimating that 1 in 2 people born after 1960 will be diagnosed with cancer.[2] Some of the earliest references to cancer appear as early as 1600 BC on ancient Egyptian papyrus paper,[3] and at that time was thought of as untreatable. In modern society it is well established that the risk of getting cancer is not only down to a person's genes (*cause of 5-10 % of cancers*),[4] but can be altered by a person's lifestyle. For example regular use of tobacco is linked to an increase chance of getting cancer and is responsible for about 22 % of cancer deaths.[5] Other factors are responsible for cancer deaths, such as obesity,[6] diet,[7] alcohol[8] and radiation.[9]

1.1.2 The biology of cancer

The word cancer covers a group of diseases whose cells have mutated to the point of having rapid and uncontrolled cell division,[1] whereas in general, healthy non-cancerous cells divide about 50 times before natural cell death occurs.[10] Cancerous tumours have hallmarks which are looked for when determining if a tumour is malignant or benign, there are 6 defined core hallmarks which cancerous tissues display[11] and there are 2 other hallmarks which have been described as emerging hallmarks that have been more recently discovered by research.[12] Along with the defining hallmarks of cancer, (*enabling characteristics have been defined*) which aid in the acquisition of the core and emerging hallmarks.[12] These hallmarks and characteristics are presented in figure 1.1 on the following page.

There are many symptoms of cancer in the body, the most common being; abnormal bleeding,[13] prolonged coughing,[14] fatigue,[15,16] and a new or unusual lump,[17] which may be a sign of a cancerous tumour. In simple terms, for a healthy cell to become cancerous, the cell's genes that are responsible for regulation of growth and differentiation need to be altered.[18] Genes affected can be subdivided into 2 categories: oncogenes and tumour suppressor genes. Oncogenes promote cell growth and reproduction,[19] whilst tumour suppression genes inhibit cell division.[19] Mutation of a healthy cell into a cancerous one often requires multiple changes to genes. These changes can be: the formation of novel oncogenes,[18] under-expression or disabling of tumour suppression genes[18] and over-expression of normal oncogenes.[18]

Cells which have been damaged in this way continue to proliferate uncontrollably, producing more cells with damaged genes, leading to the formation of a tumour.

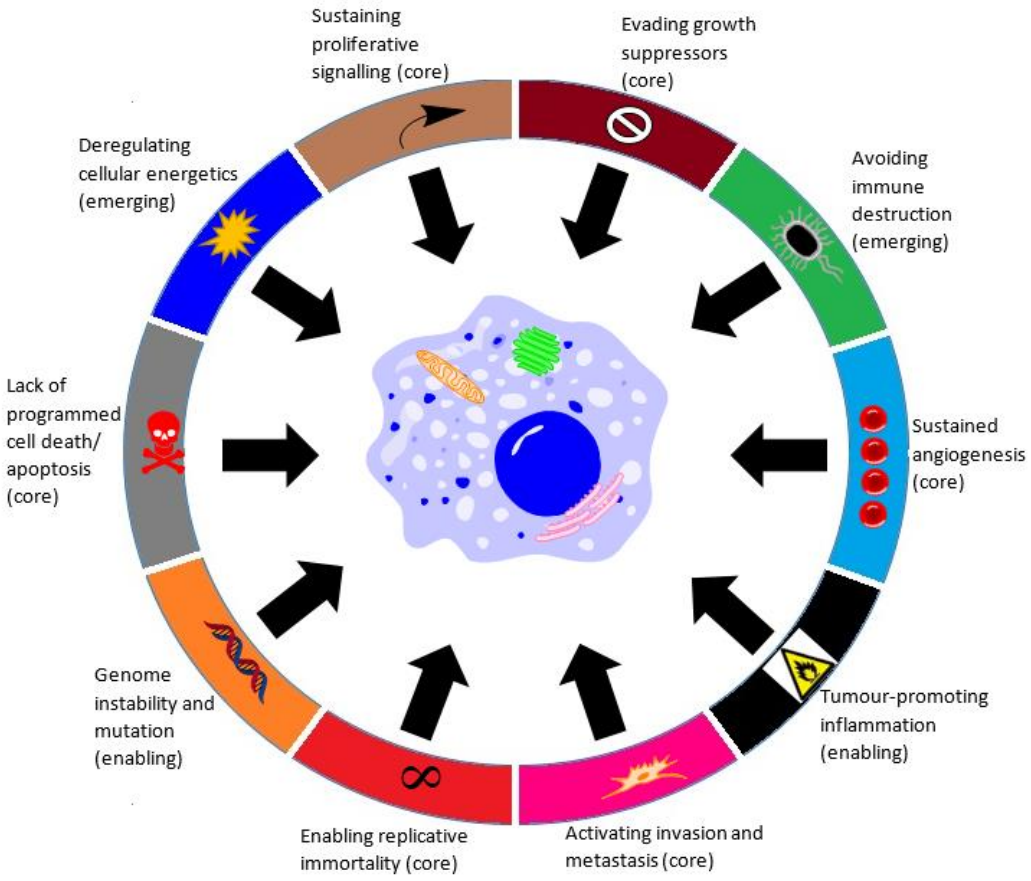

Figure 1.1. The recognized hallmarks of cancer,[12] *the different hallmarks are labelled to either being; core, emerging or an enabling characteristic.*

One of the major problems cancer causes is known as metastasis, this is a process where a part of a cancerous tumour breaks off from the main body of the tumour, enters into the bloodstream, the lymph system or numerous other systems that traverse the body and travels around the body, which often leads to the formation of a secondary tumour site. A key feature of metastasis is a secondary tumour where the cells are not from the surrounding tissues, for example if a breast cancer was to metastasize to the liver, the tumour cells at the liver would be abnormal breast cells, not liver cells. The most common secondary tumour sites are lymph nodes along with the liver, lung, brain and bones.[20]

1.2 Treatment methods

There are now many different methods which can be used to treat cancer, each method has its own advantages and disadvantages and quite often several methods of treatment are used to treat a cancer patient.[21]

1.2.1 Surgery

Surgery is often the first resort as it allows for the removal of a tumour and surrounding tissue before it is potentially able to metastasize and spread through the body.[22] It is more common in stage 1 and 2 cancers before metastasis occurs[22] however it can be used as part of a combined treatment.[23] One major limitation of surgery is that it is an incredibly invasive treatment method, and has associated risks,[24–26] risks however are increased for use in treating spinal and some brain cancers, due to the possibility of causing more damage to the body.[27] This type of treatment is only available for cancer patients with solid tumours, cancers such as leukaemia often require other forms of treatment.[21–23]

1.2.2 Radiotherapy

Radiotherapy involves the use of ionizing radiation to try and control the growth of, or kill malignant cells and is often used in conjunction with surgery. One of the major drawbacks with this form of therapy is that different cancers respond differently to radiotherapy.[28] Some cancers such as leukaemia and most lymphomas are very sensitive to radiotherapy,[29,30] whilst other cancers such as renal cell cancer and melanoma are described as radio resistant.[31] However there is research combining immunotherapy with radiotherapy which has shown promise for treating melanomas.[32]

1.2.3 Immunotherapy

Immunotherapy is the attempt to stimulate the body's immune system to fight off cancer and destroy tumours. One of the original uses of immunotherapy as a cancer treatment was the treatment of bladder cancer using the BCG vaccine, which was used as a tuberculosis vaccine.[33] There are problems with using immunotherapy for cancer treatment, the biggest being the variable efficacy of the treatment, for which several explanations have been proposed, these being; the patients treatment history, variability in cancer type and stage and the immunosuppressive nature of cancer itself,[34,35] along with only a select group of cancers being treatable using immunotherapy techniques,[36] alternatives to immunotherapy are often used, such as chemotherapy.

1.2.4 Chemotherapy

Many chemotherapy agents that are used for cancer therapy interfere with mitosis and target rapidly dividing cells. The interference with mitosis and more often the cell's DNA, leads to cell apoptosis.[37] The history of chemotherapy can be traced back to World War 1 with the introduction of mustard gas for chemical warfare, research done into nitrogen mustards and mustard gas found lymphoid suppression occurs after exposure. Mustard agents were then used to treat lymphoma in mice, providing the first true cancer chemotherapy and a step in the realisation that cancer could be treated using pharmacological agents.[38] Since then there has been constant research into new and more effective treatment agents. One issue with chemotherapy is that by their very nature the agents must be delivered in a toxic dose, leading to a wide array of side effects as the agents often attack healthy cells, one common example being hair loss. A way to overcome this is to apply prodrugs; an agent that is delivered into the body in its non-pharmaceutically active form which is then 'activated' into its cytotoxic form in the body.[39]

1.3 Prodrugs

As previously stated, prodrugs are administered to a patient in their non-pharmaceutically active form and are then metabolized within the body. Prodrugs are not only used to treat cancer, it is estimated that approximately 10 % of all drugs marketed world-wide are prodrugs, with 30 prodrugs being approved by the FDA since 2008.[39] Prodrugs can be classified into one of two groups: Type I- prodrugs that are activated intracellularly, or Type II- prodrugs that are activated extracellularly.[40]

1.3.1 CB1954

A Type I prodrug that has been extensively studied is 5-(aziridin-1-yl)-2,4-dinitrobenzamide, known as CB1954. CB1954 on its own is a mono-functional alkylating agent,[41–43] that is to say it can form one alkyl chain bond to DNA, it shows mild toxicity to cells and it has been found that it is the presence of the aziridine group that causes the mono-alkylating functionality.[42] It was found however that the CB1954 prodrug caused an unexpected toxicity when introduced to the Walker 256 rat carcinoma and further investigation led to the discovery that CB1954 was undergoing an enzymatic reduction within the Walker cells by the Walker DT-diaphorase.[42]

When this prodrug is bio activated it forms one of 2 products; 5-(aziridin-1-yl)-2-hydroxylamine-4-nitrobenzamide or 5-(aziridin-1-yl)-4-hydroxylamine-2-nitrobenzamide (*see figure 1.3 for details*). The 4-hydroxylamine derivative then undergoes a further activation step by a thioester reaction to form a final DNA reactive species; 4-(acetoxyamino)-5-(aziridin-1-yl)-2-nitrobenzamide.[44] This bio activation of CB1954 into the final product can see up to a 100,000-fold toxicity in cells on a dose dependent basis.[45]

DNA crosslinking is a process that occurs when an exogenous or endogenous agent forms a covalent linkage between 2 nucleotides of DNA. Cross-linking can occur either across two strands of DNA or between 2 nucleotides on the same strand of DNA. This binding can lead to an interference in cellular metabolism, including cellular mitosis and DNA transcription, in turn leading to cell death.[46]

It has been theorised through modelling studies that once the 4'-hydroxylamine product has been converted into its DNA cross-linking species the 4'-acetoxyamino group binds primarily at the C8 position on the deoxyguanosine (*the numbering can be seen in figure 1.2*), following which, the aziridine group binds at the O6 position on a deoxyguanosine on the opposite strand of DNA.[41,43] This is an unexpected cross-linking as many activated mustard cross-linking agents link between the N7 on 2 opposite deoxyguanosines.[47]

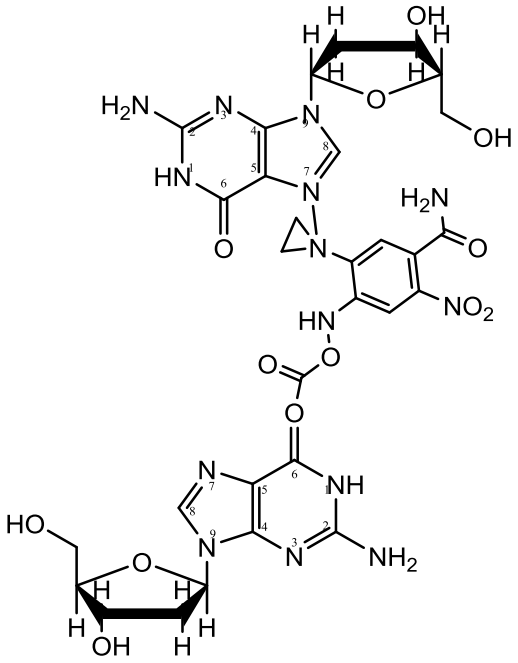

Figure 1.2. The deoxyguanosine molecule, with the atoms numbered to demonstrate where the cross-linking of the CB1954 reduction products occurs.

As well as producing the 4'- DNA reactive species, the 2'- and 4'- hydroxylamine products will also reduce to a 2'- and 4'- amino products, which are not DNA reactive species, but do present cytotoxic properties.[48] Whilst the 4'-hydroxylamine product goes on to form a DNA reactive species, the 2'-hydroxylamine product also has cytotoxic properties but has a much greater bystander effect than the 4'-hydroxylamine product. The bystander effect is toxicity shown in cells surrounding the transfected tumour cells, that have not themselves been transfected.[49–51] There are 2 types of bystander effect; local and distant,[52] local bystander effect causes the death of cells surrounding the targeted tumour, whilst the distant bystander effect can be observed in vivo and consists of tumour regression distant from the tumours which are expressing the gene. When it comes to the CB1964 reaction products the 2'-hydroxylamine causes a larger bystander effect than the 4'-hydroxylamine.[48] The reduction of CB1954 is demonstrated in Figure 1.3.

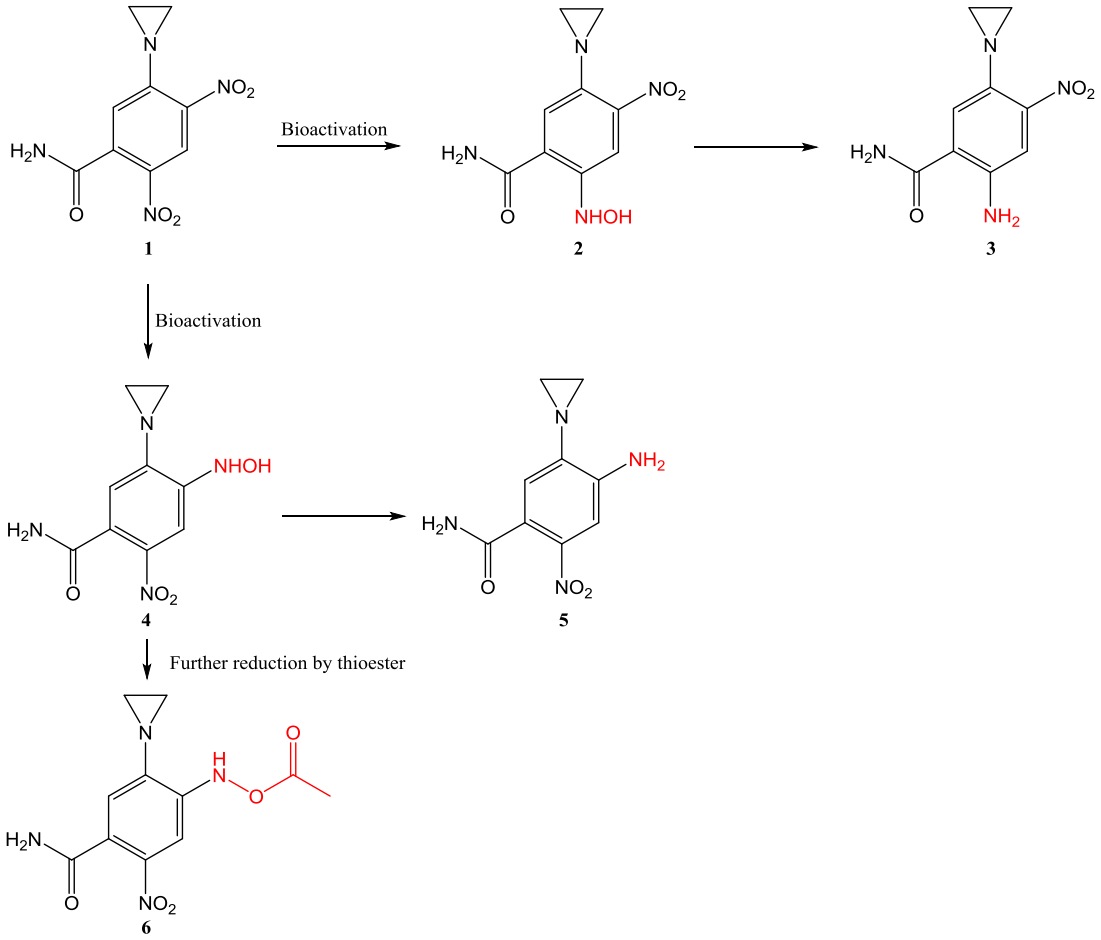

*Figure 1.3. The reduction of CB1954 (**1**) into its products: 5-(aziridin-1-yl)-2-(hydroxyamino)-4-nitrobenzamide (**2**), which further reduces to 2-amino-5-(aziridin-1-yl)-4-nitrobenzamide (**3**) and 5-(aziridin-1-yl)-4-(hydroxyamino)-2-nitrobenzamide (**4**) which can further reduce to either; 4-amino-5-(aziridin-1-yl)-2-nitrobenzamide (**5**) or 4-(acetoxyamino)-5-(aziridin-1-yl)-2-nitrobenzamide (**6**).*

1.4 Nitroreductases

The CB1954 prodrug can be reduced into its 2'- and 4'- products by a group of enzymes collectively known as nitroreductases (NTRs). There are several factors that are required for an enzyme to be classed as a nitroreductase enzyme, with these being; the use of flavin mononucleotide (FMN) as a prosthetic group, using nicotinamide adenine dinucleotide (phosphate) (NAD(P)H) as a cofactor, follow the ping-pong bi-bi mechanism, form homodimers, be strongly inhibited by dicoumarol and have the ability to reduce an NO_2 group.[53–56] The most commonly studied nitroreductase-prodrug combination is the NfnB enzyme from *Escherichia coli,*[41,43,44,54,57–61] with CB1954. This enzyme prodrug combination has made its way to clinical trials.[60,62]

All nitroreductases fall into 1 of 2 categories: type I and type II, with type I being oxygen insensitive and type II being oxygen sensitive.[63] Type I NTRs catalyse the reduction of the NO_2 groups into the nitroso, hydroxylamino and amino derivatives through the addition of electron pairs from NAD(P)H.[64,65] The type II NTRs follow a single electron transfer of the NO_2 group which produces a nitro anion radical, that can be re-oxidized aerobically to its original form.[63,65–67] Type I NTRs often follow the ping-pong bi-bi mechanism for prodrug reduction where the FMN prosthetic group found in type I NTRs acts as the electron transfer from the NAD(P)H to the CB1954. The reduction and oxidation movement of electrons and ping-pong bi-bi mechanism can be seen in Figure 1.4. This ping pong mechanism has 2 steps to it, the first is the transfer of an electron from an NAD(P)H molecule onto the FMN associated in the enzymes active site, this transfer occurs twice to yield $FMNH_2$. The NAD(P)+ molecules are replaced in the active site by a CB1954 molecule which then accepts the 2 electrons from $FMNH_2$ and is enzymatically reduced to its hydroxylamine derivative products.

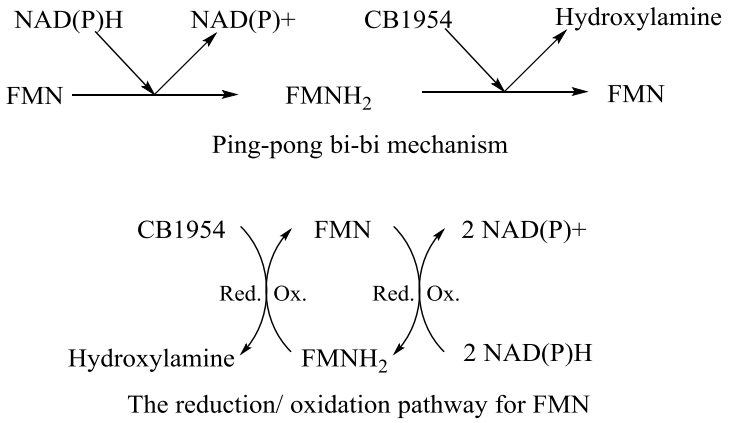

*Figure 1.4. The Ping-pong bi-bi mechanism (**top**) demonstrating the initial interaction of the NAD(P)H with the FMN releasing the electron, then the reduction of the CB1954. Also shown (**bottom**) is the reduction-oxidation mechanism showing the movement of electrons between the NAD(P)H to the CB1954.*

Flavin mononucleotide acts as a prosthetic group in NTRs and aids in one- and two- electron transfers during the enzymatic reduction of CB1954.[61] During the reduction of CB1954 FMN switches back and forth between its oxidised and reduced forms, demonstrated in Figure 1.5.

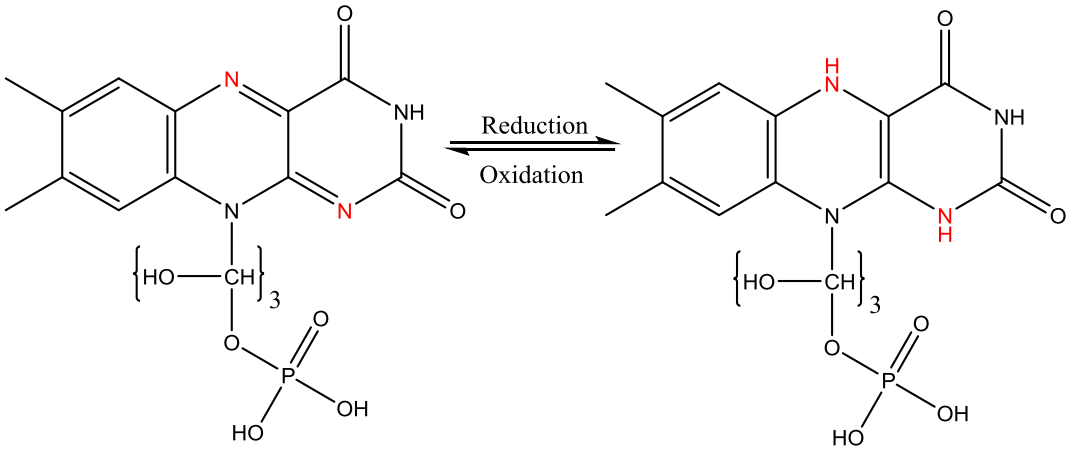

Figure 1.5. The oxidised (left) and reduced (right) forms of FMN.

Nicotinamide adenine dinucleotide (NAD) is a coenzyme found in all living cells, where its primary function is to act as an electron carrier in metabolic reactions. The intracellular concentration of NADH varies between cells by type,[68,69] for example it has been reported that in breast cancer cells the concentration is in the range of 168 µM, whilst in healthy breast cells the concentration is around 97 µM.[70] It exists in one of two forms: oxidised or reduced, abbreviated to NAD^+ and NADH respectively, demonstrated in Figure 1.6.

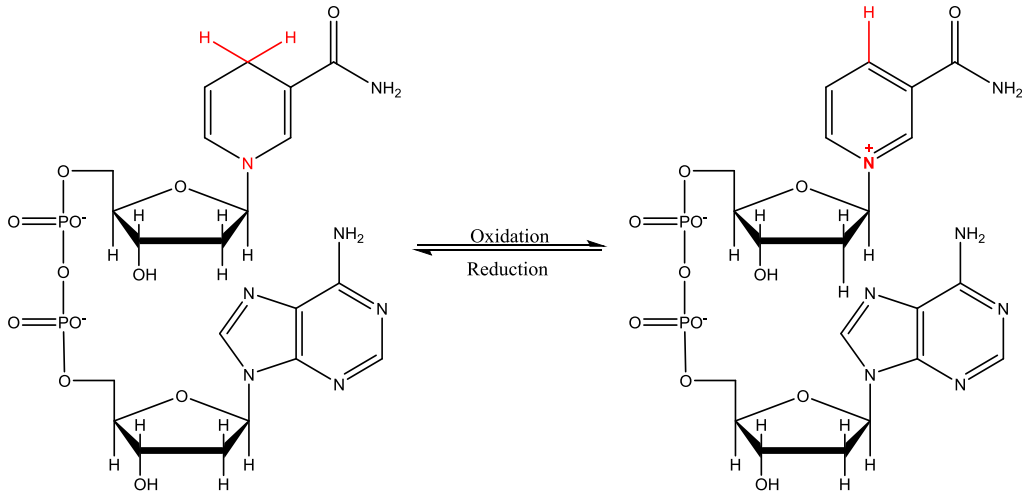

Figure 1.6. The two forms of Nicotinamide adenine dinucleotide; reduced-NADH (left) and oxidised-NAD+ (right).

It is also an important factor that needs to be taken into consideration for drug design as it can play a role in a variety of drug interactions, for example it is used in the enzymatic activation of the prodrug isoniazid used for the treatment of tuberculosis.[71] Similarly it plays a role in the enzymatic reduction of the CB1954 prodrug, by interacting with the NTRs FMN prosthetic group,[55] providing the 2 electron transfer required for the reduction of the NO_2 group into NHOH. NfnB from *E.coli*, as already mentioned is a nitroreductase, another example is YfkO from *Bacillus licheniformis*,[72] and both of these enzymes will reduce the CB1954 prodrug into its hydroxylamine products, but at different product ratios. It is thought that the reason different nitroreductases produce different CB1954 reduction product ratios is due to them having structural differences from different amino acid sequences, with the NfnB and YfkO enzymes sharing a 28 % amino acid sequence identity.[72] Both of these enzymes have been explored for their potential use in Directed Enzyme Prodrug Therapy.[41,43,60,73–76]

1.5 Directed Enzyme Prodrug Therapy

Directed Enzyme Prodrug Therapy (*DEPT*) is a form of cancer therapy that involves the delivery of a prodrug activating enzyme to a cancer site, with the intention of the enzyme being taken up into the cell. A prodrug will then be administered to the patient and when it reaches the tumour site will be bio activated into its pharmaceutically active form. This therapy reduces the overall toxicity of chemotherapy, instead of introducing cytotoxic chemicals into the entire body the cytotoxic chemicals are located in and around the tumour site. DEPT is a relatively new technique that is still undergoing much research to find suitable delivery systems that can

deliver the enzyme to the cancer site and still leave the enzyme active when it is taken into the cells.

1.5.1 Antibody Directed Enzyme Prodrug Therapy

Antibody DEPT (*ADEPT*) focuses on the use of antibodies as the delivery system for the prodrug-activating enzyme. The enzyme will be conjugated to an antibody that is specific to an antigen expressed by the tumour, so that when the antibody reaches the tumour it can bind to the cell and enter in to release the enzyme. One of the key issues with this specific type of treatment is the requirement to identify antibodies that are specific and exclusive to tumours only. Even then not all tumours of the same type will express the same antigens, for example the HER2 (*Human Epidermal growth factor Receptor 2*) is over-expressed in many types of cancers such as gastric cancer and salivary duct carcinomas. In these 2 types of cancers however HER2 is over expressed in only 7-34 % of gastric cancers,[77,78] and 30 % of salivary duct carcinomas.[79] This does limit the therapeutic potential of ADEPT.

1.5.2 Gene Directed Enzyme Prodrug Therapy

Gene DEPT (*GDEPT*) is a slightly different approach to putting an enzyme into a tumour. Here a gene encoding for the enzyme is delivered to a target site (*often using a virus*),[74] upon entry into the cell the gene will begin expressing the prodrug activating enzyme, which will activate the later administered prodrug.[74] A commonly studied combination is the use of the Herpes Simplex Virus to deliver a gene encoding for Thymidine Kinase to a target site, followed by treatment with the prodrug Ganciclovir.[80] Thymidine kinase converts GCV to GCV-monophosphate, which is then further converted to GCV-triphosphate, the cytotoxic variant of the prodrug.[81] A challenge in GDEPT is identifying suitable carriers for the genes expressing the enzymes, viruses make the ideal delivery system but safety concerns have been associated with the use of viral vectors, which has prompted the search for non-viral vectors. However many of these have shown to be less efficient than viral vectors due to short term gene expression.[80] If efficient and safe vectors can be discovered, GDEPT is a promising cancer treatment.

1.5.3 Magnetic Nanoparticle Directed Enzyme Prodrug Therapy

Magnetic Nanoparticle DEPT (*MNDEPT*) is a novel prodrug therapy being developed at Bangor University by Gwenin *et al*.[82,83] This form of prodrug therapy aims to overcome some of the issues faced by other DEPT strategies by employing a superparamagnetic nanoparticle as a directed delivery vector. The nanoparticle has a 10 nm Fe_3O_4 superparamagnetic core and

is coated with a 20 nm thick gold shell, giving a 50 nm particle called a gold magnetic nanoparticle; AuMNP. Onto this particle genetically modified NTRs are conjugated, with the genetic modification being the addition of 6 cysteine residues on each dimer of the NTR at the N-terminus.[61] The crystal structure along with the location of the N-terminus and FMN active sites are shown in Figure 1.7.

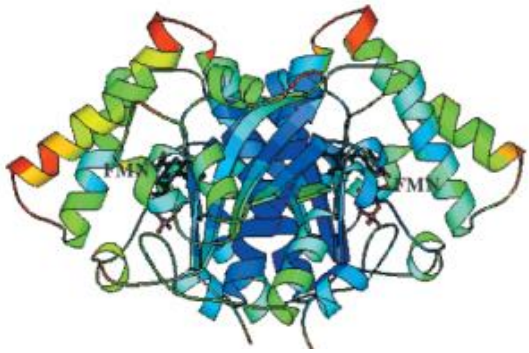

Figure 1.7. The crystal structure of the NfnB enzyme from E.coli, showing the positions of the N-terminus and the active sites with FMN in them[87]

The cysteine residues each have a sulphur atom, which forms very strong bonds with gold, with bond dissociation energies being calculated at 298 ±2 KJ mol^{-1}.[84] This AuMNP is aimed to be delivered to the target site in a body using magnetic focusing over a target area, with the desired effect being a much more efficient way to transport the prodrug activating enzymes to a tumour and reduce systemic toxicity associated with the bystander effect.[85,86] The uses and biomedical applications of nanoparticles are discussed in: Magnetic Nanoparticles in Drug Delivery: A Review, which can be found in chapter 2.

1.7 Cell penetrating Peptides

In general, it is difficult to transfer molecular cargos in and out of cells, this presents a problem when attempting to uptake medicines and other therapeutics into cells for treatment. Cell penetrating peptides (*CPPs*) are a tool that can be used to overcome this issue. CPPs are a class of peptide that possess the ability to efficiently penetrate through cellular membranes of living cells and assist in the delivery of molecular cargoes.[88,89,90] CPPs are in general: amphipathic,[89,90,91] short[90] (*20-30 amino acids in length*), have a net positive charge at physiological pH[88] and are usually comprised primarily of arginine and lysine.[90]

1.7.1 Discovery

CPPs were first discovered in 1988 by the elucidation of the structure of the Human Immunodeficiency Virus type-1 (*HIV-1*)[92] HIV-1 has a TAT (*Trans-activator of Transcription*)

protein,[92] a short sequence of this protein was found to be responsible for assisting in the uptake of HIV-1,[92,93] the sequence that assisted in uptake is called a protein transduction domain (*PTD*),[89,92] now more commonly referred to as a cell penetrating peptide. Since this initial discovery in 1988, there have been many CPPs discovered[94] such as penetratin,[90,94,95] a small peptide fragment from the homeodomain of *Antennapedia*, the gene that controls the formation of legs during development of the *Drosophila* fly.[96] Since the discovery of this new class of peptides research has expanded rapidly into the area of CPP research with many short peptides being discovered/ designed and tested for their ability to uptake into cells.

1.7.2 Classification of CPPs

Classifying CPPs is not an easy affair as there is no general consensus on methods for classification, often CPPs overlap into several different categories. For example CPPs can be classified based upon their origin; peptides derived from proteins,[96] chimeric peptides that form by the fusion of two natural sequences[97] and finally synthetic peptides, which are designed and synthesised based on studies of naturally occurring peptides.[98,99] As well as being able to classify CPPs based upon their origin, it is also possible to classify them based upon their physio-chemical characteristics, such as their hydrophobicity[88] or amphipathicity.[100] Table 1.1 demonstrates several examples of peptides classified based upon their origins, as well as the peptide sequence.

Table 1.1. A range of CPPs that have been discovered, the CPPs amino acid sequence and the CPPs classification and origin.

CPP	Sequence	Classification and (origin)	Ref.
TAT	GRKKRRQRRRPQ	Protein-derived (HIV-1)	101,102
Penetratin	RQIKIWFQNRRMKWKK	Protein-derived (Antennapedia)	95,103
Poly-arginine	$R_X (R=6<X<12)$	Synthetic (Based on TAT)	93,104
Pep-1	KETWWETWWTEWSQP KKKRKV	Chimeric (HIV reverse-transcriptase/SV40 T-antigen)	91,95,105
MPG	GALFLGFLGAAGSTMGA WSQPKKKRKV	Chimeric (HIV-gp41/SV40 T-antigen)	105,106

1.7.3 Uses of CPPs

CPPs have the potential to be used in the delivery of a variety of medicinal cargoes,[97,107–109] they have already been shown to deliver quantum dots,[89,110] oligonucleotides,[111] DNA,[112] RNA[113] and proteins.[97] Through various fluorescence techniques, there have been indications as to which organelles in the cells different CPPs are directed to after cellular uptake.[101] Whilst the initial fluorescence spectroscopy gives an indication as to where CPPs move to in the cell,

it is important to also know that CPP uptake and movement within the cell is heavily influenced by the cargo attached to the CPP,[101,114] as well as the cell type the CPP is trying to penetrate.[114,115]

1.7.4 Structures of CPPs

CPPs contain charged amino acids, which when placed in solution interact with both the solution they are in and with each other, often leading to the formation of secondary structures. Many CPPs form secondary structures either consisting of an α-helix or a β-Sheet. Peptide sequences without cysteines usually form the helices, whilst peptide sequences with cysteines form disulphide bridges, leading to β-Sheets, or sometimes a mix of both α-helixes and β-Sheets.[116,117] Quite often the solution the CPP is suspended in will account for the structure of the peptide. For instance, in water the majority of CPPs will form random coils,[118] with one exception to this being Pep-1, which will form a α-helix.[119] The secondary structure of the peptides can influence how they interact with cell membranes.[118]

1.7.5 Cellular Uptake of CPPs

A reason for the popular use of CPPs in research is their ability to penetrate into and through cell membranes using a variety of methods. The ability for CPPs to enter cells overcomes issues that may be faced when trying to administer a therapeutic compound that would either traditionally not interact with a cell membrane, or, would have been up taken into a cell *via* endocytosis. These cargoes would have instead been broken down in the endosome or recycled back into the plasma membrane and therefore have prevented the molecule from reaching its target destination.[120] It is thought that there are varieties of properties that are responsible for CPPs being able to uptake efficiently into cells, with some CPPs possessing a few of these properties, or in some cases all of them. Positive charge appears to be the most important property a CPP must possess for cellular uptake,[93,114,121,122] with cell membranes being filled with a variety of negative moieties which attract to the positive charge of a CPP.[114] Arginine has been shown through studies to be important for cellular internalization, which is attributed to the guanidinium head group,[93,123] forming bidentate hydrogen bonds with negatively charged phosphate, sulphate and carboxylate groups found on the surface of the cell membrane, as shown in Figure 1.8.[114]

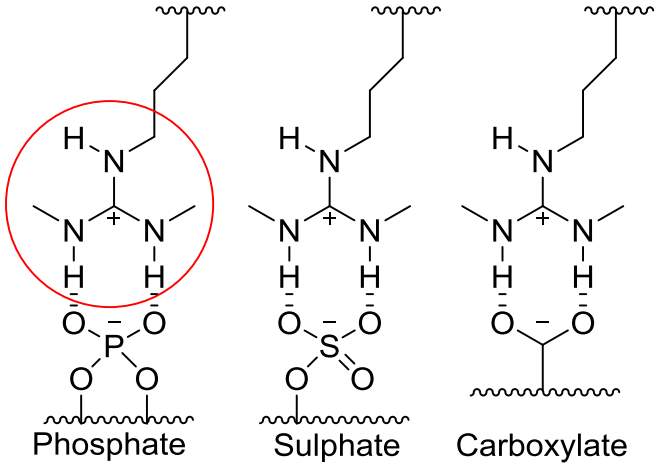

Figure 1.8. The guanidinium head-group of arginine (circled in red) can bind to phosphate, sulphate and carboxylate groups, by bidentate hydrogen bonds, assisting the CPP in binding to the cell membrane.

Along with arginine residues, the CPPs hydrophobicity has also demonstrated an importance for cellular internalization,[124–126] with uptake studies showing the removal of hydrophobic residues decreases the ability for CPPs to pass through cell membranes.[126] Another important amino acid residue that has demonstrated its vital role in cellular uptake is tryptophan,[127,128] with many studies demonstrating the importance of the addition of even a single tryptophan residue.[129] It has been found that CPPs present their most cytotoxic properties when tryptophan sits on an interface between hydrophobic alanines and hydrophilic lysines, especially so when the CPP is in a helical formation.[130] An example of tryptophan's role in CPPs is with the Pep-1 CPP (*Table 1.1*). Tryptophan residues are part of a hydrophobic domain created to interact with macromolecules.[106] When the CPP takes on a helical structure, the tryptophan residues in the CPP arrange themselves on one side of the helix, with this arrangement demonstrated in Figure 1.9,[109] and then embed themselves within the cell membrane, causing the peptide and membrane to line up perpendicular to each other, forming a pore which leads to membrane transduction.[130]

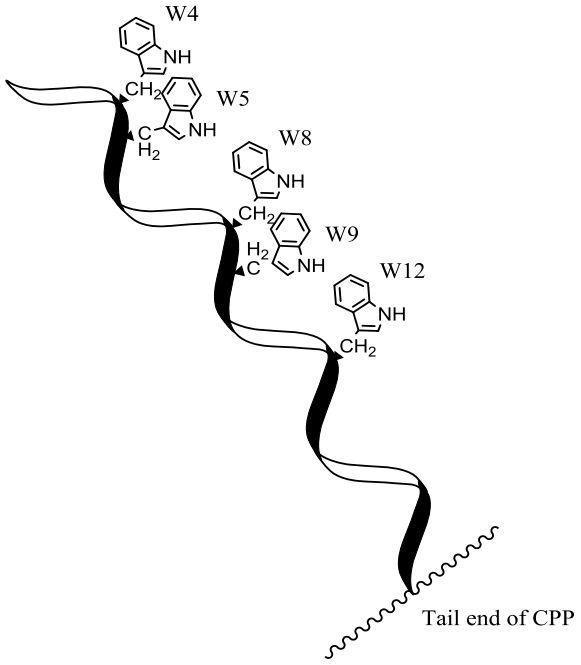

Figure 1.9. A visual representation of the tryptophan residues lining up along the alpha helix of a Pep-1 CPP.

The final property that is responsible for the uptake is the secondary structure of the CPP. It is thought that whilst this structure is not a vital deciding factor in cellular uptake,[96,131] it is agreed that flexibility in peptide structure can be helpful with regard to uptake.[114]

It is not just the CPPs structure and physiochemical properties that are responsible for cellular uptake, other factors such as cargo and cell type come into play. The environment surrounding the cell can also have an effect on the uptake[132] and can cause the CPP to uptake in a different manner to how the same CPP would uptake in a different environment.

1.8 Methods of uptake

There are different ways that a CPP can uptake cargos into cells, which will vary depending on; CPP, cargo type and cell type. Cell uptake can be divided into 2 overall categories: endocytosis and direct membrane translocation. Figure 1.10 is a representation of the majority of uptake method available to CPPs.

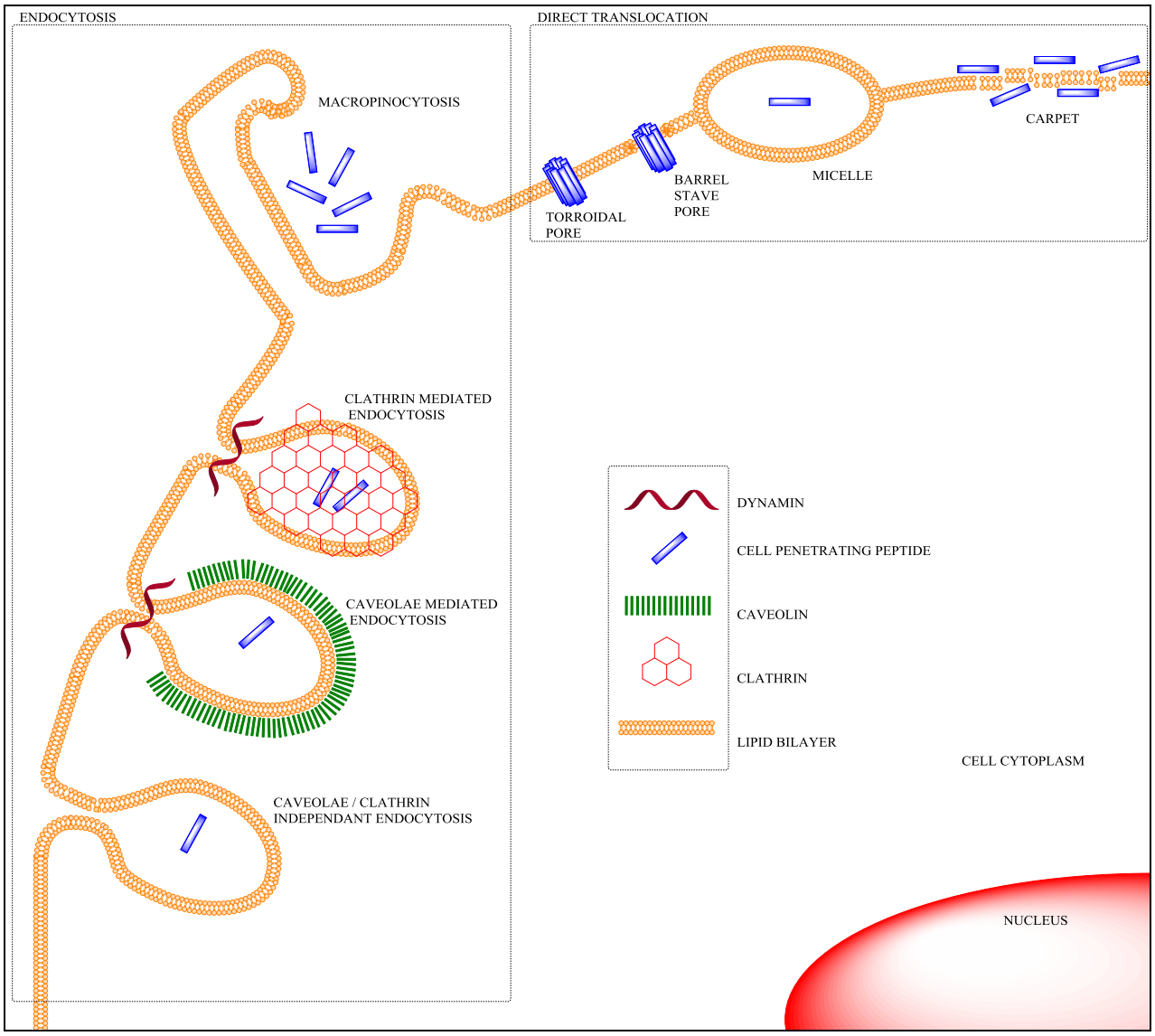

Figure 1.10. A diagram representing the methods in which CPPs can uptake into cells.[90]

1.8.1 Endocytosis

Endocytosis is a blanket term that covers the uptake of cargos into a cell that involves the formation of a vesicle/endosome. An endosome is essentially a small structure in the cell that has a phospholipid bilayer containing cytoplasmic fluid that is used to move cargos throughout the cell. The generic endocytosis pathway can be split into three basic steps: Early endosomes, late endosomes and lysosomes. Early endosomes are the organelles where endocytosed cargos

disassociate from their receptors and from which the receptors recycle back to the membrane of the cell.[133,134] Late endosomes are an intermediary after early endosomes, these are a final sorting organelle for cargos coming from: early endosomes, phagosomes and from the Golgi network.[135] They are believed to mediate the delivery of cargos into the final step of the endocytic pathway; lysosomes. These are in essence recycling organelles, with a primary function to break down cellular waste products and cargos that have been taken into cells that need breaking down for use or are pathogenic and need neutralizing. Lysosomes achieve this breakdown role by using 40 different hydrolytic enzymes, which are manufactured in the endoplasmic reticulum and transferred to the lysosome through the Golgi apparatus and late endosomes.[136] As stated endocytosis is a blanket term, under which there are a variety of different ways cells can uptake cargoes *via* an endocytic mechanism.

1.8.2 Macropinocytosis

Macropinocytosis simply put is the folding in of the cell membrane to engulf a cargo. It is a receptor-independent form of endocytosis that is usually triggered by growth factor stimulation such as macrophage colony-stimulating factor-1 (*CSF-1*).[137] Macropinocytosis has been described as 'membrane ruffling',[138] this 'ruffling' is the formation of 'lamellipodia' which usually fold back into the cell, however occasionally fold back on themselves, fusing with the cell membrane and forming macropinosomes, these macropinosomes are considered to be > 200 nm.[139,140]

1.8.3 Clathrin mediated endocytosis

Clathrin is a protein associated with the coating of vesicles during cellular uptake. It has a triskelion shape that forms a polyhedral lattice when it interacts with other clathrin triskelions. Clathrin mediated endocytosis (*CME*) is a form of receptor dependant endocytosis. On the cell membrane a receptor will bind to a target, this then 'recruits' adaptor proteins and clathrin to the cell membrane around the receptors. This build up causes a clathrin coated pit to form,[141] upon which nucleation begins around the receptor. This will form a vesicle, which is cleaved from the cell membrane *via* a fission protein such as dynamin. Clathrin vesicles are between 90-100 nm in size.[142]

1.8.4 Caveolae mediated endocytosis

Caveolins are integral membrane proteins that play a role in clathrin-independent endocytosis, with 3 types being know: Caveolin-1 and Caveolin-2 which are both found in non-muscle cells and Caveolin-3 which is exclusive to muscle cells.[143] Caveolin proteins sit within the plasma

membrane and are hairpin shaped with both the amino and carboxyl ends facing inwards, towards the cytoplasm. This type of endocytosis occurs when invaginations into the cell membrane are coated with caveolin and cavin proteins, the caveolin oligermerize together forming what is known as a lipid raft, the invagination then buds off and is removed from the membrane by a GTPase, forming the caveolae which are often 60-80 nm in size.[144] The caveolae then fuse into the early membrane system and follow the previously described pathway. One of the characterizations of caveolae is the high concentrations of lipids such as cholesterol found around the caveolin proteins, these areas of high lipid concentrations are known as lipid rafts.[145] It is of note however that lipid rafts are not just involved in membrane trafficking, they also play roles in neurotransmission and receptor trafficking, and they serve as organization areas for signalling molecules.

1.8.5 Direct membrane translocation

Direct membrane translocation (*DMT*) offers an energy independent method for cellular uptake. Whist endocytosis (an energy dependent uptake pathway) will not function below 4 °C, direct membrane translocation will still occur under conditions that would usually prevent uptake *via* endocytosis.[144] DMT is a process that occurs much faster than endocytosis and does not have the same cellular metabolic requirements, whilst it takes 5-15 minutes for endosomes to start to form,[89,146] CPPs that uptake cargos *via* DMT can enter into cells and deliver their cargos within 5 minutes.[89] DMT processes often cause membrane disruption, forming pores or gaps within the membrane that allow the CPPs to pass through.[103] It is thought that one of the primary requirements for DMT is to have primary amphipathic CPPs at a high concentration.[147]

1.8.6 Micelle formation

The inverted micelle model was suggested early on as a proposed mechanism for the uptake of penetratin,[148] with the proposed method of action being the interaction of charged peptides with the oppositely charged phospholipids on the outside of the membrane. This interaction leads to destabilization of the lipid bilayer, forming inverted micelles around the CPPs as they travel towards the inside of the cell. These micelles open out onto the cytoplasmic side of the cell.[96,103,148] Figure 1.11 is a representation of this proposed mechanism.[96]

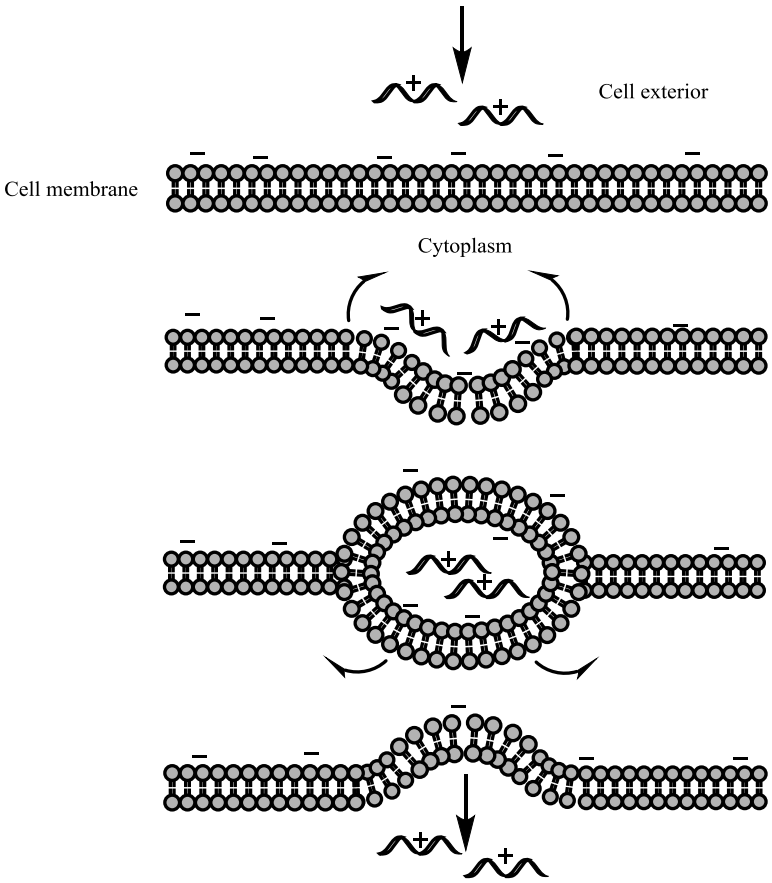

Figure 1.11. The proposed model of cell internalization by the micelle method. Here the CPP represented as a helix interacts with the negative phospholipids, inducing micelle formation. The micelle is often hydrophilic and possibly allows for the removal of cargos attached to the peptide. The half arrows indicate the movement of the membrane around the CPPs showing the formation of the micelle.

1.8.7 Carpet model

The carpet model gets its name from the proposed way the CPPs line themselves up along the membrane.[149] In this model the CPPs are able to translocate across the membrane by an extensive association and build-up of peptide on the membrane, causing a destabilization of the membrane, leading to translocation into the cell, followed by phospholipid reorganization.[150] One of the differences between the Carpet models and the other DMT uptake models is that the CPPs do not insert themselves into the membrane, nor do they assemble with their hydrophilic surfaces facing each other.[149]

1.8.8 Pore formation

Pore formation can occur one of 2 ways,[151] either the toroidal pore, or the barrel stave pore model. The barrel-stave pore model describes CPPs with α-helices forming transmembrane pores, the CPPs organise themselves in such a way that their hydrophobic surfaces interact with the membranes lipid core, which produces an aqueous pore allowing peptides to pass through.[149] The toroidal pore model functions almost identically to the barrel model, with the difference being that the peptides that insert into the membrane would interact solely with the membranes polar groups, which would induce significant membrane restructuring.[152,153] Pore formation has been studied using the Tat peptide by Herce and Garcia.[154] Their model introduces the idea of the Tat peptides acting in a cooperative manner; the Tat peptides build in concentration in a localized area of a cell membrane. When the peptide levels reach a certain density, their positive charge begins to attract the phosphate groups on the inside of the membrane, essentially causing membrane thinning. Once the bilayer has been 'thinned' sufficiently, lysine and arginine side chains on the peptides insert into the bilayer and nucleate the formation of a pore, which allows the Tat peptides to pass through by diffusing along the walls of the pore.[155]

1.9 Aims of this work

In this work both the NfnB and YfkO NTRs that have been previously genetically modified to contain 6 cysteine residues per monomer, will be tested for their ability to reduce the prodrug CB1954 and for their ability to cause cell death by the reduction of CB1954. They will be conjugated to the CPPs; HR9 and Pep-1, again being tested for their ability to reduce the prodrug CB1954 at varying CPP:NTR ratios. Following this, the kinetic and HPLC profiles of the conjugates will be determined after initial conjugation and conjugate activity has been established. Furthermore, the conjugates will be tested for their ability to cause cell death by the reduction of CB1954.

Additional to this work is the synthesis of gold-coated superparamagnetic iron nanoparticles (*AuMNPs*), along with characterization and purification of these nanoparticles. This work is adapting upon a synthesis that has been previously started in the research group, with the intention of improving the coating of the iron oxide nanoparticles, as well as the creating of nanoparticles with a uniform size and shape distribution. These AuMNPs are intended for use in our novel MNDEPT therapy and, so will be tested for their stability under various conditions, as well as conjugation to the genetically modified enzymes. The genetically modified NfnB-

Cys will be conjugated to the AuMNPs at a pre-determined ratio based on the size of the AuMNPs,[83] they will then be tested for their ability to cause cell death by the reduction of the CB1954 prodrug. Following on from this, HR9 and Pep-1 will be conjugated onto the AuMNP:NfnB-Cys at a ratio determined after the 'free' NTR:CPP conjugates have been assessed for their enzymatic activity, kinetic and HPLC profiles as well as their use in cell viability assays.

1.9 Bibliography

1 World Health Organization (WHO), *Latest global cancer data,* 2018.

2 Cancer Research UK, Cancer risks, https://www.cancerresearchuk.org/health-professional/cancer-statistics-for-the-uk#heading-Three, (accessed 15 November 2018).

3 M.Stiefel, A. Shaner and S. D. Schaefer, *Laryngoscope*, 2006, **116**, 182-188.

4 D. H. Roukos, *Expert Rev. Anticancer Ther.*, 2009, **9**, 389-392.

5 M. H. Forouzanfar, A. Afshin, L. T. Alexander, S. Biryukov, M. Brauer, K. Cercy, F. J. Charlson, A. J. Cohen, L. Dandon, K. Estep *et al.*, *Lancet*, 2016, **388**, 1659-1724.

6 L.H. Kushi, C. Doyle, M. McCullough, C. L. Rock, W. Denmark-Wahnefried, E. V. Bandera, S. Gapstur, A.V. Patel, K. Andrews, T. Gansler, and The American Cancer Society 2010 Nutrition and Physical Activity Guidelines Advisory Committee, *CA. Cancer J. Clin.*, 2012, **62**, 30-67.

7 S. Park, J. Bae, B. H. Nam, and K. Y. Yoo, *Asian Pacific J. Cancer Prev.*, 2008, **9**, 371-380.

8 H. Jayasekara, R. J. MacInnis, R. Room and D. R. English, *Alcohol and Alcoholism*, 2016, **51**, 312-330.

9 P. Anand, A. B. Kunnumakara, C. Sundaram, K. B. Harikumar, S. T. Tharakan, O. S. Lai, B. Sung and B. B. Aggarwal, *Pharm. Res.*, 2008, **25**, 2097-2116.

10 L. Hayflick and P. S. Moorhead, *Exp. Cell Res.*, 1961, **25**, 585-621.

11 D. Hanahan and R. A. Weinberg, *Cell*, 2000, **100**, 57-70.

12 D. Hanahan and R. A. Weinberg, *Cell*, 2011, **144**, 646-674.

13 B. Goff, *Clin. Obstet. Gynecol.*, 2012, **55**, 36-42.

14 D. Walsh, S. Donnelly and L. Rybiki, *Support Care Cancer*, 2000, **8**, 175-179.

15 K. Kroenke, S. A. Johns, D. Theobald, J. Wu and W. Tu, *Support Care Cancer*, 2013, **21**, 765-773.

16 S. K. Chaturvedi, P. Hopwood, and P. Maguire, *Eur. J. Cancer*, 1993, **29**, 1006-1008.

17 W. E. Barlow, *Cancer Spectrum Knowl. Environ.*, 2002, **94**, 1151-1159.

18 A. G. Knudson, *Nat. Rev. Cancer*, 2001, **1**, 157-162.

19 A. Silverstein, V. Silverstein and L. Nunn, *Cancer: Conquering a Deadly Disease,* Twenty-First Century Books, Minnesota, 2006.

20 National cancer institute: Metastatic cancer: questions and answers, https://www/cancer.gov/type/metastatic-cancer?redirect=true, (accessed 14 September 2018).

21 R. B. Mokhtari, T. S. Homayouni, N. Baluch, E. Morgatskaya, S. Kumar, B. Das and H. Yeger, *Oncotarget*, 2015, **8**, 38022-38043.

22 National Cancer Institute, Surgery to treat cancer, https://www/cancer.gov/about-cacer/treatmer/types/surgery, (accessed 15 November 2018).

23 Cancer Research UK, About Surgery, https://www.cancerresearchuk.org/about-cancer/cancer-in-general/treatment/surgery/about, (accessed 15 November 2018).

24 L. Goldman, *Ann. Surg.*, 1983, **198**, 780-791.

25 J. H. Silber, P. R. Rosenbaum, R. R. Kelz, C. E. Reinke, M. D. Neuman, R. N. Ross, O. Even-Shoshan, G. David, P. A. Saynisch, F. A. Kyle, D. W. Bratzler and L. A. Fleisher, *Ann. Surg.*, 2012, **256**, 79-86.

26 P. S. Pasulka, B. R. Bistrain, P. N. Benotti and G. L. Blackburn, *Ann. Inter. Med.*, 1986, **104**, 540-546.

27 J. J. M. Wise, J. S. M. Fischgrund, H. N. M. Herkowitz, D. M. Montgomery and L. T. M. Kurz, *Spine*, 1999, **24**, 1943-1951.

28 C. Bromford, I. Kunkler and J. Wlater, *Walter and Miller;s Textbook of radiotherapy: radiation physics, therapy and oncology*, Churchill livingstone, New York, 6th edn., 2003.

29 C. Badie, G. Iliakis, N. Foray, G. Alsbeih, G. E. Pantellias, R. Okayasu, N. Cheong, N. S. Russel, A. C. Begg, C. F. Arlett and E. P. Malaise, *Cancer Res.*, 1995, **55**, 1232-1234.

30 P. M. O'Connor, J. Jackman, D. Jondle, K. Bhatia, I. Magrath and L. W. Kohn, *Cancer Res*., 1993, **53**, 4776-4780.

31 Y. Kuwahara, M. H. Roudkenar, Y, Urushihara, Y. Saito, K. Tomita, A. M. Roushandeh, T. Saito, A. Kurimasa and M. Fukumoto, *Med. Mol. Morphol.*, 2017, **50**, 195-204.

32 E. Maverakis, L. Cornelius, G. Bowen, T. Phan, F. Patel, S. Fitzmaurice, Y. He, B. Burral, C. Duong, A. Kloxin, H. Sultani, R. Wilekn, S.Martinez, and F. Patel, *Acta Derm, Venereol.*, 205 **95**, 526-524.

33 O. Fuge, N. Vasdev, P. Allchorne, and J. Green, *Res. Reports Urol.*, 2015, **7**, 65-79.

34 M. Chiriva-Internati and A. Bot, *Int. Rev. Immuno*.m 2015, **34**, 101-103.

35 D. Pardoll, *Semin. Oncol.*, 2015, **42**, 523-538.

36 C. L. Ventola, *P&T.*, 2017, **42**, 514-521.

37 R. Gerl and D. L. Vaux, *Carcinogensis*, 2005, **26**, 263-270.

38 J. E. Fenn and R. Udelsman, *J. Am. Coll. Surg.*, 2011, **212**, 413-417.

39 J. Rautio, N.A. Meanwell, L. Di and M. J. Hageman, *Nat. Rev. Drug Discov.*, 2018, **17**, 559-587.

40 K. M. Wi, *Pharmaceuticals*, 2009, **2**, 77-81.

41 R. J. Knox, F. Friedlos and M. P. Boland, *Cancer Metastais Rev.*, 1993, **12**, 195-212.

42 R. J. Knox, M. P. Boland, F. Friedlos, B. Coles, C. Southan and J. J. Roberts, *Biochem. Pharmacol.*, 1988, **37**, 4671-4677.

43 R. Knox, P. Burke, S. Chen and D. Kerr, *Curr. Pharm. Des.*, 2003, **9**, 2091-2104.

44 R. J. Knox, F. Friedlos, R. F. Sherwood, R. G. Melton and G. M. Anlezark, *Biochem. Pharmacol.*, 1992, **44**, 2297-2301.

45 J. J. Roberts, F. Friedlos, and R. J. Knox, *Biochem, Biophys. Rev. Commun.*, 1986, **140**, 1073-1078.

46 J. Balzarini, C. Bohman, and E. De Clercq, *J. Biol. Chem.*, 1993, **268**, 6332-6337.

47 W. B. Mattes, J. A. Hartley and K. W. Kohn, *Nucleic Acids Res.*, 1986, **14**, 2971-2987.

48 N. A. Helsby, D. M. Ferry, A. V. Patterson, S. M. Pullen and W. R. Wilson, *Br. J. Cancer*, 2004, **90**, 1084-1092.

49 B. E. Huber, E. A. Austin, C. A. Richard, S. T. Davis and S. S. Good, *Proc. Natl. Acad. Sci. U.S.A.*, 1994, **91**, 8302-8306.

50 S. M. Freeman, C. N. Abboud, K. A. Whartenby, C. H. Packman, D.S. Koeplin, F. L. Moolten and G. N. Abraham, *Cancer Res.*, 1993, **53**, 5274-5283.

51 G. U. Dachs, M. A. Hunt, S. Syddall, D. C. Singleton and A. V. Patterson, *Molecules*, 2009, **14**, 4517-4545.

52 S. Duarte, G. Carle, H. Faneca, M. C. P. de Lima dn V. Pierrefite-Carle, *Cancer Lett.*, 2012, **324**, 160-170.

53 S. C. Tu, J. E. Becvar and J. W. Hastings, *Arch. Biochem. Biophys*., 1979, **193**, 110-116.

54 P. R. Race, A. L. Lovering, S. A. White, J. I. Grove, P. F. Searle, C. W. Wrighton and E. Hyde, *J. Mol. Biol.*, 2007, **368**, 481-492.

55 V. V. Gwenin, P. Poornima, J. Halliwell, P. Ball, G. Robinson and C. D. Gwenin, *Biochem. Pharmacol.*, 2015 **98**, 392-402.

56 A. Cornish-Bowden, *Fundamentals of enzyme kinetics*, Portland Press, London, UK, 4th edn., 1995.

57 S. J. Weedon, N. K. Green, I. A. McNeish, M. G. Gilligan, V. Mautner, C. J. Wrighton, A. Mountain, L. S. Young, D. J. Kerr and P. F. Searle, *Int. J. cancer*, 2000, **86**, 848-854.

58 G. A. Prosser, J. N. Copp, S. P. Syddall, E. M. Williams, J. B. Smaill, W. R. Wilson, A. V. Patterson and D. F. Ackerley, *Biochem. Pharmacol.*, 2010, **79**, 678-687.

59 C. D. Gwenin, M. Kalaji, P. A. Williams and C. M. Kay, *Biodegradation*, 2011, **22**, 463–474.

60 P. Patel, J. G. Young, V. Mautner, D. Ashdown, S. Bonney, R. G. Pineda, S. I. Collins, P. F. Searle, D. Hull, E. Peers, J. Chester, D. M. Wallace, A. Doherty, H. Leung, L. S. Young and N. D. James, *Mol. Ther*., 2009, **17**, 1292–1299.

61 C. D. Gwenin, M. Kalaji, P. A. Williams and R. M. Jones, *Biosens. Bioelectron.*, 2007, 22, 2869–2875.

62 P. F. Searle, M. J. Chen, L. Hu, P. R. Race, A. L. Lovering, J. I. Grove, C. Guise, M. Jaberipour, N. D. James, V. Mautner, L. S. Young, D. J. Kerr, A. Mountain, S. A. White and E. I. Hyde, *Clin. Exp. Pharmacol. Physiol.*, 2004, **31**, 811–816.

63 M. D. Roldán, E. Pérez-Reinado, F. Castillo and C. Moreno-Vivián, *FEMS Microbiol. Rev.*, 2008, **32**, 474–500.

64 C. Bryant and M. DeLuca, *J. Biol. Chem.*, 1991, **266**, 4119–4125.

65 F. J. Peterson, R. P. Mason, J. Hovsepian and J. L. Holtzman, *J. Biol. Chem.*, 1979, **254**, 4009–4014.

66 L. Angermaier and H. Simon, *Hoppe. Seylers. Z. Physiol. Chem.*, 1983, **364**, 1653–1663.

67 R. P. Mason and J. L. Holtzman, *Biochem. Biophys. Res. Commun.*, 1975, **67**, 1267–1274.

68 K. Yamada, N. Hara, T. Shibata, H. Osago and M. Tsuchiya, *Anal. Biochem.*, 2006, **352**, 282–285.

69 N. Ma, M. A. Digman, L. Malacrida and E. Gratton, *Biomed. Opt. Express*, 2016, **7**, 2441-2452.

70 Q. Yu and A. A. Heikal, *J. Photochem. Photobiol. B Biol.*, 2009, **95**, 46–57.

71 G. S. Timmins and V. Deretic, *Mol. Microbiol.*, 2006, **62**, 1220–1227.

72 C. D. Emptage, R. J. Knox, M. J. Danson and D. W. Hough, *Biochem. Pharmacol.*, 2009, **77**, 21–29.

73 S. O. Vass, D. Jarrom, W. R. Wilson, E. I. Hyde and P. F. Searle, *Br. J. Cancer*, 2009, **100**, 1903–1911.

74 S. Schepelmann and C. J. Springer, *Curr. Gene Ther.*, 2006, **6**, 647–670.

75 D. H. Palmer, V. Mautner, D. Mirza, S. Oliff, W. Gerritsen, J. R. M. Van der Sijp, S. Hubscher, G. Reynolds, S. Bonney, R. Rajaratnam, D. Hull, M. Horne, J. Ellis, A. Mountain, S. Hill, P. A. Harris, P. F. Searle, L. S. Young, N. D. James and D. J. Kerr, *J. Clin. Oncol.*, 2004, **22**, 1546–1552.

76 M. P. Cude and C. D. Gwenin, *ECS Trans.*, 2011, **4**, 79–89.

77 J. Rüschoff, W. Hanna, M. Bilous, M. Hofmann, R. Y. Osamura, F. Penault-Llorca, M. Van De Vijver and G. Viale, *Mod. Pathol.*, 2012, **25**, 637–650.

78 J. Meza-Junco, H. J. Au and M. B. Sawyer, *Cancer Manag. Res.*, 2011, **3**, 57–64.

79 S. I. Chiosea, L. Williams, C. C. Griffith, L. D. R. Thompson, I. Weinreb, J. E. Bauman, A. Luvison, S. Roy, R. R. Seethala and M. N. Nikiforova, *Am. J. Surg. Pathol.*, 2015, **39**, 744–752.

80 J. Zhang, V. Kale and M. Chen, *AAPS J.*, 2015, **17**, 102–110.

81 W. A. Denny, *Eur. J. Med. Chem.*, 2001, **36**, 577–595.

82 European Union Patent, EP2473197-A2, 2009.

83 V. V. Gwenin, C. D. Gwenin and M. Kalaji, *Langmuir*, 2011, **27**, 14300–14307.

84 D. L. Kokkin, R. Zhang, T. C. Steimle, I. A. Wyse, B. W. Pearlman and T. D. Varberg, *J. Phys. Chem. A*, 2015, **119**, 11659–11667.

85 A. Marín, M. Martín, O. Liñán, F. Alvarenga, M. López, L. Fernández, D. Büchser and L. Cerezo, *Reports Pract. Oncol. Radiother.*, 2015, **20**, 12–21.

86 I. M. Pope, G. J. Poston and A. R. Kinsella, *Eur. J. Cancer Part A*, 1997, **33**, 1005–1016.

87 G. N. Parkinson, J. V. Skelly and S. Neidle, *J. Med. Chem.*, 2000, **43**, 3624–3631.

88 F. Madani, S. Lindberg, Ü. Langel, S. Futaki and A. Gräslund, *J. Biophys.*, 2011, **2011**, 1-10.

89 B. R. Liu, Y. Wern Huang, J. G. Winiarz, H. J. Chiang and H. J. Lee, *Biomaterials*, 2011, **32**, 3520–3537.

90 S. Trabulo, A. L. Cardoso, M. Mano and M. C. P. de Lima, *Pharmaceuticals*, 2010, **3**, 961–993.

91 M. C. Morris, S. Deshayes, F. Heitz and G. Divita, *Biol. Cell*, 2008, **100**, 201–217.

92 M. Green and P. Loewenstein, *Cell*, 1988, **55**, 1179–1188.

93 P. A. Wender, D. J. Mitchell, K. Pattabiraman, E. T. Pelkey, L. Steinman and J. B. Rothbard, *Proc. Natl. Acad. Sci.*, 2000, **97**, 13003–13008.

94 M. Di Pisa, G. Chassaing and J. M. Swiecicki, *Biochemistry*, 2015, **54**, 194–207.

95 P. Järver and Ü. Langel, *Biochim. Biophys. Acta - Biomembr.*, 2006, **1758**, 260–263.

96 D. Derossi, S. Calvet, A. Trembleau, A. Brunissen, G. Chassaing and A. Prochiantz, *J. Biol. Chem.*, 1996, **271**, 18188–18193.

97 M. C. Morris, J. Depollier, J. Mery, F. Heitz and G. Divita, *Nat. Biotechnol.*, 2001, **19**, 1173–1176.

98 S. Futaki, T. Suzuki, W. Ohashi, T. Yagami, S. Tanaka, K. Ueda and Y. Sugiura, *J. Biol. Chem.*, 2001, **276**, 5836–5840.

99 J. Oehlke, A. Scheller, B. Wiesner, E. Krause, M. Beyermann, E. Klauschenz, M. Melzig and M. Bienert, *Biochim. Biophys. Acta - Biomembr.*, 1998, **1414**, 127–139.

100 A. Ziegler, *Adv. Drug Deliv. Rev.*, 2008, **60**, 580–597.

101 L. D. Field, J. B. Delehanty, Y. Chen and I. L. Medintz, *Acc. Chem. Res.*, 2015, **48**, 1380–1390.

102 E. Vives, P. Brodin and B. Lebleu, *J. Biol. Chem.*, 1997, **272**, 16010–16017.

103 P. E. G. Thoren, D. Persson, P. Lincoln and B. Norden, *Biophys. Chem.*, 2005, **114**, 169–179.

104 S. Futaki, T. Suzuki, W. Ohashi, T. Yagami, S. Tanaka, K. Ueda and Y. Sugiura, *J. Biol. Chem.*, 2001, **276**, 5836–5840.

105 S. Deshayes, M. C. Morris, G. Divita and F. Heitz, *Biochim. Biophys. Acta - Biomembr.*, 2006, **1758**, 328–335.

106 S. Deshayes, S. Gerbal-Chaloin, M. C. Morris, G. Aldrian-Herrada, P. Charnet, G. Divita and F. Heitz, *Biochim. Biophys. Acta - Biomembr.*, 2004, **1667**, 141–147.

107 D. Zhang, J. Wang and D. Xu, *J. Control. Release*, DOI:10.1016/j.jconrel.2016.03.020.

108 M. H. Wang and D. C. Otteson, *J. Neurosci.*, 2010, **177**, 403–419.

109 M. C. Morris, E. Gros, G. Aldrian-Herrada, M. Choob, J. Archdeacon, F. Heitz and G. Divita, *Nucleic Acids Res.*, DOI:10.1093/nar/gkm053.

110 B. R. Liu, J.-F. Li, S.-W. Lu, H.-J. Leel, Y.-W. Huang, K. B. Shannon and R. S. Aronstam, *J. Nanosci. Nanotechnol.*, 2010, **10**, 6534–6543.

111 H. Margus, K. Padari and M. Pooga, *Mol. Ther.*, 2012, **20**, 525–533.

112 J. S. Wadia and S. F. Dowdy, *Opin. Biotechnol.*, 2002, **13**, 52–56.

113 F. Heitz, M. C. Morris and G. Divita, *Br. J. Pharmacol.*, 2009, **157**, 195–206.

114 C. Bechara and S. Sagan, *FEBS Lett.*, 2013, **587**, 1693–1702.

115 S. W. Jones, R. Christison, K. Bundell, C. J. Voyce, S. M. V. Brockbank, P. Newham and M. A. Lindsay, *Br. J. Pharmacol.*, 2005, **145**, 1093–1102.

116 H. G. Boman, *Annu. Rev. Immunol.*, 1995, **13**, 61–92.

117 J. L. Dimarcq, P. Bulet, C. Hetru and J. Hoffmann, *Biopolym.*, 1998, **47**, 465–477.

118 E. Eiríksdóttir, K. Konate, Ü. Langel, G. Divita and S. Deshayes, *Biochim. Biophys. Acta - Biomembr.*, 2010, **1798**, 1119–1128.

119 S. Deshayes, A. Heitz, M. C. Morris, P. Charnet, G. Divita and F. Heitz, *Biochemistry*, 2004, **43**, 1449–1457.

120 B. D. Grant and J. G. Donaldson, *Nat. Rev. Mol. Cell Biol.*, 2009, **10**, 597–608.

121 P. M. Fischer, N. Z. Zhelev, S. Wang, J. E. Melville, R. Fåhraeus and D. P. Lane, *J. Pept. Res.*, 2000, **55**, 163–172.

122 F. Milletti, *Drug Discov. Today*, 2012, **17**, 850–860.

123 D. J. Mitchell, L. Steinman, D. T. Kim, C. G. Fathman and J. B. Rothbard, *J. Pept. Res.*, 2000, **56**, 318–325.

124 C. N. Carrigan and B. Imperiali, *Anal. Biochem.*, 2005, **341**, 290–298.

125 K. Takayama, I. Nakase, H. Michiue, T. Takeuchi, K. Tomizawa, H. Matsui and S. Futaki, *J. Control. Release*, 2009, **138**, 128–133.

126 A. Elmquist, M. Hansen and Ü. Langel, *Biochim. Biophys. Acta - Biomembr.*, 2006, **1758**, 721–729.

127 D. Delaroche, B. Aussedat, S. Aubry, G. Chassaing, F. Burlina, G. Clodic, G. Bolbach, S. Lavielle and S. Sagan, *Anal. Chem.*, 2007, **79**, 1932–1938.

128 A. Walrant, L. Matheron, S. Cribier, S. Chaignepain, M. L. Jobin, S. Sagan and I. D. Alves, *Anal. Biochem.*, 2013, **438**, 1–10.

129 J. R. Maiolo, M. Ferrer and E. A. Ottinger, *Biochim. Biophys. Acta - Biomembr.*, 2005, **1712**, 161–172.

130 A. T. Jones and E. J. Sayers, *J. Control. Release*, 2012, **161**, 582–591.

131 B. Christiaens, J. Grooten, M. Reusens, A. Joliot, M. Goethals, J. Vandekerckhove, A. Prochiantz and M. Rosseneu, *Eur. J. Biochem.*, 2004, **271**, 1187–1197.

132 S. T. Henriques and M. A. R. B. Castanho, *Biochim. Biophys. Acta - Biomembr.*, 2005, **1669**, 75–86.

133 S. Mukherjee, R. N. Ghosh and F. R. Maxfield, *Physiol. Rev.*, 1997, **77**, 759–803.

134 I. Mellman, *Annu. Rev. Cell Dev. Biol.*, 1996, **12**, 575–625.

135 W. Stoorvogel, G. J. Strous, H. J. Geuze, V. Oorschot and A. L. Schwartzt, *Cell*, 1991, **65**, 417–427.

136 G. Weissman, B. Becher, G. Weidermann and A. W. Bernheimer, *Am. J. Pathol.*, 1965, **46**, 129–147.

137 J. P. Lim and P. A. Gleeson, *Immunol. Cell Biol.*, 2011, **89**, 836–843.

138 W. Lewis, *John Hopkins Hosp. Bull.*, 1931, **49**, 17–27.

139 L. J. Hewlett, A. R. Prescott and C. Watts, *J. Cell Biol.*, 1994, **124**, 689–703.

140 J. A. Swanson and C. Watts, *Trends Cell Biol.*, 1995, **5**, 424–428.

141 A. Sorkin and M. Puthenveedu, in *Clathrin-Mediate Endocytosis*, eds. Y. Yarden and G. Tarcic, Springer New York, New York, NY, 2013.

142 S. E. Miller, S. Mathiasen, N. A. Bright, F. Pierre, B. T. Kelly, N. Kladt, A. Schauss, C. J. Merrifield, D. Stamou, S. Höning and D. J. Owen, *Dev. Cell*, 2015, **33**, 163–175.

143 J. Bossuyt, B. E. Taylor, M. James-Kracke and C. C. Hale, *FEBS Lett.*, 2002, **511**, 113–117.

144 G. J. Doherty and H. T. McMahon, *Annu. Rev. Biochem.*, 2009, **78**, 857–902.

145 Z. Korade and A. K. Kenworthy, *Neuropharmacology*, 2008, **55**, 1265–1273.

146 M. Zorko and Ü. Langel, *Adv. Drug Deliv. Rev.*, 2005, **57**, 529–545.

147 F. Duchardt, M. Fotin-Mleczek, H. Schwarz, R. Fischer and R. Brock, *Traffic*, 2007, **8**, 848–866.

148 D. Derossi, G. Chassaing and A. Prochiantz, *Trends Cell Biol.*, 1998, **8**, 84–87.

149 Y. Shai, *Biochim. Biophys. Acta - Biomembr.*, 1999, **1462**, 55–70.7

150 K. Matsuzaki, K. Sugishita, M. Harada, N. Fujii and K. Miyajima, *Biochim Biophys Acta*, 1997, **1327**, 119–130.

151 M. R. Yeaman, *Pharmacol. Rev.*, 2003, **55**, 27–55.

152 P. Lundberg and U. Langel, *J. Mol. Recognit.*, 2003, **16**, 227–33.

153 L. Yang, T. A. Harroun, T. M. Weiss, L.Ding and H. W. Huang, *Biophys. J.*, 2001, **81**, 1475–1485.

154 H. D. Herce, A. E. Garcia, J. Litt, R. S. Kane, P. Martin, N. Enrique, A. Rebolledo and V. Milesi, *Biophys. J.*, 2009, **97**, 1917–1925.

155 H. D. Herce and A. E. Garcia, *Proc. Natl. Acad. Sci.*, 2007, **104**, 20805–20810.

Chapter 2: Magnetic Nanoparticles in Drug Delivery: A review

The majority of the contents of this chapter can be found in:

Magnetic Functionalized Nanoparticles for Biomedical, Drug Delivery and Imaging Applications

Nanoscale research letters- accepted for publication May 2019

S. Anderson, V. Gwenin, C. Gwenin

2.0 Introduction

Nanoparticles have been utilised by mankind as far back as ancient Mesopotamia for creating a shining/ glittering effect on pots and cups.[1] However the first real scientific discussion surrounding the idea of nanoparticles was possibly presented in 1857 by Michael Faraday, in his Bakerian lecture, entitled: Experimental Relations of Gold (and Other Metals) to Light.[2] Since this first discussion, there has been an explosion into the study of nanoparticles, in particular medical applications of nanoparticles.[3–13] It is the physical and chemical properties of nanoparticles that makes them so desirable, for example the large surface area to volume ratio makes them ideal candidates for the delivery of drugs and other cargoes to areas around the body.[14,15] Whilst other nanomaterials present properties that make them valuable in medical applications, two examples of this are ZnO and TiO_2 nanoparticles used as UV filters in sunscreen.[16–19] There is debate however regarding the potential toxicity of these nanoparticles, with some studies indicating negative health effects,[17,20,21] however a study has indicated that it is only at very high concentrations (1.2×10^{-5} *M*) that TiO_2 nanoparticles demonstrate any cytotoxic properties,[22] and only on damaged skin as the nanoparticles are unable to permeate intact skin.[22]

One of the current trends of nanoparticle research revolves around magnetic nanoparticles in medicine for uses such as medical imaging,[23,24] and drug delivery.[25,26] Whilst Fe_3O_4 nanoparticles have already been approved for medical use by the FDA,[27] many magnetic materials are unsuitable as they can be highly toxic.[28,29] Coating a magnetic nanoparticle with a biologically inert material such as gold,[30] or a material that has pharmaceutical properties such as silver[4,31,32] may present a way around any potential toxicity issues. However there is a larger benefit to coating these nanoparticles; it is very easy to conjugate medical cargoes such as drugs[12,33,34] or DNA[35–37] onto them for delivery into and around the body.

Further to this, here is presented a review paper: Magnetic Functionalized Nanoparticles for Biomedical, Drug Delivery and Imaging Applications, that discusses some of the methods used to synthesise single metal nanoparticles as well as current published core-shell metal nanoparticle synthesis along with the bio-medical applications of these different types of nanoparticles.

2.1 Abstract

Medicine is constantly looking for new and improved treatments for diseases, which need to have a high efficacy and be cost effective, creating a large demand on scientific research to discover such new treatments. One important aspect of any treatment is the ability to be able to target only the illness and not cause harm to another healthy part of the body. For this reason metallic nanoparticles have been and are currently being extensively researched for their possible medical uses, including: medical imaging, antibacterial and antiviral applications. Superparamagnetic metal nanoparticles possess properties that allow them to be directed around the body with a magnetic field or directed to a magnetic implant, which opens up the potential to conjugate various bio-cargos to the nanoparticles that could then be directed for treatment in the body.

2.2 Background

Metal nanomaterials represent a significant doorway for the future of medicine. Although there is still much unknown about the long term safety of metal nanoparticles in medicine,[38] these particles have already found their place within various biomedical applications such as; site-specific imaging *in vivo*,[39–41] cancer detection,[42,43] cancer therapy,[44–47] neurodegenerative disease therapy, [48–50] HIV/AIDS therapy,[51–53] ocular disease therapy,[54–56] and respiratory disease therapy .[57,58] Despite the recent advances in nanomedicine there are still many obstacles in the way of nano-therapy. For instance it can be difficult to achieve a synthetic route which produces easily repeatable results, with many nanoparticle synthesis methods producing a range in both size[59–61] and shape[62–65] of nanoparticles and/or do not produce the nanomaterials in a large enough quantity to make it economically viable.[66] Another key factor is that it is relatively unknown as to the toxicity of some nanoparticles over an extended period of time due to how relatively new the field of research is.[29,67] Among the many possible uses of metal nanoparticles lies the area of drug delivery.[68,69] Due to the large surface area that nanoparticles provide,[70] they possess the ability to be able to deliver large quantities of drugs or other medical cargoes.[71]

This review first focuses on some of the current bio-medical applications of metal nanoparticles, their limitations and how to overcome them. Focusing on gold/silver iron-coated magnetic nanoparticles as new and exciting materials which can overcome the current limitations of standard metal nanoparticles, the final section focusses on the methods to generate these particles.

2.3 Bio-medical applications of gold/silver coated iron oxide nanoparticles

2.3.1 Antimicrobial agents

Bacterial infections are very common, with antibiotics being a primary method of treatment since the discovery of Penicillin in 1928 by Alexander Fleming.[72] Nanomedicine provides us with a new, broad range of possible treatment modalities, with metal nanoparticles being explored for future treatments.[73] Table 1 lists some of the nanoparticles that have been explored for antimicrobial applications. One material that has been examined for its potential use is silver, which has shown to have a variety of biomedical uses,[74] for example Sreekumar *et al*. utilized silver nanoparticles as part of a network of antimicrobial fibers. The nanoparticles varied in size from 20-120 nm, with an antibacterial efficacy against *Escherichia coli* as high as 94.3 % compared to the fibers without silver nanoparticles.[75] Whilst it has been shown that an antibiotic such as ampicillin are capable of achieving a kill rate of ≤ 99.9 % in *E.coli*,[3] the same study also reported the emergence of resistance to ampicillin in certain strains of *E.coli*. On this same note it has been reported that *E.coli* can develop a resistance to silver nanoparticles, however this resistance is not a genetic change, it is a physical response that attempts to cause the colloidal nanoparticles to aggregate.[4]

Table 1 lists antibacterial properties that have been exhibited by some metal nanoparticles and metal nanoparticle conjugates

Type of Nanoparticle	Size (nm)	Antimicrobial application	Mechanism of action	Ref
Silver as part of network of fibers	20-120	*E.coli*	Bacterial growth inhibition	75
Silver vanadate nanowires	1-20	*S. aureus*	Bacterial growth inhibition	31
Naked silver	10-25	*C. albicans, P. fluorescens, E. coli*	Bacterial growth inhibition	76
Thioguanine capped gold	3-4	*E. coli, A. fumigatus, P. aeruginosa*, and anti-cancer effect against Hep2	Bacterial growth inhibition, cellular toxicity	79
Naked gold	25	*C. pseudotuberculosis*	Vacuole formation in cell wall, and agglomeration of NPs within cells	80
Naked gold	6-40	*S. aureus, K. pneumonia, B. subtilis*	Bacterial growth inhibition	81

Also employing silver for its antibacterial properties, Holtz *et al*. designed a system of 60 nm silver vanadate nanowires 'decorated' with silver nanoparticles with a diameter of 1-20 nm.[31] This system showed to be promising against three *Staphylococcus aureus* strains, and also interestingly had a much lower growth inhibiting concentration against Methicillin-resistant Staphylococcus aureus (*MRSA*) than the antibiotic oxacillin.

A silver nanoparticle synthesis was reported by Verma *et al*. where they employed their nanoparticles against the bacteria: *Pseudomonas fluorescens, E. coli* and the fungus: *Candida albicans*.[76] The silver nanoparticles had an average minimum inhibitory growth concentration of 5.83 µg/ml across the three strains, compared to some commonly used anti-biotics such as ampicillin and neomycin which have minimum inhibitory growth concentrations of 4.0 µg/ml and 16.0 µg/ml respectively against strains of *E.coli*.[77] Of potential interest is the properties the nanoparticles displayed against *P. fluorescens* an *C. albicans*, both of which are associated with causing disease in immunocompromised patients.[78] Further investigations might find that the silver nanoparticles are a more efficient way to treat the pathogens than some of the most commonly used antibiotics, such as amphotericin B, which has extensive side effects.[10]

The synthesis of thioguanine-capped gold nanoparticles has been reported by Selvaraj *et al*. where an enhanced antimicrobial effect against several bacterium, including: *E. coli*, *Aspergillus fumigatus* and *Pseudomonas aeruginosa*.[79] It was found that the thioguanine-capped gold nanoparticles were more effective than unconjugated thioguanine as anticancer and antimicrobial agents, with their activities showing potential use as carriers for cancer drugs. In a similar manner gold nanoparticles have been reported to have an antimicrobial effect on *Corynebacterium pseudotuberculosis*,[80] nanoparticles with an average size of 25 nm, using a dose of 50 µg/ml showed a bacterial growth inhibition of 95 % after 20 minutes of exposure. Similarly naked gold nanoparticles were shown to have an antimicrobial effect on a variety of gram negative and gram positive bacteria including; *S. aureus, Klebsiella pneumonia* and *Bacillus subtilis*.[81] A dose of 1.35 µg/ml of AuNPs showed a growth inhibition of: 46.4 % ±0.4 %, 38.3 % ±0.2 % and 57.8 % ±0.2 % for *S. aureus, K. pneumonia* and *B. subtilis* respectively.

2.3.2 Antiviral

Metal nanoparticles have shown to be promising in antiviral applications; Table 2 demonstrates a range of nanoparticles that have been shown to possess antiviral properties and could potentially be applied when treating viruses. Both naked and coated silver nanoparticles[82–85] have been shown to have a range of antiviral applications when in the nano-scale range.

Table 2 presents some of the metal nanoparticles and metal nanoparticle conjugates that have been demonstrated as having antiviral properties.

Type of Nanoparticle	Size (nm)	Antiviral application	Mechanism of action	Ref
AgNPs	10-50	Hepatitis B virus (*HBV*)	Interaction with DNA, and/ or binding with virus particles	82
Ag-PS-NPs	10-80	Monkeypox virus (*MPV*)	Blocking of virus-host cell binding	83
PVP-AgNPs	30-50	Human immunodeficiency virus type 1 (*HIV-1*)	Prevention of HIV-1 transfection	84,85
Au-MES	4	Herpes simplex virus type 1 (*HSV-1*)	Competition with host cell binding	86
Gold coated with an amphiphilic sulfate ligand	2	Human immunodeficiency virus type 1 (*HIV-1*)	Binding to gp120	87
Copper iodide (CuI) nanoparticles	100-400	Feline calicivirus (*FCV*)	ROS generation and subsequent capsid protein oxidation	88
Copper iodide (CuI) nanoparticles	160	Influenza A of swine origin (*H1N1*)	Generation of Hydroxyl radicals, and degradation of viral proteins	89

Hepatitis B (*HBV*) is a viral infection that currently affects 257 million people around the world, and was responsible for 887,000 deaths in 2015 according to the World Health Organization.[90] Small (10-50 nm) naked silver nanoparticles have been tested as a possible treatment for HBV,[82] and were shown to bind efficiently to HBV and further inhibit the production of HBV RNA. The mode of action is hypothesized to be due to the AgNPs binding to the HBV dsDNA (*double stranded DNA*). Rogers *et al*. have demonstrated a use for silver nanoparticles, both naked and with a polysaccharide coating as an antiviral agent against monkeypox virus (*MPV*).[83] The nanoparticles were tested *in vitro* against MPV at a range of concentrations between: 12.5-100 µg/ml. The results of the study showed that all of the concentrations of polysaccharide coated silver nanoparticles (*Ag-PS-NPs*) used, were able to reduce MPV-induced plaque formations *in vitro*.

Silver nanoparticles may even have a role to play in the treatment of Human Immunodeficiency Virus (*HIV*).[84,85] HIV is a major health concern, with WHO estimating that 36.7 million people are living with HIV as of 2016.[91] It is important that treatments for HIV are discovered and implemented quickly and efficiently; Lara *et al.* have demonstrated the effect of silver nanoparticles (*30-50 nm*) on HIV-1 isolates showing inhibition of all strains.[85] The naked nanoparticles showed an overall IC_{50} of 0.44 mg/ml ±0.3 against HIV-1, with the mechanism of viral inhibition shown to be inhibition of virus-host cell binding. Specifically the silver nanoparticles inhibit the interaction between the gp120 protein (*an envelope glycoprotein*) and the target cell membrane receptors. Also demonstrated by the same group was the ability for silver nanoparticles coated with polyvinylpyrrolidone (*PVP*) to prevent the transfection of HIV-1 into a human cervical tissue explant model.[84] Specifically 0.15 mg/ml PVP-coated silver nanoparticles (*PVP-AgNPs*) inhibited infection by HIV-$_{IIIB}$ and HIV-$_{AZT-RV}$ isolates. This concentration of PVP-AgNPs also induced a proliferation of lymphocytes (immune cells) to the site of infection, in comparison to the control sample.[84]

It is not only silver, and coated silver nanoparticles that have been employed against viruses: 2 nm gold nanoparticles coated with an amphiphilic sulfate ligand was also shown to be effective against HIV-1.[87] These particles were shown to target the fusion process of the virus and were shown *in vitro* to bind to gp120 protein and directly neutralize the HIV-1 infection. Mercaptoethanesulfonate coated gold nanoparticles (*Au-MES*) nanoparticles showed an inhibition of herpes simplex virus type 1 (*HSV-1*) infection, possibly by inhibiting the virus binding to the host cell, or cell to cell viral spreading, or alteration of cell susceptibility to viral infection induced by the presence of the nanoparticles.[86]

Copper-iodide nanoparticles (*CuI-NPs*) have been shown to have antiviral properties on several different viruses: Feline calicivirus (*FCV*)[88] and more interestingly; Influenza A virus of swine origin (*H1N1*).[89] 100-400 nm CuI-NPs showed an antiviral property when utilized against FCV, it was hypothesized that monovalent Cu ions were responsible for the production of a reactive oxygen species (*ROS*) that caused subsequent capsid protein oxidation, leading to FCV inactivation. H1N1 virus was also shown to be inhibited by CuI-NPs, in a very similar manner, namely the production of hydroxyl radicals, leading to protein degradation. However these radicals might also prove to be toxic to non-infected tissues, which would be important to determine before a treatment would be approved for use.[92]

2.3.3 Imaging

Magnetic resonance imaging (*MRI*) scanning is a very useful tool for medical diagnosis and provides clear anatomical images. Using MRI one can visualize blood flow, physiochemical traits and the states of tissues and organs in the body.[93] Contrast agents are often employed in MRI for improved diagnostic sensitivity.[94] Conventionally used contrast agents are chelate-based, but the major drawbacks of current contrast agents is their biological stability and their toxicity levels when accumulated in cells.[95] For example, some contrast agents are iodine based and it has been reported that iodinated contrast media exposure is associated with subsequent development of incident hyperthyroidism and incident overt hypothyroidism.[96] Alternatives have been developed to provide an improved scanning efficacy by reducing the negative impact contrast agents can have on the body.[97] Alternatives include metal nanoparticles possibly conjugated with an agent which acts in a similar manner to a contrast agent for MRI scanning.[98] Table 3 shows some of the nanoparticles that have been explored for use in medical imaging. Some computed tomography (*CT*) contrast agents have issues including: short circulation half-lives[99] and potential tissue damage.[100] Due to this, metal nanoparticles have also been investigated for use in CT imaging;[101] AuNPs show promising use in imaging due to their X-ray attenuation.[102] Kojima *et al*. showed that gold nanoparticles conjugated with a PEGylated dendrimer (*PEG-AuNPs*) made for a superior contrast agent *in vitro as well as* for X-ray computed tomography, compared to the commercially available iodine agent: iopamidal.[103] The PEG-AuNPs showed a higher contrast efficiency than the commercially available iopamidal, with rapid excretion from the body.[104] The authors also noted that the PEG-AuNPs had photocytotoxic properties to enable photothermal therapy.

Table 3 demonstrates some examples of metal nanoparticles and metal nanoparticle-conjugates that have been investigated for their use in medical imaging.

Type of Nanoparticle	Size (nm)	Scanning type	Ref
PEG-AuNPs	3-8	CT	[104]
Modified AuNPs	17-23	SPECT/CT	[105]
AuNPs	130-147	PA	[106]
AuNPs with citraconic amide moieties	10	PA	[107]

Li *et al*. have demonstrated the use of coated AuNPs as an imaging tool for atherosclerosis; the AuNPs were applied in a type of medical imaging called “single photon emission computed tomography” (*SPECT*).[105] This type of imaging is very similar to using a gamma camera but it is able to provide true 3D images that can be sliced, rotated and manipulated to achieve a more

accurate analytical technique.[105] The modified nanoparticles specifically targeted atherosclerosis plaques containing apoptotic macrophages, indicating a useful tool for invasively accurate detection of atherosclerosis plaques.[105]

AuNPs have previously been demonstrated to be a possible agent for Photoacoustic imaging (*PA*), showing high spatial resolution and sensitivity.[106] PA relies on the detection of ultrasonic waves which are emitted from tissues when exposed to non-ionizing pulsed laser irradiation.[108] The intensity/ magnitude of the ultrasonic emission is responsible for the image contrast, therefore any agent that can both absorb the laser pulses and then give off heat as a result will increase the magnitude of the ultrasonic emission and AuNPs possess the ability to do both of these.[109,110] AuNPs are potentially better than organic dyes due to the organic dyes susceptibility to photo-bleaching and rapid clearing from the blood.[111]

2.3.4 Biomedical cargo delivery

Nanoparticles make for an ideal molecule for drug delivery due to the huge surface area to volume ratio they provide when compared to their bulk material.[8] In addition, it is possible to engineer nanoparticles to either avoid or interact with the immune system in specific ways.[112,113] For example it has been demonstrated that an increased hydrophobicity of nanoparticles/ sub-groups conjugated to the nanoparticles illicit and increased immune response by measuring cytokine mRNA levels in mice.[112] Focusing in the opposite direction, it has been suggested that nanoparticles can be conjugated with various ligands to directly activate the immune system to target the destruction of a tumor,[114]or by accumulation in the liver or spleen for the generation of tolerance or immunity respectively.[113]

Gold nanoparticles have been extensively studied for their delivery of medical cargo, for example: Bhumkar *et al*. have explored the application of AuNPs for trans-mucosal delivery of insulin. Gold nanoparticles were synthesized in the presence of chitosan, which acts as a polymeric stabilizer.[115] These nanoparticles were then loaded with insulin and administered both nasally and orally to diabetic rats. The results showed an overall reduction in the rat's blood glucose levels, an indication of successful movement of the nanoparticles through the mucosal membranes and into the blood stream.

More recently 'smart' AuNPs have been employed in PA.[107] These nanoparticles are roughly 10 nm in diameter and are functionalized with citraconic amide moieties which are susceptible to hydrolysis. The citraconic amides are converted into positively charged primary amino acids

at a mildly acidic pH, whilst the surface molecules adopt negative charges at physiological pH.[107] Combined these 2 properties cause the 'smart' nanoparticles to adopt both positive and negative charges allowing them to aggregate rapidly due to electrostatic attraction. These nanoparticles are referred to as 'smart' due to the nanoparticles presenting cancer-specific properties and accumulate rapidly and efficiently in cancer tissues, and show a much lower accumulation in normal tissues.[5]

Paciotti *et al*. have investigated the application of PEGylated AuNPs as a carrier for Tumor Necrosis Factor (*TNF*) which is a cell signaling protein that possess the ability to induce apoptosis in healthy cells.[33] The Au-PEG-TNF nanoparticles were injected intravenously and agglomerated significantly more in MC-38 colon carcinoma cells compared to other healthy cells/ tissues. The TNF gave not only therapeutic action on the MC-38 cells, but seemed to possess a targeting property, indicated by the lack of agglomeration in healthy cells. Another interesting observation reported was the ability for the Au-PEG-TNF nanoparticles to diminish a tumor mass compared to 'free' TNF.

Table 4: A range of nanoparticle conjugates that have been examined for medical delivery of cargos

Type of Nanoparticle	Size (nm)	Medical delivery application	Ref
Chitosan stabilized AuNPs	10-50	Delivery of insulin across trans mucosal membranes	115
PEGylated AuNPs conjugated with TNF	30-34	Delivery of TNF to cancer cells targeted by the TNF itself, TNF induces cell apoptosis	33
AuNPs conjugated to an oligonucleotide modified with thiol groups	10-20	Delivery of nucleic acids as a potential for gene therapy	116
AuNPs conjugated to antisense oligonucleotide modified with tetra-thiol groups	13	Delivery of nucleic acids as a potential for gene therapy	36
AuNPs conjugated with folic acid using a PEG linker	10	Delivery of folic acid (*Vitamin B9*), a precursor for nucleic acid production	117

Gold nanoparticles can also be used as a delivery system for nucleic acids,[37] including oligonucleotides[116] and small interfering RNA (*siRNA*).[118] Many different methods have been developed to functionalize AuNPs with nucleic acids, for example; Yonezawa *et al*. have synthesized gold nanoparticles modified with thiocholine, which then bound to DNA and

formed a fusion of wire like structures throughout the DNA.[35] Sandström *et al*. demonstrated the ability to bind nucleic acids onto gold nanoparticles,[116] and a similar modification has been carried out by Rosi *et al*. where tetrathiol-modified antisense oligonucleotides were bound to 13 nm gold nanoparticles.[36] Being able to conjugate nucleic acids to nanoparticles opens up the possibility of targeted gene delivery, which could, for example, lead to genes coding for a specific protein to be delivered to a cell that was either deficient in that protein or could not produce the protein themselves.[9] It has also been exhibited that gold nanoparticles modified with DNA can transfect cancer cells.[119] Dixit *et al.* demonstrated the selective delivery of folic acid coated AuNPs into folate receptor (*FR*) positive cancer cells, whereas when compared with a cell line that did not have folate receptors, uptake was shown to be minimal.[117] These results demonstrated the use of folate to target metal nanoparticles to FR positive cancer cells for tumor imaging and ablation.

2.4 Limitations of single metal nanoparticles and overcoming them

The principal obstacle with nanoparticle drug delivery is the ability to direct the nanoparticle to the target area.[6,7] There are several methods in use for metal nanoparticle targeting such as: antibodies,[120–122] and homing peptides.[123,124] There are however limitations to these methods, with the biggest being that before they even reach the desired target cells they have to pass through a variety of other barriers, such as: blood vessels and the blood brain barrier.[125] One way to overcome this targeting limitation is to use magnetic nanoparticles.[126] A magnetic nanoparticle targeting system works by directing the nanoparticles to a target site using an external magnetic field, it has already been demonstrated that the magnetic anisotropy of the nanoparticle is a very important factor for medical treatments,[24] with a change in anisotropy being able to the change the efficacy of hypothermia treatments.[127] Superparamagnetic metal nanoparticles have this property (*they only present magnetic properties whilst in the presence of a magnetic field*).[11] However, the benefit of magnetic nanoparticles also presents a potential limitation, due to the toxicity of many magnetic materials.[29,128,129] Despite iron being approved for various imaging uses,[29,42,43] it has been suggested in several studies that naked iron oxide nanoparticles may have some adverse effects when used in cell labelling.[17,130,131] One method that can be used to overcome any potential toxicity limitations is to coat the iron core.[21] A range of materials can be used as the coating material: silica,[132–134] polymers,[15,135] gold, [136–139] or silver.[140,141] Gold has low pharmaceutical activity[30] and silver has been used in biomedical applications for many years.[142,143]

The combination of a superparamagnetic core with an inert and safe metal coating produces metal nanoparticles with superior characteristics to non-magnetic metal particles.[23] As well as reducing toxicity, the coating also provides the potential for the conjugation of functionalized molecules onto the surface, such as drugs and biomolecules for application in the medical field.[74,76,88] It is of note that a core-shell nanoparticle still possesses the properties and uses of a nanoparticle made from the same material as just the shell, but the superparamagnetic core gives the ability to direct the nanoparticle in the body.[144] For example a gold nanoparticle with an antibody is classified as a targeting nanoparticle, introducing the core would classify the nanoparticle as a directed targeting nanoparticle.[11]

2.5 Current medicinal uses of gold coated iron oxide nanoparticles

Core-shell superparamagnetic nanoparticles have already been assessed for their biomedical uses, with a wide range of uses already being applied.[145] One of these uses is as a magnetic carrier for drug targeting.[25,26,145–147] Kayal *et al.* have tested an *in vitro* apparatus that simulates the human circulatory system as a test for the magnetic delivery of gold coated iron oxide nanoparticles (*Au-Fe_3O_4*) loaded with doxorubicin.[147] Their system had various magnetic fields of increasing strength next to a capillary through which the doxorubicin loaded particles were passed. A significant percentage of these nanoparticles were captured within the magnetic fields, strongly indicating the potential for the use of magnetic nanoparticles in drug delivery. Another use for a targeted system is the application of Au-Fe_3O_4 nanoparticles in photothermal therapy; Bhana *et al.* demonstrated the use of a core-shell system used in combination therapy deployed against 2 different cancer cell lines; head and neck (*KB-3-1*) and breast (*SK-BR-3*) with a reported decrease in cell viability of 64 % when they exposed cell lines to a combined photothermal and photodynamic therapy, compared to each modality used on its own.[148] In photothermal therapy gold nanoparticles are coated with a ligand, such as PEG,[110] these nanoparticles are irradiated with a laser, with a wavelength that matches the UV-vis λ-max of the gold nanoparticles.[147] The nanoparticles vibrate at the laser frequency which causes heat to be released causing the death of the surrounding tissue,[149] introducing a core which is superparamagnetic can allow for a more accurate targeting for use in this therapy. Similarly it has been reported by Kirui *et al.* that gold hybrid nanoparticles were deployed against SW1222 colorectal cancer in photothermal therapy, showing an increased case of cellular apoptosis after therapy, with their conclusion being that the cells showed an increased uptake, leading to a reduced laser power required to reach threshold therapeutic levels.[150] The use of core-shell nanoparticles for photothermal therapy of cancer has also been reported by other groups.[151,152]

Metal nanoparticles have already shown to have a place in contrast imaging, for example core-shell nanoparticles can also be used in T_1 and T_2 weighted imaging in MRI.[153] Research by Cho *et al.* demonstrated that gold coated iron nanoparticles can be successfully used in MRI imaging, as well as opening the route for conjugating various ligands for use in biosensors.[153] A magnetic carrier capable of imaging and photothermal therapy has been reported by Cheng *et al.* They demonstrated the magnetic targeting of multi-functional nanoparticles to a tumor in a mouse model, which could be imaged inside the tumor and showed a reduction in the tumor size when combined with photothermal therapy.[154] It is also of note that in this work both the nanoparticle dosage (*1.6 mg/kg*) and laser power (*1 W/cm*^{2}) are among the lowest applied for *in vivo* photothermal therapy. Moreover there was no obvious toxicity from the nanoparticles reported. Table 5 presents some of the currently reported uses of core-shell nanoparticles.

Table 5 Gives examples of the medical uses already been demonstrated for gold coated iron magnetic nanoparticles

Type of Nanoparticle	Medical application	Ref
Gold coated iron oxide	Targeted delivery of Doxorubicin	155
Gold coated iron oxide	Photothermal and photodynamic combination anticancer treatment	148
Gold hybrid nanoparticles	Photothermal anti-cancer therapy	150
Gold coated iron nanoparticles	T_1 and T_2 MRI imaging	154
Multi-functional gold nanoparticle	Magnetically directed tumor targeting in mice for phototherapy and imaging of the particles	154

Another medical area where such core-shell metal nanoparticles have been suggested to make an impact is in Directed Enzyme Prodrug Therapy (*DEPT*).[126,144] DEPT is a promising method of cancer treatment, with several therapies making it through to clinical trials.[156,157]The main principal of DEPT is the targeted delivery of a prodrug activating enzyme to a tumor site. Upon arrival at the tumor site, the enzyme enters the target cells where it can later activate an administered prodrug. However, the efficacy of the therapy depends on the ability to direct the enzyme to the tumor site, with current directional techniques relying on passive targeting methods such as viruses[156,158] or antibodies,[159,160] rather than an active targeting system for enzyme delivery. A novel therapy proposed by Gwenin *et al.* potentially overcomes the targeting issue.[126,161] This approach involves conjugating a genetically modified prodrug activating enzyme onto the surface of a gold coated iron oxide superparamagnetic nanoparticle

(*AuMNP*), then directing the AuMNP-enzyme conjugate to the target site using a magnetic field to increase the efficacy of the targeted therapy. Figure 2.1 presents some of the uses of a core-shell nanoparticle.

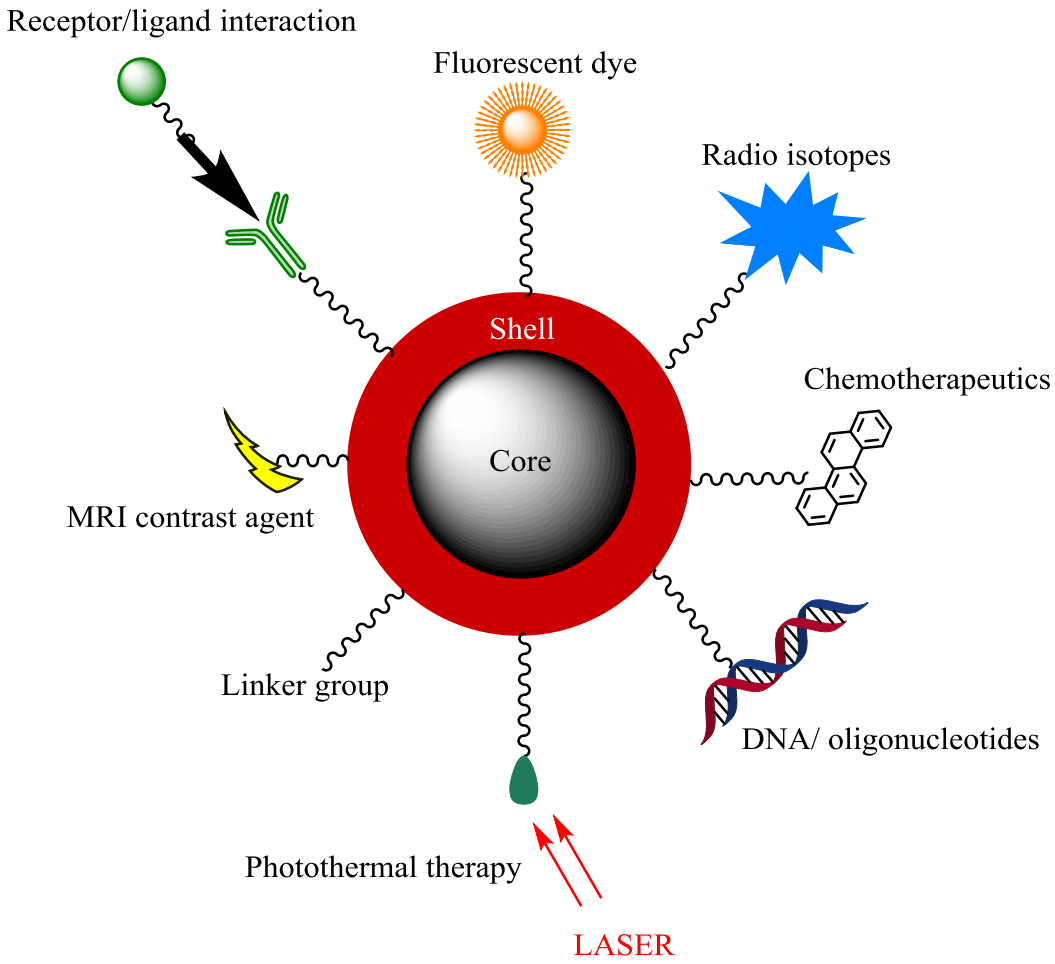

Figure 2.1. A pictorial representation of the applications of core/shell nanoparticles

One challenge that still presents itself, is synthesizing core-shell nanoparticles, there are many ways to synthesize nanoparticles,[162] but new challenges emerge when attempting to synthesize a core-shell nanoparticle.[163]

2.6 Gold and silver coated iron oxide nanoparticle synthesis

Methods for the synthesis of metallic nanoparticles have been known for many years, for example Turkevich *et al.* published a synthesis for gold nanoparticles *via* the reduction of $HAuCl_4$ in 1951.[164] Since then there have been many different routes for nanoparticle synthesis such as gas deposition,[165] sol-gel,[166] and aerosol/ vapor phase.[167] However a new challenge presents itself when attempting to synthesize metal nanoparticles consisting of a core-shell

structure, in which one metal forms the core and a second metal forms the shell, for example Fe particles degrade in water, whilst $HAuCl_4$ is a strong oxidizing agent.[163] One such example that will be discussed further is using a Fe_3O_4 (*iron oxide*) core and gold as the coating shell. In the preparation of such core-shell metal nanoparticles, two of the biggest issues are: attempting to control the rate of coating, and controlling the uniformity of the coating to create a solution of nanoparticles which are all of very similar shape and size.[168] Coating of gold or silver onto an iron oxide core can be divided into two main categories: direct coating of gold/ silver onto iron,[169] or using an intermediary layer to act as a glue between the gold and the iron layer.[170] The former category will be discussed here. The following text describes some methods that have been devised to synthesize gold and silver coated Fe_3O_4 nanoparticles.

2.6.1 Reverse micelle synthesis

A popular route for synthesizing metal nanoparticles is to use the reverse micelle method, or sometimes called the microemulsion route.[171] This method was first introduced in the 1980's when colloidal solutions of rhodium, platinum and palladium nanoparticles were first synthesized.[172]

Micelles are formed when molecules with hydrophobic and hydrophilic constituent parts come into contact with either an aqueous or hydrophobic phase.[173] The micelles will organize themselves in such a way that allows the hydrophilic part to be in contact with the aqueous phase and the hydrophobic constituent facing the hydrophobic phase.[174] In essence, a spheroid is formed with an inner shielded phase, which can furthermore contain a cargo.[168,175–177]

There are different approaches to the microemulsion route and these include: water-in-oil (*w/o),*[178] and water-in-supercritical-CO_2 (*w/sc-CO_2*).[179] A w/o emulsion occurs when water is dispersed in a hydrocarbon based continuous phase,[178] thermodynamically driven surfactant self-assembly then generates the reverse micelles, with spherical micelles being the most common shape.[168] Any added polar or ionic materials added to this mixture become compartmentalized within the micelles and nanoparticles are then formed when the micelle membranes come into contact with each other through Brownian motion.[180] A w/sc-CO_2 emulsion involves using a fluid (*CO_2*) that is in a supercritical state, i.e. above both its critical pressure and temperature.[181] This method holds particular interest as it is a more "green" approach to nanoparticle synthesis as no toxic organic solvents are required. It is also easier to recoup the product by simply lowering the pressure and releasing the fluid as CO_2 gas.[182]

The reverse micelle route has been adapted from synthesizing metal nanoparticles, to coating previously synthesized nanoparticles.[141] The first gold coated iron oxide (*Au-Fe_3O_4*) nanoparticles synthesized in reverse micelles were done almost 20 years ago.[183] This synthesis of Au-Fe_3O_4 nanoparticles was performed using a H_2O/CTAB (*cetyltrimethyl ammoniumbromide*) system to produce the micelles with sodium borohydride ($NaBH_4$) as the reducing agent, reducing gold chloride (*$HAuCl_4$*) onto the iron core. This synthesis produced a nanoparticle dispersion with an average size of 12 nm. Since this first production of Au-Fe_3O_4 NPs using micro emulsions, there have been a range of Au-Fe_3O_4 NPs synthesis routes discovered.[137,171,184–186] Figure 2.2 is a generic representation of how the nanoparticles are formed using the reverse micelle route.

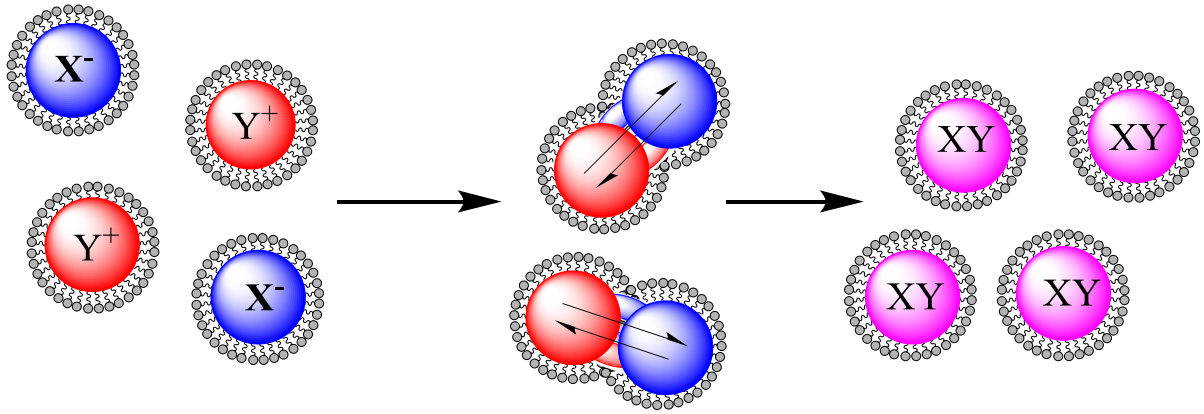

Figure 2.2 A generic representation of the interaction of reverse micelles containing salts the react to form metal nanoparticles.

Lin *et al.* published a slightly modified method to coat Fe_3O_4 with gold using a reverse micelle method.[184] The synthesis also employs a system using CTAB as the surfactant to form the reverse micelle, but with 1-butanol as a co-surfactant and octane as the oil phase, adding a water solution containing the metal ions using $NaBH_4$ to reduce $HAuCl_4$ onto the surface of the iron oxide nanoparticles. The reported optical results of the coated particles showed a shift in the absorbance peak of the UV/vis spectra from the gold colloid (*526 nm*) to the Au-Fe_3O_4 (*555 nm*). The TEM results of the coated particles indicated a size distribution of 5-15 nm, with an average size of 10 nm. This method was repeated by Pana *et al*. with a slightly larger size distribution of 5-35 nm sized Au-Fe_3O_4 nanoparticles.[186] In addition, a very similar system has been employed by Siep *et al*. with the exception of using hydrazine to reduce the $HAuCl_4$.[187]

The coating of Fe_3O_4 nanoparticles is not limited to just gold; Lopez Perez *et al*. reported on the synthesis of iron oxide nanoparticles using a system containing cyclohexane/ Brij-97 (*co-surfactant*) and an aqueous phase with iron salts of $FeSO_4.7H_2O$ and $FeCl_3.6H_2O$.[188] This system has been coated with both silver[141] and gold,[171] producing 13 nm particles. An alternative method is reported by Tamer *et al.* for the synthesis of Au-Fe_3O_4 nanoparticles.[137] This method employs a co-precipitation of iron salts in NaOH, which were then washed in $HClO_4$ to produce oxidized Fe_3O_4 nanoparticles. Coating of gold onto the Fe_3O_4 NPs occurred *via* the reduction of $HAuCl_4$ by NaOH delivered to the system by CTAB micelles. Au-Fe_3O_4 NPs were produced with an average size of 23.5 nm. After characterization particles were then modified with various functional groups to form a self-assembled monolayer (*SAM*) and further used for the capturing and detection of *E.coli*.

A modified version of the reverse micelle synthesis has been carried out by Zhang *et al*. involving the use of a laser as the initiator for the coating of iron nanoparticles with gold.[189] The process involves making a reaction mixture of iron nanoparticles encapsulated in CTAB micelles, gold nanopowder in water, and octane, then irradiating with a pulsed laser whilst vigorously stirring the reaction. The laser irradiation facilitates the thermal decomposition of the gold nanoparticles. Gold atoms and clusters formed around the iron nanoparticles, forming gold coated iron nanoparticles. The TEM results for the Au-Fe nanoparticles synthesized this way gave an average size of 18 nm with a size distribution of ±36 nm.

2.6.2 Thermal synthesis

Among the various methods of gold shell-iron core nanoparticle synthesis lies a thermal route, wherein the reaction involves heating the reaction mixture to above its boiling point,[190] and sometimes refluxing.[191,192] There are two main categories for this type of synthesis: hydrothermal (*water based solvent*)[193,194] and solvothermal (*organic based solvent*).[191,195] Whilst there are many techniques for synthesizing metal nanoparticles *via* the thermal route,[196–201] it is not possible to achieve the synthesis of the cores and coating of gold in a one pot reaction [191,192,195,197,200,202–204] in some cases Fe_3O_4 cores are synthesized *via* a reverse micelle route,[193] or a colloidal route [201] and then the particles are coated using a hydro- or solvothermal technique.[193,199,201] Whilst there are a variety of solvent systems that are used in these synthetic methods, the majority of routes involve the addition of either iron oxide nanoparticles to boiling $HAuCl_4$, or the inverse; of $HAuCl_4$ being added to boiling solutions of iron oxide nanoparticles.[197,202]

A method for the synthesis of Au-Fe_3O_4 nanoparticles has been performed by Rudakovskaya *et al*. *via* a hydrothermal technique.[199] The principle of the method follows the addition of Fe_3O_4 nanoparticles to a boiling $HAuCl_4$ solution. TEM analysis of these nanoparticles indicated an average size of 30 nm, with a general spherical shape and a size distribution between 20 and 35 nm, these images can be seen in Figure 3.3.

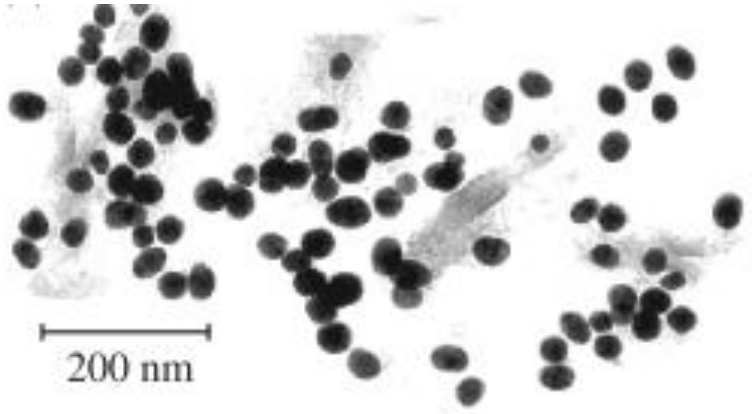

Figure 3.3. A TEM image of the nanoparticles synthesized by Rudakovskaya et al. as can be seen the nanoparticles are roughly spherically shaped with an average size of 30 nm [199]

2.6.3 Colloidal synthesis

Colloidal synthesis techniques offer a simple yet effective way of synthesizing metal nanoparticles.[205] Colloidal techniques often offer a level of simplicity over other techniques for nanoparticle synthesis, without the need for different solvents, or that it can be carried out at room temperature.[206,207] The basic principles of the synthesis involve dispersing different metal ions in an aqueous phase, adding a reducing agent to the mixture, then mixing at a controlled temperature to form insoluble nanoparticles.[164] Colloidal synthesis routes offer the benefit of not having to involve potential toxic solvents in the synthesis (*ideal if the nanoparticles are intended for biological use*). However, there are some limitations to colloidal routes such as it can be hard to control the size distribution of the final synthesized nanoparticles[208] and the shape of the nanoparticles can be heavily influenced by reagent concentration.[208] On the positive side it can however be easier to produce nanoparticles in a larger quantity.[209] This method for metal nanoparticle synthesis has been around for many years, being used for the synthesis of different types of nanoparticles such as silver[210] and gold.[164,211]

This basic method has been advanced and developed to produce different synthetic routes for the formation of gold coated iron oxide nanoparticles.[138,139,206,207,212–218] Most of the methods for the synthesis of gold coated iron oxide revolve around using various reducing agents to

reduce $HAuCl_4$ onto the surface of the iron oxide. Nadagouda *et al*. offer a proposed 'green' synthetic route, using ascorbic acid to reduce $HAuCl_4$.[207] This method however seems to show little to no control over size or shape of the coated nanoparticles due to the lack of capping agent (*an agent that binds to the outside of the nanoparticle that stops further 'growth' of the nanoparticle*) used in the synthesis.[219] A method which does show more control over the shape and size of synthesized coated particles is presented by Pal *et al.*[139] This method employs gold acetate as the gold salt, which is reduced onto the surface of 6 nm Fe_3O_4 nanoparticles to create 7 nm sized Au-Fe_3O_4 particles, which are spherical in shape. A rapid method for coating Fe_3O_4 nanoparticles is presented by Rawal *et al*. which involves dispersing Fe_3O_4 nanoparticles in a solution of $HAuCl_4$, then mixing with ethanol.[206] After 15 minutes at room temperature the reaction was stopped and the Au-Fe_3O_4 nanoparticles were then separated with a magnet. TEM analysis of the purified solution showed that the particles produced ranged in size from 30 to 100 nm and had varied shapes across the sample, these images can be seen in Figure 4.4. Whilst this synthesis technique produced the coated nanoparticles quickly, it does not appear to be a very efficient synthesis for the production of uniformly shaped and sized particles.[206]

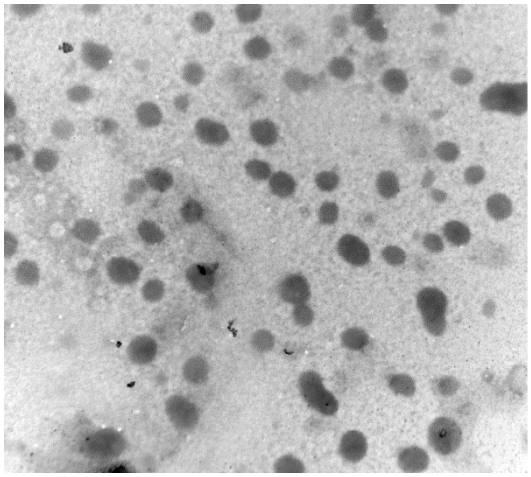

Figure 4.4. A TEM image of the nanoparticles synthesized by Rawal et al. these nanoparticles have a size distribution of 20-100 nm. [206]

Whilst some techniques offer just the reduction of gold salts, others prefer to put the reducing agent onto the surface of the iron, such as hydroxylamine.[138,213] In many cases when Fe_3O_4 nanoparticles are coated with gold, the reduction of a gold salt yields standard gold nanoparticles as well,[197] so the addition of the reducing agent onto the surface of the iron nanoparticles aims to improve the efficiency of the coating and is intended to lower the quantity of gold nanoparticles produced as a by-product.[138]

Another technique involves seeding gold onto the surface of magnetic nanoparticles which provides a more direct route of getting gold to nucleate around the magnetic core of the nanoparticles.[214,215,218] This technique involves binding gold seeds, which are smaller than the iron oxide nanoparticles in solution, to the surface of the iron oxide. When the $HAuCl_4$ is reduced in solution the Au^+ ions will seed onto the iron oxide and form a shell around the iron oxide nanoparticles. This gold seeding has been successfully employed by several groups; Goon *et al*. used polyethyleneimine to control the seeding of gold onto the surface of Fe_3O_4, producing fully coated nanoparticles.[214] However, the synthesized Au-Fe_3O_4 particles displayed high polydispersity, with particle size ranging from 40-110 nm. Levin *et al*. managed to produce gold shell-magnetic core nanoparticles with a size range of 50-70 nm, using a core functionalized with organosilane molecules to bind to the gold seeds.[215] Seeding of gold nanoparticles onto an iron core can be demonstrated with a variety of core shapes, for example Wang *et al*. demonstrated gold seeding onto rice shaped 'Nano rice' Fe_3O_4 structures, which then led to a complete thick gold shell when gold was reduced onto the surface.[218]

2.7 Conclusions

In brief, there are a variety of methods that can be used to synthesize Au-Fe_3O_4 nanoparticles, with each method having its own advantages and disadvantages. There remains many obstacles for Au-Fe_3O_4 nanoparticles before they can be routinely applied in the medical field and these include;

1) achieving a synthesis route which produces easily repeatable results,
2) producing particles of a set size[59–61] and shape,[62–65]
3) producing large enough quantities to make it economically viable,[66]

This chapter has demonstrated the wide range of techniques available to produce single metal nanoparticles, as well as the medical applications these nanoparticles possess. Following on from these single metal synthesis routes, further routes for the synthesis of core-shell metallic nanoparticles have been demonstrated, in particular the synthesis of Fe_3O_3-Au core-shell nanoparticles, along with the range of bio-medical applications these nanoparticles can already be used for. It is from two of these synthesis routes presented for single metal nanoparticles, that the synthesis for the nanoparticles to be used in this work has been developed.[213,138] Thus the work by Brown *et al*.[213] and Lyon *et al*.[138] has been combined together to create a synthesis for a gold coated iron oxide nanoparticle, intended for use in MNDEPT.

2.8 Bibliography

1 G. Reiss and A. Hutten, in *Handbook of Nanophysics: Nanoparticles and Quantum Dots*, CRC Press, 2010, pp. 2–1.

2 M. Faraday, *Philisophical Transcations R. Soc. London*, 1857, **147**, 145–181.

3 C. A. White, R. D. Toothaker, A. L. Smith and J. T. Slattery, *Antimicrob. Agents Chemother.*, 1989, **33**, 1046–1051.

4 A. Panáček, L. Kvítek, M. Smékalová, R. Večeřová, M. Kolář, M. Röderová, F. Dyčka, M. Šebela, R. Prucek, O. Tomanec and R. Zbořil, *Nat. Nanotechnol.*, 2018, **13**, 65–71.

5 H. Gao, *Acta Pharm. Sin. B*, 2016, **6**, 268–286.

6 D. Rosenblum, N. Joshi, W. Tao, J. M. Karp and D. Peer, *Nat. Commun.*, 2018, **9,** 1-3.

7 C. Buzea, I. I. Pacheco and K. Robbie, *Biointerphases*, 2007, **2**, 17-71.

8 N. Barron, O. Piskareva and M. Muniyappa, *Cytotechnology*, 2007, **53**, 65–73.

9 R. Zietse, R. Zoutendijk and E. J. Hoorn, *Nat. Rev. Nephrol.*, 2009, **5**, 193–202.

10 V. V. Mody, A. Cox, S. Shah, A. Singh, W. Bevins and H. Parihar, *Appl. Nanosci.*, 2014, **4**, 385–392.

11 G. Ajnai, A. Chiu, T. Kan, C. C. Cheng, T. H. Tsai and J. Chang, *J. Exp. Clin. Med.*, 2014, **6**, 172–178.

12 M. Schäffler, F. Sousa, A. Wenk, L. Sitia, S. Hirn, C. Schleh, N. Haberl, M. Violatto, M. Canovi, P. Andreozzi, M. Salmona, P. Bigini, W. G. Kreyling and S. Krol, *Biomaterials*, 2014, **35**, 3455–3466.

13 J. Nam, W. G. La, S. Hwang, Y. S. Ha, N. Park, N. Won, S. Jung, S. H. Bhang, Y. J. Ma, Y. M. Cho, M. Jin, J. Han, J. Y. Shin, E. K. Wang, S. G. Kim, S. H. Cho, J. Yoo, B. S. Kim and S. Kim, *ACS Nano*, 2013, **7**, 3388–3402.

14 A. Banerjee, J. Qi, R. Gogoi, J. Wong and S. Mitragotri, *J. Control. Release*, 2016, **238**, 176–185.

15 Y. Wang, R. N. Dave and R. Pfeffer, *J. Supercrit. Fluids*, 2004, **28**, 85–99.

16 AUSTRALIAN GOVERNMENT (TGA), *TGA Heal. Saf. Regul.*, 2017, 1–24.

17 H. L. Karlsson, J. Gustafsson, P. Cronholm and L. Möller, *Toxicol. Lett.*, 2009, **188**, 112–118.

18 S. Benítez-Martínez, Á. I. López-Lorente and M. Valcárcel, *Microchim. Acta*, 2016, **183**, 781–789.

19 J. W. M. Bulte and M. M. Modo, *Design and Applications of Nanoparticles in Biomedical Imaging*, Springer International Publishing, Cham, 2017, 229-255.

20 B. Trouiller, R. Reliene, A. Westbrook and P. Solaimani, *Cancer Res.*, 2009, **69**, 1–16.

21 S. L. Chia and D. T. Leong, *Heliyon*, 2016, **2**, 1–18.

22 M. Crosera, A. Prodi, M. Mauro, M. Pelin, C. Florio, F. Bellomo, G. Adami, P. Apostoli, G. De Palma, M. Bovenzi, M. Campanini and F. L. Filon, *Int. J. Environ. Res. Public Health*, 2015, **12**, 9282–9297.

23 V. I. Shubayev, T. R. Pisanic and S. Jin, *Adv. Drug Deliv. Rev.*, 2009, **61**, 467–477.

24 I. Obaidat, B. Issa and Y. Haik, *Nanomaterials*, 2015, **5**, 63–89.

25 M. Arruebo, R. Fernández-Pacheco, M. R. Ibarra and J. Santamaría, 2007, **2**, 22–32.

26 J. Dobson, *Drug Dev. Res.*, 2006, **67**, 55–60.

27 D. Bobo, K. J. Robinson, J. Islam, K. J. Thurecht and S. R. Corrie, *Pharm. Res.*, 2016, **33**, 2373–2387.

28 J. D. Donalson and D. Beyersmann, in *Ullmann's Encyclopedia of Industrial Chemistry*, Wiley-VCH, Weinheim, Germany, 2005.

29 H. Markides, M. Rotherham and A. J. El Haj, *J. Nanomater.*, 2012, **2012**, 13–15.

30 S. Dierks, Gold Materials Safety Data Sheet 2005, 1–6.

31 R. D. Holtz, a G. Souza Filho, M. Brocchi, D. Martins, N. Durán and O. L. Alves, *Nanotechnology*, 2010, **21**, 185102.

32 M. Rai, A. Yadav and A. Gade, *Biotechnol. Adv.*, 2009, **27**, 76–83.

33 G. F. Paciotti, L. Myer, D. Weinreich, D. Goia, N. Pavel, R. E. McLaughlin and L. Tamarkin, *Drug Deliv. J. Deliv. Target. Ther. Agents*, 2004, **11**, 169–183.

34 I. Fratoddi, I. Venditti, C. Cametti and M. V. Russo, *J. Mater. Chem. B*, 2014, **2**, 4204–4220.

35 T. Yonezawa, S. Onoue and N. Kimizuka, *Chem. Lett.*, 2002, **31**, 1172–1173.

36 N. L. Rosi, D. A. Giljohann, C. S. Thaxton, K. R. Abigail, Lytton-Jean., M. S. Han and C. A. Mirkin, *Science.*, 2006, **312**, 1027–1030.

37 Y. Ding, Z. Jiang, K. Saha, C. S. Kim, S. T. Kim, R. F. Landis and V. M. Rotello, *Mol. Ther.*, 2014, **22**, 1075–1083.

38 M. Hofmann-Amtenbrink, D. W. Grainger and H. Hofmann, *Nanomedicine Nanotechnology, Biol. Med.*, 2015, **11**, 1689–1694.

39 X. Gao, Y. Cui, R. M. Levenson, L. W. K. Chung and S. Nie, *Nat. Biotechnol.*, 2004, **22**, 969–976.

40 M. E. Akerman, W. C. W. Chan, P. Laakkonen, S. N. Bhatia and E. Ruoslahti, *Proc. Natl. Acad. Sci.*, 2002, **99**, 12617–12621.

41 S. Kim, Y. T. Lim, E. G. Soltesz, A. M. De Grand, J. Lee, A. Nakayama, J. A. Parker, T. Mihaljevic, R. G. Laurence, D. M. Dor, L. H. Cohn, M. G. Bawendi and J. V Frangioni, *Nat. Biotechnol.*, 2004, **22**, 93–97.

42 M. G. Harisinghani, J. Barentsz, P. F. Hahn, W. M. Deserno, S. Tabatabaei, C. Hulsbergen van de Kaa, J. de la. Rosette and R. Weissleder, *N. Engl. J. Med.*, 2003, **348**, 2491–2499.

43 Y. M. Huh, Y. Jun, H. T. Song, S. Kim, J. Choi, J. H. Lee, S. Yoon, K. Kim, J. S. Shin, J. S. Suh and J. Cheon, *J. Am. Chem. Soc.*, 2005, **127**, 12387–12391.

44 R. Duncan, *Nat. Rev. Drug Discov.*, 2003, **2**, 347–360.

45 T. M. Allen and P. R. Cullis, *Science.*, 2004, **303**, 1818–1822.

46 J. P. Micha, B. H. Goldstein, C. L. Birk, M. A. Rettenmaier and J. V. Brown, *Gynecol. Oncol.*, 2006, **100**, 437–438.

47 S. Sengupta, D. Eavarone, I. Capila, G. Zhao, N. Watson, T. Kiziltepe and R. Sasisekharan, *Nature*, 2005, **436**, 568–572.

48 E. Garcia-Garcia, K. Andrieux, S. Gil and P. Couvreur, *Int. J. Pharm.*, 2005, **298**, 274–292.

49 F. Schlachetzki, Y. Zhang, R. J. Boado and W. M. Pardridge, *Neurology*, 2004, **62**, 1275–1281.

50 N. Popovic and P. Brundin, *Int. J. Pharm.*, 2006, **314**, 120–126.

51 C. Olbrich, U. Bakowsky, C. M. Lehr, R. H. Müller and C. Kneuer, *J. Control. Release*, 2001, **77**, 345–355.

52 K. Tabatt, M. Sameti, C. Olbrich, R. H. Müller and C. M. Lehr, *Eur. J. Pharm. Biopharm.*, 2004, **57**, 155–162.

53 F. De Jaeghere, E. Allémann, F. Kubel, B. Galli, R. Cozens, E. Doelker and R. Gurny, *J. Control. Release*, 2000, **68**, 291–298.

54 R. Pignatello, C. Bucolo, G. Spedalieri, A. Maltese and G. Puglisi, *Biomaterials*, 2002, **23**, 3247–3255.

55 R. Pignatello, C. Bucolo, P. Ferrara, A. Maltese, A. Puleo and G. Puglisi, *Eur. J. Pharm. Sci.*, 2002, **16**, 53–61.

56 A. Ludwig, *Adv. Drug Deliv. Rev.*, 2005, **57**, 1595–1639.

57 A. E. John, N. W. Lukacs, A. A. Berlin, A. Palecanda, R. F. Bargatze, L. M. Stoolman and J. O. Nagy, *FASEB J.*, 2003.

58 M. Kumar, K. Xiaoyuan, A. K. Behera, G. R. Hellermann, R. F. Lockey and S. S. Mohapatra, *Genet. Vaccines Ther.*, 2003, **1**.

59 T. Teranishi and M. Miyake, *Chem. Mater.*, 1998, **10**, 594–600.

60 S. Sun and H. Zeng, *J. Am. Chem. Soc.*, 2002, **124**, 8204–8205.

61 M. P. Pileni, *Nat. Mater.*, 2003, **2**, 145–150.

62 Y. Sun and Y. Xia, *Science.*, 2002, **298**, 2176–2179.

63 L. Manna, E. C. Scher and A. P. Alivisatos, *J. Am. Chem. Soc.*, 2000, **122**, 12700–12706.

64 M. Gadogbe, S. M. Ansar, I. W. Chu, S. Zou and D. Zhang, *Langmuir*, 2014, **30**, 11520–11527.

65 R. Klajn, A. O. Pinchuk, G. C. Schatz and B. A. Grzybowski, *Angew. Chemie - Int. Ed.*, 2007, **46**, 8363–8367.

66 X. Wang, J. E. Hall, S. Warren, J. Krom, J. M. Magistrelli, M. Rackaitis and G. G. A. Bohm, *Macromolecules*, 2007, **40**, 499–508.

67 L. Mazzola, *Nat. Biotechnol.*, 2003, **21**, 1137–1143.

68 A. H. Faraji and P. Wipf, *Bioorganic Med. Chem.*, 2009, **17**, 2950–2962.

69 H. Liao, C. L. Nehl and J. H. Hafner, *Nanomedicine (Lond).*, 2006, **1**, 201–208.

70 S. Lanone and J. Boczkowski, *Curr. Mol. Med.*, 2006, **6**, 651–663.

71 R. Singh and L. J. W., *Exp. Mol .Pathol.*, 2009, **86**, 215–223.

72 F. W. E. Diggins, *Br. J. Biomed. Sci.*, 1999, **56**, 83–93.

73 G. Bao, S. Mitragotri and S. Tong, *Annu. Rev. Biomed. Eng.*, 2013, **15**, 253–282.

74 M. Rai, S. D. Deshmukh, A. P. Ingle, I. R. Gupta, M. Galdiero and S. Galdiero, *Crit. Rev. Microbiol.*, 2014, **42**, 1–11.

75 T. V. Sreekumar, A. Das, L. Chandra, A. Srivastava and K. U. Shasker Rao, *J. Biomed. Nanotechnol.*, 2009, **5**, 115–120.

76 V. C. Verma, R. N. Kharwar and A. C. Gange, *Nanomedicine*, 2010, **5**, 33–40.

77 S. A. Salmon and J. L. Watts, *Avian Dis.*, 2000, **44**, 85-98

78 A. Erdogan and S. S. C. Rao, *Curr. Gastroenterol. Rep.*, 2015, **17**, 1–7.

79 V. Selvaraj, A. Nirmala Grace, M. Alagar and I. Hamerton, *J. Biomed. Nanotechnol.*, 2010, **6**, 129–137.

80 M. M. Mohamed, S. A. Fouad, H. A. Elshoky, G. M. Mohammed and T. A. Salaheldin, *Int. J. Vet. Sci. Med.*, 2017, **5**, 23–29.

81 S. Shamaila, N. Zafar, S. Riaz, R. Sharif, J. Nazir and S. Naseem, *Nanomaterials*, 2016, **6**, 71.

82 L. Lu, R. W.-Y. Sun, R. Chen, C. K. Hui, C. M. Ho, J. M. Luk, G. K. K. Lau and C.-M. Che, *Antivir. Ther.*, 2008, **13**, 253–62.

83 J. V. Rogers, C. V. Parkinson, Y. W. Choi, J. L. Speshock and S. M. Hussain, *Nanoscale Res. Lett.*, 2008, **3**, 129–133.

84 H. H. Lara, L. Ixtepan-Turrent, E. N. Garza-Treviño and C. Rodriguez-Padilla, *J. Nanobiotechnology*, 2010, **8**, 15.

85 H. H. Lara, N. V Ayala-Nuñez, L. Ixtepan-Turrent and C. Rodriguez-Padilla, *J. Nanobiotechnology*, 2010, **8**, 1.

86 D. Baram-Pinto, S. Shukla, A. Gedanken and R. Sarid, *Small*, 2010, **6**, 1044–1050.

87 P. Di Gianvincenzo, M. Marradi, O. M. Martínez-Ávila, L. M. Bedoya, J. Alcamí and S. Penadés, *Bioorg. Med. Chem. Lett.*, 2010, **20**, 2718–2721.

88 N. Shionoiri, T. Sato, Y. Fujimori, T. Nakayama, M. Nemoto, T. Matsunaga and T. Tanaka, *J. Biosci. Bioeng.*, 2012, **113**, 580–586.

89 Y. Fujimori, T. Sato, T. Hayata, T. Nagao, M. Nakayama, T. Nakayama, R. Sugamata and K. Suzuki, *Appl. Environ. Microbiol.*, 2012, **78**, 951–955.

90 World Health Organization, *Global hepatitis report, 2017*, 2017.

91 World Health Organization (WHO), *Progress Report 2016, prevent HIV, test and treat all*, 2016.

92 B. Halliwell and J. M. C. Gutteridge, *Biochem. J.*, 1984, **219**, 1–14.

93 R. C. of Radiologists, A. Padhani, C. Allen and B. Carey, *Recommendations for Cross-Sectional Imaging in Cancer Management: Computed Tomography – CT Magnetic Resonance Imaging – MRI Positron Emission Tomography – PET-CT*, 2014, vol. Second Edi.

94 D. W. McRobbie, E. A. Moore, M. J. Graves and M. R. Prince, *MRI from picture to proton*, 2006.

95 K. J. Murphy, J. A. Brunberg and R. H. Cohan, *Am. J. Roentgenol.*, 1996, **167**, 847–849.

96 C. M. Rhee, I. Bahn, E. K. Alexander and S. M. Brunelli, *Arch. Intern. Med.*, 2012, **172**, 153.

97 M. Lee, G. Lee, S.-S. Park, C. Ju, K. T. Lim and S. Hong, 2005, **31**, 379–389.

98 B. Blasiak, F. C. J. M. Van Veggel and B. Tomanek, *J. Nanomater.*, 2013, **2013,** 1-12.

99 F. Stacul, A. J. van der Molen, P. Reimer, J. A. W. Webb, H. S. Thomsen, S. K. Morcos, T. Almén, P. Aspelin, M.-F. Bellin, O. Clement and G. Heinz-Peer, *Eur. Radiol.*, 2011, **21**, 2527–2541.

100 W. Li and X. Chen, *Nanomedicine*, 2015, **10**, 299–320.

101 M. M. van Schooneveld, D. P. Cormode, R. Koole, J. T. van Wijngaarden, C. Calcagno, T. Skajaa, J. Hilhorst, D. C. 't Hart, Z. A. Fayad, W. J. M. Mulder and A. Meijerink, *Contrast Media Mol. Imaging*, 2010, **5**, 231–236.

102 R. Cheheltani, R. M. Ezzibdeh, P. Chhour, K. Pulaparthi, J. Kim, M. Jurcova, J. C. Hsu, C. Blundell, H. I. Litt, V. A. Ferrari, H. R. Allcock, C. M. Sehgal and D. P. Cormode, *Biomaterials*, 2016, **102**, 87–97.

103 C. Kojima, Y. Umeda, M. Ogawa, A. Harada, Y. Magata and K. Kono, *Nanotechnology*, 2010, **21**, 245104.

104 Y. Umeda, C. Kojima, A. Harada, H. Horinaka and K. Kono, *Bioconjug. Chem.*, 2010, **21**, 1559–1564.

105 X. Li, C. Wang, H. Tan, L. Cheng, G. Liu, Y. Yang, Y. Zhao, Y. Zhang, Y. Li, C. Zhang, Y. Xiu, D. Cheng and H. Shi, *Biomaterials*, 2016, **108**, 71–80.

106 Y. Wang, X. Xie, X. Wang, G. Ku, K. L. Gill, D. P. O'Neal, G. Stoica and L. V. Wang, *Nano Lett.*, 2004, **4**, 1689–1692.

107 J. Song, J. Kim, S. Hwang, M. Jeon, S. Jeong, C. Kim and S. Kim, *Chem. Commun.*, 2016, **52**, 8287–8290.

108 M. Xu and L. V. Wang, *Rev. Sci. Instrum.*, 2006, **77, 1-22**.

109 X. Huang, I. H. El-Sayed, W. Qian and M. A. El-Sayed, *J. Am. Chem. Soc.*, 2006, **128**, 2115–2120.

110 L. R. Hirsch, R. J. Stafford, J. A. Bankson, S. R. Sershen, B. Rivera, R. E. Price, J. D. Hazle, N. J. Halas and J. L. West, *Proc. Natl. Acad. Sci.*, 2003, **100**, 13549–13554.

111 O. Woodford, A. Harriman, W. McFarlane and C. Wills, *ChemPhotoChem*, 2017, **1**, 317–325.

112 D. F. Moyano, M. Goldsmith, D. J. Solfiell, D. Landesman-Milo, O. R. Miranda, D. Peer and V. M. Rotello, *J. Am. Chem. Soc.*, 2012, **134**, 3965–3967.

113 D. Boraschi and A. Duschl, *Nanoparticles Immune Syst. Saf. Eff.*, 2013, **11**, 2621–2624.

114 T. Lammers, F. Kiessling, W. E. Hennink and G. Storm, *J. Control. Release*, 2012, **161**, 175–187.

115 D. R. Bhumkar, H. M. Joshi, M. Sastry and V. B. Pokharkar, *Pharm. Res.*, 2007, **24**, 1415–1426.

116 P. Sandström, M. Boncheva and B. Åkerman, *Langmuir*, 2003, **19**, 7537–7543.

117 V. Dixit, J. Van Den Bossche, D. M. Sherman, D. H. Thompson and R. P. Andres, *Bioconjug. Chem.*, 2006, **17**, 603–609.

118 D. A. Giljohann, D. S. Seferos, A. E. Prigodich, P. C. Patel and C. A. Mirkin, *J. Am. Chem. Soc.*, 2009, **131**, 2072–2073.

119 T. Niidome, K. Nakashima, H. Takahashi and Y. Niidome, *Chem. Commun.*, 2004, **17,** 1978-1979.

120 A. D. Friedman, S. E. Claypool and R. Liu, *Curr. Pharm. Des.*, 2013, **19**, 6315–29.

121 F. Fay and C. J. Scott, *Immunotherapy*, 2011, **3**, 381–394.

122 T. Carter, P. Mulholland and K. Chester, *Immunotherapy*, 2016, **8**, 941–958.

123 A. C. Okur, P. Erkoc and S. Kizilel, *Colloids Surfaces B Biointerfaces*, 2016, **147**, 191–200.

124 A. King, C. Ndifon, S. Lui, K. Widdows, V. R. Kotamraju, L. Agemy, T. Teesalu, J. D. Glazier, F. Cellesi, N. Tirelli, J. D. Aplin, E. Ruoslahti and L. K. Harris, *Sci. Adv.*, 2016, **2**, 1–16.

125 W. M. Pardridge, *Drug Discov. Today*, 2007, **12**, 54–61.

126 V. V. Gwenin, C. D. Gwenin and M. Kalaji, *Langmuir*, 2011, **27**, 14300–14307.

127 F. Bødker, S. Mørup and S. Linderoth, *Phys. Rev. Lett.*, 1994, **72**, 282–285.

128 J. D. Donaldson and D. Beyersmann, in *Ullmann's Encyclopedia of Industrial Chemistry*, Wiley-VCH Verlag GmbH & Co. KGaA, Weinheim, Germany, 2005, pp. 467–497.

129 J. Crossgrove and W. Zheng, *NMR Biomed.*, 2004, **17**, 544–553.

130 K. Soto, K. M. Garza and L. E. Murr, *Acta Biomater.*, 2007, **3**, 351–358.

131 T. J. Brunner, P. Wick, P. Manser, P. Spohn, R. N. Grass, L. K. Limbach, A. Bruinink and W. J. Stark, *Environ. Sci. Technol.*, 2006, **40**, 4374–4381.

132 E. Mine, A. Yamada, Y. Kobayashi, M. Konno and L. M. Liz-Marzán, *J. Colloid Interface Sci.*, 2003, **264**, 385–390.

133 M. G. Cerruti, M. Sauthier, D. Leonard, D. Liu, G. Duscher, D. L. Feldheim and S. Franzen, *Anal. Chem.*, 2006, **78**, 3282–3288.

134 Y. Kobayashi, R. Nagasu, K. Shibuya, T. Nakagawa, Y. Kubota, K. Gonda and N. Ohuchi, *J. Nanoparticle Res.*, 2014, **16**.

135 B. Tural, N. Özkan and M. Volkan, *J. Phys. Chem. Solids*, 2009, **70**, 860–866.

136 D. Chen, J. Li, C. Shi, X. Du, N. Zhao, J. Sheng and S. Liu, *Chem. Mater.*, 2007, **19**, 3399–3405.

137 U. Tamer, D. Cetin, Z. Suludere, I. H. Boyaci, H. T. Temiz, H. Yegenoglu, P. Daniel, I. Dinçer and Y. Elerman, *Int. J. Mol. Sci.*, 2013, **14**, 6223–6240.

138 J. L. Lyon, D. A. Fleming, M. B. Stone, P. Schiffer and M. E. Williams, *Nano Lett.*, 2004, **4**, 719–723.

139 S. Pal, M. Morales, P. Mukherjee and H. Srikanth, *J. Appl. Phys.*, 2009, **105**, 1–4.

140 N. R. Jana, *Analyst*, 2003, **128**, 954.

141 E. Iglesias-Silva, J. Rivas, L. M. León Isidro and M. A. López-Quintela, *J. Non. Cryst. Solids*, 2007, **353**, 829–831.

142 J. W. Alexander, *Surg Infect*, 2009, **10**, 289–292.

143 D. E. Marx and D. J. Barillo, *Burns*, 2014, **40**, 9–18.

144 European Union Patent, EP2473197-A2, 2009.

145 S. C. McBain, H. H. P. Yiu and J. Dobson, *Int. J. Nanomedicine*, 2008, **3**, 169–180.

146 O. Veiseh, J. W. Gunn and M. Zhang, *Adv. Drug Deliv. Rev.*, 2010, **62**, 284–304.

147 S. Kayal and R. V. Ramanujan, *J. Nanosci. Nanotechnol.*, 2010, **10**, 5527–5539.

148 S. Bhana, G. Lin, L. Wang, H. Starring, S. R. Mishra, G. Liu and X. Huang, *ACS Appl. Mater. Interfaces*, 2015, **7**, 11637–11647.

149 N. S. Abadeer and C. J. Murphy, *J. Phys. Chem. C*, 2016, **120**, 4691–4716.

150 D. K. Kirui, D. A. Rey and C. A. Batt, *Nanotechnology*, 2010, **21**.

151 S. Lal, S. E. Clare and N. J. Halas, *Acc. Chem. Res.*, 2008, **41**, 1842–1851.

152 G. A. Sotiriou, F. Starsich, A. Dasargyri, M. C. Wurnig, F. Krumeich, A. Boss, J. C. Leroux and S. E. Pratsinis, *Adv. Funct. Mater.*, 2014, **24**, 2818–2827.

153 S. J. Cho, B. R. Jarrett, A. Y. Louie and S. M. Kauzlarich, *Nanotechnology*, 2006, **17**, 640–644.

154 L. Cheng, K. Yang, Y. Li, X. Zeng, M. Shao, S. T. Lee and Z. Liu, *Biomaterials*, 2012, **33**, 2215–2222.

155 S. Kayal and R. V. Ramanujan, *J. Nanosci. Nanotechnol.*, 2010, **10**, 5527–5539.

156 P. F. Searle, M. J. Chen, L. Hu, P. R. Race, A. L. Lovering, J. I. Grove, C. Guise, M. Jaberipour, N. D. James, V. Mautner, L. S. Young, D. J. Kerr, A. Mountain, S. A. White and E. I. Hyde, *Clin. Exp. Pharmacol. Physiol.*, 2004, **31**, 811–816.

157 P. Patel, J. G. Young, V. Mautner, D. Ashdown, S. Bonney, R. G. Pineda, S. I. Collins, P. F. Searle, D. Hull, E. Peers, J. Chester, D. M. Wallace, A. Doherty, H. Leung, L. S. Young and N. D. James, *Mol. Ther.*, 2009, **17**, 1292–1299.

158 D. H. Palmer, V. Mautner, D. Mirza, S. Oliff, W. Gerritsen, J. R. M. Van der Sijp, S. Hubscher, G. Reynolds, S. Bonney, R. Rajaratnam, D. Hull, M. Horne, J. Ellis, A. Mountain, S. Hill, P. A. Harris, P. F. Searle, L. S. Young, N. D. James and D. J. Kerr, *J. Clin. Oncol.*, 2004, **22**, 1546–1552.

159 K. D. Bagshawe, in *Prodrugs: Challenges and rewards*, eds. S. Valentino, R. Borchardt, M. Hageman, R. Oliyai, H. Maag and T. W. Jefferson, Springer, New York, 2005, pp. 526–536.

160 S. K. Sharma, K. A. Chester and K. D. Bagshawe, *Handb. Ther. Antibodies Second Ed.*, 2014, **1**–**4**, 475–486.

161 C. D. Gwenin, M. Kalaji, P. A. Williams and R. M. Jones, *Biosens. Bioelectron.*, 2007, **22**, 2869–2875.

162 F. E. Kruis, H. Fissan and A. Peled, *J. Aerosol Sci.*, 1998, **29**, 511–535.

163 M. Chen, S. Yamamuro, D. Farrell and S. A. Majetich, *J. Appl. Phys.*, 2003, **93**, 7551–7553.

164 P. C. Stevenson, J. Turkevich and Hillier, *Discuss. Faraday. Soc.*, 1951, **11**, 55–75.

165 B. R. Cuenya, *Thin Solid Films*, 2010, **518**, 3127–3150.

166 S. Laurent, D. Forge, M. Port, A. Roch, C. Robic, L. Vander Elst and R. N. Muller, *Chem. Rev.*, 2008, **108**, 2064–2110.

167 D. Ling and T. Hyeon, *Small*, 2013, **9**, 1450–1466.

168 J. Eastoe, M. J. Hollamby and L. Hudson, *Adv. Colloid Interface Sci.*, 2006, **128**–**130**, 5–15.

169 S. Moraes Silva, R. Tavallaie, L. Sandiford, R. D. Tilley and J. J. Gooding, *Chem. Commun.*, 2016, **52**, 7528–7540.

170 C. L. Fang, K. Qian, J. Zhu, S. Wang, X. Lv and S.-H. Yu, *Nanotechnology*, 2008, **19**, 125601.

171 E. Iglesias-Silva, J. L. Vilas-Vilela, M. A. López-Quintela, J. Rivas, M. Rodríguez and L. M. León, *J. Non. Cryst. Solids*, 2010, **356**, 1233–1235.

172 M. Boutonnet, J. Kizling, P. Stenius and G. Maire, *Colloids and Surfaces*, 1982, **5**, 209–225.

173 C. Tanford, *J. Phys. Chem.*, 1974, **78**, 2469–2479.

174 M. P. Pileni, *Langmuir*, 1997, **13**, 3266–3276.

175 J. D. Holmes, P. a Bhargava, B. a Korgel and K. P. Johnston, *Langmuir*, 1999, **15**, 6613–6615.

176 H. Ohde, X. R. Ye, C. M. Wai and J. M. Rodriguez, *Chem. Commun.*, 2000, **2354**, 2353–2354.

177 H. Ohde, C. M. Wai, H. Kim, J. Kim and M. Ohde, *J. Am. Chem. Soc.*, 2002, **124**, 4540–4541.

178 E. E. Carpenter, C. T. Seip and C. J. O'Connor, *J. Appl. Phys.*, 1999, **85**, 5184–5186.

179 K. T. Lim, H. S. Hwang, W. Ryoo and K. P. Johnston, *Langmuir*, 2004, **20**, 2466–2471.

180 A. S. Bommarius, J. F. Holzwarth, D. I. C. Wang and T. A. Hatton, *J. Phys. Chem.*, 1990, **94**, 7232–7239.

181 J. Liu, P. Raveendran, Z. Shervani, Y. Ikushima and Y. Hakuta, *Chem. - A Eur. J.*, 2005, **11**, 1854–1860.

182 J. Liu, Y. Ikushima and Z. Shervani, *Curr. Opin. Solid State Mater. Sci.*, 2003, **7**, 255–261.

183 E. E. Carpenter, C. Sangregorio and C. J. Connor, *IEEE Trans. Magn.*, 1999, **35**, 3496–3498.

184 J. Lin, W. Zhou, A. Kumbhar, J. Wiemann, J. Fang, E. E. Carpenter and C. J. O'Connor, *J. Solid State Chem.*, 2001, **159**, 26–31.

185 S. J. Cho, J. C. Idrobo, J. Olamit, K. Liu, N. D. Browning and S. M. Kauzlarich, *Chem. Mater.*, 2005, **17**, 3181–3186.

186 O. Pana, C. M. Teodorescu, O. Chauvet, C. Payen, D. Macovei, R. Turcu, M. L. Soran, N. Aldea and L. Barbu, *Surf. Sci.*, 2007, **601**, 4352–4357.

187 C. T. Seip and C. J. O'Connor, *Nanostructured Mater.*, 1999, **12**, 183–186.

188 J. A. Lopez Perez, M. A. Lopez Quintela, J. Mira, J. Rivas and S. W. Charles, *J. Phys. Chem. B*, 1997, **101**, 8045–8047.

189 J. Zhang, M. Post, T. Veres, Z. J. Jakubek, J. Guan, D. Wang, F. Normandin, Y. Deslandes and B. Simard, *J. Phys. Chem. B*, 2006, **110**, 7122–7128.

190 S. Takami, T. Sato, T. Mousavand, S. Ohara, M. Umetsu and T. Adschiri, *Mater. Lett.*, 2007, **61**, 4769–4772.

191 H. Y. Park, M. J. Schadt, L. Wang, I. I. S. Lim, P. N. Njoki, S. H. Kim, M. Y. Jang, J. Luo and C.-J. Zhong, *Langmuir*, 2007, **23**, 9050–9056.

192 H. L. Liu, P. Hou, W. X. Zhang and J. H. Wu, *Colloids Surfaces A Physicochem. Eng. Asp.*, 2010, **356**, 21–27.

193 S. Banerjee, S. O. Raja, M. Sardar, N. Gayathri, B. Ghosh and A. Dasgupta, *J. Appl. Phys.*, 2011, **109**, 1-7.

194 X. Sun, C. Zheng, F. Zhang, Y. Yang, G. Wu, A. Yu and N. Guan, *J. Phys. Chem. C*, 2009, **113**, 16002–16008.

195 P. M. Aneesh, K. A. Vanaja and M. K. Jayaraj, 2007, **6639**, 66390J.

196 M. Brust, M. Walker, D. Bethell, D. J. Schiffrin and R. Whyman, *J. Chem. Soc., Chem. Commun.*, 1994, 801–802.

197 Z. Ban, Y. A. Barnakov, F. Li, V. O. Golub and C. J. O'Connor, *J. Mater. Chem.*, 2005, **15**, 4660-4662.

198 Y. Zhai, J. Zhai, Y. Wang, S. Guo, W. Ren and S. Dong, *J. Phys. Chem. C*, 2009, **113**, 7009–7014.

199 P. G. Rudakovskaya, E. K. Beloglazkina, A. G. Majouga and N. V. Zyk, *Mendeleev Commun.*, 2010, **20**, 158–160.

200 F. Mohammad, G. Balaji, A. Weber, R. M. Uppu and C. S. S. R. Kumar, *J. Phys. Chem. C. Nanomater. Interfaces*, 2010, **114**, 19194–19201.

201 H. Zhou, J. Lee, T. J. Park, S. J. Lee, J. Y. Park and J. Lee, *Sensors Actuators, B Chem.*, 2012, **163**, 224–232.

202 L. Wang, J. Luo, Q. Fan, M. Suzuki, I. S. Suzuki, M. H. Engelhard, Y. Lin, N. Kim, J. Q. Wang and C.-J. Zhong, *J. Phys. Chem. B*, 2005, **109**, 21593–21601.

203 I. Robinson, L. D. Tung, S. Maenosono, C. Wälti and N. T. K. Thanh, *Nanoscale*, 2010, **2**, 2624-2630.

204 N. Dahal, V. Chikan, J. Jasinski and V. Leppert, *Chem. Mater.*, 2008, **17**, 6389–6395.

205 Y. Wei, B. Han, X. Hu, Y. Lin, X. Wang and X. Deng, *Procedia Eng.*, 2012, **27**, 632–637.

206 R. Rawal, S. Chawla and C. S. Pundir, *Biosens. Bioelectron.*, 2012, **31**, 144–150.

207 M. N. Nadagouda and R. S. Varma, *Cryst. Growth Des.*, 2007, **7**, 2582–2587.

208 T. Ahmad, I. A. Wani, J. Ahmed and O. A. Al-Hartomy, *Appl. Nanosci.*, 2014, **4**, 491–498.

209 T. K. Sau and C. J. Murphy, *J. Am. Chem. Soc.*, 2004, **126**, 8648–8649.

210 B. Nowack, H. F. Krug and M. Height, *Environ. Sci. Technol.*, 2011, **45**, 1177–1183.

211 B. V Enustun and J. Turkevich, *J. Am. Chem. Soc.*, 1963, **85**, 3317–3328.

212 K. R. Brown, D. G. Walter and M. J. Natan, *Chem. Mater.*, 2000, **12**, 306–313.

213 I. Y. Goon, L. M. H. Lai, M. Lim, P. Munroe, J. J. Gooding and R. Amal, *Chem. Mater.*, 2009, **21**, 673–681.

214 C. S. Levin, C. Hofmann, T. A. Ali, A. T. Kelly, E. Morosan, P. Nordlander, K. H. Whitmire and N. J. Halas, *ACS Nano*, 2009, **3**, 1379–1388.

215 L. L. Ma, A. U. Borwankar, B. W. Willsey, K. Y. Yoon, J. O. Tam, K. V Sokolov, M. D. Feldman, T. E. Milner and K. P. Johnston, *Nanotechnology*, 2013, **24**, 1-33.

216 A. J. Wagstaff, S. D. Brown, M. R. Holden, G. E. Craig, J. A. Plumb, R. E. Brown, N. Schreiter, W. Chrzanowski and N. J. Wheate, *Inorganica Chim. Acta*, 2012, **393**, 328–333.

217 H. Wang, D. W. Brandl, F. Le, P. Nordlander and N. J. Halas, *Nano Lett.*, 2006, **6**, 827–832.

218 Z. Xu, Y. Hou and S. Sun, *J. Am. Chem. Soc.*, 2007, **129**, 8698–8699.

219 C. M. Phan and H. M. Nguyen, *J. Phys. Chem. A*, 2017, **121**, 3213–3219.

Chapter 3:
The synthesis, purification and characterization of AuMNPs

3.0 Introduction

It is well established that nanoparticles represent the future for many fields of science and medicine, with some nanoparticles already being approved for use in medical treatments.[1,2] As previously mentioned in section 1.5.3 Gwenin *et al.* have patented a novel anti-cancer treatment involving the use of a gold coated superparamagnetic iron oxide nanoparticle as a carrier for a prodrug activating enzyme,[3,4] with the aim being to use magnetic fields to direct the enzyme:AuMNP conjugate towards a solid tumour site. The nanoparticles in question for use need to be spherical, have a consistent smooth gold coating and be approx. 50 nm in diameter. There are a variety of ways that can be used to synthesise gold coated iron nanoparticles,[3,5–10] with many techniques being able to produce a range in both size[11–13] and shape[14–17] of yielded nanoparticles. Synthesis of the particles alone is not the only issue that needs to be overcome, quite often when coating iron oxide nanoparticles we do not achieve a coating on 100 % of the nanoparticles which is undesirable, despite iron nanoparticles being approved for medical use.[18–23] One final but important set of data for any system being used in medical treatments is the stability of the treatment in various media. That is to say can the nanoparticles remain suspended in solution when put into the body, or would they potentially aggregate?

Here in this chapter the development of the AuMNP synthesis will be discussed along with purification methods attempted on the nanoparticles. Finally, the stability of the AuMNPs in various liquid media will be examined to assess the potential use of the nanoparticles as a viable medical treatment.

3.1 AuMNP Synthesis

As previously stated the synthesis method described here is based upon 2 different published methods.[24,25] 10 nm Fe_3O_4 nanoparticles (*3 mg/ml, 220 µl*) were mixed with sodium citrate dihydrate (*100 mM, 4.5 ml*) and H_2O (*145.5 ml*), this mixture was allowed to degas under argon for 30 minutes, after which time the mixture was stirred at 1000 rpm, and was left stirring at this speed for the rest of the synthesis. After 30 minutes of stirring, 5 nm gold nanoparticle (*1 ml*) 'seeds' were added to the reaction mixture at a rate of 1 ml per minute. 1 hour after the addition of the gold 'seeds' $HAuCl_4.3H_2O$ (*1 % w/v, 5 ml*) was added at a rate of 1 ml per minute giving the solution a yellow tinge. The reaction was then left to homogenise for 5 minutes upon which NH_2OH (*200 mM, 1 ml*) was added at a rate of 0.5 ml per minute, after which time the solution was heated to 60 $^{\circ}$C and left for 1 hour. Upon initial addition of the

NH_2OH, the mixture changed colour from being transparent with a yellow tinge, to an opaque deep purple colour, however after the mixture heats to 60 ˚C the reaction mixture turns a red colour. 1 hour after the addition of NH_2OH sodium citrate dihydrate (*100 mM, 4.5ml*) was added and the solution was left to mix for another hour, after which time the reaction mixture was removed from the vessel and centrifuged at 2750 rpm for 1 hour at 20 ˚C to separate the AuMNPs. After centrifugation, the supernatant was placed in conical flasks on top of a 1T magnet measuring 50 mm x 50 mm x 20 mm and left overnight to separate out the magnetic material, as demonstrated in Figure 3.1.

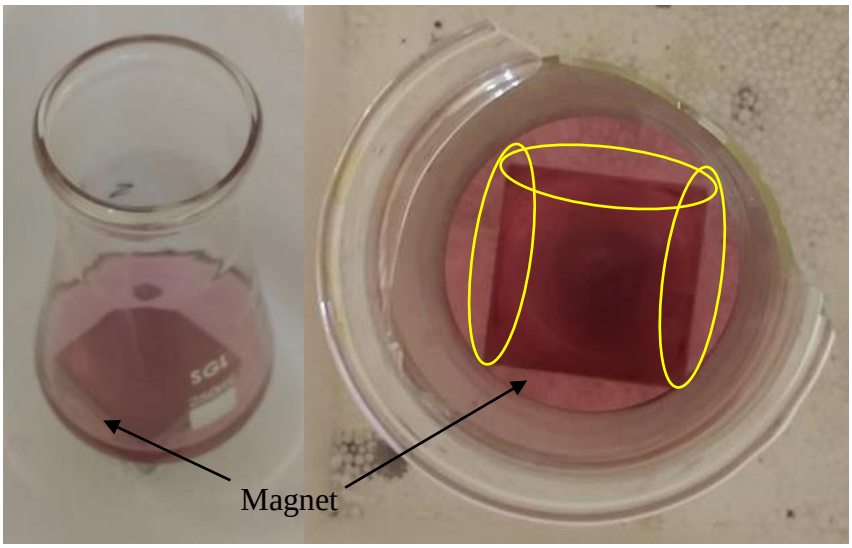

Figure 3.1. The nanoparticles placed into a glass conical flask on top of a 1 tesla magnet (left). The AuMNPs have separated out along the edge of the magnet which are ringed in yellow (right).

The conical flasks were left overnight, and the supernatant was removed the following day after the AuMNPs had been separated to the bottom of the conical flask. The AuMNP pellet that formed (*Figure 3.1*) was transferred into an 8 ml glass vial and placed on the side of a raised magnet, and again left overnight for a pellet to form on the side of the vial. The following day the supernatant was removed from the vial without disturbing the pellet, and was replaced with sodium citrate dihydrate (*7 ml, 1 mM*). This media replacement is a 'wash' step to replace any non-magnetic nanoparticles and reaction media with sodium citrate, to act as a stabilizing agent for the AuMNPs. This step is repeated 3 times, after which the pellet is suspended in 1 ml of 1 mM sodium citrate dihydrate, then characterized by UV-Vis spectroscopy to determine the size of the AuMNPs by assessing the λ-max of the gold peak.[26] Figure 3.2 presents a typical full spectrum scan of the AuMNPs post synthesis and purification. Each synthesis produces an equivalent of 1 ml of between 0.3-0.6 absorbance.

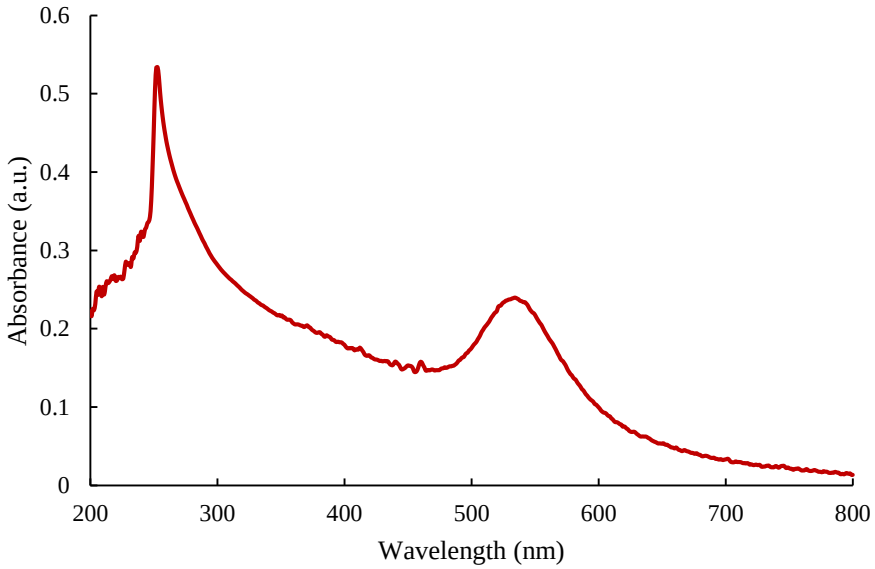

Figure 3.2. A typical spectra of the AuMNPs following synthesis, centrifugation and magnetic purification. The λ-max of this particular scan is 535 nm, which based on literature would give a diameter of 59 nm,[26] however that is assuming perfectly spherical nanoparticles. As can be observed with the gold peak not being symmetrical and smooth, the nanoparticles are not perfectly spherical, this can also be observed in the TEM images in figures 2.4, 2.6, 2.8, 2.10 and 2.12.

Figure 3.3 is a flow diagram of how the AuMNP synthesis takes place, initially 5 nm gold nanoparticles are 'seeded' onto the 10 nm Fe_3O_4 nanoparticles/ cores (**1**), leading to the formation of gold 'seeded' iron cores (**2**). Following this $HAuCl_4$ is reduced in solution with the seeded cores which deposits gold onto the seeded iron cores causing the growth/ nucleation of the nanoparticles. It is of note that the $HAuCl_4$ being reduced also forms gold nanoparticles, possibly from nucleation around any gold seeds that did not attach to the Fe_3O_4 (**3**). Finally, the gold nanoparticles are magnetically purified from solution leaving the 50 nm AuMNPs (**4**).

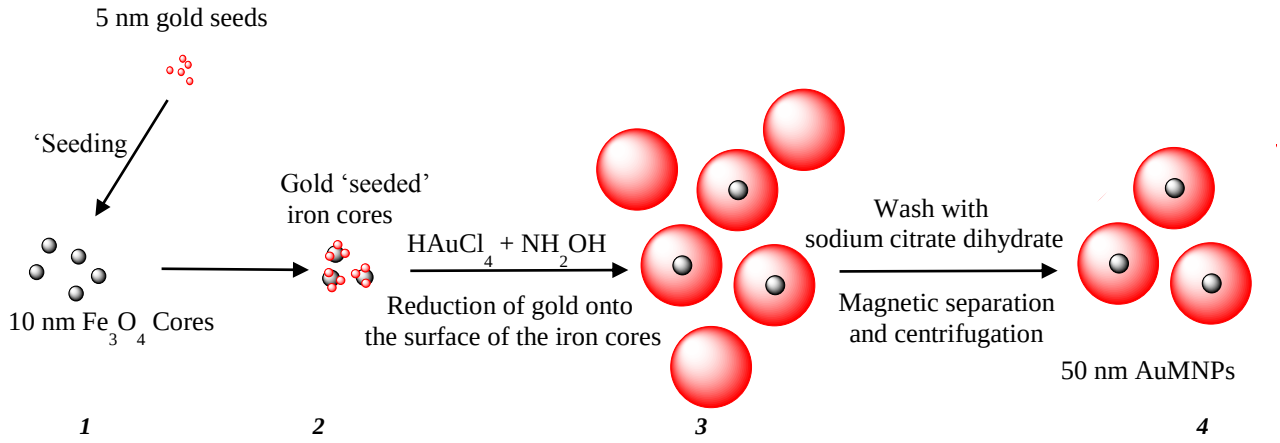

*Figure 3.3. A schematic representation of the synthesis of AuMNPs, the Fe_3O_4 cores are firstly seeded with 5nm gold nanoparticles (**1**), creating gold 'seeded' iron cores (**2**) after which $HAuCl_4$ is reduced in solution causing the release of Au+ ions, and stimulating the nucleation of gold shells around the iron cores (**3**), as well as the growth of gold nanoparticles (**3**). These gold nanoparticles are purified out by centrifugation and magnetic separation to leave the 50 nm AuMNPs (**4**).*

3.2 Characterization of AuMNPs

3.2.1 UV-Vis

An easy and efficient way to analyse many materials including nanoparticles is using Ultraviolet-Visible light spectroscopy (*UV-Vis*). This type of analysis can produce a lot of information about a material based on what type/ wavelength of light it absorbs. Gold spherical nanoparticles absorb light between 500-600 nm, dependant on size.[9,27,28] The gold peak (the area between 500-600 nm where the nanoparticles show absorbance) can give information about the particle including: size based on the λ-max of the gold peak,[26] size distribution based on the broadness and width of the peak,[26] and shape of the nanoparticle based on the shape of the peak.[29] The AuMNPs synthesised here have been analysed by UV-vis to characterize the shape and size of the nanoparticles.

3.2.2 Transmission electron microscopy

Another method for nanoparticle characterisation is transmission electron microscopy (*TEM*), this form of microscopy involves a beam of electrons being fired through a specimen mounted on a film. Some electrons pass through the film, whilst others interact with the sample which produces a contrast image, based on differing electron densities being captured by an electron lens. TEM scans were performed on samples from the various protocols used for AuMNP synthesis described in Table 3.1, these images are presented below.

3.2.3 Zeta potential

In simple terms zeta potential is a measure of the electric potential between a dispersion medium, and the layer of medium on the surface of a dispersed particle. In specific terms it is the electric potential in the double layer at the slipping plane location, relative to a location in the bulk dispersion medium. Zeta potential is a way to measure the stability of a colloidal suspension, and how susceptible the suspension is to aggregation or flocculation.

3.2.4 Dynamic light scattering

Dynamic light scattering (*DLS*) is a technique that can be used to determine the size of particles in a solution, and give a size distribution of said particles.[31] DLS works by sending a light source such as a laser through a polarizer into a sample. The particles within the solution are hit by the polarized light source causing the light to scatter as it interacts with the sample. This scattered light goes through a separate polarizer where the light is detected by a photomultiplier, and is converted into a visible image.

3.3 Improving the synthesis of the AuMNPs

When looking at how to improve the synthesis of nanoparticles, it must first be considered as to what needs to be improved, such as the size, shape, yield etc. It can be easier to alter and improve some factors of the synthesis over others. For example it has been noted that the ratio of gold to iron for AuMNP synthesis is important on the final shape.[28] However it is not just the ratio of the gold to iron that can affect the final shape, the number of iterations of Au^{3+} can determine the final nanoparticle shape, with 1 iteration being ideal for spherical particles.[28] Based on various literature slight changes were made to the original AuMNP synthesis in order to synthesise 50 nm AuMNPs, these differences are presented in Table 3.1.

Table 3.1. The following 5 different AuMNP synthesis protocols that were attempted for the synthesis and purification of AuMNPs following on from work previously done are presented below.

Protocol	Fe_3O_4 volume (ml)	Fe:Au ratio	Component of synthesis taken post centrifugation	Post synthesis purification	Synthesis attempts
Protocol 1	3.00	1:0.1	Pellet	Magnetic separation	50
Protocol 2	3.00	1:0.1	Supernatant	Magnetic separation	50
Protocol 3	0.22	1:1.5	Supernatant	Magnetic separation	150
Protocol 4	0.22	1:1.5	Supernatant	Magnetic separation, centrifugation 11000 rpm 20 minutes	300
Protocol 5	0.22	1:1.5	Supernatant	Magnetic separation, centrifugation 1500 rpm 2 hrs	500+

3.3.1 Protocol 1

Protocol 1 was the original AuMNP synthesis that had been developed within the research group. This protocol analysed the pellet from the AuMNP synthesis after magnetic purification and centrifugation. The pellet was analysed by TEM and UV-vis as presented in Figures 3.4 and 3.5, respectively. The TEM image has several key features of discussion; the first is the small number of misshapen black ‘spots’ on the image, these are the AuMNPs which show no size or shape control. Another issue in point is the large quantity of uncoated Fe_3O_4 nanoparticles, shown in grey which would indicate that the seeding and coating process is not

working. A point re-iterated by the UV-Vis spectra, which shows no properly defined gold peak or λ-max.

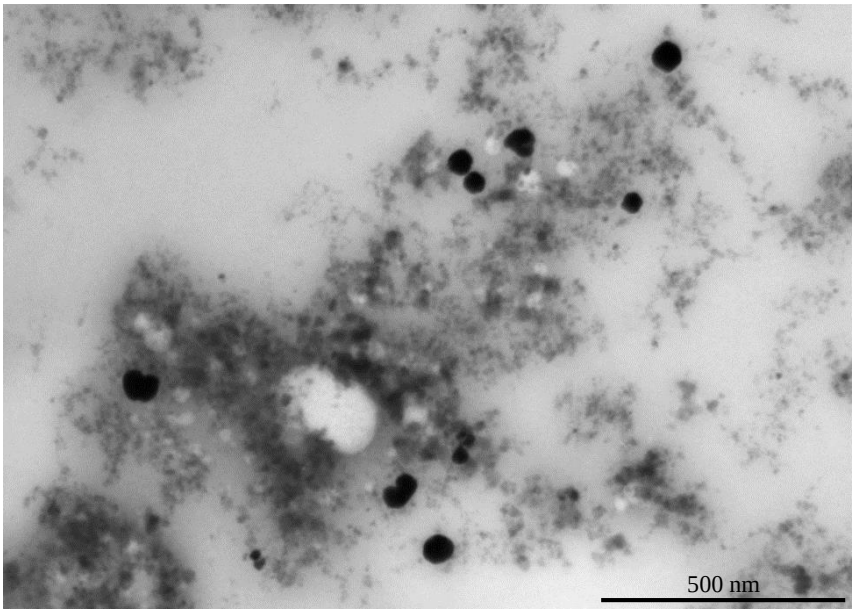

Figure 3.4. A TEM image of the pellet of an AuMNP synthesis following protocol 1, after magnetic separation, as can be seen there AuMNP yield is very low, with any AuMNPs present being distorted in shape and size. The average size of the nanoparticles in this TEM are 51 nm with a standard deviation of ± 9 nm from a sample size of 10.

Following the TEM image and UV-Vis scan of the pellet, it was decided to analyse the supernatant from the reaction to assess if the desired AuMNPs were staying in suspension post centrifugation.

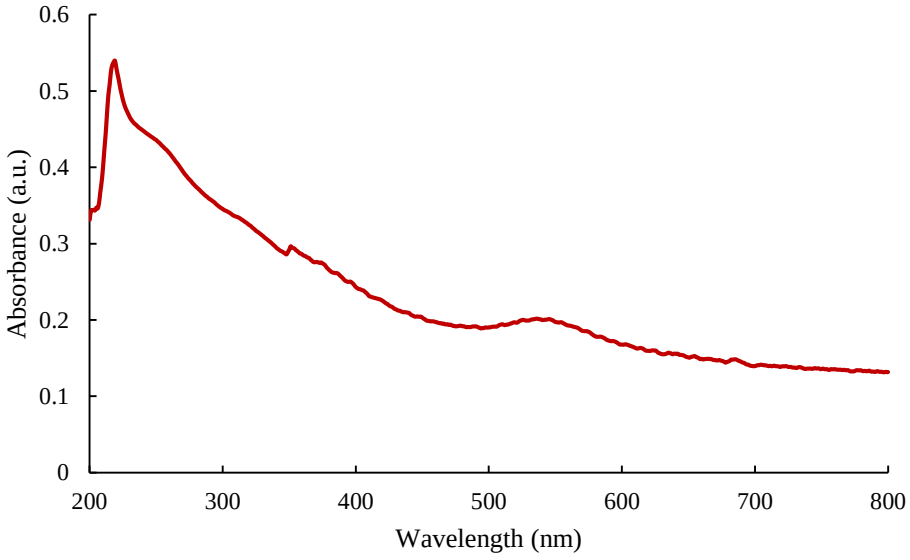

Figure 3.5. A UV-Vis scan of the pellet of an AuMNP synthesis following protocol 1, after magnetic separation. Here the gold peak is not very pronounced indicating poor coating with no even shape distribution.

3.3.2 Protocol 2

Whilst protocol 1 was based on the examination of the pellet of the synthesis after centrifugation, protocol 2 examines the supernatant. The following TEM image and UV-vis spectra of the supernatant of protocol 2 are presented as Figures 3.6 and 3.7 respectively, the TEM image presents more AuMNPs with a better spherical nature than before with a lot less Fe_3O_4 nanoparticles, however there are still misshapen nanoparticles, with a wide size distribution and still showing a low concentration of nanoparticles. The TEM image and UV-Vis spectra of protocol 2 demonstrate that there are more spherical AuMNPs in the supernatant than the pellet, however they do not demonstrate a uniformity in their nature, nor does the UV-Vis have a defined gold peak that would be expected for a UV-Vis scan of gold nanoparticles. Literature suggests that the ratio of iron to gold is very important for the shape determination when synthesising a core-shell nanoparticle consisting of Fe-Au. The ideal ratio for producing spherical nanoparticles with a thick shell is presented as 1:1.5 of Fe:Au,[28] whilst ratios below this produce 'knobbly' nanoparticles with thin shells and are non-uniform in shape. It is also of note that the iterations of gold chloride used when synthesising the particles is of upmost importance, with 1 iteration being ideal for spherical particle production.[28] A single iteration is defined as continuous addition of $HAuCl_4$.

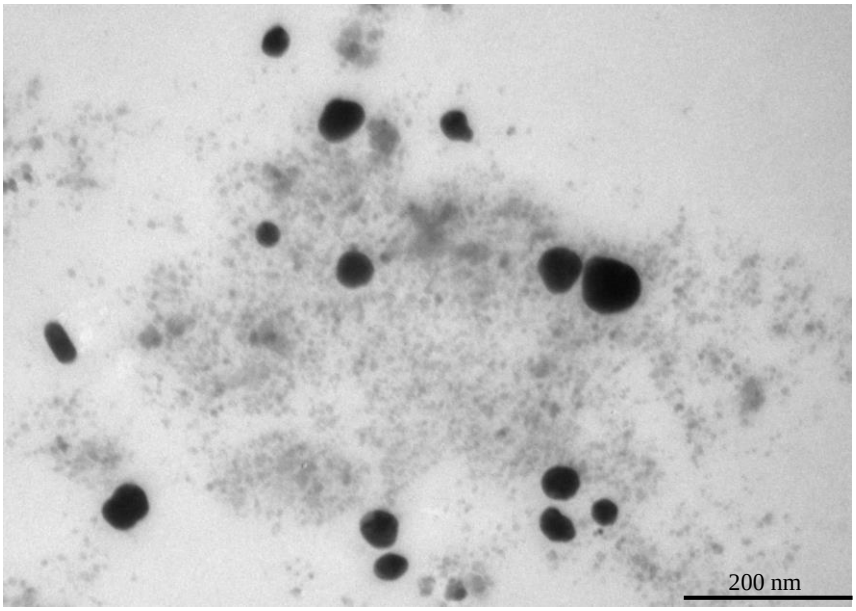

Figure 3.6. A TEM image of the supernatant of an AuMNP synthesis following protocol 2, here there are more gold nanoparticles with a more spherical shape than before, however there are still misshapen nanoparticles with a large size distribution. The average size of nanoparticles in this TEM are 41 nm with a standard deviation of ± 15 nm from a sample size of 14.

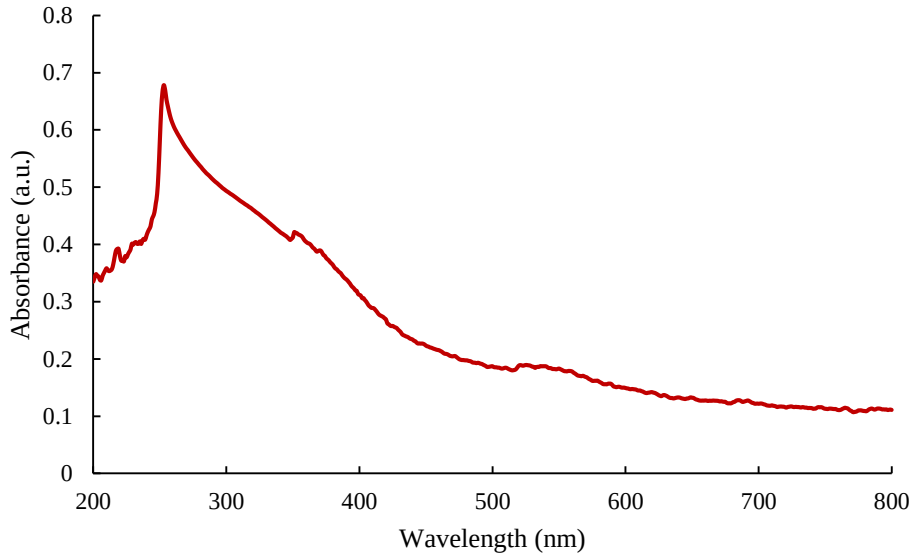

Figure 3.7. The UV-Vis spectra of the supernatant of an AuMNP synthesis following protocol 2, after magnetic separation. There is no defined peak between 500-600 nm as would be expected with gold nanoparticles.

3.3.3 Protocol 3

Protocol 3 of the AuMNP synthesis was developed based on the aforementioned information on the importance of the Fe:Au ratio, and previous work done in the group on the number of gold iterations. The AuMNPs produced following this new protocol were analysed again by TEM and UV-vis, with the data for both being presented on the following page. The TEM image (Figure 3.8) shows an improvement of both the shape and size distribution of the AuMNPs synthesised. The UV-Vis scan of Figure 3.9 demonstrates a more defined gold peak, (λ-max 537 nm), which according to theoretical data relates to nanoparticles with a size of approx. 62 nm.[26] Whilst the desired size is approx. 50 nm, this theoretical data is for perfectly spherical nanoparticles, the AuMNPs synthesised following protocol 3 are not perfectly spherical in nature, and are much closer to 50 nm in size according to the scale bar at the bottom right of the image.

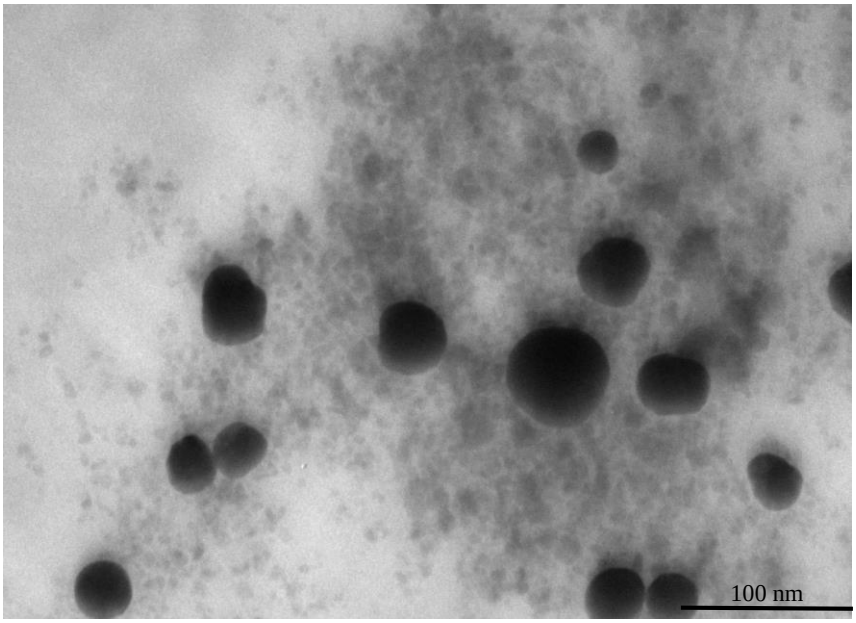

Figure 3.8. A TEM image of AuMNPs synthesised following protocol 3, showing a much improved shape and size distribution of the AuMNPs. The average size of nanoparticles in this TEM are 32 nm with a standard deviation of ± 10 nm from a sample size of 12.

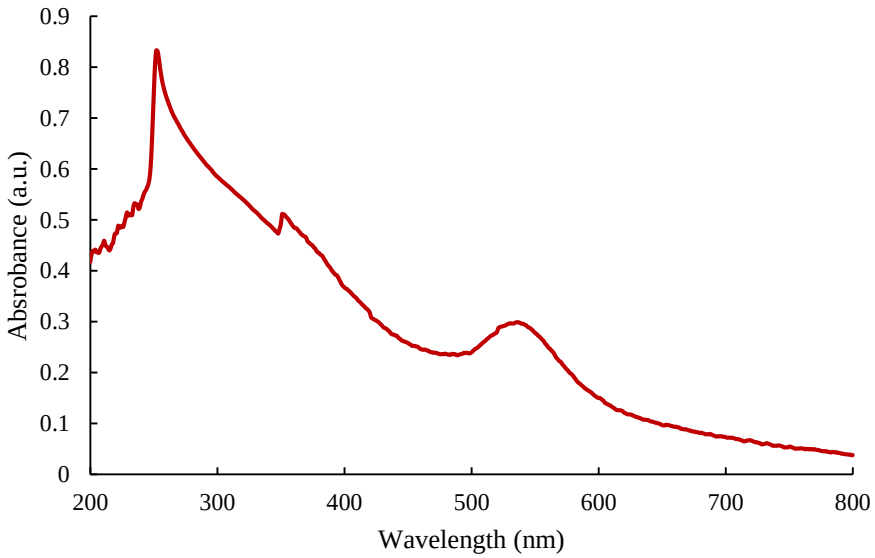

Figure 3.9. A UV-Vis scan of the AuMNPs synthesised following protocol 3, this UV-Vis demonstrates a much better defined gold peak than previous scans, with the λ-max of the gold peak being 537 nm.

Protocol 3 demonstrated a greatly improved synthesis method of AuMNPs than protocols 1 and 2, however as the TEM demonstrates there is still uncoated Fe_3O_4 nanoparticles in the final purification media. A purification method is required to remove the un-desired iron.

3.3.4 Protocol 4

The AuMNPs synthesised following protocol 4 were centrifuged for 20 minutes at 11000 rpm to attempt to separate the AuMNPs from Fe_3O_4, the samples were scanned before and after centrifugation by UV-Vis, with the pellet sample being sent for TEM. As can be observed in Figure 3.10, both Fe_3O_4 and AuMNPs can be pictured indicating unsuccessful separation of the 2 different particles. The UV-Vis spectra in figure 3.11 confirms that there was no successful separation of the particles.

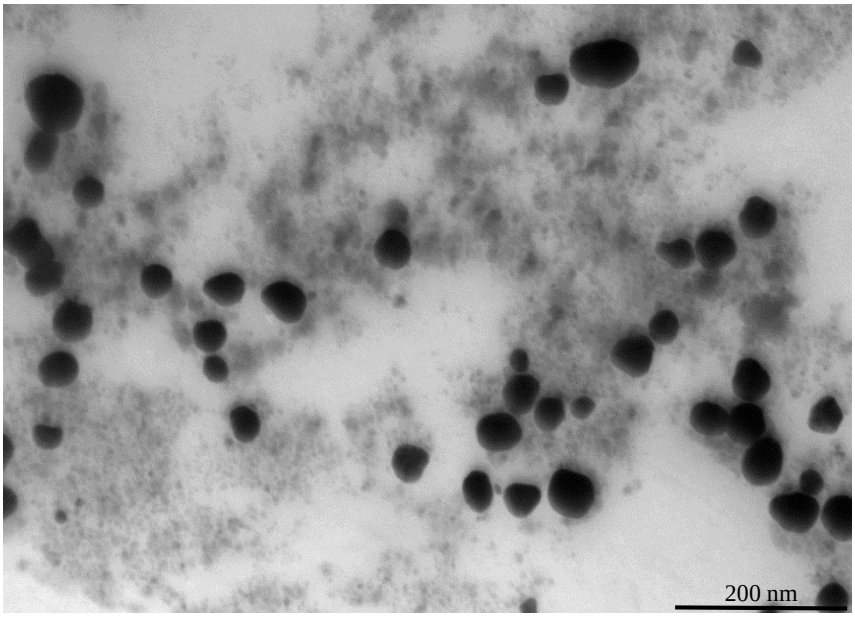

Figure 3.10. A TEM image of AuMNPs synthesised and purified following protocol 4, where the sample was centrifuged at 11000 rpm for 20 minutes. There are a number of AuMNPs present, however there seems to be no uniform size or general shape to the nanoparticles. The average sizeof nanoparticles in this TEM image is 36 nm with a standard deviation of ± 10 nm from a sample size of 40 nanoparticles.

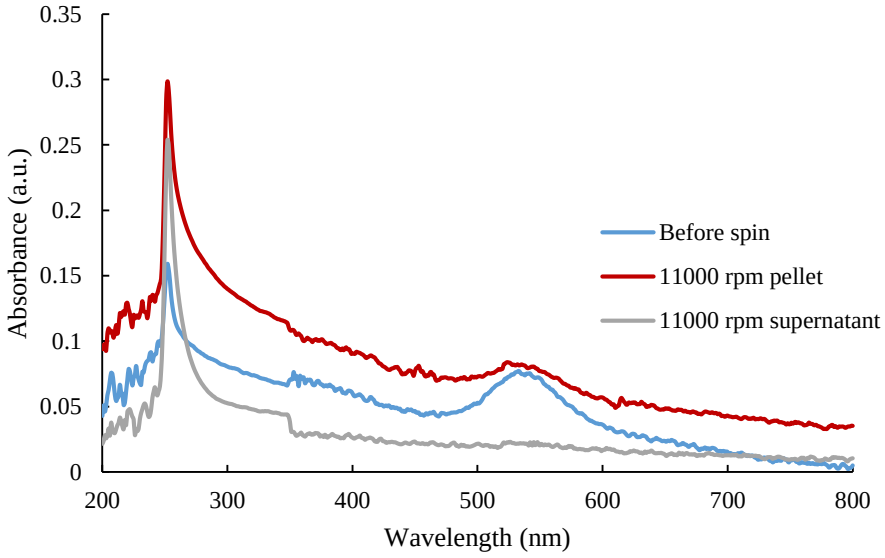

Figure 3.11. The UV-Vis scan of AuMNPs synthesised and purified following protocol 4. The sample before centrifugation is presented as the blue line, the pellet after centrifugation is presented as a red line and the grey line is the supernatant after centrifugation. The scan shows the before and after scans of the particles, with no clear purification have occurred.

Protocol 4 spectra unsuccessful for its attempts to purify the AuMNPs from excess Fe_3O_4, with the UV-Vis showing a decrease in the absorbance of the gold peak indicating a loss of AuMNP. It was believed that centrifuging the AuMNPs at a high speed for a low period of time was the wrong way to separate the AuMNPs and excess Fe_3O_4.

3.3.5 Protocol 5

Protocol 5 is similar to protocol 4 except for the time and rpm that the sample was spun at. AuMNPs from protocol 5 were spun at 1500 rpm for 2 hours to attempt nanoparticle separation. The TEM and UV-Vis spectra are presented below, Figure 3.12 is the TEM image of the AuMNPs after centrifugation, as can be seen in the image there is a big decrease in the number of Fe_3O_4 nanoparticles, whilst the concentration of AuMNP nanoparticles has increased, with the AuMNPs demonstrating a spherical shape with a tighter size distribution.

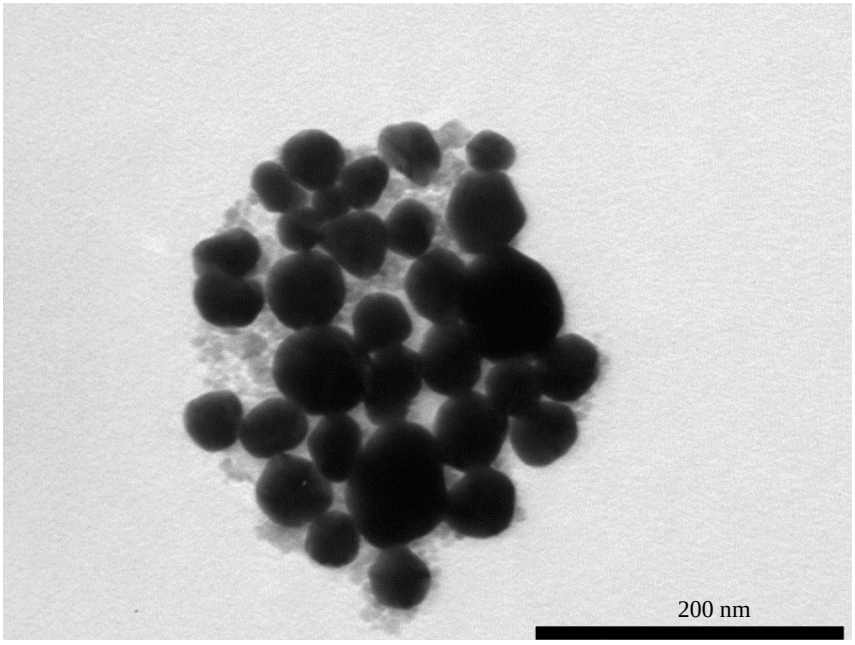

Figure 3.12. A TEM image of AuMNPs synthesised and purified following protocol 5, as can be seen there is a very low count of Fe_3O_4 nanoparticles, with a higher concentration of AuMNP nanoparticles which are more spherical in shape and have similar sizes. The average size of nanoparticles in this TEM image is 45 nm with a standard deviation of ±11 nm from a sample size of 30 nanoparticles.

The UV-Vis spectra of Figure 3.13 presents a scan before the AuMNPs were centrifuged that has a gold peak which is not that uniform in shape, which after centrifugation, becomes a much sharper, cleaner gold peak more indicative of AuMNPs with a tighter shape and size distribution. The drop in absorbance at 350-400 nm indicates a loss of Fe_3O_4 nanoparticles in the pellet compared to the starting sample, indicating successful purification.

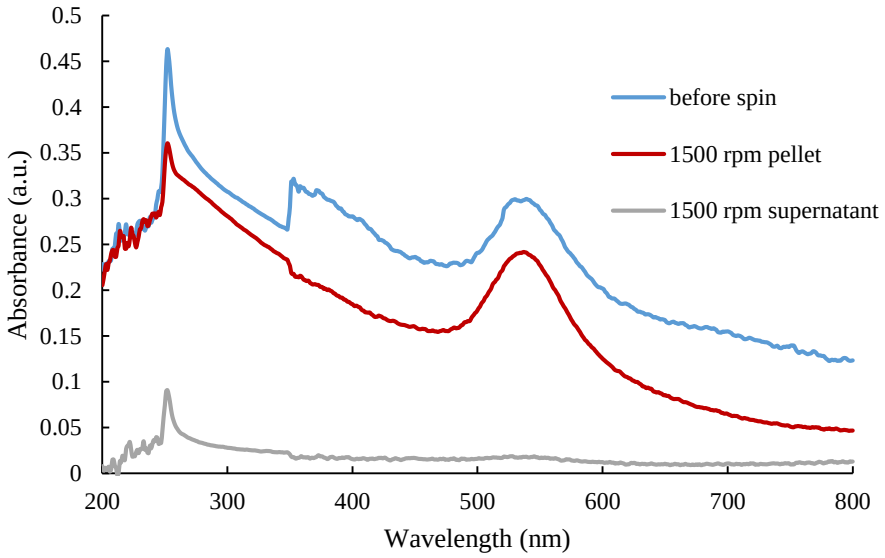

Figure 3.13. Presents a UV-Vis scan of the AuMNPs before and after centrifuging at 1500 rpm for 2 hours. The sample before centrifugation is presented as the blue line, the pellet after centrifugation is presented as a red line and the grey line is the supernatant after centrifugation. As can be seen the scan of the re-suspended pellet has a much smoother gold peak than the before scan, this indicates a much more uniform shape dispersion as well as size dispersion, there is also less iron in the sample based on the drop in absorbance at around 350-400 nm, which is where the Fe_3O_4 nanoparticles absorb.

Protocol 5 shows a final AuMNP product which have a spherical shape, tight size distribution and a low Fe_3O_4 nanoparticle count. There are still some Fe_3O_4 nanoparticles observed in the TEM image. Other purification attempts were made to remove these final Fe_3O_4 nanoparticles including: silica column purification, gravitational sephadex column purification, glycerol centrifugation with layered glycerol of varying concentration. However none of these methods of purification were successful in removing the final Fe_3O_4 nanoparticles. Based on this it was decided to proceed with using the AuMNPs with this small quantity of Fe_3O_4 nanoparticles, based on the principal use of Fe_3O_4 nanoparticles already having been approved for use in various medical treatments.

3.3.6 Zeta potential

Zeta potential for the purified nanoparticles was carried out by Malvern Scientific Solutions LTD. A sample of AuMNPs was examined 5 times to determine an average Zeta Potential, this data is reported in table 3.2, with a mean result of -35.24 mV being obtained for the AuMNPs. It is regarded that a result of ±30 or higher indicates a stable solution,[32] which would indicate that the AuMNPs are stable in solution. However it was noted by the company that when examining the overall zeta potential distribution there are; 'multiple charged species within the sample', with a broad distribution shown for these peaks. These two peaks could indicate two separately charged species within the solution, or be a result of zeta polydispersity. Since there

is excess iron in the solution it is possible that this second peak is present because of this. Finally the peak distribution does extend towards 0 mV, indicating that the species within the region will tend to flocculate or aggregate together.

Table 3.2. The results for the Zeta potential determined on a sample of AuMNPs performed by Malvern Scientific Solutions LTD.

	Zeta Potential (mV)
Repeat 1	-34.96
Repeat 2	-33.07
Repeat 3	-37.05
Repeat 4	-33.58
Repeat 5	-37.54
Mean	-35.24
Standard deviation	±2.007

3.3.7 Dynamic light scattering

Dynamic light scattering was also performed on a sample of AuMNPs by Malvern Scientific Solutions LTD. Three different types of measurement were applied to the sample to determine the average size of the nanoparticles in solution: Dynamic Light Scattering (*DLS*), Depolarized Dynamic Light Scattering (*DDLS*) and Multi Angle Dynamic Light Scattering (*MADLS*) for particle size distribution. Here DLS was used to measure particles by measuring time dependant fluctuations in scattered light from the AuMNPs as they freely diffuse in solution. DLS calculated the AuMNPs to have an average size of 99 nm. However when calculating the correlation curve for the DLS to measure data quality, the Y-intercept was found to be ~0.85, whereas for a good sample the Y-intercept should be closer to a value of 1. To examine the possible reason for the reduced Y-intercept, DDLS was employed. Traditionally DLS uses a single vertical polarized laser, which for spherical particles would cause scattered photons to arrive at the detector polarized, however for non-spherical particles light can become depolarized. DDLS employs a horizontal polarized laser in conjunction with a vertical polarized laser.

Figure 3.14 is the data for the DDLS provided by Malvern Scientific Solutions LTD. Here the top graph is the particle size distribution for samples of AuMNP subjected to only a vertical polarized laser. Whereas the addition of the horizontal polarizer filters out vertically polarized photons, the bottom graph is the particle overlay when a horizontal filter is also applied to the solution. In Figure 3.14 there is an observable peak with a shoulder peak present, it is believed that this shoulder peak is the uncoated iron oxide as it is around 10 nm, whilst the larger broader

peaks are nearer to the region of 50 nm, much closer to the size of the AuMNPs. The Y-intercept of these particle distributions was much closer to a value of 1 than previously.

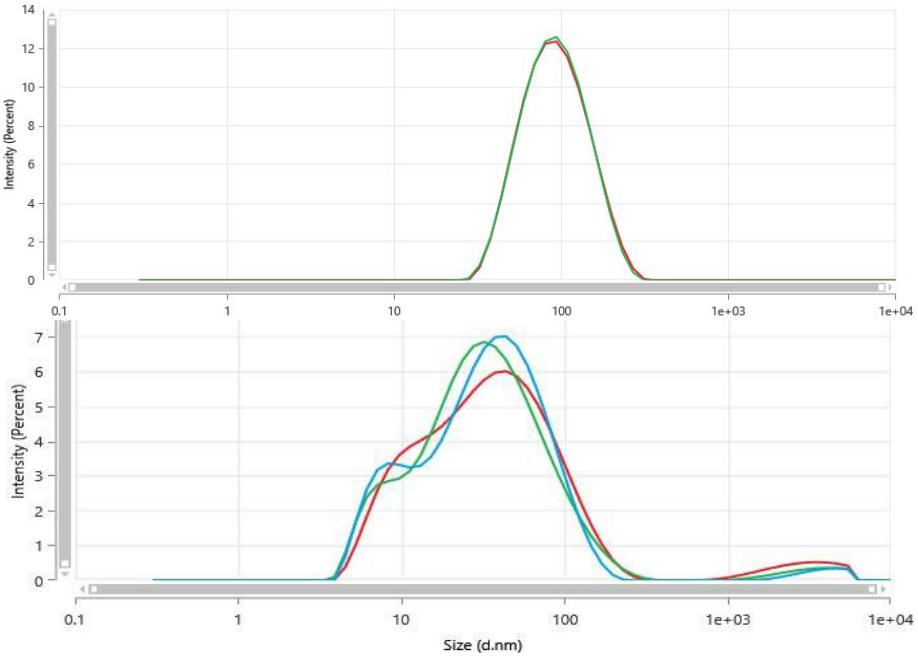

Figure 3.14. The DDLS data for the AuMNP sample is shown above (provided by Malvern Scientific Solutions LTD.). The top graph is the size distribution obtained for just the vertical polarized light scattering sample. By the addition of a horizontal polarized light sample, the vertically polarized photons are filtered out, producing the size distribution shown by the bottom graph. The bottom graph has a broad peak with a shoulder peak. This shoulder peak is the peak for the uncoated iron nanoparticles, whilst this larger peak is the AuMNPs themselves.

Particle size distribution was performed using MADLS, here multiple scattering angles are combined together to produce a single particle size distribution (*PSD*), the MADLS combines a forward, side and back scatter of photons from the sample and can overlay the data using autocorrelation functions to produce a PSD. Here the MADLS produces two peaks for the AuMNP sample, the data for which is presented in Table 3.3.

Table 3.3 The presented data for the two particle size distributions reported by Malvern Scientific Solutions LTD. Peak one shows an average size distribution of 77.42 nm, this most likely correlates to the AuMNPs in solution, whilst peak 2 has an average particle size distribution of 352.98 nm.

	Peak one (nm)	Peak two (nm)
Repeat 1	75.63	345.3
Repeat 2	78.35	350.5
Repeat 3	78.28	362.8
Mean	**77.42**	**352.9**
Standard deviation	±1.55	±8.99

Peak one shows an average size distribution of 77.42 nm, this most likely correlates to the AuMNPs in solution, whilst peak 2 has an average particle size distribution of 352.98 nm. This peak is possibly from AuMNPs that have started to flocculate in solution, it was noted that when the sample arrived there was some sedimentary build up, and the Zeta data previously reported indicates some AuMNPs would be susceptible to flocculation.

3.4 Additional purification of AuMNPs

3.4.1 Centrifugation

One commonly used method for the separation and purification of samples is centrifugation. Spinning samples at high speeds is an easy and effective way to separate materials in a sample based on their relative density.[33] The synthesis of AuMNPs described in this paper uses centrifugation during the synthesis of the particles prior to magnetic separation. The sample is spun at 2750 rpm for 1 hr at 20^{o}C, this separates out the AuMNPs and gold nanoparticles into the supernatant whilst pulling out misshapen and particles that are larger than the desired 50 nm.

3.4.2 Magnetic separation

Due to the nature of the reduction of $HAuCl_4$, the synthetic route used in the described method yields both gold coated iron cores and pure gold nanoparticles, there is also often uncoated Fe_3O_4 nanoparticles. These AuNPs need to be removed from the product. The best and easiest way to do this via magnetic purification. The product is placed in conical flasks on top of a 1T magnet measuring 50 mm x 50 mm x 20 mm and left for 24 hours, after which time the supernatant is removed. The remaining component is a majority of magnetic particles, however some AuNPs will still remain. The next step in this purification is to place the remaining component from the conical flask into 8 ml glass vials and place these at the side of the magnet. This will pull any magnetic material to the side of the vial, as shown in Figure 3.15. Exchanging the supernatant after 24 hours, repeating this process another two times to remove any non-magnetic AuNPs.

Figure 3.15. An image of a pellet of AuMNPs collected on the side of a glass vial after being left next to a magnet for 24 hrs.

3.5 Stability of AuMNPs

The stability of AuMNPs was analysed to assess how the AuMNPs might behave in various media. To assess the AuMNPs stability, a sample was suspended in varying media, and/or varying physical conditions (*temperature etc.*). These varying conditions are detailed in table 3.4. The AuMNPs were said to have lost stability when they showed signs of aggregation either by UV-Vis spectrometry or by visual inspection.

Table 3.4. The following are the experimental parameters changed/ under test for the AuMNP stability experiments.

Factors being assessed for AuMNP stability
H_2O
Phosphate buffer (50 mM, pH 7.4)
Dulbecco's Phosphate Buffered Saline
Sodium Citrate Dihydrate (1 mM)
NaCl (1 mM-5 M)
Temperature (-20 °C, 0 °C, 25 °C, 37°C)
pH (1-12)
Dulbecco's Modified Eagle's Medium (with 10 % Fetal Bovine Serum, 1 % L-Glutamine ad 1 % Penicillin Streptomycin)

Aggregation here is said to occur when the gold peak λ-max shows a constant increase over time, with the peak broadening and decreasing in absorbance. Aggregation can also be observed by eye as the solution of nanoparticles becomes darker in colouration from red to purple, and black sediment can be seen to form. The final key feature is that the aggregated nanoparticles cannot be re-suspended into solution even under sonication. A sample of non-aggregated gold nanoparticles can be observed in Figure 3.16 next to aggregated gold nanoparticles.

*Figure 3.16. A picture of 'naked' gold nanoparticles (**left**) and the same 'naked' gold nanoparticles mixed with a salt solution (**right**). The right hand photo shows that the nanoparticles have aggregated, as seem by the blue colouration and particulates in the bottom of the tube.*

3.5.1 H_2O

Deionized water (*dH_2O*) was the first medium the stability of the AuMNPs was measured in. Here 500 µl 1 OD (*optical density*) of AuMNPs were suspended in 500 µl of dH_2O, with a UV-vis full spectrum scan of the sample performed at the start of the experiment and every 24 hours after. The AuMNPs show that they do not aggregate in dH_2O up to and including 96 hrs. The data for the experiment is presented in figure 3.17.

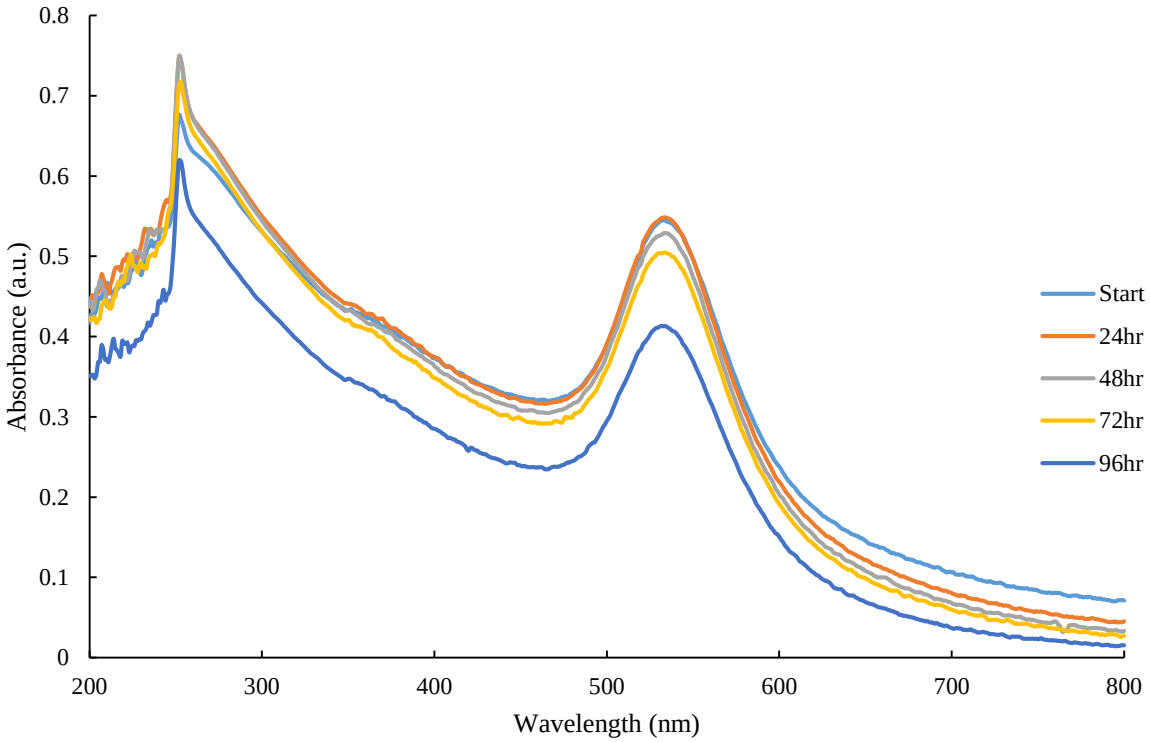

Figure 3.17. The overlay of the UV-vis full spectrum scans of the sample of AuMNPs suspended in dH_2O with scans being performed from the start of the experiment every 24 hours up to and including 96 hrs. No aggregation was observed in the sample, both by eye and in the above scans.

3.5.2 50 mM Phosphate Buffer

The stability of AuMNPs in 50 mM phosphate buffer was assessed by mixing 500 µl of 0.5 OD AuMNPs with 500 µl of a 100 mM phosphate buffer to achieve a final concentration of 50 mM, then scanned to establish the initial UV spectrum of the sample. The sample was then scanned every 24 hours. As can be seen in Figure 3.18, the sample was stable after 120 hours, with no λ-max gold peak shift. The loss in concentration can be attributed to the AuMNPs adhering to the sides of the Eppendorfs, which were observed to have a pink tinge (assumed to be AuMNPs).

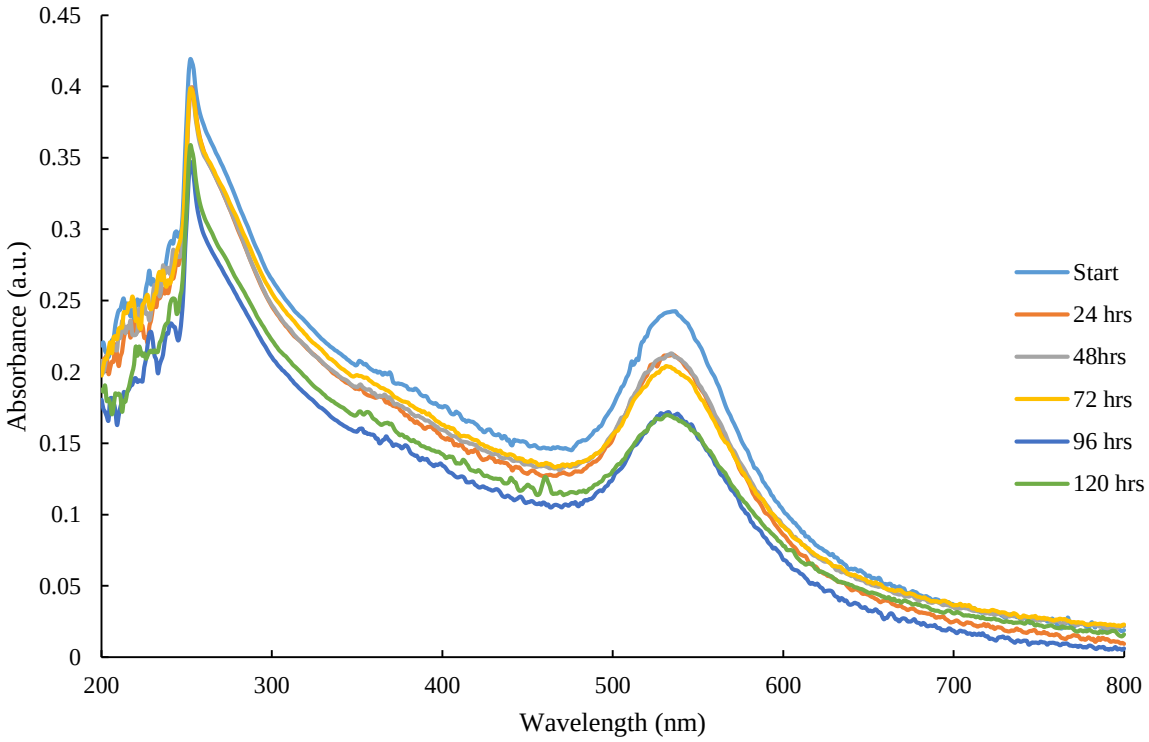

Figure 3.18. The UV-Vis full spectrum scans of the AuMNPs suspended in phosphate buffer, here no aggregation was observed up to and including 120 hrs after addition of the AuMNPs to the phosphate buffer.

3.5.3 PBS

The stability of AuMNPs in phosphate buffered saline was assessed by suspending 500 µl 0.5 OD AuMNP in 500 µl of Dulbecco's sterile phosphate buffered saline. The final concentration of NaCl in the Eppendorf was 77 mM, however the sample also contains 1 mM potassium phosphate monobasic and 5.6 mM of sodium phosphate dibasic. The suspension was scanned after 24 hours at which point the sample was starting to show the beginning of aggregation by the shift in the gold peak, and the UV scan at 48 hrs had shown the sample had fully crashed. This aggregation is shown by the grey line in Figure 3.19 with the initial scan of the AuMNP

suspension being shown in blue. It is of note that despite the NaCl concentration being 77 mM the sample still aggregated, when compared to the NaCl stability results presented in Table 3.5, 77 mM NaCl should not cause a sample to aggregate, however the presence of the potassium phosphate monobasic and sodium phosphate dibasic, may be the attributing factors to the sample aggregation.

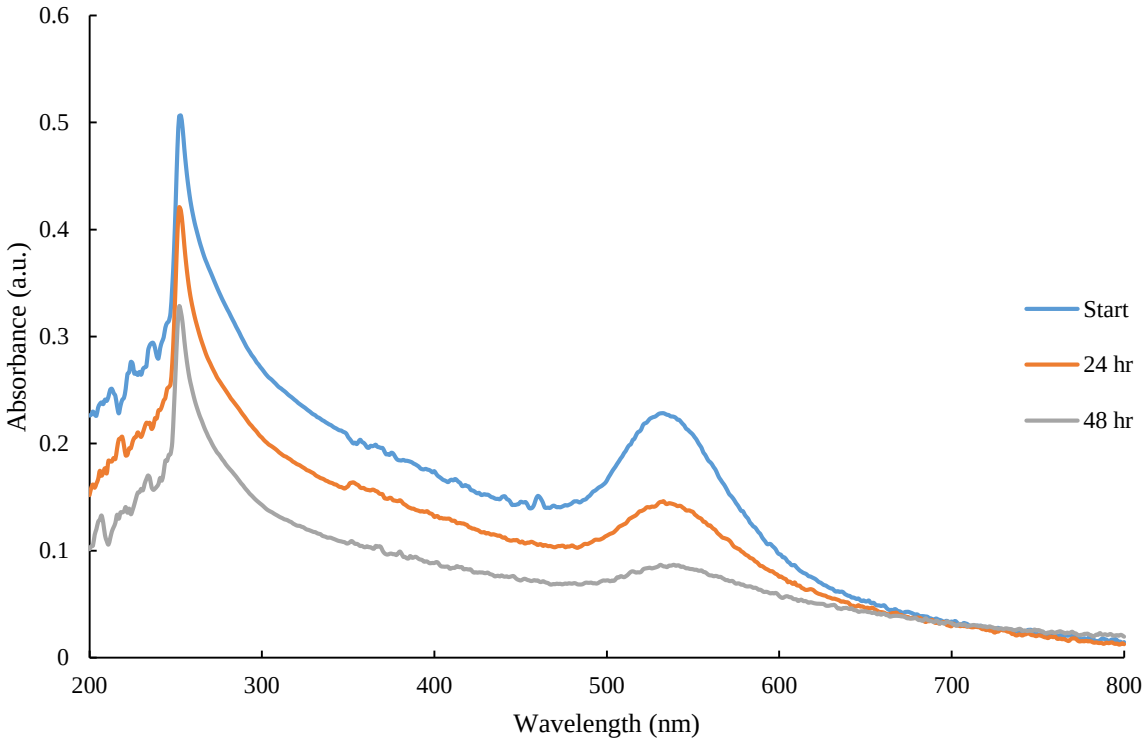

Figure 3.19. The overlay of UV-Vis full spectrum scans for AuMNPs suspended in PBS are shown. The sample showed the beginnings of aggregation in the UV scan after 24 hours, and by 48 hrs the sample showed heavy signs of aggregation, both by eye and UV-vis spectroscopy.

3.5.4 Sodium Citrate Dihydrate

The AuMNPs are synthesized in a solution containing sodium citrate dihydrate at a concentration of approximately 3 mM and then, after magnetic separation and purification the AuMNPs are suspended in 1 mM sodium citrate dihydrate. To assess the stability of AuMNPs in 1 mM sodium citrate dihydrate, a sample of AuMNPs were separated on a 1 tesla magnet followed by re-suspension in 1 ml 1 mM sodium citrate dihydrate, then scanned via UV-Vis every 24 hours. Figure 3.20 shows the sample showed no signs of aggregation up to and including 96 hours and there was no indication that the sample was going to aggregate after the 96 hours.

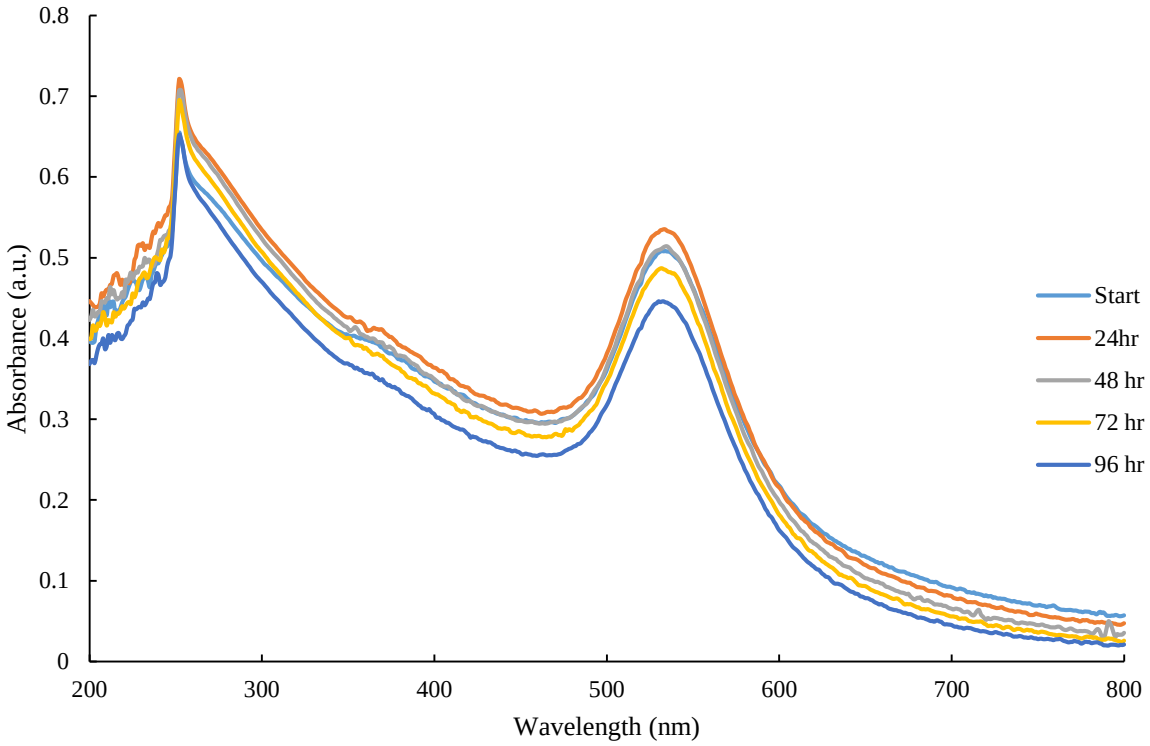

Figure 3.20. The overlay of the UV-Vis spectra of the stability scans of AuMNPs suspended in sodium citrate, here no signs of aggregation occur, which is as expected, as the AuMNPs are synthesised and purified in sodium citrate, if aggregation were to occur, it would more than likely have occurred during the synthesis or purification.

3.5.5 NaCl

The stability trials of NaCl were carried out at 37 ˚C to simulate human body temperature. 500 µl of a NaCl solution was mixed with 500 µl of a 0.5 OD AuMNP solution to produce the final concentrations of NaCl shown in table 3.5.

Table 3.5. Presented are the concentrations of NaCl used in the various AuMNP stability trials, solutions with NaCl concentrations of 1-200 mM showing no signs of aggregation, whereas concentrations of 500 mM up to and including 5 M showed heavy signs of aggregation after 24 hrs, both visibly by eye, and when scanned using UV-Vis spectroscopy.

NaCl concentration (mM)	Time before aggregation
1	Did not show aggregation
10	Did not show aggregation
50	Did not show aggregation
100	Did not show aggregation
200	Did not show aggregation
500	Showed aggregation after 96 hours
1000	Showed aggregation after 1 hour
2000	Showed aggregation after 1 hour
5000	Showed aggregation after 1 hour

These solutions were then immediately scanned via UV-Vis to give an initial reading of the gold peak, and were then scanned every 24 hours, or until they had shown aggregation. From Table 3.5 it can be seen the AuMNPs were stable in NaCl in concentrations up to 100 mM, however the 100 and 200 mM scans, whilst not displaying signs of aggregation did display a drop in the gold peak with each passing scan. This is a possible sign that the nanoparticles were either flocculating or adhering to the sides of the Eppendorfs indicating that the concentrations of NaCl were not causing aggregation, they were starting to cause the destabilization of the AuMNPs in solution. The sample with 500 mM NaCl showed aggregation after 96 hours, whilst samples with a concentration at 1000 mM and above mM showed aggregation after 1 hour.

3.5.6 Temperature

To assess the stability of AuMNPs at various temperatures, 1 ml solutions of 0.4 OD (Optical Density-*taken as the absorbance reading of the gold peak of the AuMNPs*) AuMNPs were scanned, then placed in eppendorfs and left at different temperatures. The samples were scanned every 24 hours (*note that the sample at -20 ˚C was defrosted before scanning*). The sample left at -20 degrees showed aggregation after 24 hours, however since the sample was frozen it is unclear as to whether aggregation occurred during the freezing or upon the defrosting of the sample. All the other samples showed no aggregation after 96 hours. However the samples did show a change in peak heights, this could be attributed to the particles flocculating or adhering to the side of the Eppendorfs, the sample which showed the least change over time was the sample kept at 4 ˚C. Table 3.6 shows an overview of the temperatures and the stability of the nanoparticles.

Table 3.6. The 4 temperatures used for examining AuMNP aggregation, only the solution stored at -20 ˚C showed aggregation, which began to show after the first scan at 24 hrs, the other temperature stored solutions showed no signs of aggregation.

Temperature of solution (˚C)	Time before aggregation
-20	Showed aggregation after 24 hours
4	Did not show aggregation
20	Did not show aggregation
37	Did not show aggregation

2.5.7 pH

The human body has a pH of 7.4,[34] therefore the stability of any nanoparticle that would enter the body needs to be assessed at that pH. The aim of the pH stability trials was to build up a pH stability profile of the nanoparticles to assess the viability of the particles for use in the body. For this solutions of 1 mM sodium citrate were pH altered to values of 1-12, at this point

it is important to note that sodium citrate dihydrate itself acts as a buffer between a pH range of 3.0-6.2.[35] Therefore the solutions with a pH higher or lower than this range were not acting as buffers, however the solution was kept as sodium citrate for continuity within the experiment. Table 3.7 describes which solutions kept the nanoparticles stable. In which solutions the nanoparticles aggregated, which here were pH solutions of 1-3.

Table 3.7. The various pH of solutions of sodium citrate used to assess the pH stability of AuMNPs are presented below, with pH solutions 1, 2 and 3 showing aggregation after 24 hours, whereas pH solutions of 4-12 showed no signs of aggregation after 96 hours.

pH of solution	Time before aggregation
1	Showed aggregation after 24 hours
2	Showed aggregation after 24 hours
3	Showed aggregation after 24 hours
4	Did not show aggregation
5	Did not show aggregation
6	Did not show aggregation
7	Did not show aggregation
8	Did not show aggregation
9	Did not show aggregation
10	Did not show aggregation
11	Did not show aggregation
12	Did not show aggregation

3.5.8 Dulbecco's Modified Eagle Medium

The main aim of the AuMNPs is to be used in cancer therapy treatment, therefore the stability of the AuMNPs in any sort of biological medium needs to be assessed. The AuMNPs were suspended in Dulbecco's Modified Eagle Medium (*DMEM*) with 1 % L-glutamine, 1 % penicillin streptomycin and 10 % Fetal Bovine Serum (*FBS*) and the sample was scanned every 24 hours. This solution was used as it is the cell growth medium used for cell viability experiments discussed in chapters 4 and 5 of this document. Here the AuMNPs showed no signs of aggregation at 96 hours Figure 3.21 shows that the AuMNPs did not show aggregation after 120 hours, the rise in absorbance can be attributed to being unable to keep a 100 % sterile environment in the UV-Vis spectrometer, and there is possible growth of some contaminant in the media. Regardless the AuMNPs did not aggregate in the cell culture media.

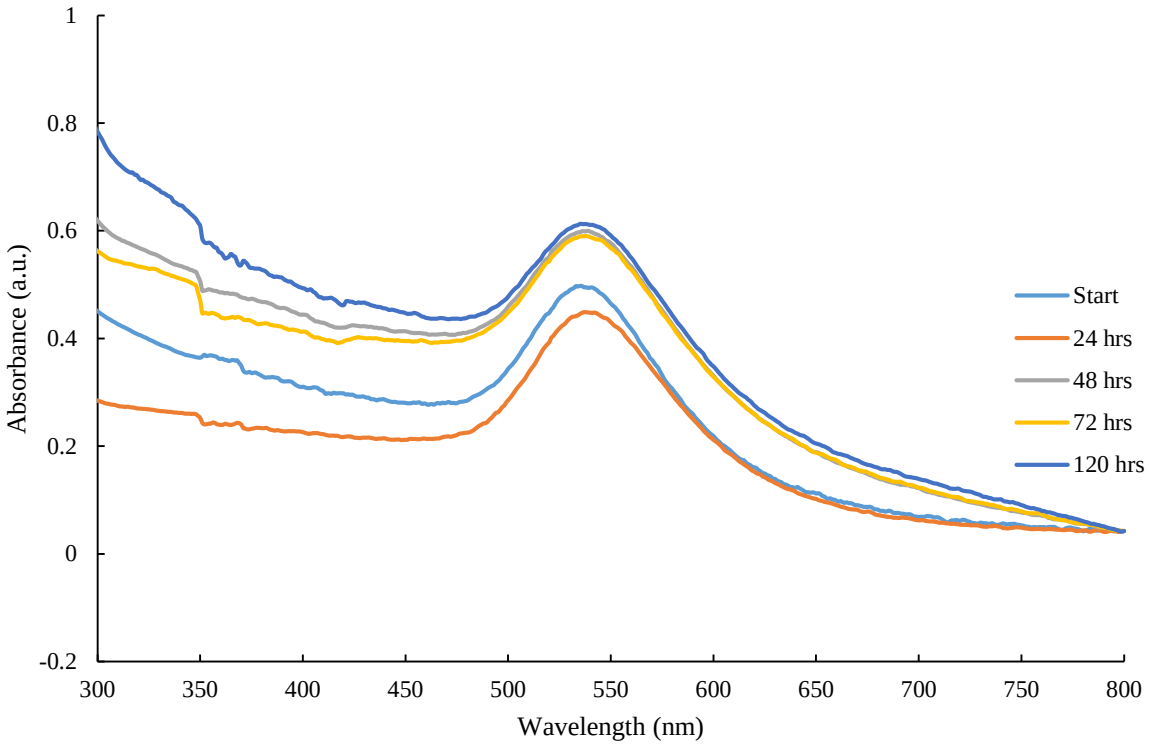

Figure 3.21. The final stability trial completed with AuMNPs is presented. Here the AuMNPs were suspended in a solution of DMEM containing 10 % fetal bovine serum (FBS), 1 % L-glutamine and 1 % penicillin streptomycin..

3.6 Conclusion

In summary, a synthesis for 50 nm AuMNPs has been developed, following several different experimental procedures in an attempt to achieve a spherical nature to the nanoparticles, with an average size of 45 nm ±11 nm. Purification of the nanoparticles has been partially achieved, using magnetic purification it is possible to remove any non-magnetic particles, such as pure gold nanoparticles, which are produced when $HAuCl_4$ is reduced in the synthesis solution. In addition to this centrifugation at 1500 rpm for 2 hrs has shown to decrease some of the excess iron which was found to be present in the solutions after purification by TEM. Many other purification techniques such as column purification, density gradient centrifugation and filtration were attempted but were unsuccessful in separating the iron, and more often caused aggregation of the AuMNPs, or caused the AuMNPs to irreversibly bind to the purification substrates. Whilst some of the iron is removed from solution, iron does still remain which will need to be assessed for any issues this may cause in cell viability experiments. Finally the purified AuMNPs were tested for their stability in various solutions, showing stability in dH_2O, 50 mM phosphate buffer, sodium citrate, DMEM, various pH altered solutions, various solutions stored at differing temperatures and solutions of varying concentrations of NaCl. The

AuMNPs did however show aggregation in solutions of PBS, solutions of NaCl with concentrations of 500 mM and above, solutions stored at -20 $^{\circ}$C and solutions of sodium citrate pH altered to 3 and below. This work indicates that the AuMNPs synthesised can go on to be used in cell viability experiments for assessing the initial use of MNDEPT as an anti-cancer treatment.

3.7 Bibliography

1 D. Bobo, K. J. Robinson, J. Islam, K. J. Thurecht and S. R. Corrie, *Pharm. Res.*, 2016, **33**, 2373–2387.

2 C. L. Ventola, *P T*, 2017, **42**, 742–755.

3 European Union Patent, EP2473197-A2, 2009.

4 V. V. Gwenin, C. D. Gwenin and M. Kalaji, *Langmuir*, 2011, **27**, 14300–14307.

5 M. G. Cerruti, M. Sauthier, D. Leonard, D. Liu, G. Duscher, D. L. Feldheim and S. Franzen, *Anal. Chem.*, 2006, **78**, 3282–3288.

6 M. Chen, S. Yamamuro, D. Farrell and S. A. Majetich, *J. Appl. Phys.*, 2003, **93**, 7551–7553.

7 S. J. Cho, J. C. Idrobo, J. Olamit, K. Liu, N. D. Browning and S. M. Kauzlarich, *Chem. Mater.*, 2005, **17**, 3181–3186.

8 S. J. Cho, B. R. Jarrett, A. Y. Louie and S. M. Kauzlarich, *Nanotechnology*, 2006, **17**, 640–644.

9 E. Iglesias-Silva, J. L. Vilas-Vilela, M. A. López-Quintela, J. Rivas, M. Rodríguez and L. M. León, *J. Non. Cryst. Solids*, 2010, **356**, 1233–1235.

10 S. Kayal and R. V. Ramanujan, *J. Nanosci. Nanotechnol.*, 2010, **10**, 5527–5539.

11 T. Teranishi and M. Miyake, *Chem. Mater.*, 1998, **10**, 594–600.

12 M. P. Pileni, *Nat. Mater.*, 2003, **2**, 145–150.

13 S. Sun and H. Zeng, *J. Am. Chem. Soc.*, 2002, **124**, 8204–8205.

14 Y. Sun and Y. Xia, *Science (80-.).*, 2002, **298**, 2176–2179.

15 L. Manna, E. C. Scher and A. P. Alivisatos, *J. Am. Chem. Soc.*, 2000, **122**, 12700–12706.

16 R. Klajn, A. O. Pinchuk, G. C. Schatz and B. A. Grzybowski, *Angew. Chemie - Int. Ed.*, 2007, **46**, 8363–8367.

17 M. Gadogbe, S. M. Ansar, I. W. Chu, S. Zou and D. Zhang, *Langmuir*, 2014, **30**, 11520–11527.

18 A. F. Kopp, M. Laniado, F. Dammann, W. Stern, E. Gronewaller, T. Balzer, C. Schimpfky and C. D. Claussen, *Radiology*, 1997, **204**, 749–756.

19 P. R. Ros, P. C. Freeny, S. E. Harms, S. E. Seltzer, P. L. Davis, T. W. Chan, A. E. Stillman, L. R. Muroff, V. M. Runge and M. A. Nissenbaum, *Radiology*, 1995, **196**, 481–488.

20 P. Reimer, E. J. Rummeny, H. E. Daldrup, T. Balzer, B. Tombach, T. Berns and P. E. Peters, *Radiology*, 1995, **195**, 489–496.

21 C. W. Jung and P. Jacobs, *Magn. Reson. Imaging*, 1995, **13**, 661–674.

22 D. Stark, F. Hahn, J. Wittenberg, L. E. Todd and T. Ferrucci, *Radiology*, 1988, 297–301.

23 H. E. Daldrup-Link, *Radiology*, 2017, **284**, 616–629.

24 K. R. Brown, D. G. Walter and M. J. Natan, *Chem. Mater.*, 2000, **12**, 306–313.

25 J. L. Lyon, D. A. Fleming, M. B. Stone, P. Schiffer and M. E. Williams, *Nano Lett.*, 2004, **4**, 719–723.

26 W. Haiss, N. T. K. Thanh, J. Aveyard and D. G. Fernig, *Anal. Chem*, 2007, **79**, 4215–4221.

27 J. Lin, W. Zhou, A. Kumbhar, J. Wiemann, J. Fang, E. E. Carpenter and C. J. O'Connor, *J. Solid State Chem.*, 2001, **159**, 26–31.

28 L. L. Ma, A. U. Borwankar, B. W. Willsey, K. Y. Yoon, J. O. Tam, K. V Sokolov, M. D. Feldman, T. E. Milner and K. P. Johnston, *Nanotechnology*, 2013, **24**, 1-12.

29 K. L. Kelly, E. Coronado, L. L. Zhao and G. C. Schatz, *J. Phys. Chem. B*, 2003, **107**, 668–677.

30 B. Berne and R. Pecora, *Dynamic Light Scattering*, Courier Dover Publications, 2000.

31 D. Hanaor, M. Michelazzi, C. Leonelli and C. C. Sorrell, *J. Eur. Ceram. Soc.*, 2012, **32**, 235–244.

32 O.M. Griffith, *Practical Techniques for Chentrifugal separations*, ThermoFisher, 2010

33 G. K. Schwalfenberg, *J. Environ. Public Health*, 2012, **2012**, 1–7.

34 E. Wood, *Biochem. Educ.*, 1987, **15**, 97.

Chapter 4:

Cell Penetrating Peptides

Some of the data discussed in chapter 4 can be found in the following publications:

Time dependent HPLC analysis of the product ratio of enzymatically reduced prodrug CB1954 by a modified and immobilised nitroreductase

European Journal of Pharmaceutical Sciences 127 (2019) 217–224.

Patrick Ball, Emma Thompson, Simon Anderson, Vanessa Gwenin, Chris Gwenin.

Cell penetrating peptides as a tool for the cellular uptake of a modified nitroreductase for use in Directed Enzyme Prodrug Therapy

Submitted to The Journal of Controlled Release for peer review.

S.D. Anderson, P. Ball, V.V. Gwenin, R.J. Hobbs, L.A. Bennie, J.A. Coulter, C.D. Gwenin.

4.0 Introduction

Nitroreductase enzymes have shown their potential as effective agents in a range of DEPT treatments that have already been devised.[1–4] Much research has been done into finding the most efficient way to transfer enzymes into a tumour site, be it delivery with an antibody,[5,6] or using a virus to deliver a gene coding for a prodrug activating enzyme to a tumour, for later expression at the tumour site.[7,8] Despite this there is still one major barrier/ obstacle that must be addressed when attempting these medical treatments, and that is providing a method to efficiently enter into a cell through the cell membrane, without losing the cargo to the cell's endo-lysosomal system.

CPPs offer this modality to enter a cell without disruption of the cargo.[9] Many CPPs have been investigated for their properties, with a variety of CPPs being discovered as naturally occurring; such as the TAT peptide from HIV-1[10] or have been synthesized based on natural CPPs; such as the poly-arginine family,[11,12] whilst others are chimeric, that is constructed from 2 separate CPPs; for example the PEP family of CPPs.[13–15] These CPPs have already demonstrated their ability to aid in the uptake of a variety of cargos such as; nucleic acids,[16,17] proteins[18,19] and quantum dots.[20,21] It is unclear however if the CPPs will possess the ability to conjugate to the nitroreductase enzyme that are desired for use in MNDEPT and if they will conjugate what effect they may have on the nitroreductases ability to reduce the CB1954 prodrug or on the product formation from the prodrug. Here the CPPs HR9 and Pep-1 (*amino acid sequences are presented in table 4.1*) were conjugated to the genetically modified NfnB-Cys and YfkO-Cys nitroreductases, and upon successful conjugation what effect this has on the enzymes ability to reduce the CB1954 prodrug and the hydroxylamine product formation, as well as examining how this conjugation effects the enzymes kinetic profile using Michaelis-Menten kinetic analysis of the enzyme-prodrug systems.

Table 4.1. The amino acid sequences of the 2 CPPs being examined in this work,

CPP	Amino acid sequence
HR9	*HCCCCCCRRRRRRRRRCCCCCCH*
Pep-1	*KETWWETWWTEWSQPKKKRKV*

HPLC is an analytical technique used to separate and identify different components of a liquid mixture, the technique involves using a pump to pass the liquid through a column containing an adsorbent medium. Different components will interact slightly differently with the adsorbent material, and can be displaced from the medium by using various solvent gradients. The materials then pass through the column and are scanned by UV-Vis at varying wavelengths. The time at which a material elutes off the column is known as the retention time. Here the 2- and 4 –NHOH products have different retention times of roughly 9-10 minutes for the 2-NHOH and roughly 5 minutes for the 4-NHOH. A typical chromatogram of an NfnB-Cys reaction with CB1954 is presented in Figure 4.1. The product ratios for NfnB-Cys and YfkO-cys when reacted with CB1954 are presented in table 4.1, the ratio for NfnB-Cys of 2-:4-NHOH is 32:68, whilst for YfkO-Cys the ratio is 1:99. This shows a considerable difference between the 2 enzymes, and would indicate that YfkO-Cys is the preferential choice of enzyme as it produces primarily the product that becomes the DNA cross reacting species desired for anti-cancer therapy.

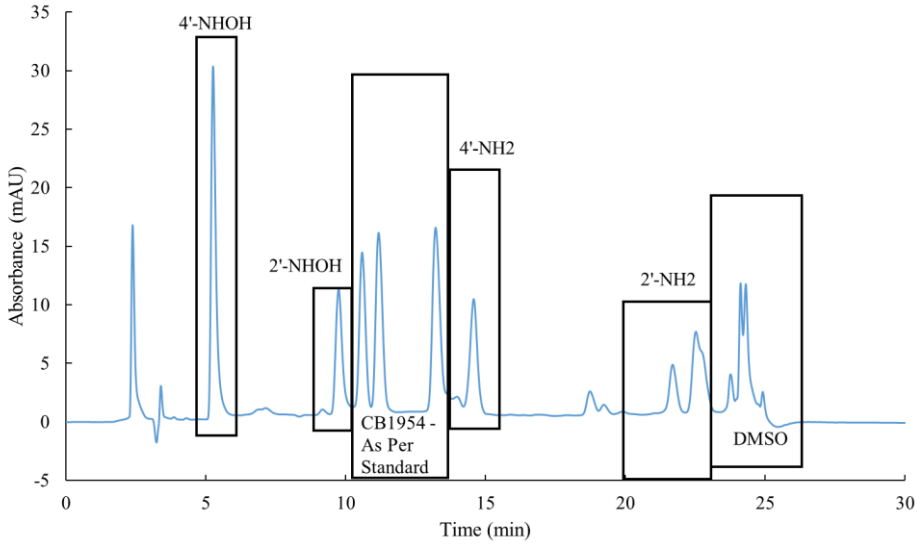

Figure 4.1. A typical chromatogram of an NfnB-Cys reaction with CB1954 analysed by HPLC at a wavelength of 400 nm. The retention times of the 2-and 4-NHOH are 9 minutes and 5 minutes respectively. The CB1954 is shown with 3 peaks with the first peak showing a retention time of 11 minutes and the third peak showing a retention time of 13.5 minutes. The 2-and 4-NH2 final derivative product peaks are also shown having a retention time of 22 minutes and 14.5 minutes respectively.

Michaelis-Menten kinetics are used to assess and describe the rate of enzymatic reactions by relating the rate of reaction (v) to the concentration of substrate (S).[43,44] The formula for deriving the rate of reaction is given as:

$$v = \frac{Vmax[S]}{Km + [S]}$$

Where Vmax is the maximum rate achieved by the system when saturated with substrate. Km is the Michaelis constant, which is the substrate concentration where the reaction rate is exactly half of Vmax. When analysing data there are other functions that are looked at, with this first one being; Kcat which is enzyme product turnover (*measured per second: S^{-1}*).

The equation for determining Kcat is given as:

$$Vmax = Kcat[E]_0$$

Where $[E]_0$ is initial enzyme concentration measured. The higher the Kcat number, the number of substrates turned over in one second becomes higher. After determining Kcat, the enzyme efficiency can be determined by the constant Kcat/Km measured per concentration per second (*here measured as: $\mu M^{-1}S^{-1}$*), which gives a measure of the catalytic efficiency of the enzyme substrate system.

4.1 Expression, purification and characterization of a modified nitroreductase

The NfnB enzyme from *E.coli* has previously shown its ability to reduce the prodrug CB1954[23] with a DEPT combination therapy reaching stage II clinical trials.[7,24] In order for MNDEPT to be successful the enzyme needs to be conjugated onto AuMNPs, in order to do this the *nfnb* gene has been previously genetically modified to include 6 additional cysteine residues at each N-terminus,[25] these cysteine residues each include a sulphur atom. Sulphur forms very strong bonds to gold, with a bond dissociation enthalpy somewhere in the region of 253.6 ± 14.6 kJ mol^{-1}. [26] This high bond strength makes an Au-S bond ideal for conjugation of the enzyme to AuMNPs.

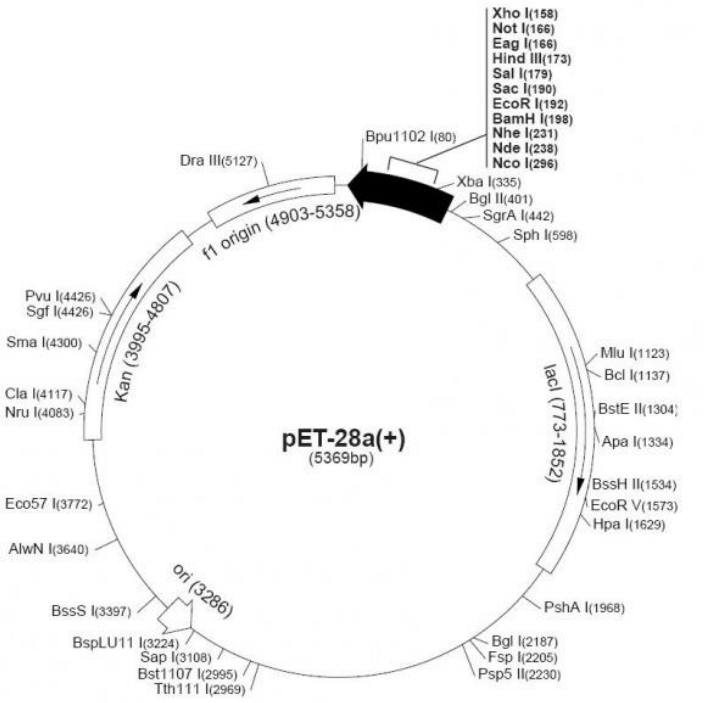

Figure 4.2. The pET-28a(+) plasmid vector site map, showing the LacL region, the kanamycin resistant gene, and the restriction enzyme locations within the black arrow.[27,28]

The modified *nfnb-cys* gene has previously been inserted into the pET-28a(+) plasmid vector (*see figure 4.2 for plasmid map*) for expression.[25,29,30] The pET-28a(+) plasmid vector was chosen for several reasons; firstly it contains antibiotic resistant genes towards kanamycin,[27,28] which enables selective growth on an agar plate that has been laced with kanamycin, ensuring that only bacterial contain the pET-28a(+) plasmid grow. The second reason for the selection of pET-28a(+) is that during enzyme expression, the plasmid codes for additional histidine residues on the N-terminus end of the protein, which enables metal ion affinity chromatography (*IMAC*) to be used to purify the protein.[2,30] The pET-28a(+) vector also contains the LacI repressor region, this region typically prevents the expression of the protein, however a trigger of the lac operon can induce the expression of this gene. Typically within a cell, allolactose is used as an inhibitor of the Lac repressor, however the binding of allolactose to the receptor can be hydrolysed. due to this in molecular biology Isopropyl β-D-1-thiogalactopyranoside (*IPTG*) can be used in place of allolactose.[31] It functions in much the same way, however it has a sulphur atom which creates a non-hydrolysable chemical bond with the repressor, allowing for continued enzyme expression. The plasmid also contains the T7 promotor region which is a section with many different restriction enzyme sites,[27,28] this enables the insertion of a variety

of different genes using different restriction enzymes, the T7 region also contains the previously mentioned His-tag coding sites.

4.1.1 Enzyme expression

An agar plate which has *E.coli Rosetta* containing plasmids that code for a specific nitroreductase has a colony picked and placed into a sterile glass vial containing 5 ml of Lysogeny Broth (*LB*) media (*Tryptone 1 % w/v, NaCl, 1 % w/v, Yeast extract 0.5 % w/v*) and kanamycin (*2.5 µl, 100 mg/ml*). *Rosetta E.coli* is a strain of E.coli that has additional transfer RNA molecules that are able to 'recognise' rarer codons for expression, which allows for the expression of a wider variety of codons, that otherwise could not be expressed.[32] This inoculant is vortexed for 16 hrs at 1500 rpm, to allow bacterial cell growth. The following day the inoculant is added to 500 ml LB media containing kanamycin (*250 µl, 100 mg/ml*). The flask is mixed constantly at 180 rpm at 37 $^{\circ}$C. The growth of the expression is checked against a reference using a colorimeter (*SIS, WPA colour-wave*), when the absorbance has reached 0.6, IPTG (*2 ml, 100 mM*) is added to the flask to induce the expression of the nitroreductase. The flask is left to mix at 37 $^{\circ}$C for 4 hours. After the 4 hours the contents of the flask are centrifuged at a speed of 8000 rpm, for 10 minutes at 4 $^{\circ}$C, with the pellet being collected and stored at -20 $^{\circ}$C until needed for purification.

4.1.2 Enzyme purification

The frozen pellet from the enzyme expression is taken into imidazole (*10 ml, 10 mM, pH 7.2*) and left to thaw at room temperature. Once the pellet has suspended it is transferred to a thick walled glass vial and sonicated (*40 % amplitude, 2 minutes, and 30 second pulse*) to break down the bacterial cell wall and other cellular structures to release the nitroreductase into solution. This mix is then centrifuged (*20,000 rpm, 1 hr, 4 $^{\circ}$C*) to pellet out the larger cell debris, leaving the nitroreductase and other smaller cell proteins in the supernatant. The nitroreductase is separated out from the other small cellular proteins using metal ion affinity chromatography (*IMAC*) with Ni^{2+} as the metal ion. As previously mentioned during the expression of the nitroreductase, the pET28a+ plasmid vector adds an additional 6 histidine residues on the end of each monomer. During IMAC these His-tags complex with the Ni^{2+} as depicted in Figure 4.2, which allows the other cellular proteins to be removed by washing through with increasing concentrations of imidazole (*50-800 mM, 5 ml, pH 7.2*). At higher concentrations of imidazole the nitroreductases complexed to the Ni^{2+} are replaced by the imidazole, flushing the nitroreductase out of the column. Following IMAC, the nitroreductases are subjected to a PD10

sephadex column to remove final impurities and allow a media change from imidazole, to phosphate buffer (*50 mM, pH 7.4*).

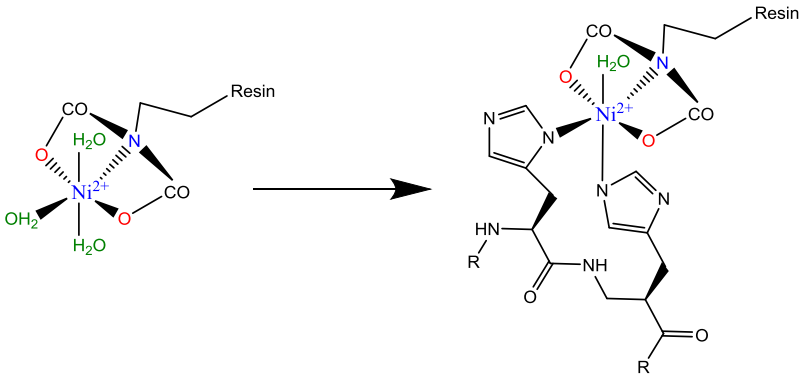

Figure 4.3. The Ni^{2+}used in IMAC, shown not complexed (left) and complexed to 2 histidine residues (right).

4.1.3 Bradford enzyme concentration determination

Post purification the enzyme concentration is assessed using the Bradford assay. This assay uses the dye Coomassie Brilliant Blue G-250 (*figure 4.4*), which exists in 3 different coloured states depending on its charge; cationic (*red*), neutral (*green*), anionic (*blue*).[33]

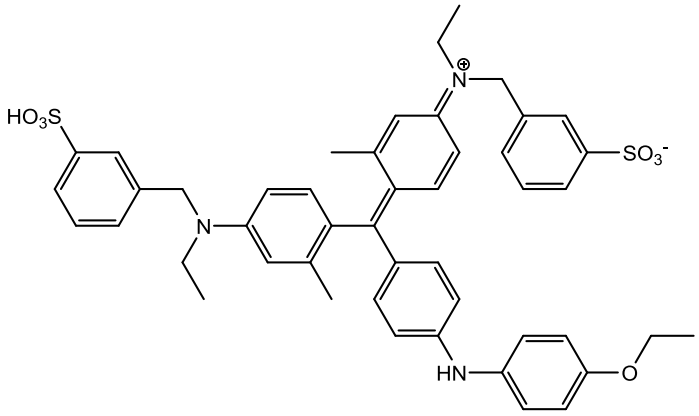

Figure 4.4. Coomassie Brilliant Blue G-250 stain, the binding dye used in the Bradford assay.

The dye interacts with proteins through Van der Waals interactions which causes the native state of the protein to be interrupted exposing hydrophobic pockets within the tertiary structure of the protein. The tertiary pockets bind to the dye causing a shift in charge from cationic to anionic, causing a colour change in the dye from red to blue. This anionic bound form of the dye, which is held to the protein through hydrophobic and ionic interactions, can be measured quantitatively through the dyes absorption at 595 nm.[34] The absorbance of the dye at 595 nm is proportional to the amount of protein in a sample. Here the nitroreductase concentration is measured by using the Bradford assay to determine an absorption value of the dye, which is

then compared to a calibration standard of know concentrations of Bovine Serum Albumin (*BSA*). Typical concentrations of NfnB-Cys and YfkO-Cys achieved are in the range of 5-9 mg/ml and 2-7 mg/ml, respectively.

4.1.4 Enzyme characterization using gel electrophoresis

A technique that is used for protein analysis is sodium dodecyl sulfate polyacrylamide gel electrophoresis (*SDS-PAGE*), a technique that can separate proteins based on each proteins molecular weight.[35,36] The main principal of the technique is the creation of an acrylamide based porous gel, with pore size varying dependant on the ratio of Bis-acrylamide used in the gel production, with different percentages of acrylamide allowing for separating of different ranges of proteins, for example 10 % gels can cover 1-100 kDa,[36] whilst 16 % gels can cover 1-70 kDa proteins.[36] The acrylamide is oxidised to produce a 3D polymer, which forms the basis of the gel.[37] SDS is an anionic detergent used in the gel to destabilized the chemical interactions such as hydrogen-bonding, hydrophobic and ionic interactions that make up the three-dimensional structures of the protein,[38] which causes the protein to linearize for more fluid migration through the gel. Additionally, prior to being placed into the gel the protein mix can be denatured using a combination of high temperature ($95^{O}C$) and a chemical such as β-Mercaptoethanol to break di-sulfide bridges.[39] An SDS-PAGE gel runs vertically, with the cathode at the top of the gel and anode at the bottom. When the protein is placed into a gel and has a negative charge, the passing of an electrical charge across the gel causes the negative proteins to migrate through the gel towards the cathode, with small proteins being able to navigate through the gel matrix easier, and quicker than larger proteins, causing a separation of proteins based on their molecular weight. Typically an SDS-PAGE gel consists of 2 parts: a stacking and resolving gel.[35,36] The stacking gel is on top of the resolving gel,[35] and is of a lower acrylamide percentage than the resolving gel, this gel is designed to stack proteins of similar weights together before they move onto the resolving gel.[39] Which is designed for final protein separation, this dual gel allows for more efficient protein separation.[35,36,40]

4.1.4.1 NfnB-Cys/ YfkO-Cys SDS-PAGE gel

To produce a SDS-PAGE gel, a 12 % resolving gel is required with a 5 % stacking gel, the stacking gel is placed on top of the resolving gel, with the purpose being to stack similar weighted proteins together which are then separated in the resolving gel.[37] The resolving gel was made by mixing ddH_2O (*2.1 ml*), Bis-acrylamide (*1.5 ml, 40 %*), SDS (*50 µl, 10 %*), Ammonium persulfate (*APS*) (*50 µl, 10 %*) and Tris-HCl (*1.25 ml, 1.5 M, pH 8.8*). The

polymerising of the Bis-acrylamide started upon the addition of TEMED (*Tetramethyl ethylenediamine*) (*5 µl*), this mixture was then quickly placed into a cast and had butanol saturated water placed on top to allow the gel to set with a flat top, for the later addition of a stacking gel. When the resolving gel set, a stacking gel was made by mixing ddH_2O (*1.455 ml*), Bis-acrylamide (*250 µl, 40 %*), SDS (*20 µl, 10 %*), APS (*20 µl, 10 %*) and Tris-HCl (*250 µl, 1 M, pH 6.8*), as before the addition of TEMED (*5 µl*) to the mixture began the polymerization process, this gel mixture was quickly pipetted into the cast on top of the resolving gel, and a comb was placed on top of the gel before it has set, to allow the gel to set with gaps formed by the comb, which become wells for placing protein samples. When the entire is set, the gel is placed into a running tank which is filled with a SDS running buffer (*Tris 3 g, glycine 14.4 g, SDS 1 g, made to 1 L with* ddH_2O).

The samples to be run through the gel are prepared by mixing the sample with a 2x loading buffer, which is made by mixing; Tris-HCl (*1 ml, 100 mM, pH 6.8*), SDS (*4 ml, 10 %*) glycerol (*4ml, 50 %*) bromophenol blue (*500 µl, 1 %*) and made up with ddH_2O (*9.7 ml*). The dye is placed into 970 µl aliquots and has 30 µl of β-Mercaptoethanol added when it is required. 10 µl of loading dye is mixed with 20 µl of protein sample and heated at 95 ˚C for 5 minutes to denature the protein structure.

For the NfnB-Cys purification, 20 µl of each imidazole concentration used for elution of the protein is mixed with 10 µl of loading dye and heated at 95 ˚C for 5 minutes. Then 15 µl of a sample was placed into each well of the SDS-PAGE gel which had been previously placed into the running tank. A protein ladder of known molecular weights was placed in one lane to act as a reference sample. The gel was run at 100 V until the samples had migrated partially through the stacking gel and the protein ladder could be seen to be separating, after this the voltage was increased to 200 V and the gel was left to run for 40 minutes, or until the ladder had reached the bottom of the gel. After running, the gel requires characterization by staining with Coomassie Brilliant Blue (*Coomassie Brilliant Blue 250 mg, methanol 45 ml,* ddH_2O *45 ml, glacial acetic acid 10 ml*). The gel was carefully removed from the cast and placed into a flat bottomed container and was covered with the stain until the stain just covered the gel, this was left on the gel for 1 hour. After 1 hour the stain is removed and de-stain (*IMS 200 ml,* ddH_2O *500 ml, glacial acetic acid 100 ml*) is added to the container. De-stain is changed after one hour, then the gel was left stain overnight, with de-stain being removed the following day and the gel is able to be analysed for the protein molecular weight.

Figure 4.5 is the SDS-PAGE gel of an NfnB-Cys purification, with the dimeric and monomeric units being circled in yellow. The monomer has a molecular weight of approx. 27.3 kDa giving a dimeric weight of 54.6 kDa.[30] The gel aligns with these weights.

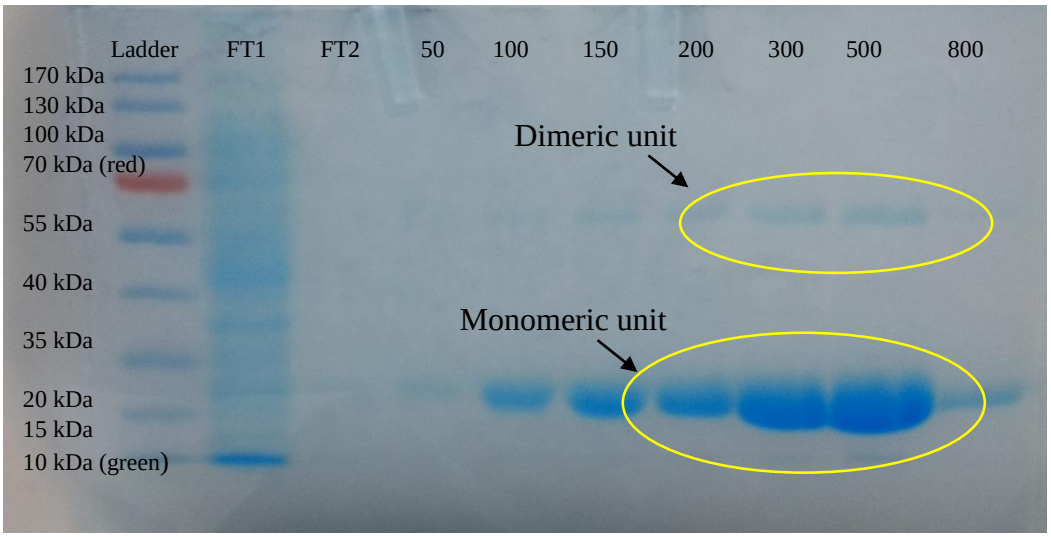

Figure 4.5. NfnB-Cys purification SDS-PAGE, the NfnB-Cys elutes strongest in 500 mM imidazole, with the gel image showing some NfnB-Cys has denatured into the monomeric units, which when referenced against the protein ladder have a molecular weight approx. 27.3 kDa, with the dimer having a molecular weight of around 54 kDa, both of these are referenced against the reported literature weight of NfnB-Cys of 54.6 kDa.[30]

The purification and SDS-PAGE gel of YfkO-Cys was carried out as described for NfnB-Cys, the SDS-PAGE gel of YfkO-Cys is presented in Figure 4.6. Here the monomer band is placed around 30 kDa against the protein ladder reference, with the dimer band being around 60 kDa. These weights are referenced against the reported literature weights for YfkO,[41] with compensation being made for the cysteine and histidine tags.

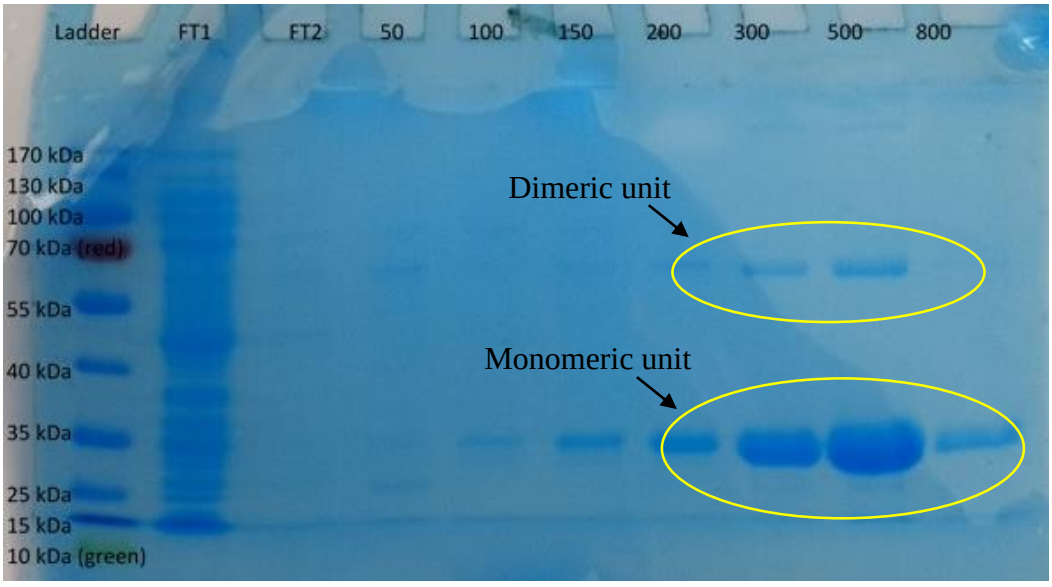

Figure 4.6. YfkO-Cys SDS page gel. Here the YfkO-Cys elutes strongest in the 500 mM imidazole fraction. The monomer can be seen to have a molecular weight of around 30 kDa with the dimer having a molecular weight of around 60 kDa, these match up with literature values for the molecular weight of YfkO, with the Cys and His tags being compensated for.[41]

4.2 Enzymatic activity of modified nitroreductase

After purification and SDS-PAGE characterization, the NfnB-Cys and YfkO-Cys enzymes needs to be assessed for its activity towards the CB1954 prodrug, in order to confirm that the enzyme has actually been successfully synthesised, and to continue further work with the enzyme.

The activity of the enzyme is assessed by UV-vis spectroscopy, measuring the wavelengths from 200-800 nm every 90 seconds for 15 minutes. In the reference cuvette NfnB-Cys (*25µM*) is mixed with NADH (*300 µM*), DMSO (*10 µl*) to act as the CB1954 blank, and is made up to 1 ml with 50 mM phosphate buffer (*pH 7.2*). The sample cuvette under test is made up exactly the same minus the 10 µl of the DMSO, leaving the final volume at 990 µl. The sample is scanned against the reference following the 250-500 nm scan over 90 seconds to establish a baseline of the reaction. After the first scan CB1954 (*10 µl, 10 mM*) is added to the sample cuvette, after which the UV spectra of the cuvette is measured every 90 seconds. Figure 4.6 is a UV-Vis spectra of the activity of the NfnB-Cys enzyme. The spectra demonstrates a drop in absorbance over time at 340 nm, and an increase in absorbance over time at 420 nm, these relate to the NADH being consumed in the reaction[29,30] and the hydroxylamine being produced respectively.[2,30] Full spectrum (*200-800 nm*) wavelength scans were also carried out on the controls; CB1954, NADH, NfnB-Cys and DMSO for comparison to the enzymatic activity scans.

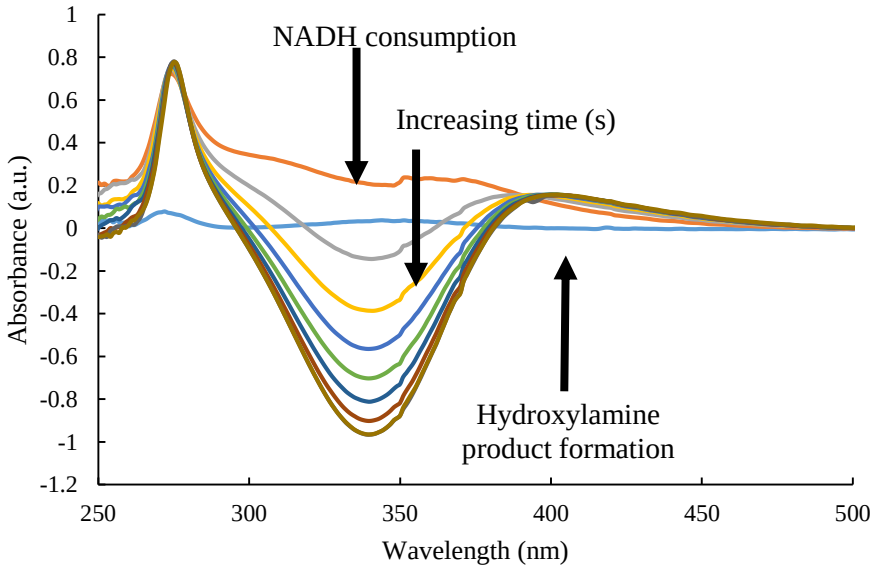

Figure 4.7. The UV-Vis spectra of the enzymatic activity assay of NfnB-Cys (25 µg/ml) with CB1954 (100 µM) and NADH (300µM) over 15 minutes, with the spectra (250-500 nm) being measured every 90 seconds. The drop in absorbance at 340 nm is the consumption of NADH whilst the increase in absorbance at 420 nm is the formation of the hydroxylamine products.

The YfkO-Cys enzyme was also tested for its ability to reduce the CB1954 prodrug, similarly to the NfnB-Cys the YfkO-Cys was examined by UV-Vis spectroscopy, using the same concentrations of enzyme, NADH and CB1954 as previously stated. Figure 4.8 is the spectra for the YfkO-Cys activity scan, as before this spectra demonstrates a drop in absorbance at 340 nm over time and an increase in absorbance at 420 nm, following the same trend as the NfnB-Cys indicating the NADH being consumed, forming the CB1954 hydroxylamine reduction products.

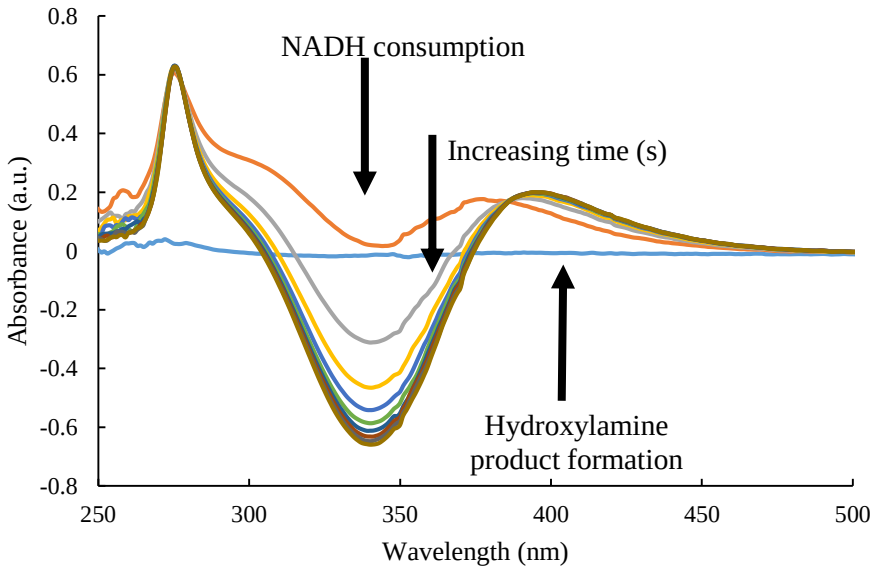

Figure 4.8. The UV-Vis spectra of the enzymatic activity assay of YfkO-Cys (25 µg/ml) with CB1954 (100 µM) and NADH (300µM) over 15 minutes, with the spectra (250-500 nm) being measured every 90 seconds. The drop in absorbance at 340 nm is the consumption of NADH whilst the increase in absorbance at 420 nm is the formation of the hydroxylamine products.

4.3 Reaction profile of modified nitroreductase

CB1954 can be reduced to one of 2 products: 2-hydroxyalmine and 4-hydroxylamine derivatives. These products are produced at different ratios, depending on the enzyme reducing the CB1954.[23] High Performance Liquid Chromatography (*HPLC*) can be used to examine the product different retention times, and to determine a ratio of the 2:4 NHOH based on the area under each peak.[42]

Samples to be run on HPLC were prepared in a 15ml falcon tube covered in foil as follows: NADH (*120 µl, 10 mM*) NTR (*116 µg/ml*), CB1954 (*20 µl, 50 mM*) and made to a final volume of 1080 µl using PB (*50 mM, pH 7.2*). This mixture was incubated at 25 ˚C for 30 min, being degassed under nitrogen (*g*) for the final 15 min of the reaction. 750 µl of the de-gassed reaction was placed into a chromacol select 2 ml vial (*2-SVW8-CPK*) and placed into the HPLC

machine. The solvent mixture was an acetonitrile/water at a 10:90 ratio, with the acetonitrile increasing at 1 % per minute. After the HPLC had been running for 20 minutes the acetonitrile concentration was increased to 40 % per minute, and further increasing to 100 % acetonitrile after 22 min. Eluents were scanned at 420 nm with product peaks being identified upon comparison with reagent standards run before the reaction, following the same protocol. Ratios of the 2- and 4-hydroxylamine products were determined at 420 nm, where both products have equal absorbance.[1] The HPLC produces chromatogram which is then exported to Microsoft excel, where the data can be graphically analysed, and the product ratios can be determined. These product ratios for CB1954 reacting with NfnB-Cys and YfkO-Cys are presented in Table 4.2. As well as running a reaction mixture through HPLC, control runs were performed of CB1954, NADH, DMSO and enzyme for comparison to the final chromatogram.

Table 4.2. The ratio of 2:4 NHOH products produced after a 30 minute reaction time for the NfnB-Cys and YfkO-Cys enzymes, reaction product ratios were determined using HPLC.

Enzyme	2:4 NHOH ratio
NfnB-Cys	32:68
YfkO-Cys	1:99

To determine the Michaelis-Menten kinetic parameters of CB1954 when using NfnB-Cys or YfkO-Cys, product formation at 420 nm was measured over time. In each well of the 96-well plate, CB1954 (*5 µl, 0.1-10 mM*), NADH (*20 µl, 20 mM*) and PB (*50 mM, pH 7.2*) were combined and incubated at 37 ˚C for 3 minutes before the purified NTR (*10 µg/ml*) was added. The Dimethyl sulfoxide (*DMSO*) solvent concentration was always kept constant at 5 % v/v to avoid any negative effect.[42] The amount of hydroxylamine product produced per second was determined by using the change in absorbance over 20 seconds and the hydroxylamine product's molar extinction coefficient (ε = *1200* M^{-1} cm^{-1} *at 420 nm*).[1,2,30,42,45–47] The data gathered was transferred to SigmaPlot where a non-linear regression tool was used to generate a Michaelis-Menten hyperbolic curve and a report containing the kinetic information of the system under test. The Michaelis-Menten kinetics for NfnB-Cys and YfkO-Cys are presented in Table 4.3.

Table 4.3. Michaelis-Menten kinetic data obtained for the NfnB-Cys and YfkO-Cys enzymes, obtained by varying the concentration of CB1954 using NADH as the cofactor.

Enzyme	Vmax (μMS^{-1})	Kcat (S^{-1})	Km (µM)	Kcat/Km ($\mu M^{-1}S^{-1}$)
NfnB-Cys	19±1.3	55±0.67	5000±700	$0.01089\pm3.8x10^{-3}$
YfkO-Cys	6.5±1.2	39±0.89	830±250	$0.04714\pm3.6x10^{-3}$

The data obtained for the Michaelis-Menten kinetics for the enzyme-substrate systems of NfnB-Cys and YfkO-Cys with CB1954 give some interesting results. The initial discussion point is the comparison of Vmax (*maximum rate of the system*), here NfnB-Cys presents a Vmax of 19.37 μMS^{-1}, whilst YfkO-Cys presents a Vmax of 6.53 μMS^{-1} almost 3 times lower than NfnB-Cys. However the Km of YfkO-Cys is 834 µM, 6 times lower than the Km value of 5078.37 µM obtained for NfnB-Cys. The same trend is observed for the Kcat values of both enzymes, with NfnB-Cys having a Kcat value of 55.34 S^{-1} compared to YfkO-Cys having a value of 39.33 S^{-1}. This trend is not observed when examining the Kcat/Km values for the 2 enzymes, in fact the catalytic efficiency of 0.04714 $\mu M^{-1}S^{-1}$ for YfkO-Cys demonstrates a value almost 5 times more efficient than the value obtained for NfnB-Cys of 0.01089 $\mu M^{-1}S^{-1}$, indicating YfkO-Cys is a much better option for use in combination with the CB1954 prodrug, based on kinetic data.

4.4 Conjugation of CPP with modified nitroreductase

As mentioned one of the key features that most therapeutic moieties need is the function to uptake into cells, quickly and efficiently. CPPs can be conjugated to a variety of materials and have been shown to increase the cellular uptake of nucleic acids,[16,17,48,49] proteins[15,18,50] and nanoparticles.[17,20,51,52] CPPs can be conjugated to materials at a variety of ratios non-covalently by incubation at temperatures ranging from 'room temperature' to 37 ˚C,[11,21,49] or can be conjugated covalently chemically with the incorporation of thiol groups.[53–55]

Typically, conjugation of materials to CPPs can be measured using gel retardation techniques,[21,56] with conjugation to materials such as quantum dots being detected using fluorescence imaging.[21,56] Here however, neither the CPP or nitroreductases possess natural fluorescence properties, as such it was determined the best way to establish if CPP conjugation onto the nitroreductases was successful was to use coomassie blue staining as done with the previously described SDS-PAGE analysis.

Native PAGE gels were used to attempt to prove a successful conjugation between the NfnB-Cys and HR9. Native gels were prepared as described in section 4.1.4.1 with the exception that no SDS was used in the preparation, and the sample loading dye contained no SDS or β-Mercaptoethanol. Further to this the samples were not heat treated prior to being run on the gel. Figure 4.9 is an image of a native PAGE gel run testing the conjugation between NfnB-Cys and HR9.

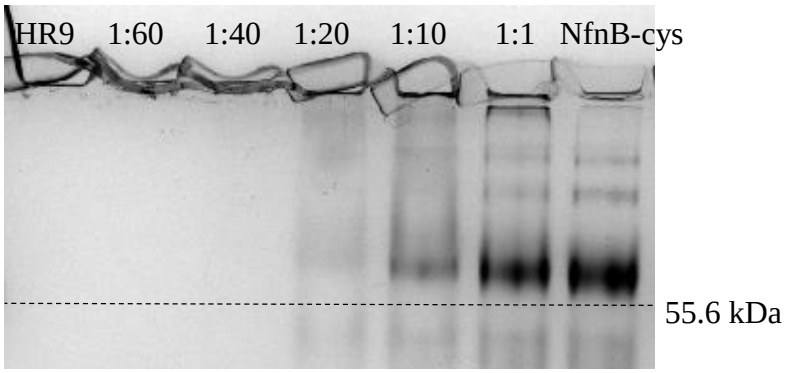

Figure 4.9. An image of the native PAE gel run on the conjugation of NfnB-Cys with HR9 at varying ratios

This gel had unconjugated NfnB-Cys in the far right hand lane with an increasing ratio of HR9 up to just HR9 moving right to left. Here there is an indication that the HR9 is conjugating to the NfnB-Cys by the bands 'laddering' up the gel moving right to left, however at ratios above 1:20 there is no protein band present indicating that the conjugate is possibly unable to enter the gel, possibly due to either pore size or more realistically the pH and/ or charge of the gel prevented any migration into and through the gel. Another method was required to fully analyse the conjugation between NfnB-Cys and HR9.

As previously mentioned typically when proteins are characterised by gel electrophoresis, SDS-PAGE techniques are used, however for the conjugation of CPPs to nitroreductases an agarose gel would be better for determining successful conjugation. This is because the gel is horizontal, as such the wells for sample placement can be placed in the middle of the gel, which would allow differently charged proteins to travel in different directions, and then be stained as previously described. Also agarose gels contain no denaturing products, so the CPP:NTR conjugates could be examined in their native states. If conjugation was successful it would be expected that as the ratio of CPP increased, the conjugate would have its migration through the gel retarded more and more, showing a gradient effect of movement.

Here a 0.5 % agarose gel was made by dissolving 0.5 g of agarose in 100 ml TBE buffer (*Tris-base 10.8 g, boric acid 5.5 g, EDTA 4 ml, 500 mM, made up to 1 L, pH 8*), and heated to ensure full dissolution of the agarose, taking care not to boil and degrade the agarose. The solution was poured into a cast with a comb used to create wells during the gel's setting process. To prepare samples, NfnB-Cys or YfkO-Cys was mixed with varying volumes of either HR9 or Pep-1 to create ratios ranging from 1: 0.1 (*NTR:CPP*) to 1:15. These samples were then placed into a heat block at 37 $^{\circ}$C for 30 minutes. After 30 minutes the samples were removed and then individually mixed with a native, non-denaturing loading dye (*Tris-HCl 1 ml, 100 mM, pH 6.8, glycerol 4ml, 50 %, bromophenol blue 500 µl, 1 % and made up with ddH_2O 9.7 ml*). Each sample was placed into a well (*with the volume differing for each well, as to ensure identical nitroreductase concentration in each well*), so that from left to right was unconjugated enzyme, leading through an increasing ratio of CPPs and finally unconjugated CPP, (*the unconjugated enzyme and CPP were also subjected to being heated at 37 $^{\circ}$C for 30 minutes*). The gel was then placed into a running tank and covered with TBE running buffer, the gel was run for 1 hour at 100 V. After this time, the gel was removed from the tank, placed into a container, covered with Coomassie Brilliant Blue stain and left staining overnight. The following day the stain was carefully removed from the gel, and de-stain was poured onto the gel (*IMS 200 ml, ddH_2O 500 ml, glacial acetic acid 100 ml*). The de-stain was changed whenever it became saturated with dye. When the dye had been sufficiently removed from the gel, and the stained proteins could be viewed, the gel was photographed, and any movement of the conjugates through the gel could be determined.

Figure 4.10 is the agarose gel analysis of NfnB-Cys conjugating with HR9, it can be observed in this gel that the unconjugated NfnB-Cys migrates towards the bottom of the gel (***the cathode***) whilst the unconjugated HR9 migrates heavily towards the anode. As the ratio of NfnB-Cys conjugated to the HR9 increases, the conjugates migration through the gel is retarded, as the ratio increases, a point is reached where the charge from the CPPs is able to overcome the opposite charge from the NfnB-Cys causing the conjugate to remain in the well, it is possible that at a higher ratio the conjugate would migrate towards the anode. When mixed together, the ratio of NfnB-Cys and HR9 in each mixture was calculated to be what is presented on the gel image, however it is feasible that there are a variety of ratios within each mixture, but with the majority of ratios being the desired ratio. This range of ratios would cause a slightly different overall charge for conjugates with varying ratios. This slight charge difference would cause the different ratio conjugates to migrate at different rates though the gel, this could

explain the streaking effect seen in all the gels, (*note that there is no streaking observed in the unconjugated enzyme sample wells*).

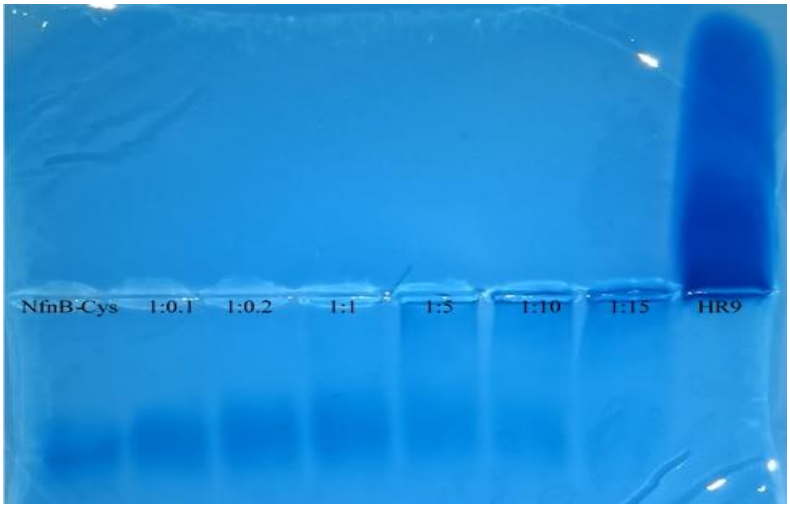

Figure 4.10. The agarose conjugation gel of NfnB-Cys and HR9, the left hand lane is unconjugated NfnB-Cys, with the lanes running left to right having conjugates with an increasing HR9 ratio up to 1:15, the final lane is unconjugated HR9..

This conjugation analysis was repeated using Pep-1, the resulting gel is presented in Figure 4.11 on the following page, and here the gel shows a similar effect as in Figure 4.10, whereby the ratio of Pep-1 increases the conjugates migration through the gel is retarded. When the ratio increases to 1:5 the migration to the bottom of the gel (***the anode***) is almost non-existent with the conjugate starting to show migration towards the top of the gel (***the cathode***). This change in migration observed is due to the charge of the conjugate reversing from the build-up of CPP. As the ratio increases to 1:10 and 1:15 the conjugate migrates even further towards the cathode. Both Figure 4.10 and Figure 4.11 confirm that HR9 and Pep-1 can conjugate successfully onto NfnB-Cys.

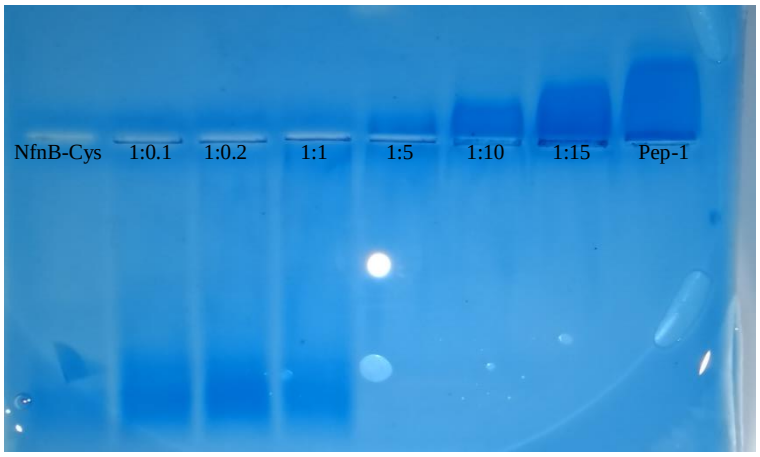

Figure 4.11. The agarose conjugation gel of NfnB-Cys and Pep-1, the left hand lane is unconjugated NfnB-Cys, with the lanes running left to right having conjugates with an increasing Pep-1 ratio up to 1:15, the final lane is unconjugated Pep-1.

YfkO-Cys was also examined for its ability to conjugate with the CPPs: HR9 and Pep-1. The gels were repeated following the same protocol that was used for NfnB-Cys. Figure 4.12 is an image of the agarose conjugation gel of YfkO-Cys:HR9, again here the same trend observed with NfnB-Cys conjugated to CPPs can be observed with YfkO-Cys:HR9. However here the conjugate's migration through the gel is retarded at a much lower ratio (*1:0.2*), and at ratios 1:10 and 1:15 the conjugate migrates towards the cathode, in the same manner as unconjugated HR9.

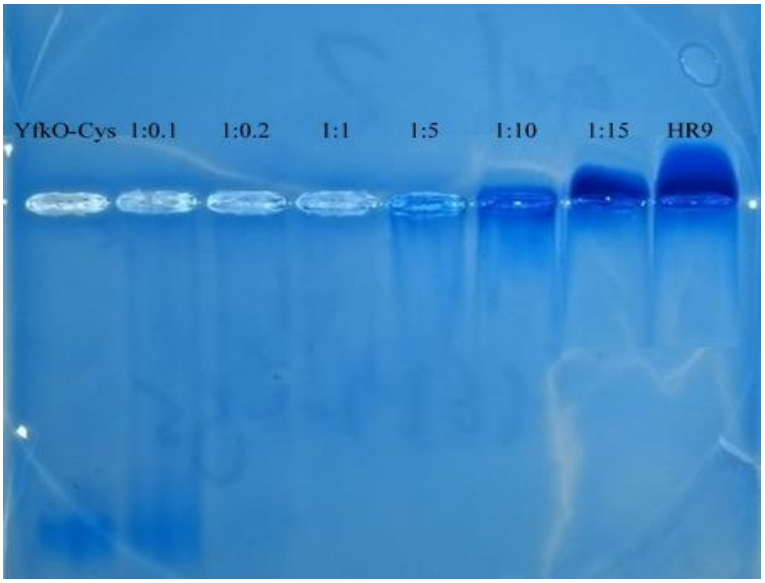

Figure 4.12. The agarose conjugation gel of YfkO-Cys and HR9, the left hand lane is unconjugated YfkO-cys, with the lanes running left to right having conjugates with an increasing HR9 ratio up to 1:15, the final lane is unconjugated HR9.

.

The final conjugation gel is YfkO-Cys:Pep-1, this gel is presented in Figure 4.13 on the following page, here there is a demonstration of the effect seen in the other gels, where the CPP retards the migration of the conjugate. However the effect is not as pronounced as with the other conjugates. It can be observed that at ratios 1:5, 1:10 and 1:15 there is migration towards the cathode, however most lanes still show protein migration towards the anode. As the ratio increases the intensity of the bands decrease, since the concentration of nitroreductase was kept constant in each well, this can lead to the conclusion that the CPP is conjugating to the YfkO-Cys, however it is possibly not conjugating across all the YfkO-Cys molecules, which is why there is still YfkO-Cys observable migrating towards the anode at the higher CPP concentrations.

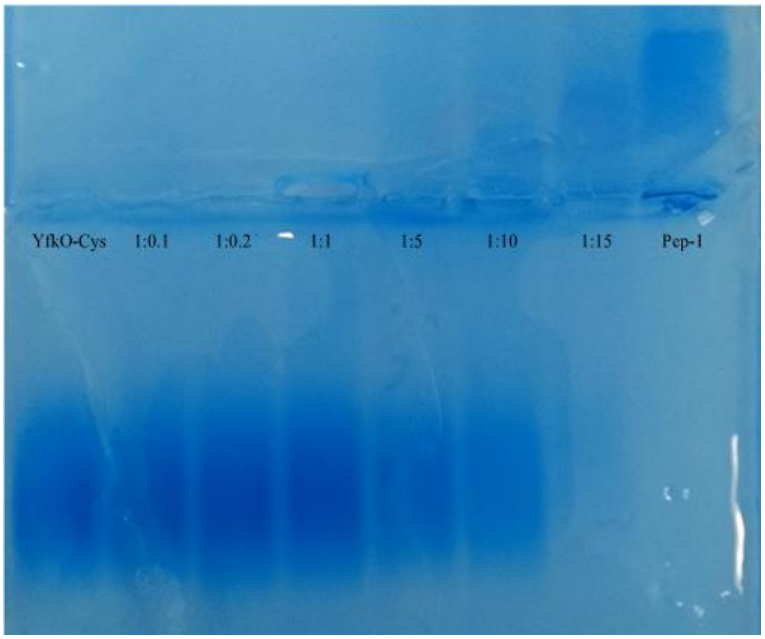

Figure 4.13. The agarose conjugation gel of YfkO-Cys and Pep-1, the left hand lane is unconjugated YfkO-cys, with the lanes running left to right having conjugates with an increasing Pep-1 ratio up to 1:15, the final lane is unconjugated Pep-1.

It has been demonstrated that both the enzymes: NfnB-Cys and YfkO-Cys can successfully conjugated onto the CPPs; HR9 and Pep-1. Each of the NTR:CPP conjugates show a different ratio required to overcome the nitroreductases negative charge to cause the conjugate to migrate towards the cathode.

4.5 Enzymatic activity of NTR:CPP conjugate

It has been established that NfnB-Cys and YfkO-Cys can successfully conjugate to the cell penetrating peptides; HR9 and Pep-1, however one important factor needed to be assessed if work with the CPPs was to be completed. That is to examine any effect the conjugation of CPPs has on the enzymatic activity of the enzyme, if the CPPs completely inhibited the activity of the enzymes there would be little to no point using them. Enzymatic activity scans were carried out as described in section 3.2 on the conjugates using the same ratios as for the gel electrophoresis in section 3.4. These scans were done in triplicate for each NTR:CPP conjugate for every ratio, and the change of absorbance at 420 nm was recorded for each ratio to be examined against the change of absorbance at 420 nm for unconjugated enzyme.

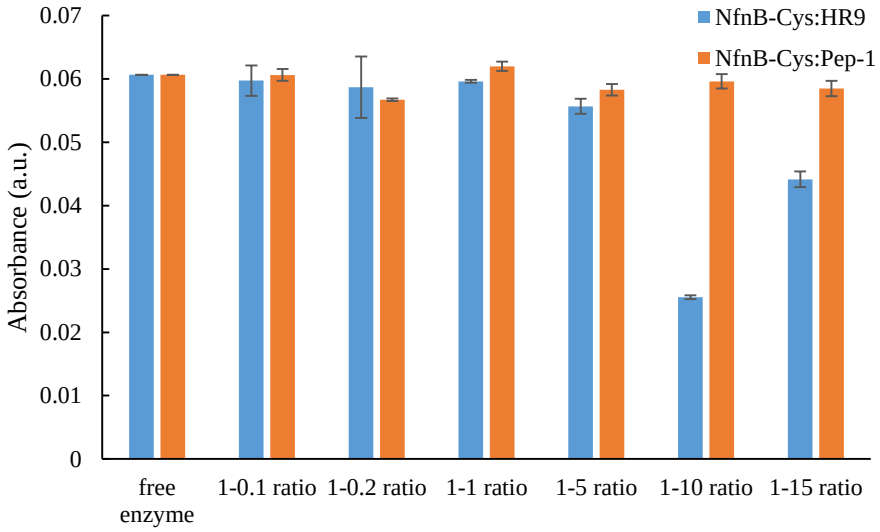

Figure 4.14. A comparison of the change of absorbance at 420 nm for NfnB-Cys conjugated to HR9 and Pep-1 at ratios ranging from 1:0.1 to 1:15, as well as the change in 420 nm for unconjugated NfnB-Cys. The unconjugated enzyme has a change in absorbance of 0.06, and all ratios up to 1:5 show little variance from this value. At 1:10 and 1:15 ratio the NfnB-Cys:Pep-1 shows no change, whereas the NfnB-Cys HR9 shows a major drop in the change of absorbance.

Figure 4.14 is a graphical representation of the change of absorbance at 420 nm over time for the NfnB-Cys enzyme and NfnB-Cys:CPP conjugates. The NfnB-Cys:Pep-1 conjugates show no major change in absorbance across all ratios, whilst the NfnB-Cys:HR9 shows no major change up to and including a ratio of 1:5, however above this ratio there is a considerable drop in the change of absorbance seen, indicating that at these ratios the CPP is interfering with the ability of the enzyme to produce the 2-and 4-NHOH reaction products.

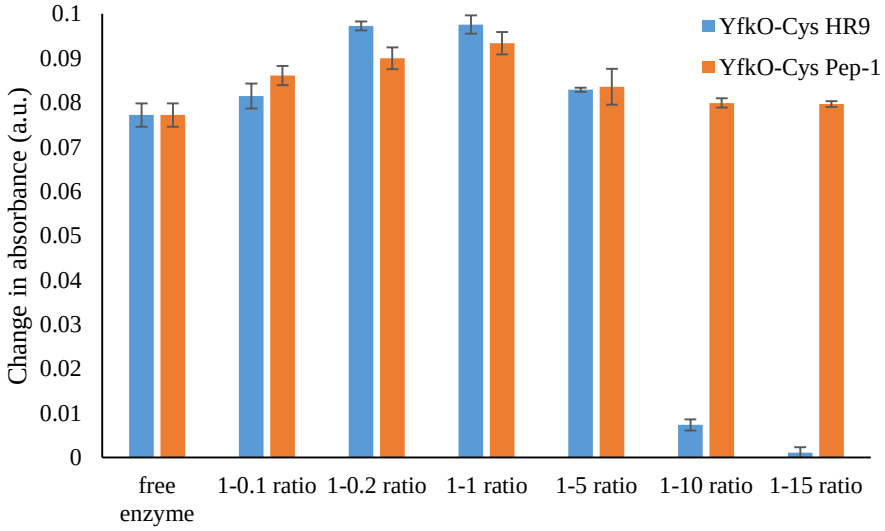

Figure 4.15. A comparison of the change of absorbance at 420 nm over time for YfkO-Cys conjugated to HR9 and Pep-1 at ratios ranging from 1:0.1 to 1:15, as well as the change in 420 nm for unconjugated YfkO-Cys. Here both NTR:CPP conjugates show and increase in the change of absorbance as the ratio of CPP increases up to a 1:1 ratio.

Figure 4.15 is a graphical representation of the change of absorbance at 420 nm over time observed for various ratios of YfkO-Cys conjugated with HR9 and Pep-1. Both sets of

conjugates at ratios up to and including 1:1 show a gradual increase in the change observed, where the 1:5 ratios show a change of absorbance in the range observed for the unconjugated YfkO-Cys. Above these ratios both conjugates follow the trends observed for the NfnB-Cys:CPP conjugates; the YfkO-Cys:Pep-1 change of absorbance remains comparable to unconjugated YfkO-Cys whilst the YfkO-Cys:HR9 shows a sharp drop in the change of absorbance at a ratio of 1:10 and an almost non-existent change of absorbance at a ratio of 1:15.

Comparing both sets of data shows at lower ratios both NfnB-Cys and YfkO-Cys show consistent changes of absorbance when conjugated to HR9 and Pep-1 at a ratio of 1:1, due to this it was decided that continuing work with these systems was all to be carried out at a ratio of 1:1 for both enzymes with both CPPs, However other future work could be carried out examining which CPP ratio is the most ideal for cellular uptake and the ability for these ratios to cause cell death in cell viability experiments.

4.6 Reaction profile of NTR:CPP conjugate

Once it had been established that NfnB-Cys and YfkO-Cys still retain activity when conjugated with HR9 and Pep-1 at a ratio of 1:1, the reactions profiles of the conjugates needed to be established in the same way for the unconjugated NfnB-Cys and YfkO-Cys described in section 3.3 using HPLC and Michaelis-Menten kinetics. HPLC was carried out as previously described in section 3.3, samples to be run on HPLC were prepared in a 15 ml falcon tube covered in foil as follows: NADH (*120 µl, 10 mM*) NTR/ NTR:CPP (*116 µg/ml*), CB1954 (*20 µl, 50 mM*) and made to a final volume of 1080 µl using PB (*50 mM, pH 7.2*). This mixture was incubated at 25 ˚C for 30 min, being degassed under nitrogen (*g*) for the final 15 min of the reaction. 750 µl of the de-gassed reaction was placed into a chromacol select 2 ml vial (*2-SVW8-CPK*) and placed into the HPLC machine. The solvent mixture was an acetonitrile/water at a 10:90 ratio, with the acetonitrile increasing at 1 % per minute. After the HPLC had been running for 20 minutes the acetonitrile concentration was increased to 40 % per minute, and further increasing to 100 % acetonitrile after 22 mins. Eluents were scanned at 420 nm with product peaks being identified upon comparison with reagent standards run before the reaction, following the same protocol. Ratios of the 2’ and 4’-hydroxylamine products were determined at 420 nm, where both products have equal absorbance.[1]

Table 4.4. The ratio of 2:4 NHOH products produced after a 30 minute reaction time for the NfnB-Cys:HR9, NfnB-Cys:Pep-1, YfkO-Cys:HR9 and YfkO-Cys:Pep-1 NTR:CPP conjugates, reaction product ratios were determined using HPLC.

Conjugate	2:4 NHOH ratio
NfnB-Cys:HR9	36:64
NfnB-Cys:Pep-1	35:65
YfkO-Cys:HR9	4:96
YfkO-Cys:Pep-1	7:93

The 2-:4-NHOH product ratios obtained for the HPLC reactions of NfnB-Cys and YfkO-Cys with HR9 and Pep-1 are presented in Table 4.3. It can be seen that NfnB-Cys when conjugated with HR9 and Pep-1 at a 1:1 ratio produces a product ratio of 36:64 and 35:65 respectively. For YfkO-Cys when conjugated with HR9 and Pep-1 the ratios produced are 4:96 and 7:93 respectively. These show slight change from the unconjugated enzymes, both for NfnB-Cys and YfkO-Cys, the ratios of the conjugated and unconjugated enzymes are presented for comparison in Table 4.5, the biggest deviation from the unconjugated ratio is for YfkO-Cys:Pep-1 where the ratio changes from 1:99 for unconjugated YfkO-Cys to 7:93 for the conjugated. However all of the conjugates show no major deviation from the ratios obtained for the unconjugated enzymes, and this change is probably due to the CPPs causing slight conformational changes to the structure of the enzymes, which has previously been shown to cause a change in the ratio obtained.[23]

Table 4.5. A comparison of the CB1954 reaction product ratios of the unconjugated enzymes; NfnB-Cys and YfkO-Cys compared when conjugated with the cell penetrating peptides; HR9 and Pep-1.

Enzyme/ Enzyme CPP conjugate	2:4 NHOH ratio	Enzyme/ Enzyme CPP conjugate	2:4 NHOH ratio
NfnB-Cys	32:68	YfkO-Cys	1:99
NfnB-Cys:HR9	36:64	YfkO-Cys:HR9	4:96
NfnB-Cys:Pep-1	35:65	YfkO-Cys:Pep-1	7:93

To determine the Michaelis-Menten kinetic parameters of CB1954 when using NfnB-Cys:CPP or YfkO-Cys:CPP conjugates, product formation at 420 nm was measured over time. In each well of the 96-well plate, CB1954 (*5 µl, 2-100 mM*), NADH (*20 µl, 20 mM*) and PB (*50 mM, pH 7.2*) were combined and incubated at 37 °C for 3 minutes before the purified NTR (*50 µg/ml*) was added. The Dimethyl sulfoxide (*DMSO*) solvent concentration was always kept constant at 5 % v/v to avoid any negative effect.[42] The amount of hydroxylamine product produced per second was determined by using the change in absorbance over 20 seconds and the hydroxylamine product's molar extinction coefficient (ε = *1200* M^{-1} cm^{-1} *at 420 nm*).[1,2,30,42,45–47]

The data gathered was transferred to SigmaPlot where a non-linear regression tool was used to generate a Michaelis-Menten hyperbolic curve and a report containing the kinetic information of the system under test. It is of note that there were slight changes made between this protocol and the protocol discussed in section 3.3, the changes were an increase prodrug and enzyme concentration used, and due to this only the enzyme efficiency (*Kcat/Km*) can be directly compared to the unconjugated enzymes.

Table 4.6 is the data obtained for the Michaelis-Menten kinetic analysis of the NfnB-cys and YfkO-Cys CPP conjugates.

Table 4.6. Michaelis-Menten kinetic data obtained for the NfnB-Cys:HR9, NfnB-Cys:Pep-1, YfkO-Cys:HR9 and YfkO-Cys:Pep-1 NTR:CPP conjugates, obtained by varying the concentration of CB1954 using NADH as the cofactor.

Conjugate	Vmax (μMS^{-1})	Kcat (S^{-1})	Km (µM)	Kcat/Km ($\mu M^{-1}S^{-1}$)
NfnB-Cys:HR9	8.0±1.4	9.1±0.82	3400±900	$0.00263\pm4.6x10^{-4}$
NfnB-Cys:Pep-1	7.4±1.2	8.4±0.73	2400±700	$0.00354\pm6.5x10^{-4}$
YfkO-Cys:HR9	5.3±1.1	5.7±0.56	2000±600	$0.00278\pm5.6x10^{-4}$
YfkO-Cys:Pep-1	5.5±1.5	5.9±0.68	2400±600	$0.00250\pm4.8x10^{-4}$

Here both the NfnB-Cys conjugates have Vmax values obtained being: 7.98 μMS^{-1} and 7.43 μMS^{-1} for NfnB-Cys:HR9 and NfnB-Cys Pep-1 respectively, which shows a slightly higher maximum rate for the HR9 than Pep-1 when conjugated to NfnB-Cys. The YfkO-Cys conjugates have Vmax values as follows: 5.25 μMS^{-1} and 5.47 μMS^{-1} for YfkO-Cys:HR9 and YfkO-Cys Pep-1 respectively, which shows a slightly higher maximum rate for the Pe-1 than HR9, which is contrary from the NfnB-Cys systems. However it does show that both NfnB-Cys conjugate systems have a higher Vmax than both YfkO-Cys conjugate systems. The Km value obtained for NfnB-Cys:HR9 is 3443.57 µM which is higher than the value of 2381.00 µM obtained for NfnB-Cys:Pep-1, which is to be expected based on the higher Vmax for the NfnB-Cys:HR9 system. The same trend is observed for the YfkO-Cys conjugates with YfkO-Cys:Pep-1 having a Km of 2376.91 µM, and YfkO-Cys:HR9 having a Km value of 2047.95 µM, where the YfkO-Cys:pep-1 system having a higher Vmax. Both NfnB-Cys conjugate systems showed a higher Kcat than the YfkO-Cys conjugate systems, with values obtained of 9.06 S^{-1} and 8.44 S^{-1} for NfnB-Cys:HR9 and NfnB-Cys:Pep-1 respectively, whereas the YfkO-

Cys conjugate systems obtained Kcat values of 5.70 S^{-1} and 5.94 S^{-1} for YfkO-Cys:HR9 and YfkO-Cys:Pep-1 respectively. The final set of data obtained for the conjugate systems is the enzymatic efficiency (*Kcat/Km*), all systems had values similar to each other, except for NfnB-Cys which had a value of 0.00354 $\mu M^{-1}S^{-1}$, whilst the systems NfnB-Cys:HR9, YfkO-Cys:HR9 and YfkO-Cys:Pep-1 had values of 0.00263 $\mu M^{-1}S^{-1}$, 0.00278 $\mu M^{-1}S^{-1}$ and 0.00250 $\mu M^{-1}S^{-1}$ respectively. This data points to the conclusion that out of the 4 conjugate systems NfnB-Cys:Pep-1 at a ratio of 1:1 is the most efficient at product turnover.

Table 4.7 is a comparison of the enzymatic product turnover efficiency (*Kcat/Km*) of the unconjugated enzyme systems, with the NTR:CPP conjugate systems. The immediate piece of information to point out is how drastically low the Kcat/Km values of the conjugate systems are compared to the unconjugated systems. The NfnB-Cys:HR9 system shows 25 % of the efficiency of the NfnB-Cys system, whilst the NfnB-Cys:Pep-1 system shows just over 33 % of the efficiency of the NfnB-Cys system. Again the same is observed for the YfkO-Cys conjugate systems, however the YfkO-Cys:HR9 and YfkO-Cys:Pep-1 show 5.8 % the enzymatic efficiency compared to unconjugated YfkO-Cys.

Table 4.7Michaelis-Menten kinetic data obtained for NfnB-Cys and YfkO-Cys compared when the enzymes are conjugated to the cell penetrating peptides: HR9 and Pep-1.

Enzyme/ Enzyme CPP conjugate	**Kcat/Km ($\mu M^{-1}S^{-1}$)**	**Enzyme/ Enzyme CPP conjugate**	**Kcat/Km ($\mu M^{-1}S^{-1}$)**
NfnB-Cys	0.01089	YfkO-Cys	0.04714
NfnB-Cys:HR9	0.00263	YfkO-Cys:HR9	0.00278
NfnB-Cys:Pep-1	0.00354	YfkO-Cys:Pep-1	0.00250

4.7 Conclusion

The data presented in this chapter discussed the conjugation of CPPs with NfnB-Cys and YfkO-Cys. Initially the CPPs: HR9 and Pep-1 were examined for their ability to conjugate to the enzymes at various ratios, with data showing that conjugation is achievable. The conjugates have then been assessed for how the conjugation of CPPs at different ratios effects the change of absorbance over 15 minutes at 420 nm when reacted with CB1954. All sets of conjugates up to a ratio of 1:5 showed no major effects on the change of absorbance, above a ratio of 1:5 all Pep-1 conjugates again showed no impact on the change of absorbance whilst all HR9 conjugates above a 1:5 ratio showed an impact on the change of absorbance, with the YfkO-Cys conjugates showing the biggest impact. From these results it was decided to only continue using the 1:1 ratio for all future work, for which the product reaction profiles were assessed

using HPLC and Michaelis-Menten kinetics. The HPLC was used to assess the 2-and 4-NHOH product peak ratios and how conjugation of CPPs affects those peak ratios, with slight changes to the ratios being observed for the conjugates. The biggest change observed was the enzymatic efficiency values obtained for the Michaelis-Menten kinetic data of the CPP conjugates. All conjugates showed dramatic decrease in efficiency with NfnB-Cys conjugates demonstrating 25 % and 33 % efficiency for NfnB-Cys:HR9 and NfnB-Cys:Pep-1 respectively compared to unconjugated NfnB-Cys, whilst the YfkO-Cys conjugates both demonstrated only a 5.8 % efficiency compared to unconjugated YfkO-Cys. Cell viability experiments need to be done to assess if the CPP's ability to uptake into cells can overcome this issue observed with enzymatic efficiency.

4.8 Bibliography

1 P. R. Race, A. L. Lovering, S. A. White, J. I. Grove, P. F. Searle, C. W. Wrighton and E. Hyde, *J. Mol. Biol.*, 2007, **368**, 481–492.

2 V. V. Gwenin, P. Poornima, J. Halliwell, P. Ball, G. Robinson and C. D. Gwenin, *Biochem. Pharmacol.*, 2015, **98**, 392–402.

3 P. F. Searle, M. J. Chen, L. Hu, P. R. Race, A. L. Lovering, J. I. Grove, C. Guise, M. Jaberipour, N. D. James, V. Mautner, L. S. Young, D. J. Kerr, A. Mountain, S. A. White and E. I. Hyde, *Clin. Exp. Pharmacol. Physiol.*, 2004, **31**, 811–816.

4 G. A. Prosser, J. N. Copp, A. M. Mowday, C. P. Guise, S. P. Syddall, E. M. Williams, C. N. Horvat, P. M. Swe, A. Ashoorzadeh, W. A. Denny, J. B. Smaill, A. V. Patterson and D. F. Ackerley, *Biochem. Pharmacol.*, 2013, **85**, 1091–1103.

5 K. D. Bagshawe, in *Prodrugs: Challenges and rewards*, eds. S. Valentino, R. Borchardt, M. Hageman, R. Oliyai, H. Maag and T. W. Jefferson, Springer, New York, 2005, pp. 526–536.

6 R. J. Knox, F. Friedlos and M. P. Boland, *Cancer Metastasis Rev.*, 1993, **12**, 195–212.

7 D. H. Palmer, V. Mautner, D. Mirza, S. Oliff, W. Gerritsen, J. R. M. Van der Sijp, S. Hubscher, G. Reynolds, S. Bonney, R. Rajaratnam, D. Hull, M. Horne, J. Ellis, A. Mountain, S. Hill, P. A. Harris, P. F. Searle, L. S. Young, N. D. James and D. J. Kerr, *J. Clin. Oncol.*, 2004, **22**, 1546–1552.

8 N. G. Rainov, *Hum. Gene Ther.*, 2000, **11**, 2389–2401.

9 P. Järver and Ü. Langel, *Biochim. Biophys. Acta - Biomembr.*, 2006, **1758**, 260–263.

10 M. Green and P. Loewenstein, *Cell*, 1988, **55**, 1179–1188.

11 S. Futaki, T. Suzuki, W. Ohashi, T. Yagami, S. Tanaka, K. Ueda and Y. Sugiura, *J. Biol. Chem.*, 2001, **276**, 5836–5840.

12 P. A. Wender, D. J. Mitchell, K. Pattabiraman, E. T. Pelkey, L. Steinman and J. B. Rothbard, *Proc. Natl. Acad. Sci.*, 2000, **97**, 13003–13008.

13 M. C. Morris, S. Deshayes, F. Heitz and G. Divita, *Biol. Cell*, 2008, **100**, 201–217.

14 M. C. Morris, E. Gros, G. Aldrian-Herrada, M. Choob, J. Archdeacon, F. Heitz and G. Divita, *Nucleic Acids Res.*, 2007, **35**, 2-10.

15 M. C. Morris, J. Depollier, J. Mery, F. Heitz and G. Divita, *Nat. Biotechnol.*, 2001, **19**, 1173–1176.

16 T. Kato, H. Yamashita, T. Misawa, K. Nishida, M. Kurihara, M. Tanaka, Y. Demizu and M. Oba, *Bioorganic Med. Chem.*, 2016, **24**, 2681–2687.

17 B. R. Liu, J. S. Liou, Y. J. Chen, Y. W. Huang and H. J. Lee, *Mar. Biotechnol.*, 2013, **15**, 584–595.

18 L. Kurzawa, M. Pellerano and M. C. Morris, *Biochim. Biophys. Acta - Biomembr.*, 2010, **1798**, 2274–2285.

19 M. H. Wang and D. C. Otteson, *J. Neurosci.*, 2010, **177**, 403–419.

20 B. R. Liu, S. Y. Lo, C. C. Liu, C. L. Chyan, Y. W. Huang, R. S. Aronstam and H. J. Lee, *PLoS One*, 2013, **8**, 1–12.

21 B. R. Liu, J. F. Li, S. W. Lu, H. J. Leel, Y. W. Huang, K. B. Shannon and R. S. Aronstam, *J. Nanosci. Nanotechnol.*, 2010, **10**, 6534–6543.

22 S. Deshayes, M. C. Morris, G. Divita and F. Heitz, *Biochim. Biophys. Acta - Biomembr.*, 2006, **1758**, 328–335.

23 P. Ball, E. Thompson, S. Anderson, V. Gwenin and C. Gwenin, *Eur. J. Pharm. Sci.*, 2019, **127**, 217–224.

24 P. Patel, J. G. Young, V. Mautner, D. Ashdown, S. Bonney, R. G. Pineda, S. I. Collins, P. F. Searle, D. Hull, E. Peers, J. Chester, D. M. Wallace, A. Doherty, H. Leung, L. S. Young and N. D. James, *Mol. Ther.*, 2009, **17**, 1292–1299.

25 C. D. Gwenin, M. Kalaji, P. A. Williams and R. M. Jones, *Biosens. Bioelectron.*, 2007, **22**, 2869–2875.

26 Y. R. Luo, *Q. Rev. Chem. Soc.*, 2009, **9**, 65–97.

27 Addgene, *pET28a+ gene map, https://www.addgene.org/vector-database/2565/* (accessed 21st November 2018).

28 Novagen, *pET28a+ site map, http://www.merckmillipore.com/GB/en/product/pET-28a+-DNA-Novagen,EMD_BIO-69864,* (accessed 21st November 2018).

29 C. D. Gwenin, M. Kalaji, P. A. Williams and C. M. Kay, *Biodegradation*, 2011, **22**, 463–474.

30 V. V. Gwenin, C. D. Gwenin and M. Kalaji, *Langmuir*, 2011, **27**, 14300–14307.

31 A. J. F. Griffiths, S. R. Wessler, S. B. Carrol and J. Doebley, *Introduction to genetic analysis*, W.H. Freeman & Compnay, 11th edn., 2015.

32 G. Grogan, *Practical Biotransformations; A Beginner's Guide.*, Wiley, Chichester (UK), 2009.

33 S. J. Compton and C. G. Jones, *Anal. Biochem.*, 1985, **151**, 369–374.

34 M. M. Bradford, *Anal. Biochem.*, 1976, **72**, 248–254.

35 S. Gallagher and J. Sasse, in *Current protocols in Pharmacology*, John Wiley and Sons, 1998, pp. 1–10.

36 H. Schägger, *Nat. Protoc.*, 2006, **1**, 16–22.

37 D. E. Garfin, in *Guide to Protein Purification*, 2nd edn., 2009, vol. 182, pp. 497–513.

38 N. Saraswathy and P. Ramalingam, in *Concepts and Techniques in Genomics and Proteomics*, Elsevier, 2011, pp. 147–158.

39 C. Arndt, S. Koristka, H. Bartsch and M. Bachmann, *Protein Electrophor. Methods Protoc.*, 2012, **869**, 287–304.

40 A. J. Harwood, in *The nucleic acid protocol handbook*, 2000, pp. 73–75.

41 C. D. Emptage, R. J. Knox, M. J. Danson and D. W. Hough, *Biochem. Pharmacol.*, 2009, **77**, 21–29.

42 S. O. Vass, D. Jarrom, W. R. Wilson, E. I. Hyde and P. F. Searle, *Br. J. Cancer*, 2009, **100**, 1903–1911.

43 K. Johnson and R. Goody, *Biochemistry*, 2012, **50**, 8264–8269.

44 A. Cornish-Bowden, *Perspect. Sci.*, 2015, **4**, 3–9.

45 P. M. Swe, J. N. Copp, L. K. Green, C. P. Guise, A. M. Mowday, J. B. Smaill, A. V. Patterson and D. F. Ackerley, *Biochem. Pharmacol.*, 2012, **84**, 775–783.

46 G. A. Prosser, A. V. Patterson and D. F. Ackerley, *J. Biotechnol.*, 2010, **150**, 190–194.

47 G. A. Prosser, J. N. Copp, S. P. Syddall, E. M. Williams, J. B. Smaill, W. R. Wilson, A. V. Patterson and D. F. Ackerley, *Biochem. Pharmacol.*, 2010, **79**, 678–687.

48 S. Deshayes, S. Gerbal-Chaloin, M. C. Morris, G. Aldrian-Herrada, P. Charnet, G. Divita and F. Heitz, *Biochim. Biophys. Acta - Biomembr.*, 2004, **1667**, 141–147.

49 B. R. Liu, M. Der Lin, H. J. Chiang and H. J. Lee, *Gene*, 2012, **505**, 37–45.

50 A. Gautam, J. S. Nanda, J. S. Samuel, M. Kumari, P. Priyanka, G. Bedi, S. K. Nath, G. Mittal, N. Khatri and G. P. S. Raghava, *Sci. Rep.*, 2016, **6**, 1-13.

51 T. Asai, T. Tsuzuku, S. Takahashi, A. Okamoto, T. Dewa, M. Nango, K. Hyodo, H. Ishihara, H. Kikuchi and N. Oku, *Biochem. Biophys. Res. Commun.*, 2014, **444**, 599–604.

52 L. D. Field, J. B. Delehanty, Y. Chen and I. L. Medintz, *Acc. Chem. Res.*, 2015, **48**, 1380–1390.

53 Y. Wei, N. R. Jana, S. J. Tan and J. Y. Ying, *Bioconjug. Chem.*, 2009, **20**, 1752–1758.

54 Y. E. Koshman, S. B. Waters, L. A. Walker, T. Los, P. de Tombe, P. H. Goldspink and B. Russell, *J. Mol. Cell. Cardiol.*, 2008, **45**, 853–856.

55 F. L. Xue, J. Y. Chen, J. Guo, C. C. Wang, W. L. Yang, P. N. Wang and D. R. Lu, *J. Fluoresc.*, 2007, **17**, 149–154.

56 B. R. Liu, Y. Wern Huang, J. G. Winiarz, H. J. Chiang and H. J. Lee, *Biomaterials*, 2011, **32**, 3520–3537.

Chapter 5:
Cell viability of enzyme:CPP conjugate

Some of the results discussed in chapter 5 can be found in:

Cell penetrating peptides as a tool for the cellular uptake of a modified nitroreductase for use in Directed Enzyme Prodrug Therapy.
Submitted to The Journal of Controlled Release for peer review.

S.D. Anderson, P. Ball, V.V. Gwenin, R. Hobbs, L.A. Bennie, J.A. Coulter, C.D. Gwenin.

5.0 Introduction to cell culture studies

Cell culture is a generic term for the process of generating cultures of cells *in vivo* outside of the cells natural environment.[1,2] Cells are often grown this way in laboratories for ease of studies involving the cells, from observations of cellular mechanisms, to examining effects of various chemicals on the viability of the cells.[3,4] It is also a way to carefully control the conditions in which the cells are grown, such as; temperature, gases (CO_2, O_2), growth hormones and nutrients (*i.e. amino acids, minerals carbohydrates etc.*), with different cells having different requirements for healthy growth. Cells used in cell culture studies are often derived from a single cell removed from tissue,[5] known as primary cells, with cells replicating from these cells being secondary cells. These secondary cells exhibit similar characteristics to the primary cells but will not indefinitely replicate. Traditionally cells will only replicate a predetermined number of times before natural self-termination occurs, this number is known as the Hayflick limit.[6] It is possible however to immortalize cell lines to replicate indefinitely, either through random mutation, or deliberate modification, such as artificial expression of the telomerase gene. This cell immortalization allows for prolonged studies of cells *in vitro*. The cell culture work discussed in this section involves the use of primary and secondary cells.

When it comes to measuring cell viability, there are a variety of different techniques that can be used.[7–9] One common method is the MTT (1-(4,5-dimethylthiazol-2-yl)-3-5-diphenyl-tetrazolium bromide) assay.[10,11] The MTT assay is a colourmetric assay utilized in cell culture experiments for determining the percentage of cells alive compared to a control well. Mitochondrial oxidoreductase enzymes are capable of reducing MTT into insoluble formazan crystals.[12,13] This reduction is shown in Figure 5.1.

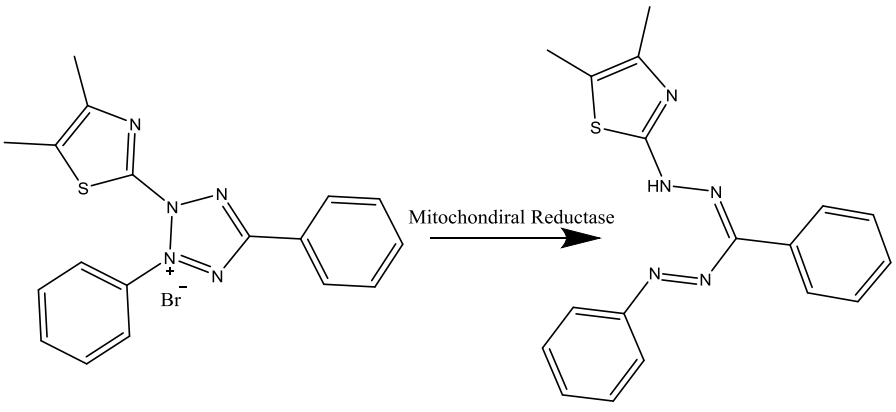

Figure 5.1. The reduction of MTT into insoluble formazan crystals that takes place in the cell, mediated by mitochondrial reductases.

Once MTT is treated onto cells and left for a predetermined time, the formed formazan crystals can be solubilized with a detergent or DMSO, creating a purple solution,[12] with the concentration of the solution being directly proportional to the number of viable cells.[14] This solution can be analysed by UV-vis spectroscopy at 570 nm.[11] By comparing the absorbance of different samples treated with MTT, a percentage survival can be compared to control cells treated with MTT.

The cancer cell line that will be examined in this work is SK-OV-3, an ovarian adenocarcinoma that has already been examined in use with various nitroreductases and CB1954.[15–17] An image of SK-OV-3 cells can be seen in Figure 5.2 taken when the cells are at close to 100 % confluency. Confluency is the term used to describe the percentage of growth area in a flask or plate has live cells growing on it, i.e. 50 % confluency has cells covering 50 % of the growth area.[18]

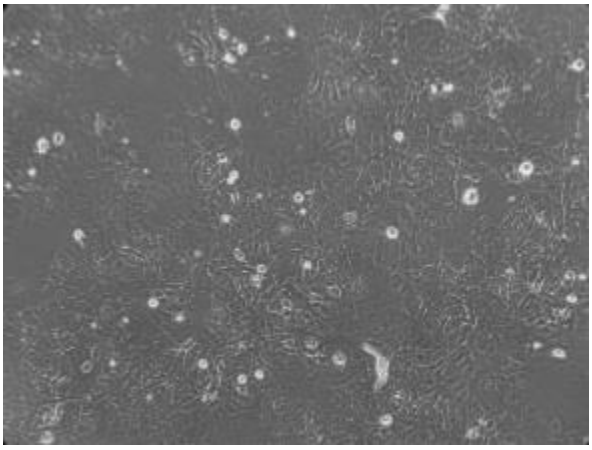

Figure 5.2. A picture of SK-OV-3 cells taken at 100x magnification at close to 80 % confluency taken under a microscope.

The aim of the cell culture work was to assess the ability for both the NfnB-Cys and YfkO-Cys nitroreductase to reduce the CB1954 prodrug in living cells and cause cell death in SK-OV-3 cells. These nitroreductases would then be conjugated with the CPPs HR9 and Pep-1, to assess for an increase in uptake of NfnB-Cys or YfkO-Cys. Increased cell death caused by the conjugates would be looked for as an indicator of increased cellular uptake. The individual toxicity of the nitroreductases and CPPs would also be assessed. It is important to note that no additional NAD(P)H is added to the wells, meaning that for the CB1954 to be successfully reduced both the CB1954 and nitroreductase would need to uptake into the cells. This allows for an examination of cell death caused only by internalized nitroreductase, which can allow for a direct comparison between the nitroreductase and NTR:CPP conjugate cell kills.

The MTT assay was performed as previously described with slight modification.[11] SK-OV-3 cells were seeded into a 96-well plate (*Corning, USA*) at a density of 1 x 10^4 cells per well, in 100 µl Dulbecco's Modified Eagle Medium (*DMEM*) containing 10 % FBS, 1 % L-glutamine and 1 % penicillin-streptomycin and were allowed to attach to the plate overnight in a CO_2 (*5 %*) incubator overnight at 37^OC. After 16 hrs, the media was carefully aspirated off and fresh media containing increasing concentrations from 25 nM to 200 nM of NTR or NTR:CPP conjugate (*50 µl*) was added to the wells with CB1954 (*50 µl, 20 µM*) along with wells only containing NTR, NTR:CPP conjugate (*200 nM*), CB1954 (*100 µl, 10 µM*) or DMEM (*100 µl*) as controls. After a 4hr incubation in a CO_2 (*5%*) incubator at 37^OC, the treatment media was carefully aspirated off and fresh media (*100 µl*) was added. The cells were left for 48 hrs in a CO_2 (*5 %*) incubator at 37^OC, after which MTT (*20 µl, 5 mg/ml*) was added and then left for 4 hrs in a CO_2 (*5 %*) incubator at 37^OC. The media was then aspirated off and DMSO (*100 µl*) was used to dissolve the purple formazan crystals and the absorbance was read at 570 nm using a Thermoscientific Varioskan Flash plate reader. All cell culture data presented in this chapter was carried out using this protocol.

5.1 Cell penetrating peptide toxicity

CPPs ability to penetrate into cells has already been discussed here; however, their ability to efficiently penetrate cell membranes could lead to overloading the cells at higher concentrations, inadvertently leading to unwanted cell death, which would lead to cell kill data showing an 'improved' cell kill when CPPs are involved. Whereas the 'improved' cell death is actually caused by the CPP directly. In order to prove this is not the case, the two CPPs under investigation in this work were treated onto SK-OV-3 cells at a concentration range between 25-200 nM (*in line with a 1:1 conjugation ratio with the NfnB-Cys concentration intended to be used*).

Figure 5.3 is an overlay showing the toxicity of HR9 and Pep-1 to SK-OV-3 at up to 200 nM. Both CPPs show no specific levels of toxicity towards the SK-OV-3 at any concentration, indicating that they can be used in cell culture treatments with NfnB-Cys and YfkO-Cys without risk of additional toxicity towards the cells.

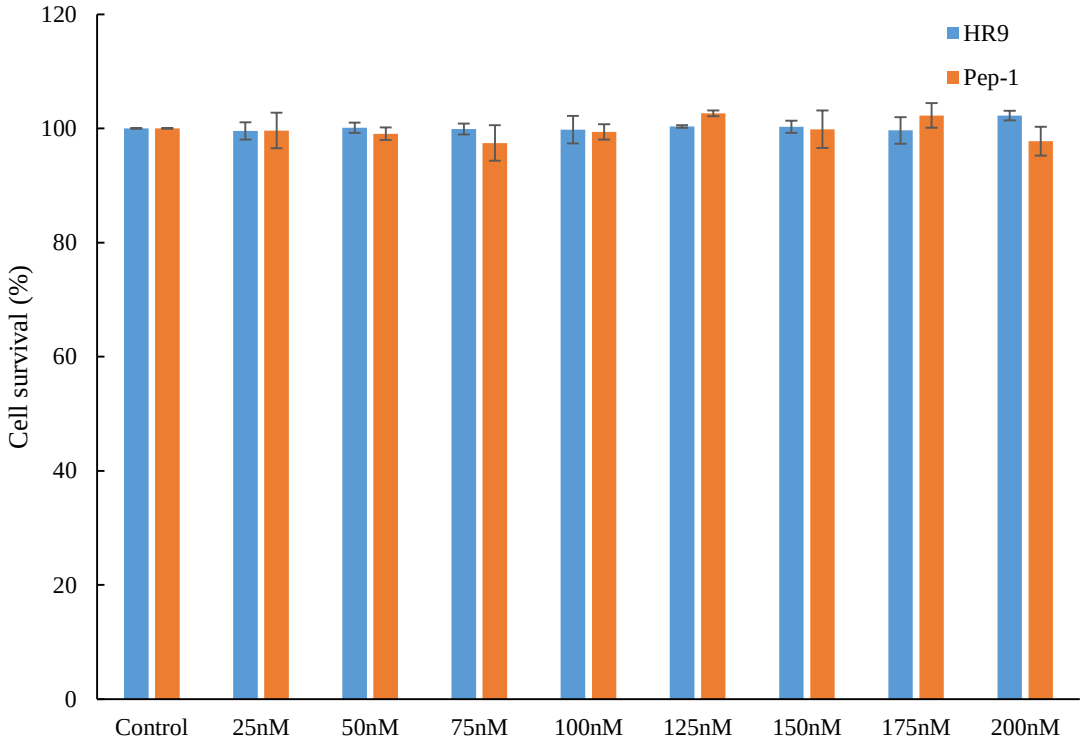

Figure 5.3. The cell viability of SK-OV-3 cells treated with HR9 up to 200 nM, the HR9 shows no major toxicity compared to the control lanes that only had cell culture growth medium added.

5.2 NfnB-Cys toxicity

The NfnB enzyme has been previously reported to be able to reduce the CB1954 prodrug in SK-OV-3 cells and cause cell death.[15] Here we have genetically modified NfnB with cysteine tags, the ability for NfnB-Cys to cause cell death in SK-OV-3 will be assessed along with the individual toxicity of NfnB-Cys towards SK-OV-3 and the toxicity of CB1954.

Statistical analysis was carried out on the results of the cell viability assays to determine if the results yielded proved to be important or not. 3 statistical test were used for this analysis: Anova single factor test, Bonferroni correction and the Dunnet's test. The Anova test was used to assess if each overall set of cell viability data contained any significant data using a significance level (α-value/ p-value) of 0.05 (95 % confidence level) the Anova test also provides an f-statistic which is a significance value determined by the difference between the f-value and the $f_{critical}$-value, the f value must be larger than the $f_{critical}$-value for statistically significant results, with a larger difference between these values indicating a higher level of statistical significance (all the Anova data for each test can be found in the appendices). The Bonferroni correction was used to create a tighter value required for a data set to be considered statistically significant, and reduce the possibility of a false positive result. This was done by dividing the α-value by the number of samples in each set, yielding a new α-value of 0.005 (99.5 % confidence) meaning that we can be 99.5 % confident that if a data set has a α-value below 0.005, then that data set is statistically significant. The Dunnett's test was carried out by determining the critical value for each set of data by using the following equation:

$$D_{dunnet} = t_{dunnet}\sqrt{\frac{2MS}{n}}$$

Where MS is the means squared value determined from the Anova single factor test, n is the number of groups (9) and t_{dunnet} is determined from the Dunnet table (see appendix). For a data point to be considered significant the difference between the average means of that data point from the control value must exceed this critical value. Data points that exceed this critical value (indicating a significant statistical data point) are marked in green in the data tables in the appendices, and are circled in red on the graphical representations of the cell viability assay data. It is of note that the Dunnet's test could not be performed on the nanoparticle cell viability data as the minimum number of degrees of freedom (df) required for the test is 5 and these tests had 4. The degrees of freedom refers to the number of significant data points.

5.2.1 Unconjugated NfnB-Cys

Figure 5.4 presents the data obtained for the NfnB-Cys cell viability assay with CB1954. As can be observed the CB1954 shows no toxicity at 10 uM and the NTR shows minimal toxicity at 200 nM, with the standard deviation being within range of 100 % cell viability. The concentration range of 25-200 nM NfnB-Cys shows a maximum cell viability of 76 % at 200 nM NfnB-Cys. Each data point (n) was done over 3 96 well micro-titre plates, with the being 8 repeats across 3 plates (shown on graphs). This will be used as the base point, for referencing the cell kill ability of the NfnB-Cys:CPP conjugates and for further reference against YfkO-Cys.

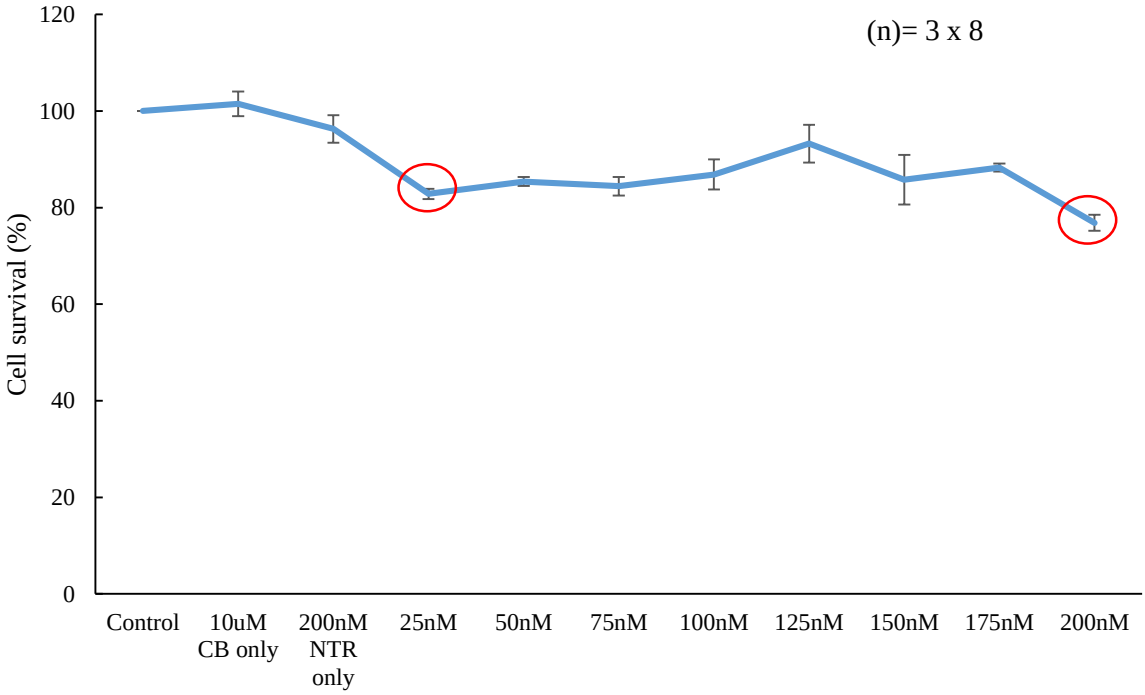

Figure 5.4. The cell viability of SK-OV-3 treated with NfnB-Cys up to 200 nM and 10 µM CB1954, control lanes were also run with untreated SK-OV-3, 10 µM CB1954 and 200 nM NfnB-Cys. At 200 nM NfnB-Cys, the SK-OV-3 has a 76 % cell survival rate. Statistically significant data points are ringed in red, error bars are ± 1 standard deviation, and (n) is the number of repeats each data point had.

5.2.2 NfnB-Cys conjugated with HR9

The cell viability data for NfnB-Cys:HR9 at a 1:1 ratio is presented in Figure 5.5, with the NfnB-Cys:HR9 control lane showing no major toxicity towards the cells. However in comparison to unconjugated NfnB-Cys, all conjugate concentrations from 25-200 nM show a decrease in cell viability, with the 200 nM conjugate concentration presenting a cell viability

of 58 %. This is an 18 % increase in cell death compared to free NfnB-Cys, indicating that the HR9 is successfully aiding the cellular internalization of NfnB-Cys.

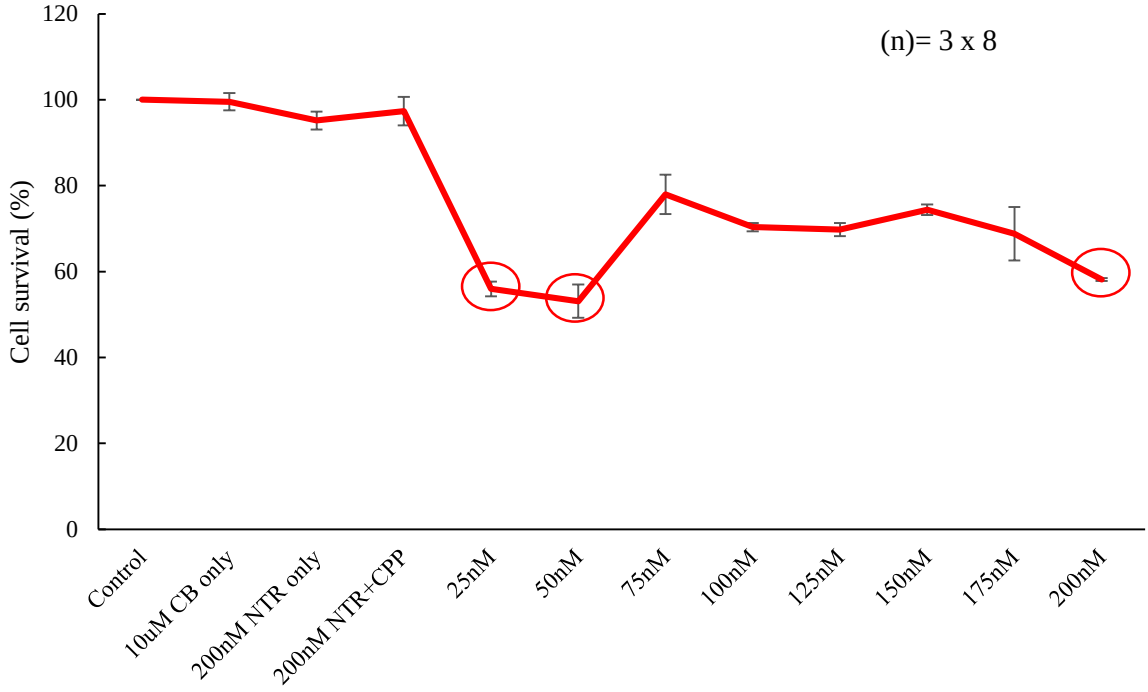

Figure 5.5. The cell viability of SK-OV-3 treated with NfnB-Cys conjugated to HR9 at a 1:1 ratio, at a range of 25-200 nM, with 10 μM CB1954. Control lanes of untreated SK-OV-3, 10 μM CB1954 200 nM NfnB-Cys and 200 nM NfnB-Cys:HR9 were also run. The NfnB-Cys:HR9 shows a cell survival of 58 % at 200 nM NfnB-Cys:HR9. Statistically significant data points are ringed in red, error bars are ± 1 standard deviation and (n) is the number of repeats each data point had.

5.2.3 NfnB-Cys conjugated with Pep-1

The data for the cell viability of NfnB-Cys;Pep-1 is presented in Figure 5.6. Similarly to the NfnB-Cys:HR9 data the NfnB-Cys:pep-1 data shows minimal toxicity for the NfnB-Cys:Pep-1 conjugate and a decrease in the cell viability shown for the cells treated with NfnB-Cys:Pep-1 and CB1954. However the decrease in cell viability shown at 200 nM NfnB-Cys:Pep-1 is a further 8 % to 68 % cell viability. This indicates that the pep-1 is aiding the cellular uptake of NfnB-Cys but possibly to a lesser extent than HR9.

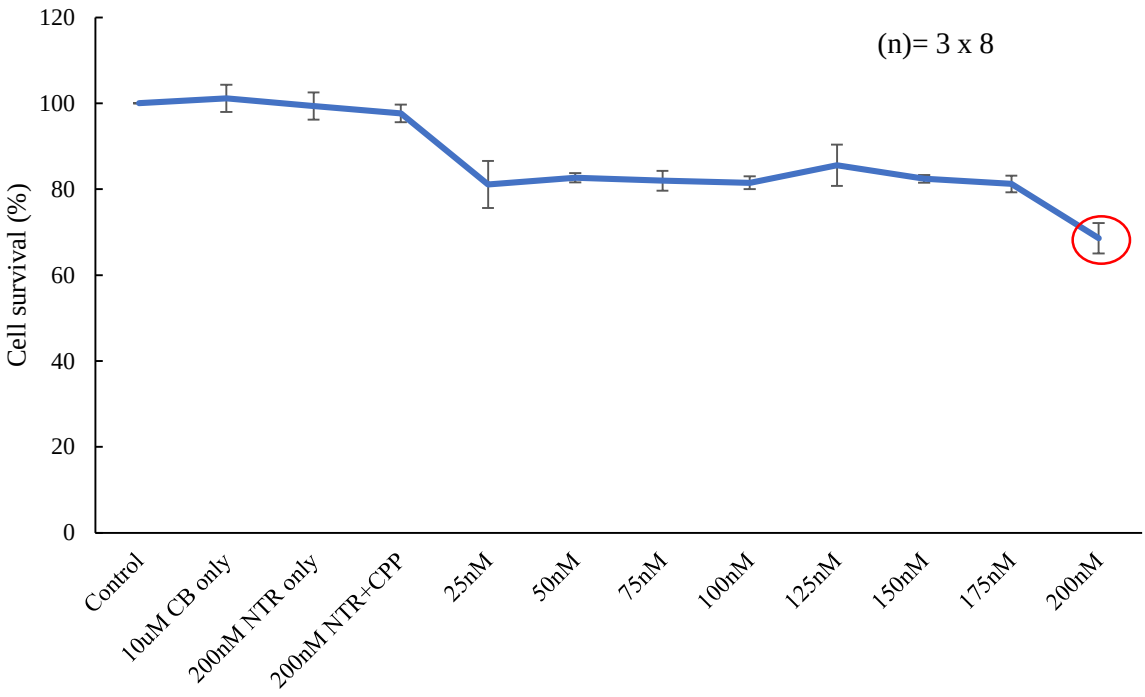

Figure 5.6. The cell viability of SK-OV-3 treated with NfnB-Cys conjugated to Pep-1 at a 1:1 ratio, at a range of 25-200 nM, with 10 µM CB1954. Control lanes of untreated SK-OV-3, 10 µM CB1954 200 nM NfnB-Cys and 200 nM NfnB-Cys:Pep-1 were also run. The NfnB-Cys:Pep-1 shows a cell survival of 68 % at 200 nM NfnB-Cys:Pep-1. Statistically significant data points are ringed in red, error bars are ± 1 standard deviation and (n) is the number of repeats each data point had.

5.2.4 Comparison of cell viability

NfnB has been examined for its ability to cause cell death with CB1954 in SK-OV-3, previously it has been reported that NfnB causes up to 100 % cell death when treated onto SK-OV-3 cells with: 50 µM CB1954 and 200 µM NAD(P)H.[15] However this cannot be directly correlated to the results presented here as excess NAD(P)H was added into wells with NfnB, which would begin the reduction of the CB1954 before uptake into cells, whereas this work with NfnB-Cys exclusively looks at cell death caused after cellular uptake.

When comparing the cell viability of NfnB-Cys with both NfnB-Cys:CPP conjugates, it is of note that both NfnB-Cys:CPP conjugates show an increase in the cell death caused across the concentration range of tested nitroreductase, with the NfnB-Cys:HR9 conjugate showing the most improvement in cell death caused. This result is interesting when compared back to the kinetic data presented in section 3.6, the kinetic data indicated that the enzymatic catalytic efficiency for NfnB-Cys:HR9 and NfnB-Cys:Pep-1 had decreased by 75 % and 66 % respectively. This would indicate that the NfnB-Cys:CPP conjugates should show a decreased cell kill, however this increased cell kill gives an indication that when conjugated to CPPs the

NfnB-Cys does have an increased cellular uptake than unconjugated NfnB-Cys. Figure 5.7 is a side-by-side presentation of the cell viability data for NfnB-Cys and the NfnB-Cys:CPP conjugates.

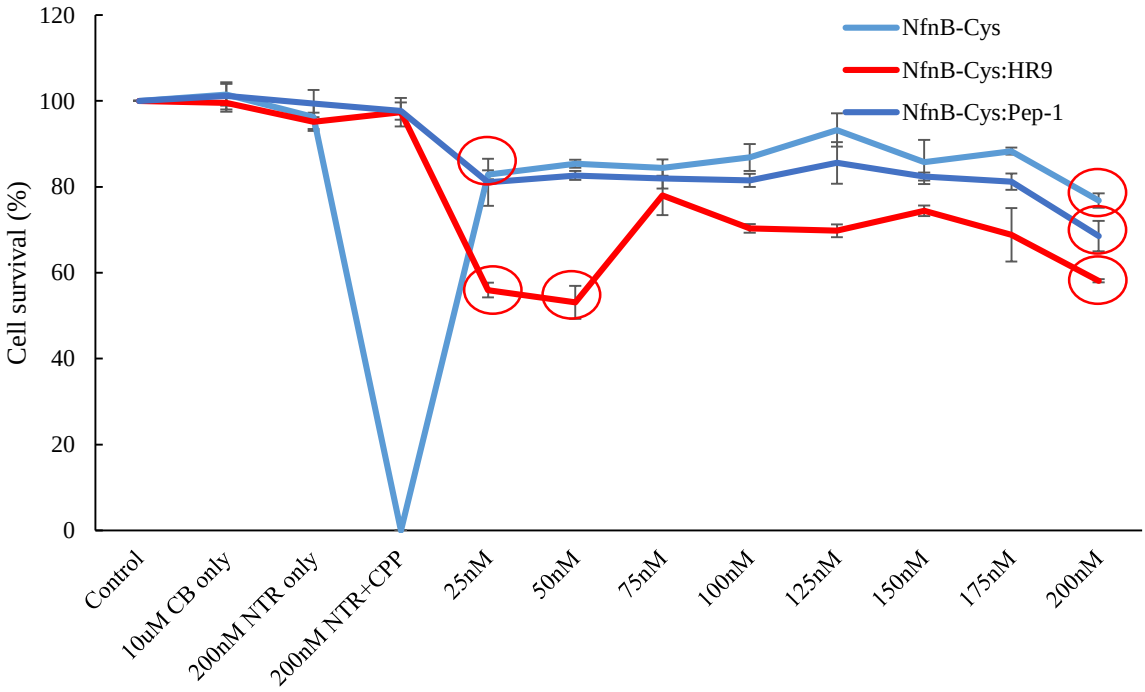

Figure 5.7. A comparison of the cell viability of cells treated with 10 uM CB1954 and either: NfnB-Cys, NfnB-Cys:HR9 or NfnB-Cys:Pep-1. The cells treated with NfnB-Cys:HR9 show a major decrease in cell viability compared to NfnB-Cys than the cells treated with NfnB-Cys:Pep-1. This would indicate that for NfnB-Cys, HR9 is able to uptake a larger number of NfnB-Cys enzymes than Pep-1. The NfnB-Cys:HR9 control lane shows the same minimal toxicity as NfnB-Cys:Pep-1. Statistically significant data points are ringed in red.

5.3 YfkO-Cys toxicity

After establishing the cell viability of SK-OV-3 treated with NfnB-Cys and NfnB-Cys:CPP conjugates had been established, cell viability assays could be performed with YfkO-Cys, a different nitroreductase, for a comparison of the 2 enzymes behaviour in cell culture, both free and conjugated with HR9 and Pep-1.

5.3.1 Unconjugated YfkO-Cys

The cell viability data for YfkO-Cys is presented in Figure 5.8. Here as with NfnB-Cys the enzyme on its own at 200 nM shows no toxicity to SK-OV-3 cells, with the concentration range of 25-200 nM YfkO-Cys causing cell death with 10 uM CB1954. As a comparison point again the cell viability at 200 nM YfkO-Cys will be a reference point for other cell viability experiments. Here the cell viability at 200 nM YfkO-Cys is 64 %, a 12 % decrease from NfnB-

Cys. This is expected based on the HPLC and kinetic data, the HPLC shows that the YfkO-Cys produces almost 100 % of the 4-NHOH (*the DNA crosslinking product*) and the kinetic profile has an enzymatic efficiency over 4 times greater than NfnB-Cys, both of these together should lead to an increased cell kill, which is observed in Figure 5.8.

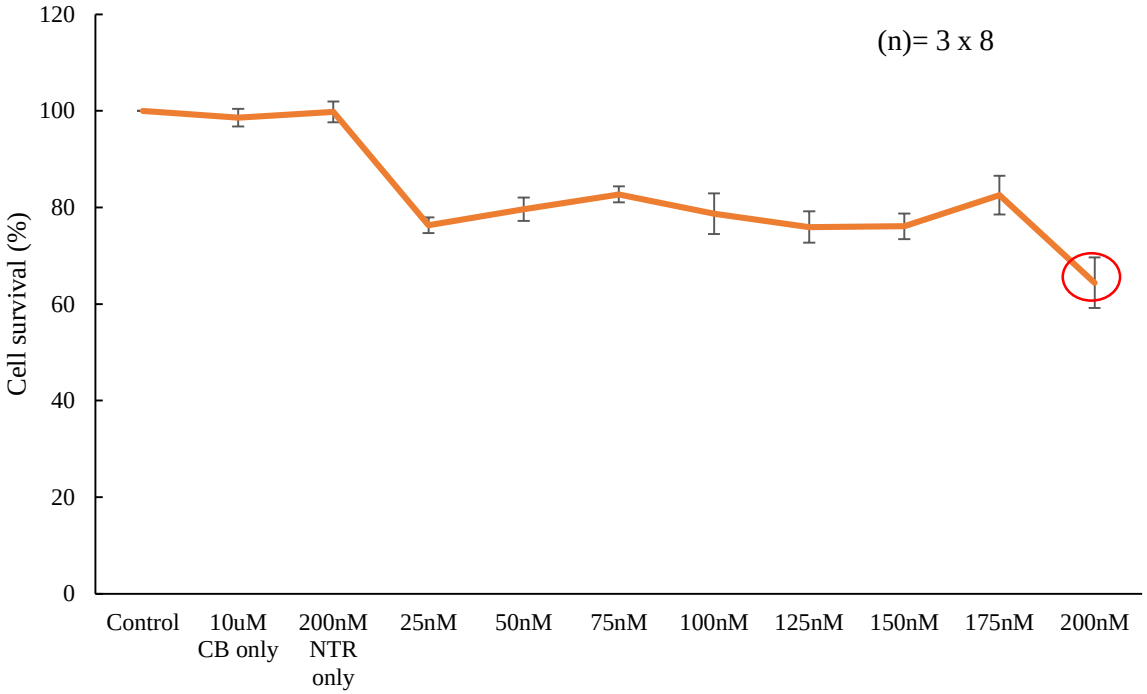

Figure 5.8. The cell viability of SK-OV-3 treated with YfkO-Cys up to 200 nM and 10 µM CB1954, control lanes were also run with untreated SK-OV-3, 10 µM CB1954 and 200 nM YfkO-Cys. At 200 nM NfnB-Cys, the SK-OV-3 has a 64 % cell survival rate. Statistically significant data points are ringed in red, error bars are ± 1 standard deviation and (n) is the number of repeats each data point had.

5.3.2 YfkO-Cys conjugated with HR9

Figure 5.9 is the cell viability data obtained for the YfkO-Cys:HR9 cell viability assay. Similarly to YfkO-Cys the YfkO-Cys:HR9 conjugate shows minimal toxicity to Sk-OV-3 at 200 nM, with increasing toxicity shown towards the cells when treated with both YfkO-Cys:HR9 and CB1954. All the treatment concentrations of YfkO-Cys:HR9 show a marked improvement on the cells treated with just YfkO-Cys in Figure 5.8. Most notably the YfkO-Cys:HR9 shows a cell survival of 55 % at 200 nM, which is a 9 % increase in cell death from the unconjugated YfkO-Cys. Since the control cells show no marked increase in cell death over the unconjugated YfkO-Cys, this increase in cell death could be attributed to the CPP enabling an increase in the amount of YfkO-Cys able to penetrate into the cells.

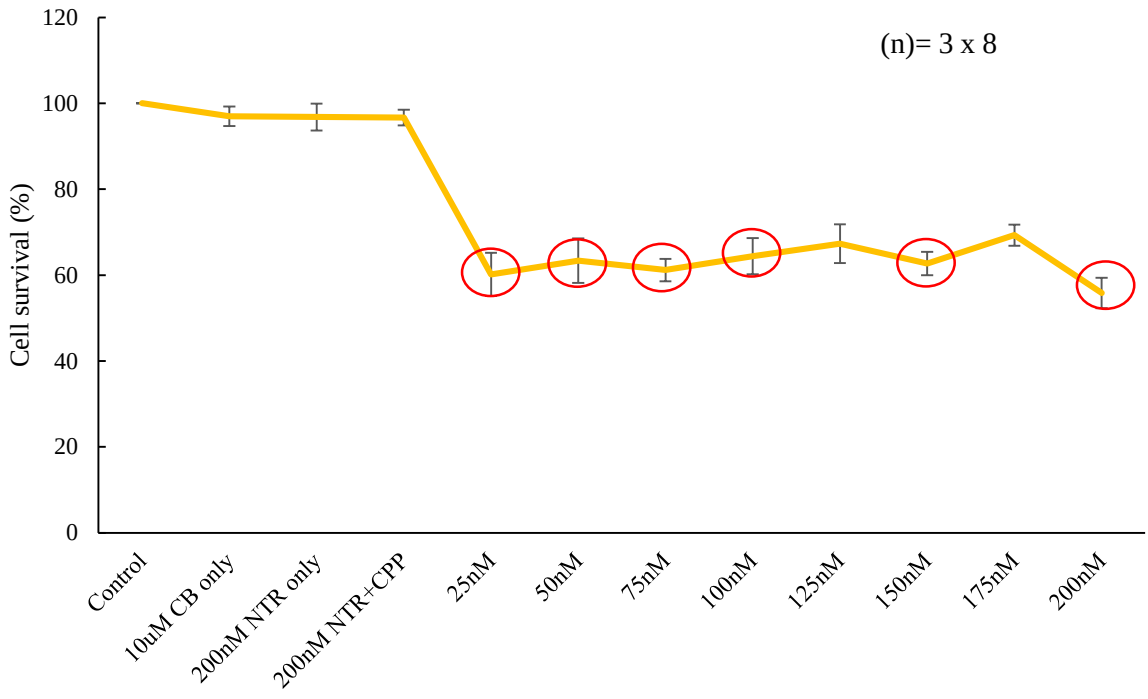

Figure 5.9. The cell viability of SK-OV-3 treated with YfkO-Cys conjugated to HR9 at a 1:1 ratio, at a range of 25-200 nM, with 10 µM CB1954. Control lanes of untreated SK-OV-3, 10 µM CB1954 200 nM NfnB-Cys and 200 nM YfkO-Cys:HR9 were also run. The YfkO-Cys:HR9 shows a cell survival of 55 % at 200 nM YfkO-Cys:HR9. Statistically significant data points are ringed in red, error bars are ± 1 standard deviation and (n) is the number of repeats each data point had.

5.3.3 YfkO-Cys conjugated with Pep-1

The YfkO-Cys:Pep-1 cell viability assay data is presented in Figure 5.10, here as with the YfkO-Cys:HR9 treatment samples presented in Figure 5.9 there is an improvement in the cell kill caused by the conjugate. Initially the data would indicate that at 200 nM YfkO-Cys:Pep-1 and 10 µM CB1954, there is a 51 % cell survival rate, however the YfkO-Cys:Pep-1 control lane does show a 6 % increase in toxicity towards the cells than the YfkO-Cys control lane on its own. Taking this into account and adjusting for this toxicity, the cell death caused by the CB1954 reduction products becomes 57 %, which has a 2 % higher cell survival rate than YfkO-Cys:HR9. Despite this toxicity shown by the YfkO-Cys:Pep01 conjugate there is an improvement over the unconjugated YfkO-Cys.

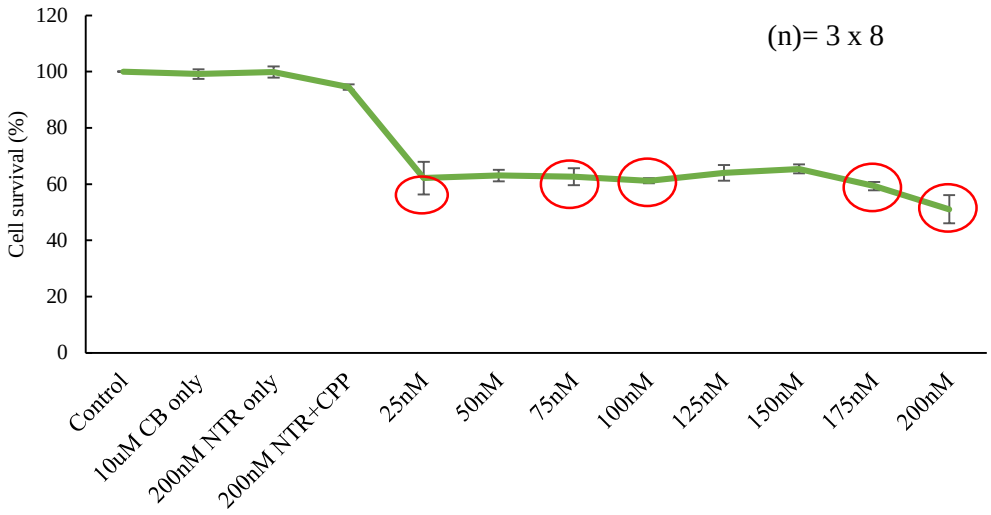

Figure 5.10. The cell viability of SK-OV-3 treated with YfkO-Cys conjugated to Pep-1 at a 1:1 ratio, at a range of 25-200 nM, with 10 µM CB1954. Control lanes of untreated SK-OV-3, 10 µM CB1954 200 nM YfkO-Cys and 200 nM YfkO-Cys:Pep-1 were also run. The NfnB-Cys:Pep-1 shows a cell survival of 51 % at 200 nM NfnB-Cys:Pep-1. Statistically significant data points are ringed in red, error bars are ± 1 standard deviation and (n) is the number of repeats each data point had.

5.3.4 Comparison of cell viability

Figure 5.11 is a side-by-side comparison of the YfkO-Cys, YfkO-Cys:HR9 and YfkO-Cys:Pep-1 cell viability assay data.

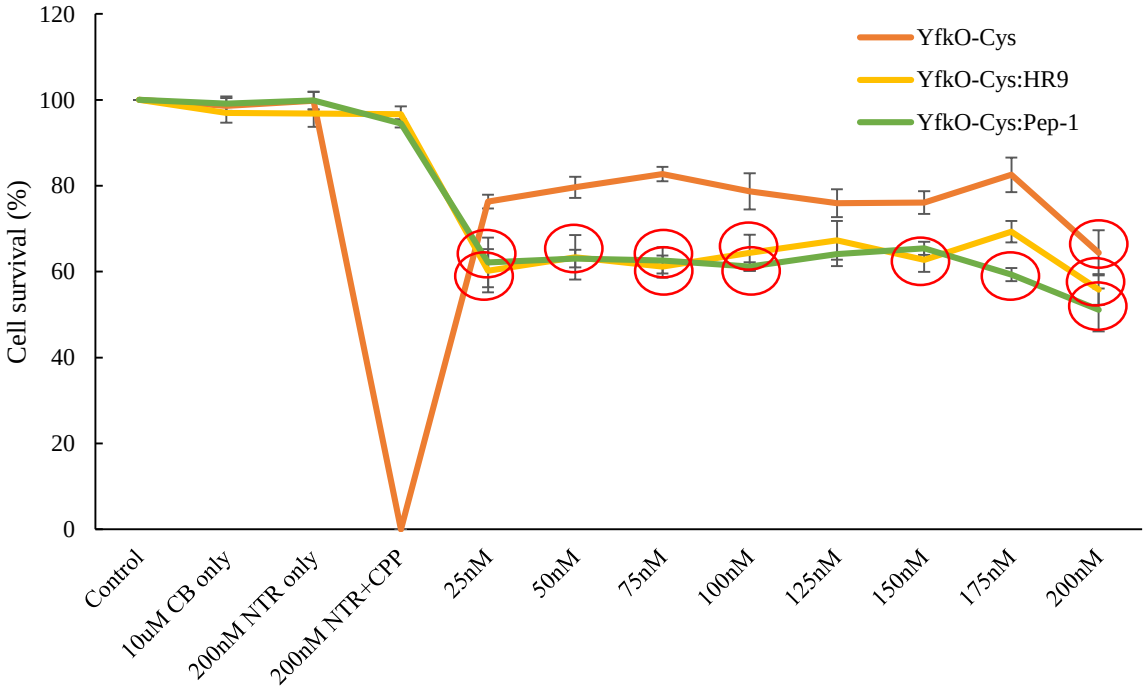

Figure 5.11. A comparison of the cell viability of cells treated with 10 µM Cb1954 and either: YfkO-Cys, YfkO-Cys:HR9 or YfkO-Cys:Pep-1. The cells treated with YfkO-Cys:HR9 and YfkO-Cys:Pep-1 both show a decreased cell survival rate, with the Pep-1 conjugate having 5 % decreased cell survival than the HR9 conjugated. This would indicate that Pep-1 is the better CPP to use for the uptake of YfkO-Cys. Statistically significant data points are ringed in red.

Both CPP conjugates show a decrease in cell viability from unconjugated YfkO-Cys, of 9 % and 13 % for YfkO-Cys:HR9 and YfkO-Cys:Pep-1 respectively. However as mentioned, the Pep-1 conjugate does show toxicity towards SK-OV-3, so when the data is adjusted the YfkO-Cys:Pep-1 conjugate has a 7 % increase is toxicity from unconjugated YfkO-Cys. Despite this, the fact the both CPPs still present an overall increase in cell death indicates that they are successfully increasing the overall cellular uptake of YfkO-Cys.

5.4 Nanoparticles in cell culture

For the past 20 years or so nanoparticles have been introduced into various medical applications, such as TiO_2 nanoparticles as a UV protection layer in sunscreen,[19,20] to Fe_3O_4 nanoparticles in medical imaging.[21] Gold nanoparticles have been explored for their many possible medical applications, from hyperthermia treatments,[22–24] to imaging,[25–29] and as carriers for therapeutic moieties.[30–33] Gold nanoparticles are of interest particularly due to the low biological interactions gold has with the body.[34,35] The coating of various nanomaterials with a gold shell has also been widely examined,[36–40] with many articles detailing different molecules and chemicals that can be conjugated onto gold nanoparticles for use in medicinal treatments.[31,32,41,42] Gold coated iron oxide superparamagnetic nanoparticles have been examined for their applications as a targeted magnetic drug carrier, with promise being shown for their use. [43–47]

Whilst the MTT assay can be used for our nitroreductases, it is possible that the excess iron in the AuMNPs may interact with MTT and cause excess production of the formazan crystals giving a bias in the data.[48,49] A brief experiment involving the addition of AuMNPs to cells does show a bias in the production of excess formazan crystals, this bias can be seen in Figure 5.12 where the 3 right hand lanes show a much paler purple than the rest of the wells, these 3 paler lanes were the control lanes which were seeded at 1000 cells per well of SK-OV-3 cells and treated with growth media only. Whilst the much darker coloured wells were all treated with AuMNPs, with the darker colouration indicating an excess production of formazan crystals, most probably caused by the excess iron in the solution.

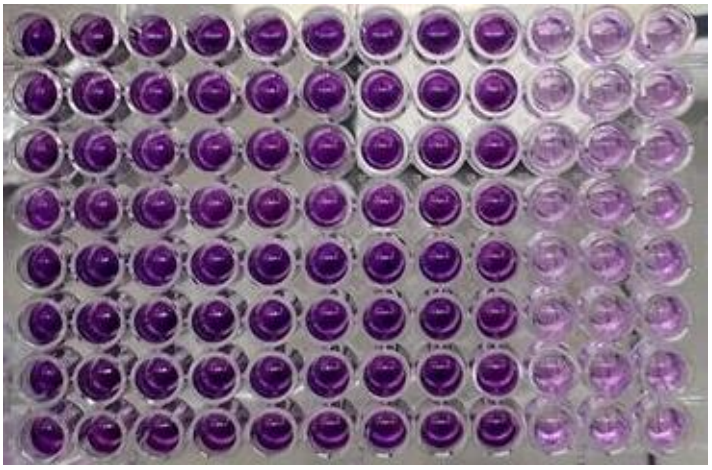

Figure 5.12. A picture of cells treated with AuMNPs, then further treated with MTT, 3 lanes on the right are cells treated only with culture media, the other lanes were all treated with AuMNPs which have cross reacted with the MTT causing an excess production of formazan crystals.

Due to this interaction of the excess iron with MTT, a different method needs to be employed to determine cell viability, one such method is the Calcein assay, which uses cellular esterases to reduce non-fluorescent Calcein-AM into Calcein which is fluorescent, with an excitation/ emission bandwidth of 495/515 nm.[50] The reduction of Calcein AM into Calcein is shown in Figure 5.13.

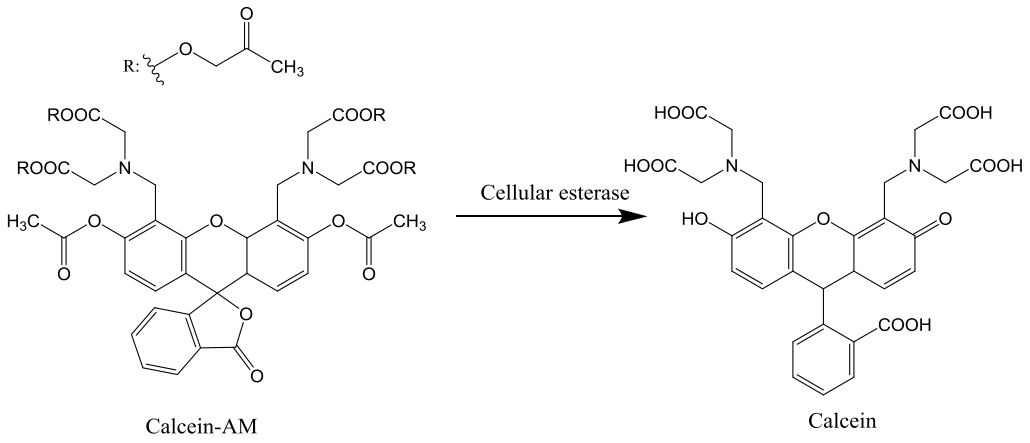

Figure 5.13. The reduction of Calcein-AM into the fluorescent Calcein by cellular esterases.

The aim of the experiments presented here is to prove conjugation of NfnB-Cys onto gold nanoparticles and AuMNPs at a ratio of 1:270.[51] This will be followed by subsequent enzymatic activity assays of the conjugates. The conjugates will then be tested in cell culture for their ability to reduce the CB1954 prodrug and to assess any toxicity they present towards the cells. Finally the CPP HR9 will be conjugated onto the AuNP:NfnB-Cys and AuMNP:NfnB-Cys conjugates at a ratio of 1:270:1, these conjugates will again be tested in cell culture for their ability to reduce CB1954 in cells causing cell death. Finally, Darkfield microscopy will be

performed on a variety of nanoparticle:enzyme:CPP conjugates to assess if the nanoparticles are internalized into the cells. The AuMNP synthesis has a low yield, meaning there was no excess of AuMNPs to repeat experiments if needs be, due to this AuNPs were used in experiments initially, as an indication of how the AuMNPs might behave before they were used. Also due to the nature of the AuMNPs being difficult to manufacture in bulk, only NfnB-Cys and the CPP were examined in conjunction with the AuMNPs.

5.5 Conjugation of NfnB-Cys with nanoparticles

Gwenin *et al.* have previously reported on the ability of NfnB-Cys to conjugate to the surface of gold spherical nanoparticles at various ratios,[51] with Au-S bonds having a bond dissociation energy of 298 ±2 KJ mol^{-1},[52] making the gold coating an ideal carrier material for the nitroreductases. Conjugation of NfnB-Cys onto the surface of gold nanoparticles involves adding NfnB-Cys to gold colloid at a ratio of 1 gold nanoparticle:270 enzymes and leaving the sample at 4 ˚C for 24 hours to allow the surface of the gold to be coated with NfnB-Cys.[53] UV-vis spectroscopy can be used to look for a successful conjugation in a sample of gold nanoparticles. As previously mentioned the λ-max of the gold peak on a UV-Vis spectrum directly relates to the size of the nanoparticle[54] and, as the size of the nanoparticle increases, the λ-max of the gold peak also increases in wavelength.[54] Therefore when conjugating NfnB-Cys onto the outside of a gold nanoparticle, the size/ diameter of the nanoparticle technically increases, which causes the λ-max of the gold peak to increase.[51] This increase in wavelength is known as red-shift, which here indicates a change in the dielectric constant of the particles surface.[55] When conjugating NfnB-Cys onto gold nanoparticles, red-shift is looked for to confirm successful conjugation.[51]

5.5.1 AuNPs

AuNPs were conjugated with NfnB-Cys at a ratio of 1:270, a UV-Vis spectrum was obtained of the nanoparticles before and after conjugation to look for a change in the λ-max of the gold peak, indicating successful conjugation. Figure 5.14 is an overlay of the UV-vis spectra obtained before and after conjugation, the blue line represents the AuNPs before conjugation with a λ-max of 518 nm, the orange line is the AuNP:NfnB-Cys conjugate, with the λ-max of the gold peak being 524 nm, an increase of 6 nm. This increase indicates successful conjugation of the NfnB-Cys onto the AuNPs.

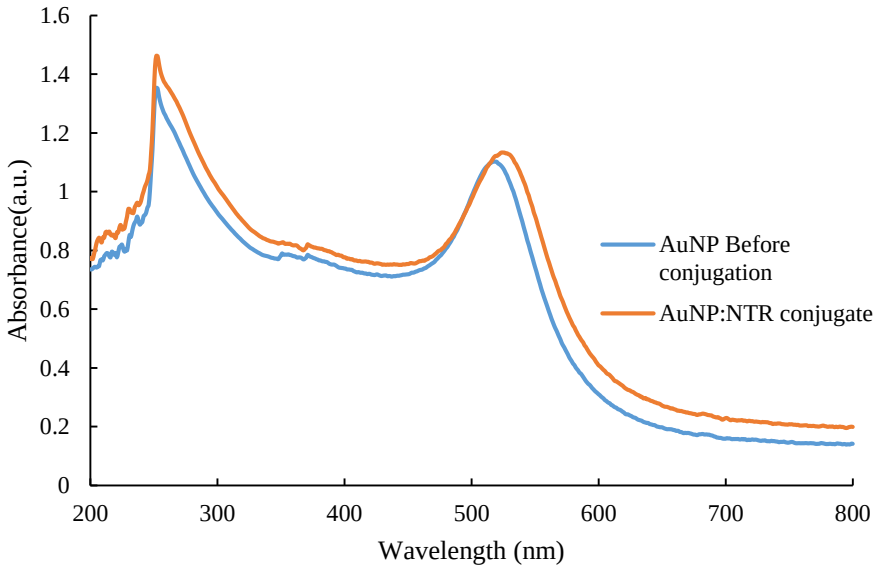

*Figure 5.14 The overlay of the UV-vis spectra obtained for the conjugation of NfnB-Cys with AuNPs, the λ-max of the gold peak shifts by 6 nm from 518 nm before (**blue line**) to 524 nm after conjugation (**orange line**). This increase in λ-max of the gold peak indicates a successful conjugation of the NfnB-cys onto the AuNPs.*

5.5.2 AuNP:NfnB-Cys enzymatic activity

After conjugation of the NfnB-Cys onto the surface of the AuNPs was confirmed, the samples had to be assessed by UV-vis for their ability to still reduce the CB1954 prodrug to ensure that the orientation of the NfnB-Cys molecules was correct in the monolayer, leaving the active sites of the enzymes exposed.[53] This was done as described previously in section 4.2. To a reference cuvette was added; AuNP:NfnB-Cys (*25 µg/ml*) NADH (*15 µl, 20 mM*), DMSO (*10 µl*) and made up to 1 ml with phosphate buffer (*50 mM, pH 7.4*). A sample cuvette was made up in exactly the same manner, except no DMSO was added and the total volume was made up to 980 µl with phosphate buffer instead of 1 ml. A full wavelength scan (*200-800 nm*) was performed of the sample cuvette against the reference cuvette to establish a baseline of the reaction, after which CB1954 (*10 µl, 10mM*) was added to the sample cuvette. The sample cuvette then had a full wavelength scan (*200 800 nm*) performed every 90 seconds for 45 minutes to examine the reaction. As before, a drop at 340 nm and increase at 420 nm was looked for the NADH being consumed[10,53] and hydroxylamine products being formed,[11,56] respectively. Figure 5.15 is the UV-Vis spectrum of the activity scan performed on the AuNP:NfnB-Cys conjugate.

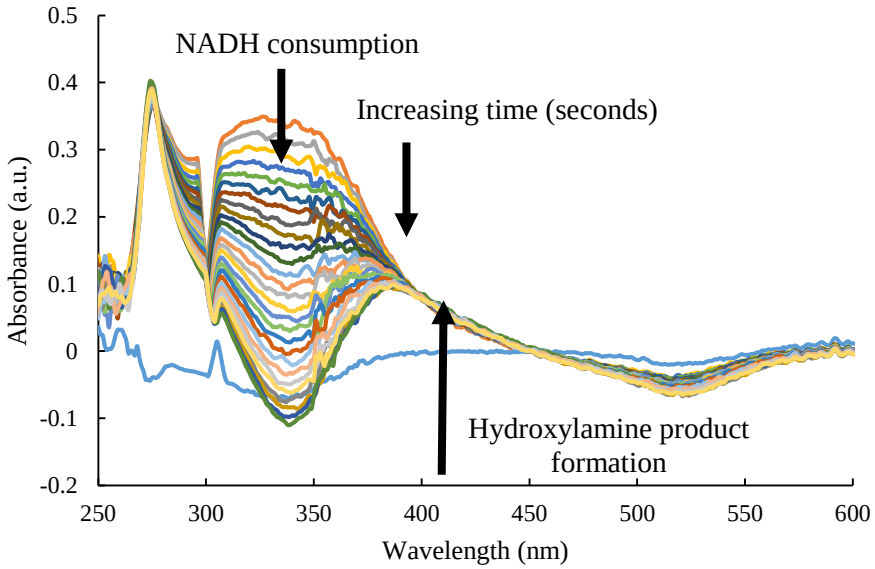

Figure 5.15. Here is presented the spectra for the enzymatic activity assay performed on the AuNP:NfnB-Cys conjugate. As can be observed over increasing time there is a decrease in the absorbance at 340 nm, which indicates the consumption of NADH. There is also an increase at 420 nm, however this is masked by an artefact on the spectra at around 520 nm, possibly cause by the gold nanoparticles local environment changing in the sample cuvette during the reaction.

The drop in absorbance at 340 nm shown in the figure is the NADH being consumed for the reduction of the CB1954 prodrug, to produce the hydroxylamine products with absorption at 420 nm.[11,56] The increase in absorbance at 420 nm cannot be viewed due to an artefact at around 520 nm causing the spectra to drop to a negative absorbance which is masking the increase at 420 nm. This location of the artefact on the spectrum would lead to a conclusion that it is caused by the gold nanoparticles and are experiencing a change in their environment slightly, causing the drop in absorbance compared to the reference sample. This change in environment could be to do with the enzyme reducing the prodrug, leaving NAD+ and hydroxylamine in the local environment to the nanoparticles.

5.5.3 AuMNPs

After being able to show conjugation of NfnB-Cys onto AuNPs, conjugation needed to be shown onto AuMNPs. Conjugation was carried out onto AuMNPs at a ratio of 1:1080, this increased ratio is due to the size of the AuMNPs being bigger than the AuMNPs previously used. Since their size is increased, so too has the available surface area, so in order to achieve a full monolayer a higher ratio is required, which has been calculated based on the number of NfnB-Cys molecules/surface area on the AuNPs and translated over to the AuMNPs. The conjugation was performed by mixing AuMNPs with a determined volume and concentration

of NfnB-Cys in order achieve a full monolayer. This mixture was placed at 4 °C over night to allow binding to the nanoparticle surface. UV-vis was performed on the nanoparticles before and after conjugation, Figure 5.16 is an overlay of these scans.

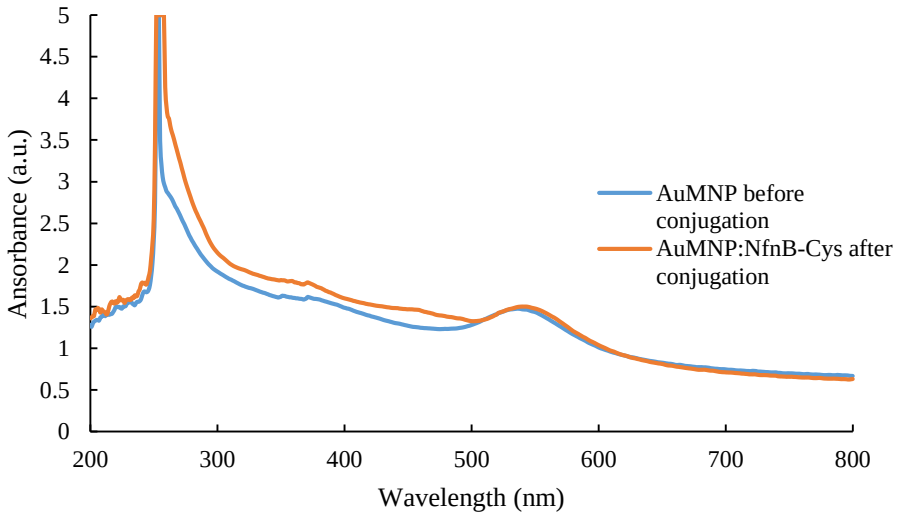

*Figure 5.16. The overlay of the UV-vis spectra obtained for the conjugation of NfnB-Cys with AuMNPs, the λ-max of the gold peak shifts by 5 nm from 536 nm before (**blue line**) to 540 nm after conjugation (**orange line**). This increase in λ-max of the gold peak indicates a successful conjugation of the NfnB-Cys onto the AuMNPs.*

The initial scan before conjugation (*blue line*) gold peak has a λ-max of 536 nm, after conjugation (*orange line*) the gold peak of the sample has a λ-max of 540 nm. This red-shift once again indicates successful conjugation of the NfnB-Cys molecules onto the surface of the AuMNPs.

5.5.4 AuMNP:NfnB-Cys enzymatic activity

The sample which showed successful conjugation of NfnB-Cys onto AuMNPs must be assessed for the ability of the enzyme to still reduce the CB1954 prodrug. This was done as before in section 4.2; to a reference cuvette was added; AuMNP:NfnB-Cys (*25 µg/ml*) NADH (*15 µl, 20 mM*), DMSO (*10 µl*) and made up to 1 ml with phosphate buffer (*50 mM, pH 7.4*). A sample cuvette was made up in exactly the same manner, except no DMSO was added and the total volume was made up to 980 µl. A full wavelength scan (*200-800 nm*) was performed of the sample cuvette against the reference cuvette to establish a baseline of the reaction, after which CB1954 (*10 µl, 10mM*) was added to the sample cuvette. A full wavelength scan (200 800 nm) was performed every 90 seconds for 45 minutes to examine the reaction. As before a drop in 340 nm and increase at 420 nm indicated the NADH being consumed[10,53] and hydroxylamine products being formed,[11,56] respectively. Figure 5.17 is the UV-vis spectra of the enzymatic activity assay performed on the AuMNP:NfnB-Cys conjugate.

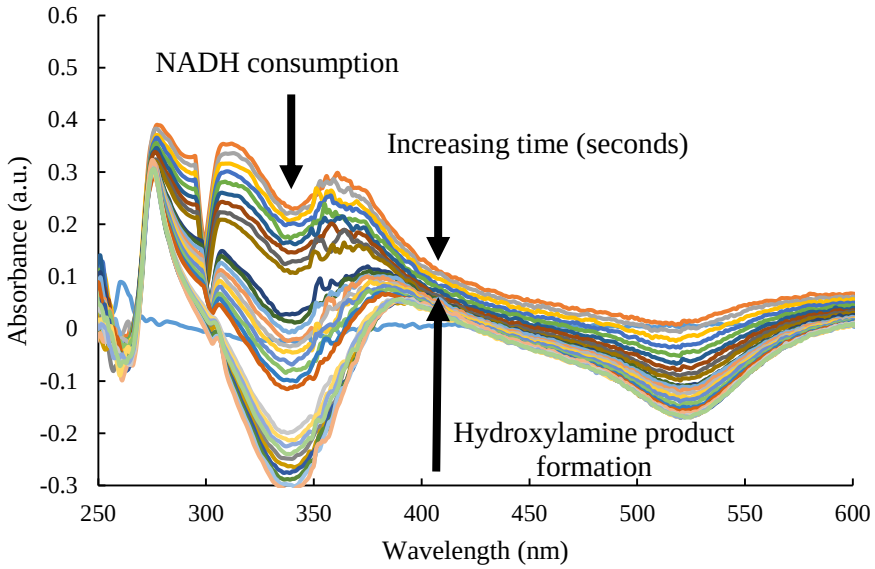

Figure 5.17. The UV-vis spectra of the enzymatic activity assay of the AuMNP:NfnB-Cys conjugate. Here there is a decrease in absorbance at 340 nm over time, indicating the consumption of NADH. Once again, there is an artefact on the UV-vis spectra at around 520 nm, which is masking the hydroxylamine absorbance and is probably caused by the change in environment surrounding the AuMNPs.

The UV-vis spectra of the AuMNP:NfnB-Cys activity assay shows similar features to the AuNP:NfnB-Cys activity spectra. Firstly, there is a drop in absorbance at 340 nm indicating a consumption of the NADH. At 420 nm there should be an increasing absorbance which correlates to the production of the hydroxylamine product, however instead there is a decrease. There is however, once again an artefact at around 520 nm, which would indicate a change in the environment surrounding the AuMNPs, this artefact is masking the increase at 420 nm. If there were no increasing absorbance at 420 nm the decrease in absorbance would be linear with the decrease in absorbance at around 520 nm, as it is the decrease in absorbance is not a linear decrease, indicating that the hydroxylamine is absorbing at 420 nm but the artefact of the gold AuMNPs is masking the hydroxylamine absorbance.

Following the conjugation and activity assays of both AuNPs and AuMNPs with NfnB-Cys, the conjugates were examined in cell culture for their ability to cause cell death by the reduction of CB1954.

5.6 AuNP cell viability assays

Gold nanoparticles have been explored by many different research groups in many different ways for how they can be applied in therapeutics.[31,32,57–61] Here they will be assessed for their ability to carry NfnB-Cys into a cell and the subsequent enzymatic reduction of the CB1954 prodrug by the NfnB-Cys conjugated onto the nanoparticles. The CPP HR9 will also be

conjugated onto a sample of AuNP:NfnB-Cys at a ratio of 1:270:1 *(AuNP:NfnB-Cys:HR9)* to examine if the CPP is able to aid in increasing the uptake of AuNP:NfnB-Cys and therefore have more enzymes within the cells to reduce CB1954 and cause an increased cell death. This initial cell culture data should indicate how the AuMNPs might behave when they are subjected to cell culture conditions.

5.6.1 Gold nanoparticles

Whilst it would be preferential to know if the gold nanoparticles present any toxicity towards SK-OV-3 cells, when added into DMEM, the nanoparticles will immediately aggregate and change in colour from red to blue, rending them unusable for testing toxicity. Figure 5.18 is a picture of gold nanoparticles and gold nanoparticles that have been mixed with DMEM. The colour change from red to blue is associated with nanoparticle aggregation.

*Figure 5.18. A picture of 'naked' gold nanoparticles (**left**) and DMEM added to gold nanoparticles (**right**). The right hand photo shows that the nanoparticles have aggregated, as seem by the blue colouration and particulates in the bottom of the tube.*

5.6.2 AuNP:NfnB-Cys

The cell viability assay was performed with AuNP:NfnB-Cys using SK-OV-3 cells. As mentioned the AuMNPs are difficult to produce in bulk, due to this the number of concentration samples was reduced to 4: 25, 50, 100 and 200 nM to ensure that the range of concentrations was consistent with the previously performed cell culture experiments. Since AuNPs were being used before the AuMNPs, this reduction in total number of concentrations was also done here.

To perform AuNP:NfnB-Cys Calcein cell viability assays; SK-OV-3 cells were seeded into a 96-well plate (*Corning, USA*) at a density of 1 x 10^4 cells per well, in 100 µl DMEM containing 10 % FBS, 1 % L-glutamine and 1 % penicillin-streptomycin and were allowed to attach to the

plate overnight in a CO_2 (*5 %*) incubator overnight at 37 °C. After 16 hrs, the media was carefully aspirated off and fresh media containing increasing concentrations from 25 nM to 200 nM of AuNP:NfnB-Cys (*50 µl*) was added to the wells with CB1954 (*50 µl, 20 µM*) along with wells only containing AuNP:NfnB-Cys (*200 nM*), CB1954 (*100 µl, 10 µM*), dH_2O (*100µl*) or DMEM (*100 µl*) as controls. A water control was used as the AuNPs are bought in a very weak stabilizing agent that is dissolved in water, which may show some toxicity to the SK-OV-3. After a 4hr incubation in a CO_2 (*5 %*) incubator at 37 °C, the treatment media was carefully aspirated off and fresh media (*100 µl*) was added. The cells were left for 48 hrs in a CO_2 (*5 %*) incubator at 37 °C, after which the media was carefully aspirated off and 1x Calcein DW buffer (*100 µl*) was added to each well. This was again carefully aspirated off after which 1x Calcein DW buffer (*50 µl*) was added along with 2x Calcein AM (*50 µl*).The plate was then incubated for 30 minutes in a CO_2 (*5 %*) incubator at 37 °C. The fluorescence of the sample was measured using an excitation/emission filter of 495/515 nm using a Thermoscientific Varioskan Flash plate reader. All cell culture data presented in this chapter was carried out using this protocol.

The cell culture data obtained for AuNP:NfnB-Cys conjugate is presented in Figure 5.19, here the 200 nM AuNP:NfnB-Cys control shows some minor toxicity at less than 2 %, around what can be seen with unconjugated enzymes, the water control also shows no toxicity, indicating that the minor toxicity for the 200 nM AuNP:NfnB-Cys control is related to the enzyme. The 25 -200 nM treatments show a cell survival that is somewhat comparable to unconjugated NfnB-Cys with the AuNP:NfnB-Cys presenting a cell survival of 81 % at 200 nM AuNP:NfnB-Cys: 5 % higher than the unconjugated NfnB-Cys presented at 200 nM. It is unknown however, how many nanoparticles are actually internalized into the cell, thereby it is unknown if a comparable number of NfnB-Cys molecules are in the cells as would be seen with the unconjugated NfnB-Cys. Due to not having the kinetic profiles of the AuNP:NfnB-Cys conjugates this cannot be a known factor. Further work here would be to examine the uptake of the conjugate itself.

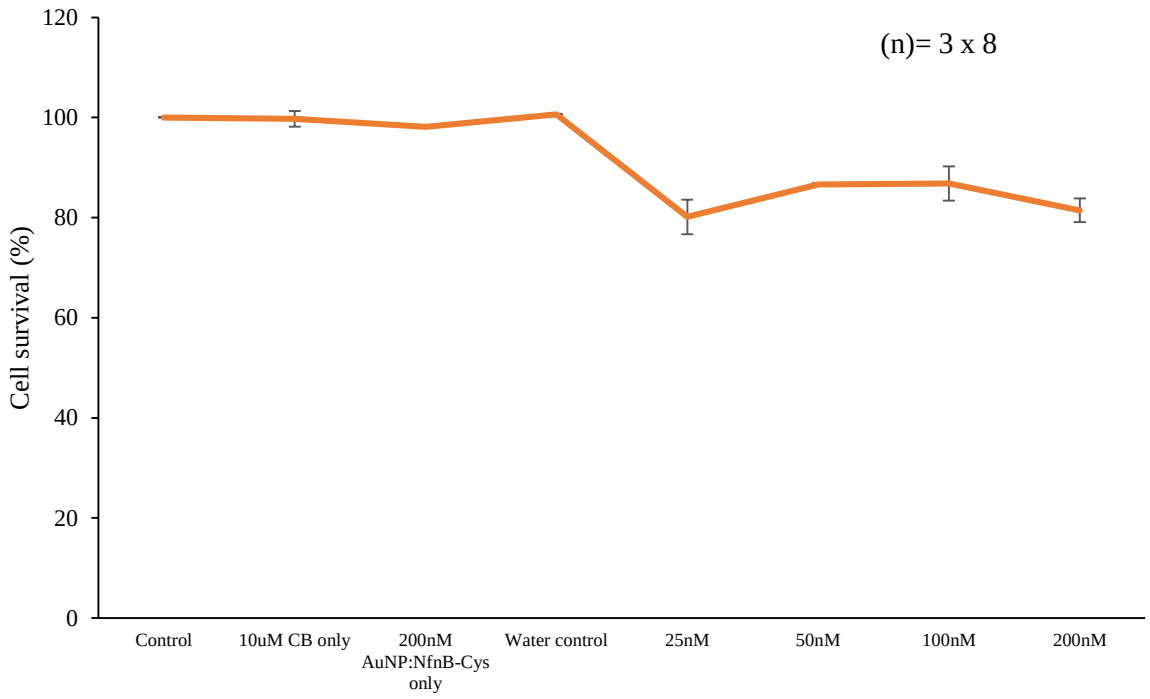

Figure 5.19. The cell culture data for the cell viability assay of the AuNP:NfnB-Cys conjugate. The conjugate on its own at 200 nM presents toxicity less than 2 %, whilst the dH_2O control shows no toxicity. The value: (n) is the number of repeats each data point had. error bars are ± 1 standard deviation, the data was shown to be statistically significant above the p-value of 0.005 however there are not enough data points to establish specific significant data points.

5.6.3 Au:NfnB-Cys:HR9

The main aim of this project is to see if CPPs can aid the uptake of a nanoparticle:enzyme conjugate, here the CPP HR9 was conjugated to an AuNP:NfnB-Cys conjugate at a ratio of 1:270:1 to create an AuNP:NfnB-Cys:HR9 conjugate. The conjugate was treated onto cells in the exact same manner and the Calcein assay was used to determine the cell survival rate at the same concentrations of AuNP:NfnB-Cys to assess for an increased cell death, an indication of increased uptake.

Figure 5.20 presents the data obtained for the AuNP:NfnB-Cys:HR9 cell viability assay. The AuNP:NfnB-Cys:HR9 conjugate presents no toxicity at 200 nM control, whilst the sample range has a decreasing cell viability with increasing concentration of AuNP:NfnB-Cys:HR9, with the 200 nM sample having a cell survival of 74 %, 7 % lower than the 200 nM sample of AuNP:NfnB-Cys and 2 % lower than the cell survival for unconjugated NfnB-Cys at 200 nM. This would indicate that a higher number of AuNP:NfnB-Cys:HR9 conjugates are entering the cells and reducing CB1954, than with the AuNP:NfnB-Cys conjugates.

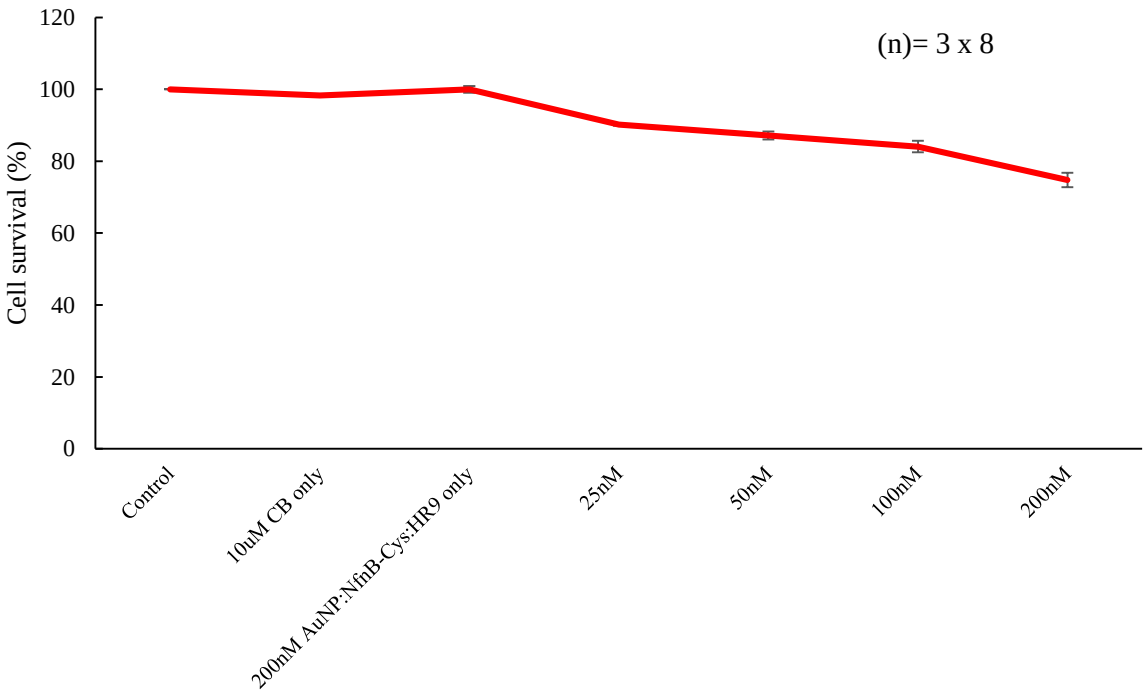

Figure 5.20 The cell culture data of the AUNP:NfnB-Cys:HR9 conjugate. Here the conjugate shows no toxicity on its own at a 200 nM control. The value: (n) is the number of repeats each data point had. error bars are ± 1 standard deviation, the data was shown to be statistically significant above the p-value of 0.005 however there are not enough data points to establish specific significant data points.

5.6.4 Comparison

Figure 5.21 is a side by side comparison of the cell kills of; NfnB-Cys, AuNP:NfnB-Cys and AuNP:NfnB-Cys-HR9, showing the percentage of cell survival in each sample at varying concentrations. The AuNP:NfnB-Cys cell kills are comparable to the free NfnB-Cys with the 200 nM AuNP:NfnB-Cys treatment having a slightly higher cell survival than NfnB-Cys, whilst the AuNP:NfnB-Cys:HR9 treatment having a decreased cell survival than both the AuNP:NfnB-Cys and free NfnB-Cys.

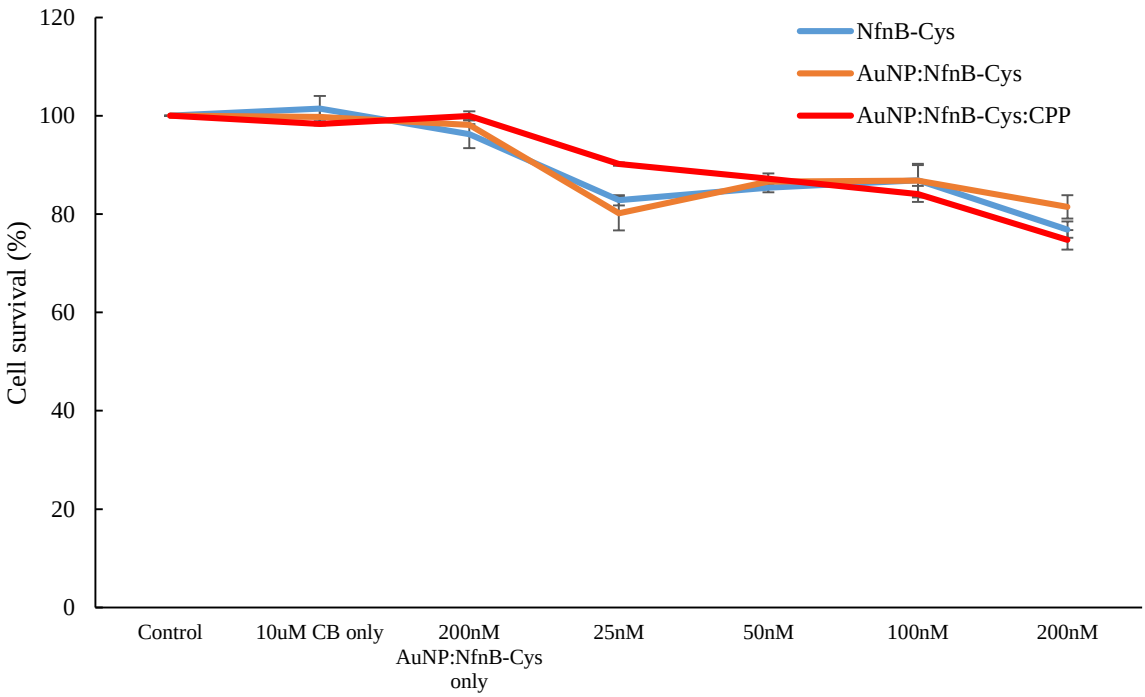

Figure 5.21. A side by side comparison of the cell kills with treatments: NfnB-Cys, AuNP:NfnB-Cys and AuNP:NfnB-Cys:HR9. The 200 nM treatment concentration for AuNP:NfnB-Cys:HR9 shows the highest cell death with a 74 % cell survival, compared to a cell survival of 77 % and 81 % for NfnB-Cys and AuNP:NfnB-Cys respectively.

5.7 AuMNP cell kills

Once it had been established how gold nanoparticles behaved in cell culture, it gives an indication of how the synthesised AuMNPs might behave under similar conditions. Here AuMNPs will be conjugated with NfnB-Cys at a ratio of 1:1080 to achieve a full monolayer covering, (*as with AuNPs*) and treated onto cells to examine its ability to reduce the prodrug CB1954 causing cell death. HR9 will then be conjugated onto the AuMNP:NfnB-Cys at a ratio of 1:1080:1 to examine if the addition of the HR9 can cause and increase cell death, indicating the HR9 increases the cellular uptake of the conjugate.

5.7.1 Gold coated iron oxide nanoparticles

Before examining the ability for the AuMNP:NfnB-Cys conjugate to cause cell death, the AuMNPs were treated onto cells at 4 concentrations at a range of 25-200 nM. The AuMNPs show no toxicity at any of the concentrations tested, indicating the AuMNPs were safe to use in terms of causing excess cell death. Figure 5.22 presents this data.

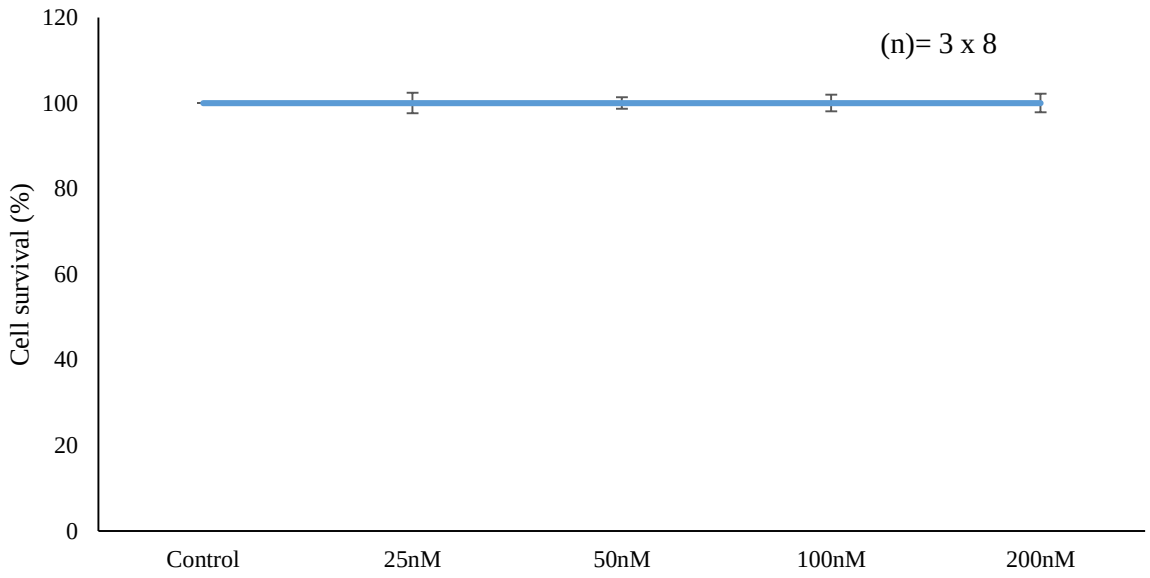

Figure 5.22. The AuMNP cell viability data presented shows that at concentrations up to and including 200 nM, the AuMNPs present no excess toxicity towards the cells. The value: (n) is the number of repeats each data point had, error bars are ± 1 standard deviation, the data was shown to be statistically significant above the p-value of 0.005 however there are not enough data points to establish specific significant data points.

5.7.2 AuMNP:NfnB-Cys

After determining the potential toxicity of the AuMNPs, NfnB-Cys was conjugated onto AuMNPs at a ratio of 1:1080, once conjugation was confirmed as presented in section 5.1.3 the conjugate was then tested in cell culture as previously described.

Figure 5.23 presents the cell viability data for the AuMNP:NfnB-Cys conjugate. The AuMNP:NfnB-Cys conjugate showed no toxicity towards the cells at a control of 200 nM, when under test with CB1954 the conjugate demonstrated a cell survival of 89 % at 25 nM, which decreased with an increasing concentration of AuMNP:NfnB-Cys up to a cell survival of 74 % at 200 nm AuMNP:NfnB-Cys. This result is the same survival rate as demonstrated with unconjugated NfnB-Cys. This gives a good basis for the ability of the AuMNP:NfnB-Cys conjugate to cause cell death and potentially shows promise for its use in MNDEPT.

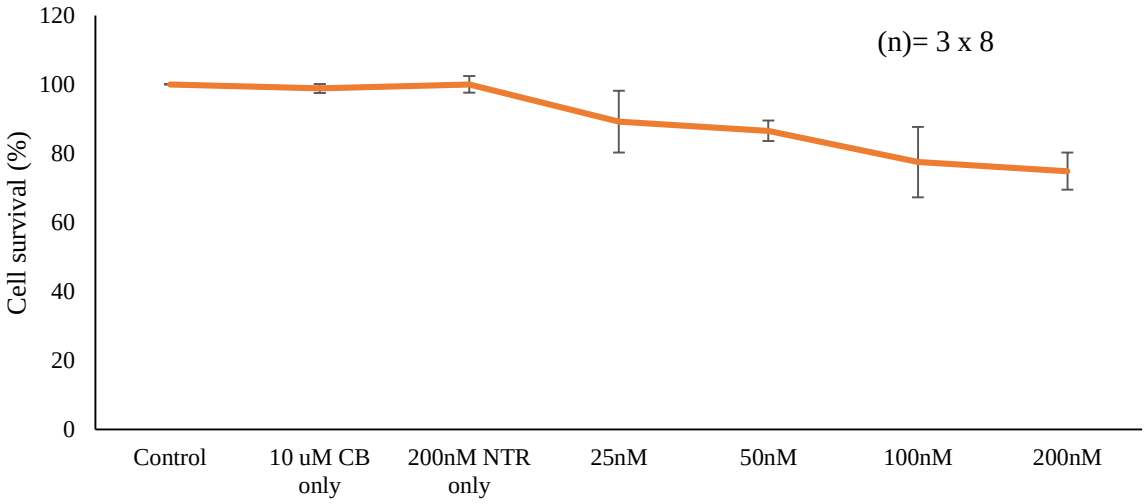

Figure 5.23. The AuMNP:NfnB-Cys cell culture data shows that with an increasing concentration of AuMNP:NfnB-Cys the cell survival rate drops from 25-200 nM, indicating an increased internalization of conjugate with increased treatment dose. This conjugate shows its potential to be used in MNDEPT. The value: (n) is the number of repeats each data point had, error bars are ± 1 standard deviation, the data was shown to be statistically significant above the p-value of 0.005 however there are not enough data points to establish specific significant data points.

5.7.3 AuMNP:NfnB-Cys:HR9

The final cell viability experiment is the conjugation of HR9 onto the AuMNP:NfnB-Cys conjugate to examine if the cellular uptake of the AuMNP:NfnB-Cys conjugate can be increased by the HR9 causing an increased cell death. As with the AuNP tests, the HR9 will be conjugated at a ratio of 1:1 compared to the nanoparticle, giving a final ratio of 1:1080:1 of AuMNP:NfnB-Cys:HR9. The AuMNP:NfnB-cys:HR9 conjugate was treated onto cells in the same manner as before and the Calcein assay was performed to determine cell viability. Figure 5.24 presents the cell viability data obtained for the treatment of AuMNP:NfnB-Cys:HR9 onto cells.

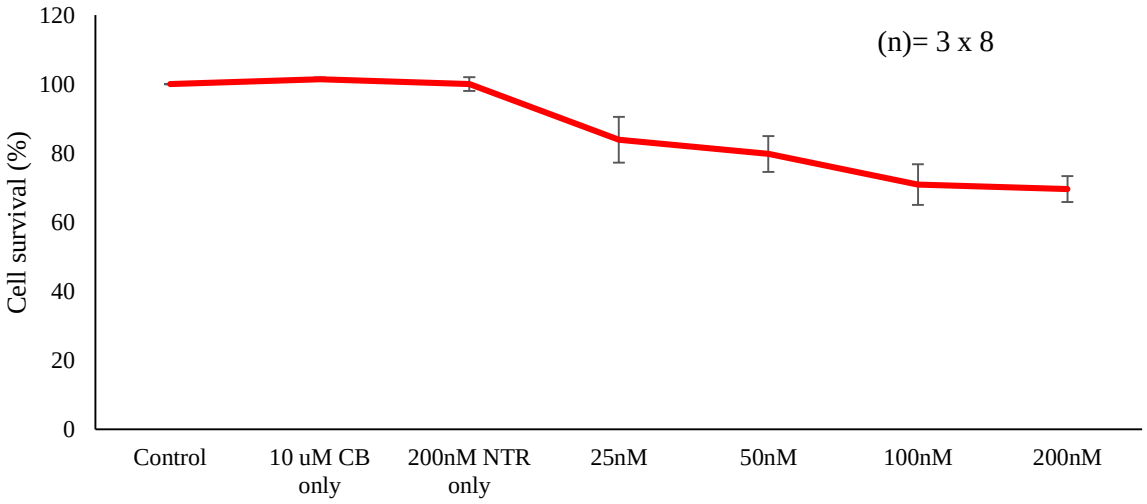

Figure 5.24. Here is presented the data obtained from the cell viability assay performed using the AuMNP:NfnB-Cyus:HR9 conjugate. The value: (n) is the number of repeats each data point had error bars are ± 1 standard deviation, the data was shown to be statistically significant above the p-value of 0.005 however there are not enough data points to establish specific significant data points.

Again the 200 nM AuMNP:NfnB-Cys:HR9 control shows no toxicity towards the cells, with the concentrations under test following the same trend as before with and increasing sample concentration resulting in a decreasing cell viability. The cell survival at 25 nM is 83 %, dropping to 69 % at 200 nM AuMNP:NfnB-Cys:HR9. This is a 5 % increase in cell death caused by an increased uptake from conjugating the HR9 onto the AuMNP:NfnB-Cys conjugate.

5.7.4 Comparison

The cell culture data for the treatments of; AuMNP, AuMNP:NfnB-Cys and AuMNP:NfnB-cys:HR9 are presented side by side in Figure 5.25 for a comparison of the ability of each treatment to cause cell death. The data indicates that the AuMNP:NfnB-Cys:HR9 treatment causes the highest cell kill, with a 69 % cell survival, whilst the AuMNP:NfnB-Cys had a 74 % cell survival rate, almost on par with the 76 % of NfnB-Cys. The addition of the CPP onto the conjugate causes a 5 % increase in cell death at 200 nM treatment concentration.

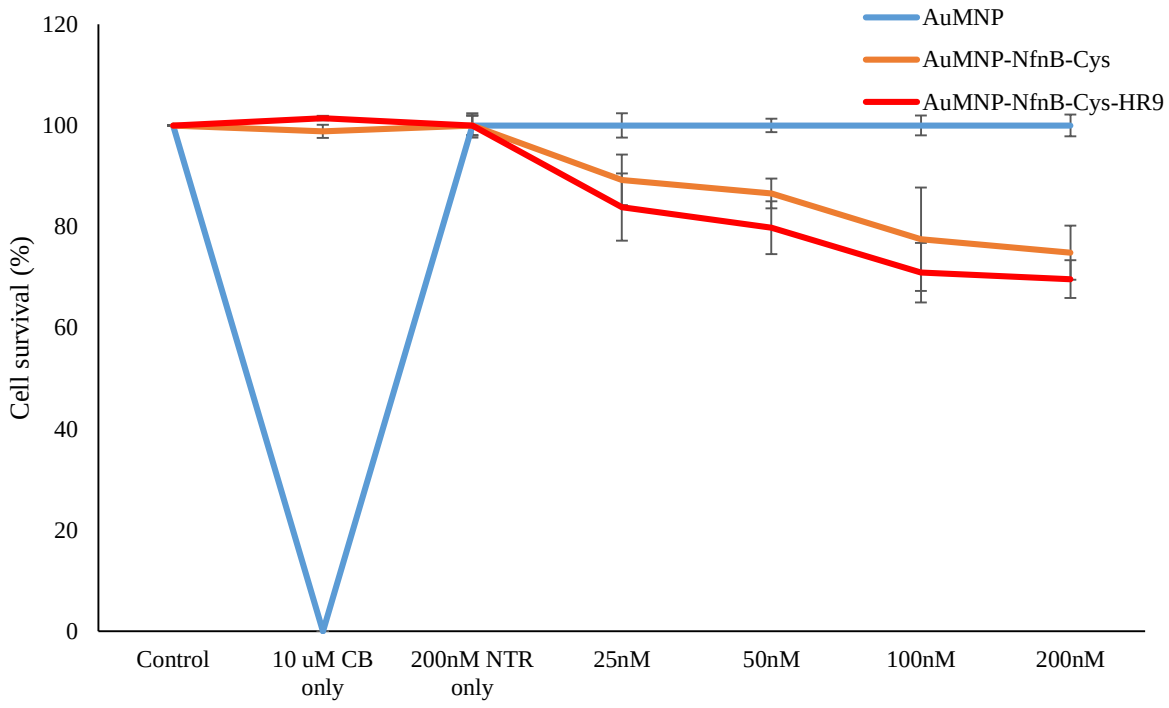

Figure 5.25. Here the data for the cell culture treatments of; AuMNP, AuMNP:NfnB-Cys and AuMNP:NfnB-Cys:HR9 are presented side by side for comparison of cell viability. The addition of the HR9 onto the AuMNP:NfnB-Cys conjugate caused an increase in cell death of 5 % compared to the AuMNP:NfnB-Cys. Whilst the AuMNP shows no toxicity towards the SK-OV-3.

5.8 Comparison of nanoparticle kills with free enzyme and conjugate kills

The Cell survival at a 200 nM treatment concentration for all cell culture treatments are presented for direct comparison in table 5.1.

*Table 5.1. The compared toxicity for treatments of various cell culture treatments at 200 nM. The treatments all show an improved toxicity when conjugated with a CPP. Further to this the treatments involving AuNPs or AuMNPs both show results comparable to the unconjugated NfnB-Cys. Data points that's showed statistical significance are marked with a *.*

Sample	Cell survival at 200 nM sample concentration (%)
NfnB-Cys*	76±4.92
NfnB-Cys:HR9*	58±0.35
NfnB-Cys:Pep-1*	68±3.54
YfkO-Cys*	65±5.23
YfkO-Cys:HR9*	55±3.56
YfkO-Cys:Pep-1*	57±4.97
AuNP:NfnB-Cys	81±2.35
AuNP:NfnB-Cys:HR9	74±1.94
AuMNP	100±2.16
AuMNP:NfnB-Cys	74±2.03
AuMNP:NfnB-Cys:HR9	69±3.73

When comparing the cell culture data for NfnB-Cys and YfkO-Cys, YfkO-Cys has an initial 19 % greater toxicity at 200 nM than NfnB-Cys. This difference becomes 3 % when comparing the data for YfkO-Cys:HR9 with NfnB-Cys:HR9, however the change in toxicity presented for the HR9 conjugates from the unconjugated enzymes is greater for NfnB-Cys, indicating that HR9 is much more efficient at internalizing NfnB-Cys than YfkO-Cys. For the Pep-1 conjugates, the NfnB-Cys shows an 8 % increase in toxicity, whilst after adjusting for individual toxicity the YfkO-Cys:Pep-1 conjugate shows an increase in toxicity of 7 % over unconjugated YfkO-Cys. To conclude, the nitroreductases NfnB-Cys and YfkO-Cys both uptake into SK-OV-3 and reduce CB1954 to cause cellular toxicity, with YfkO-Cys showing a higher cell death rate than NfnB-Cys. The conjugation of HR9 and Pep-1 onto these enzymes at a 1:1 ratio causes an increase in cell death for all conjugate with YfkO-Cys:Pep-1 showing the least increase in cell kill with a 7 % increase in cell death, whilst NfnB-Cys:HR9 showing the most increase of 18 % increase of cell death.

When nanoparticles are introduced the percentage survival of cells increases by 5 % when treated with AuNP:NfnB-Cys, but has a 2 % decrease when treated with AuMNP:NfnB-Cys. The addition of HR9 at a 1:1 ratio with the nanoparticle shows an increase in cell death caused for both nanoparticle treatments. The AuNP:NfnB-Cys:HR9 conjugate demonstrates a 7 %

decrease in cell viability to 74 %, whilst the AuMNP:NfnB-Cys:HR9 conjugate has a 5 % decrease in cell viability to 69 %. This data indicates that the nanoparticle conjugates are able to enter into cells without causing an excess of toxicity and are still able to reduce the CB1954 prodrug, causing cell death.

5.9 Darkfield imaging

Dark-field microscopy is a form of microscopy that is used to produce sample images where the background of the image is black and uses light scattered by the sample to create the image compared to bright-field illumination, where the image is produced by shining a light source directly onto a sample. At CytoViva, Darkfield imaging has been enhanced to produce high resolution images, able to visualise individual nanoparticles in cells and combined with hyperspectral imaging to provide a UV-vis spectrum of a point in an image. By using an untreated sample of cells, a spectrum sample of the untreated call can be taken and compared with differences when treated with nanoparticles.

A sample of SK-OV-3, SK-OV-3 cells treated with AuMNPs, SK-OV-3 cells treated with AuMNP:NfnB-Cys and SK-OV-3 cells treated with AuMNP:NfnB-Cys:HR9 were sent to CytoViva for hyperspectral enhanced Darkfield imaging. The imaging was done to try and achieve an insight into how the addition of the HR9 improves the cellular uptake and where within the cell the conjugate was taken after uptake. Figure 5.26 is an example image of cells treated with 15 nm gold nanoparticles, with the nanoparticles highlighted in red on the right side image.[62]

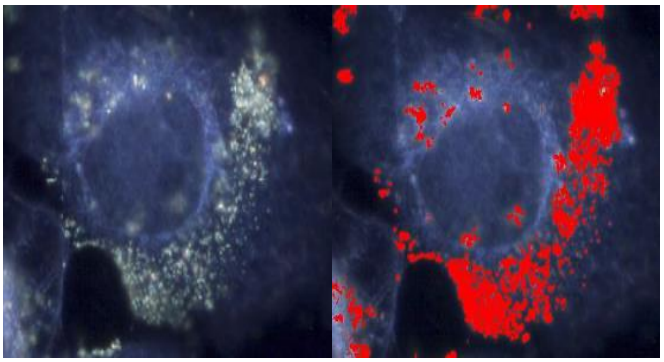

Figure 5.26. A side by side image of an example Darkfield hyperspectral image of cells treated with 15 nm gold nanoparticles. The nanoparticles inside the cell are highlighted in red in the right hand side image.[62]

Figure 5.27 are images of the samples sent for Darkfield imaging, the image consists of 4 images of the cells with various treatments on the left (*labelled a*) and repeated on the right with nanoparticles highlighted in red (*labelled b*).

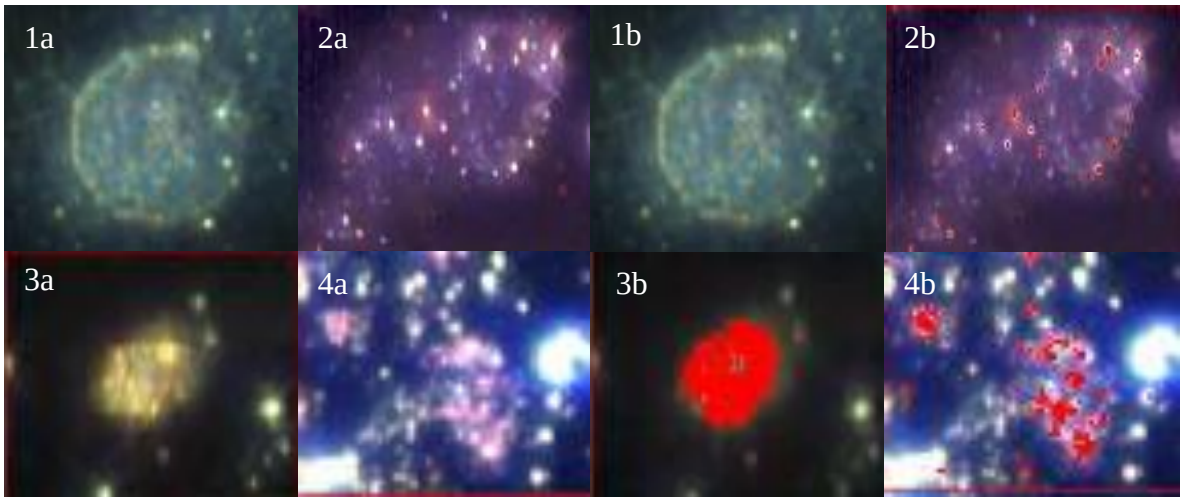

*Figure 5.27. The hyperspectral imaging of SK-OV-3 (**1a+1b**), SK-OV-3 treated with AuMNPs (**2a+2b**), SK-OV-3 treated with AuMNP:NfnB-Cys (**3a+3b**) and SK-OV-3 treated with AuMNP:NfnB-Cys:HR9 (**4a+4b**). The nanoparticles are highlighted in red in all the (**'b'**) images. Images **2a** and **2b** show uptake of some AuMNPs, with this uptake greatly increase for images **3** and **4**, of AuMNP:NfnB-Cys and AuMNp:NfnB-Cys:HR9 respectively. It cannot be said if the uptake is increased for sample **4**, however when comparing with the cell culture data, it would indicate an increase in uptake.*

The untreated SK-OV-3 (*1a, 1b*) is a reference image for the comparison of cells treated with; AuMNP (2a, 2b), AuMNP:NfnB-Cys (*3a, 3b*) and AuMNP:NfnB-Cys:HR9 (*4a, 4b*). Sample 2 shows some uptake of naked AuMNPs into cells, with a large increase in the uptake when treated with AuMNP:NfnB-Cys (*3a+3b*). Whilst when treated with AuMNP:NfnB-Cys:HR9 (*4a+4b*) there is an increase in the cellular uptake of these nanoparticles, which, when examining and comparing with the cell culture data would agree with an increased uptake.

5.10 Higher resolution Darkfield imaging

The initial darkfield imaging performed on the set of cells treated with nanoparticles provided an insight into the ability for the AuMNP/ AuMNP conjugates to penetrate into cells, however the quality of the images was lacking so samples were sent to Queens University Belfast, School of Pharmaceutical Sciences in an attempt to yield higher resolution images. Figure 5.28 are these higher resolution images. There are 4 samples, sample A is untreated SK-OV-3 cells, B is SK-OV-3 treated with AuMNPs, C is SK-OV-3 treated with AuMNP:NfnB-Cys conjugate and sample D is SK-OV-3 treated with AuMNP:NfnB-Cys:HR9 conjugate. Samples were also treated with 4', 6-diamidino-2-phenylinadol (DAPI) for cell nucleus staining, showing in blue on Figure 5.2,8.

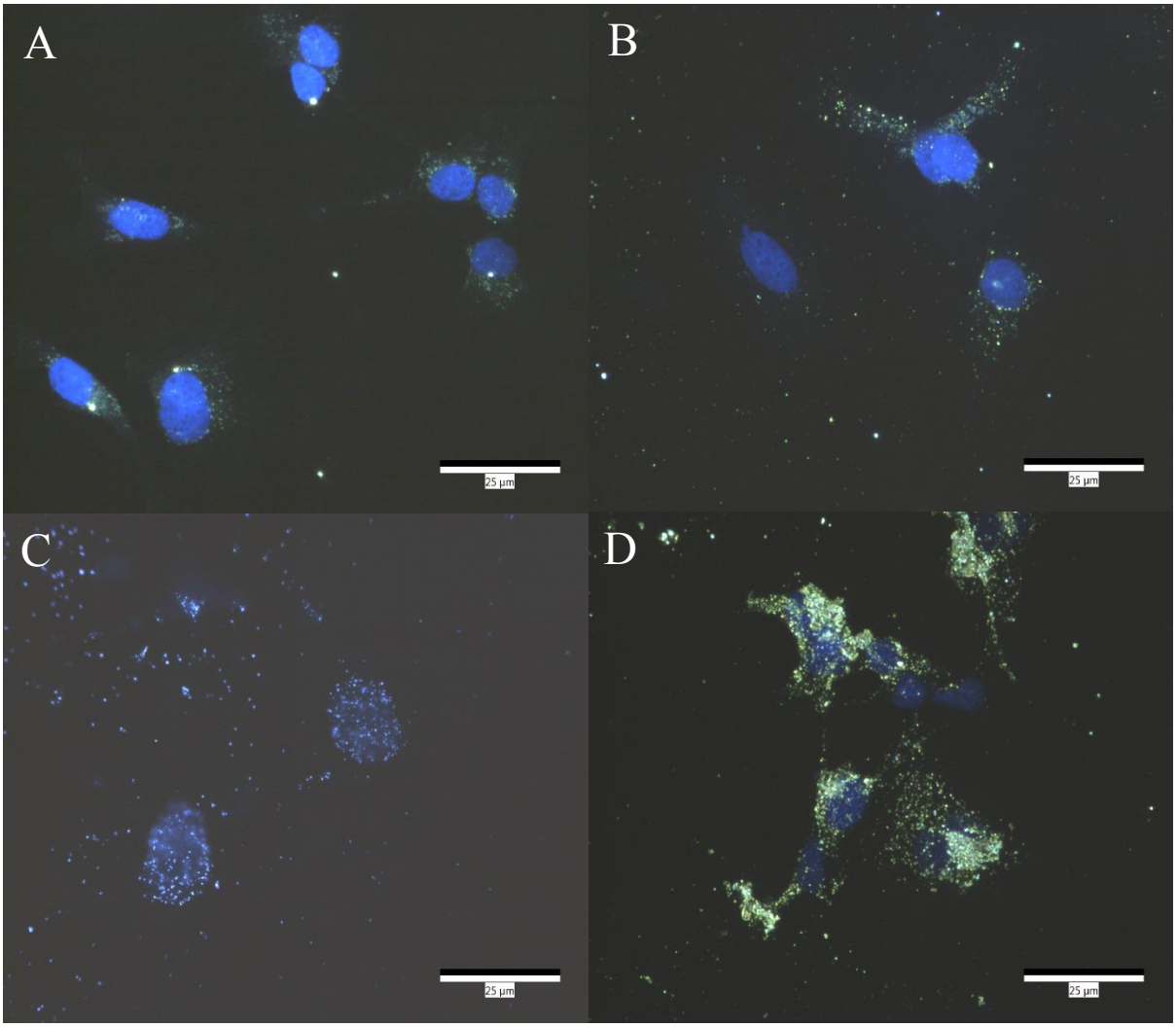

Figure 5.28. Improved darkfield imaging with clearer resolutions are shown above. A is SK-OV-3 cells treated with growth medium, whilst B are SK-OV-3 cells treated with AuMNPs, the yellow dots are the nanoparticles within the cells. C is SK-OV-3 cells treated with AuMNP:NfnB-Cys conjugates, there is a marked increase in the number of nanoparticles within the cells, inparticular within the nucleus of the cells. D shows the most drastic change where SK-OV-3 cells were reated with AuMNP:NfnB-Cys:HR9 conjugates where the cells are flooded with the nanoparticles conugates.

This new darkfield imaging shows a much higher resolution and image quality than the previous set. Sample A allows us to map untreated SK-OV-3 cells to get a comparison when AuMNPs are treated, in sample B. Here there is a small increase in the number of bright yellow/orange spots which are the AuMNPs, Whilst Sample C shows a large increase in the number of nanoparticles actually within the nucleus of the cell when the cells are treated with AuMNP:NfnB-Cys. The most striking image however is sample D where cells are treated with AuMNP:NfnB-Cys:HR9 which shows a visually improved quantity of nanoparticles with the cells and cell nuclei. This is a very good indication that the addition of the CPP is causing a large increase in the uptake of the AuMNP conjugate.

5.11 Conclusions and future work

Here a novel synthesis method for AuMNPs has been demonstrated, along with changes to the synthesis to improve the morphology of the nanoparticles produced. The AuMNPs are purified under magnetism to remove any excess non-magnetic gold nanoparticles produced by the synthesis, also by centrifugation to remove nanoparticles larger than ~ 50 nm and in an attempt to separate out the excess iron oxide nanoparticles that were uncoated within the synthesis. These AuMNPs have been further characterised by: TEM, UV-Vis, DLS and their zeta potential calculated. The TEM images indicated that experimental changes during the development of the synthesis had an improvement of the produced nanoparticles. The original nanoparticle synthesis yielded a low count of nanoparticles as well as a mismatch in both shape and size of the nanoparticles. By changing the experimental parameters of the synthesis, the size of the nanoparticles improved to be roughly 50 nm, along with both the shape and size distribution improving as well as the overall number of nanoparticles present post purification. This improvement in the nanoparticle morphology was also supported by UV-Vis with the λ-max of the gold peak being in the area of 50 nm as well as the shape of the gold peak improving in size and smoothness indicating an improved morphology of the nanoparticles. The DLS of the nanoparticles initially indicated that the nanoparticles had an average size of almost 100 nm, much larger than suggested by TEM and UV-Vis. Further analysis using DLS to scan with light sources from different angles demonstrated that the nanoparticles were in fact scattering light in multiple directions that could not be detected by DLS. This DLS imaging demonstrated the nanoparticles were in fact much closer to the 50 nm suggested by TEM and UV-Vis. The size distribution done by DLS produced a reported size distribution of 77 nm, with the calculated zeta potential of the nanoparticles being calculated at -35.2 mV indicating that the nanoparticles were above the threshold for stability. However it was noted that the distribution value of the nanoparticles did extend towards 0 mV indicating some of the nanoparticles within the solution would tend to flocculate or aggregate.

Finally the nanoparticles have been assessed for their stability, as well as the aggregation behaviour of the AuMNPs in various mediums. The AuMNPs were first tested for their stability in dH_2O and 1 mM sodium citrate dihydrate, the solution they are 'washed' with and kept in post synthesis and purification. The AuMNPs demonstrated no observable aggregation at up to and including 96 hours. The experiments were repeated using; phosphate buffer (*50 mM, pH*

7.4), phosphate buffered saline (*PBS*), NaCl (*1 mM-5 M*) 1 mM sodium citrate dihydrate at various temperatures (*-20 ˚C, 0 ˚C, 25 ˚C, 37 ˚C*), pH altered 1 mM sodium citrate dihydrate (*pH 1-12*) and finally Dulbecco's Modified Eagle's Medium (*with 10 % Fetal Bovine Serum, 1 % L-Glutamine and 1 % Penicillin Streptomycin*) to assess of the AuMNPs might behave in cell culture experiments. The AuMNPs showed aggregation in PBS, NaCl above 200 mM and when stored at -20 ˚C and pH altered solutions at pH of 1, 2 and 3. The AuMNPs were stable in all of the other mediums and experimental parameters used for assessing stability, including Dulbecco's Modified Eagle's Medium (*with 10 % Fetal Bovine Serum, 1 % L-Glutamine and 1 % Penicillin-Streptomycin*) indicating they could be used in cell culture experiments.

In the work discussed here it has been shown that the previously genetically modified nitroreductases: NfnB-Cys and YfkO-Cys have been successfully expressed, purified and characterized by SDS-PAGE. Further to this both the nitroreductases have been successfully conjugated with the CPPs: HR9 and Pep-1 at varying rations, with conjugation being analysed using native agarose gel electrophoresis. From this, the NTR:CPP conjugates were assessed for their ability to reduce the CB1954 prodrug, with the product production being assessed using UV-Vis by measuring the change in absorbance at 420 nm over time. The results displayed that up to a 1:1 ratio all NTR:CPP combinations displayed no major change in the change of absorbance at 420 nm, whilst above this ratio some conjugates displayed no change, whilst others exhibited a drastic drop in the change at 420nm. From this for all further work involving nitroreductases and CPPs the ratio would be 1:1, with the exception being when using nanoparticles, where the CPPs would be in a 1:1 ratio with the nanoparticle itself, not the nitroreductases. The enzymatic reaction profile of the NTR:CPP conjugates was assessed by HPLC to determine how (if at all) the conjugation of the CPP changes the hydroxylamine product formation ratio from the unconjugated nitroreductases. All conjugates showed minimal changes to the ratio of products, indicating a possible slight structural or kinetic change to the enzymes. Further to this Michaelis-Menten kinetic parameters of the conjugates were determined, with the NfnB-Cys:CPP conjugates demonstrating up to a 75 % loss in enzymatic efficiency, whilst the YfkO-Cys:CPP conjugates showed an enzymatic efficiency of up to 20 times less than unconjugated YfkO-Cys. This drop in efficiency and change in product ratio, could cause issues when the conjugates are used in combination with CB1954 in cell culture.

Cell culture experiments using the NTR:CPP conjugates demonstrated that for all conjugates, the addition of the CPP to the enzyme decreased the cell survivability, with differing

combinations of NTR:CPP having different increases of cell death, with NfnB-Cys:HR9 demonstrating the largest decrease in cell survivability and NfnB-Cys:Pep-1 displaying the smallest difference in cell survivability. The CPPs were also assessed independently for any excess toxicity they displayed towards the cells, of which none was observed, indicating that the increase in toxicity observed is from an increased uptake of nitroreductase.

After determining a synthetic route for the formation of AuMNPs and the successful use of CPPs at aiding an increase uptake of nitroreductases, the nanoparticles were conjugated with NfnB-Cys and HR9 to assess if the CPPs can aid in the increased uptake of the AuMNP:NfnB-Cys conjugate. Identical experiments were also carried out using single metal gold nanoparticles (*AuNPs*) first to assess how the AuMNPs might behave in cell culture. This was done due to the low yield the AuMNP synthesis produced. The AuNPs were successfully conjugated with NfnB-Cys with the conjugate retaining enzymatic activity, the conjugate was then tested in cell culture and further conjugated with HR9 at a 1:1 ratio with the AuMNP. This final conjugate demonstrated a decrease in cell survivability compared to the AuNP:NfnB-Cys conjugate on its own, indicating an increase in cellular uptake of the conjugate, again the conjugate demonstrated no toxicity when tested on its own. This set of experiments was repeated using AuMNPs with the same trend in results being observed, indicating that the AuMNP:NfnB-Cys:HR9 conjugate does present a viable system for use in MNDEPT.

Further work for this project would be to continue to improve the synthesis method for AuMNPs to attempt to coat a higher percentage of the iron oxide nanoparticles, as well as being able to produce a tighter size distribution of the AuMNPs and if needs be find a way to remove the excess uncoated iron oxide nanoparticles. Further to the current established NTR:CPP conjugate reaction product ratio, the same needs to be done with the nanoparticle conjugates by HPLC along with the kinetic parameters of the conjugates. Different ratios of CPPs could also be used on the unconjugated enzymes to assess for an optimum ratio for maximum uptake and cell death, which could then be further adapted onto work involving AuMNPs. Finally the testing of a wider range of enzymes on a range of cell types should be done to establish a database for which enzymes are able to cause the most cell death in different cell types with and without the use of CPPs and conjugation to AuMNPs.

5.12 Bibliography

1 P. V. Pham, *Omi. Technol. Bio-Engineering*, 2018, 449–469.

2 Miltenyi Biotec, L. M. Côrtes, R. M. Silva, B. A. Pereira, C. Guerra, *et al.*, *Vitr. Cell. Dev. Biol. Anim.*, 2010, **45**, 1–120.

3 J. R. Maiolo, M. Ferrer and E. A. Ottinger, *Biochim. Biophys. Acta - Biomembr.*, 2005, **1712**, 161–172.

4 G. Maguire, *ACS Med. Chem. Lett.*, 2016, **7**, 441–443.

5 B. Alberts, A. Johnson, J. Lewis, M. Raff, R. Keith and P. Walter, *Molecular Biology of the Cell*, Garland Science, New York, 4th editio., 2002.

6 L. Hayflick and P. S. Moorhead, *Exp. Cell Res.*, 1961, **25**, 585–621.

7 J. L. Chen, T. W. J. Steele and D. C. Stuckey, *Environ. Sci. Technol.*, 2015, **49**, 13463–13471.

8 F. Fan and K. V. Wood, *Assay Drug Dev. Technol.*, 2007, **5**, 127–136.

9 É. Karászi, K. Jakab, L. Homolya, G. Szakács, Z. Holló, B. Telek, A. Kiss, L. Rejtô, S. Nahajevszky, B. Sarkadi and J. Kappelmayer, *Br. J. Haematol.*, 2001, **112**, 308–314.

10 C. D. Gwenin, M. Kalaji, P. A. Williams and C. M. Kay, *Biodegradation*, 2011, **22**, 463–474.

11 V. V. Gwenin, P. Poornima, J. Halliwell, P. Ball, G. Robinson and C. D. Gwenin, *Biochem. Pharmacol.*, 2015, **98**, 392–402.

12 T. Mosmann, *J. Immunol. Methods*, 1983, **65**, 55–63.

13 M. V. Berridge and A. S. Tan, *Arch. Biochem. Biophys.*, 1993, **303**, 474–482.

14 J. V Castell and M. J. Gomez-Lechon, Eds., *In Vitro Methods in Pharmaceutical Research*, 1996.

15 S. O. Vass, D. Jarrom, W. R. Wilson, E. I. Hyde and P. F. Searle, *Br. J. Cancer*, 2009, **100**, 1903–1911.

16 P. F. Searle, M. J. Chen, L. Hu, P. R. Race, A. L. Lovering, J. I. Grove, C. Guise, M. Jaberipour, N. D. James, V. Mautner, L. S. Young, D. J. Kerr, A. Mountain, S. A. White and E. I. Hyde, *Clin. Exp. Pharmacol. Physiol.*, 2004, **31**, 811–816.

17 P. R. Race, A. L. Lovering, S. A. White, J. I. Grove, P. F. Searle, C. W. Wrighton and E. Hyde, *J. Mol. Biol.*, 2007, **368**, 481–492.

18 F. Haenal, N. Garbow, Perkin-Elmer, *Cell Counting and Confluency Analysis as Quality Controls in Cell-Based Assays, http://www.perkinelmer.co.uk/lab-solutions/resources/docs/011833_01_APP.pdf*, (accessed 28 November 2018).

19 S. Benítez-Martínez, Á. I. López-Lorente and M. Valcárcel, *Microchim. Acta*, 2016, **183**, 781–789.

20 R. Arvidsson, S. Molander and B. A. Sandén, *J. Ind. Ecol.*, 2012, **16**, 343–351.

21 H. E. Daldrup-Link, *Radiology*, 2017, **284**, 616–629.

22 I. Obaidat, B. Issa and Y. Haik, *Nanomaterials*, 2015, **5**, 63–89.

23 F. Mohammad, G. Balaji, A. Weber, R. M. Uppu and C. S. S. R. Kumar, *J. Phys. Chem. C. Nanomater. Interfaces*, 2010, **114**, 19194–19201.

24 V. I. Shubayev, T. R. Pisanic and S. Jin, *Adv. Drug Deliv. Rev.*, 2009, **61**, 467–477.

25 T. A. Larson, J. Bankson, J. Aaron and K. Sokolov, *Nanotechnology*, 2007, **18**.

26 L. Cheng, K. Yang, Y. Li, X. Zeng, M. Shao, S. T. Lee and Z. Liu, *Biomaterials*, 2012, **33**, 2215–2222.

27 D. K. Kirui, D. A. Rey and C. A. Batt, *Nanotechnology*, 2010, **21**.

28 S. Moraes Silva, R. Tavallaie, L. Sandiford, R. D. Tilley and J. J. Gooding, *Chem. Commun.*, 2016, **52**, 7528–7540.

29 S. Bhana, G. Lin, L. Wang, H. Starring, S. R. Mishra, G. Liu and X. Huang, *ACS Appl. Mater. Interfaces*, 2015, **7**, 11637–11647.

30 V. Dixit, J. Van Den Bossche, D. M. Sherman, D. H. Thompson and R. P. Andres, *Bioconjug. Chem.*, 2006, **17**, 603–609.

31 G. Ajnai, A. Chiu, T. Kan, C. C. Cheng, T. H. Tsai and J. Chang, *J. Exp. Clin. Med.*, 2014, **6**, 172–178.

32 A. Kumar, X. Zhang and X.-J. Liang, *Biotechnol. Adv.*, 2013, **31**, 593–606.

33 D. R. Bhumkar, H. M. Joshi, M. Sastry and V. B. Pokharkar, *Pharm. Res.*, 2007, **24**, 1415–1426.

34 S. Dierks, 2005, 1–6.

35 A. M. Alkilany and C. J. Murphy, *J. Nanoparticle Res.*, 2010, **12**, 2313–2333.

36 C. Tanford, *J. Phys. Chem.*, 1974, **78**, 2469–2479.

37 M. Ohde, H. Ohde and C. M. Wai, *Chem. Commun. (Camb).*, 2002, **1**, 2388–9.

38 C. L. Kitchens, M. C. McLeod and C. B. Roberts, *Langmuir*, 2005, **21**, 5166–5173.

39 E. Iglesias-Silva, J. L. Vilas-Vilela, M. A. López-Quintela, J. Rivas, M. Rodríguez and L. M. León, *J. Non. Cryst. Solids*, 2010, **356**, 1233–1235.

40 J. Lin, W. Zhou, A. Kumbhar, J. Wiemann, J. Fang, E. E. Carpenter and C. J. O'Connor, *J. Solid State Chem.*, 2001, **159**, 26–31.

41 J. P. M. Almeida, A. Y. Lin, E. R. Figueroa, A. E. Foster and R. A. Drezek, *Small*, 2015, **11**, 1453–1459.

42 A. Li Volsi, D. Jimenez de Aberasturi, M. Henriksen-Lacey, G. Giammona, M. Licciardi and L. M. Liz-Marzán, *J. Mater. Chem. B*, 2016, **4**, 1150–1155.

43 M. Arruebo, R. Fernández-Pacheco, M. R. Ibarra and J. Santamaría, 2007, **2**, 22–32.

44 J. Dobson, *Drug Dev. Res.*, 2006, **67**, 55–60.

45 S. Kayal and R. V. Ramanujan, *J. Nanosci. Nanotechnol.*, 2010, **10**, 5527–5539.

46 S. C. McBain, H. H. P. Yiu and J. Dobson, *Int. J. Nanomedicine*, 2008, **3**, 169–180.

47 O. Veiseh, J. W. Gunn and M. Zhang, *Adv. Drug Deliv. Rev.*, 2010, **62**, 284–304.

48 S. Habtemariam, *Phyther. Res.*, 1995, **9**, 603–605.

49 A. R. Lupu and T. Popescu, *Toxicol. Vitr.*, 2013, **27**, 1445–1450.

50 K. E. Herold and A. Rasooly, *Biosensors and Molecular Technologies for Cancer Diagnostics*, Taylor & Francis group, LLC, 2012.

51 V. V. Gwenin, C. D. Gwenin and M. Kalaji, *Langmuir*, 2011, **27**, 14300–14307.

52 D. L. Kokkin, R. Zhang, T. C. Steimle, I. A. Wyse, B. W. Pearlman and T. D. Varberg, *J. Phys. Chem. A*, 2015, **119**, 11659–11667.

53 C. D. Gwenin, M. Kalaji, P. A. Williams and R. M. Jones, *Biosens. Bioelectron.*, 2007, **22**, 2869–2875.

54 W. Haiss, N. T. K. Thanh, J. Aveyard and D. G. Fernig, *Anal. Chem*, 2007, **79**, 4215–4221.

55 J. Turkevich, *Gold Bull.*, 1985, **18**, 125–131.

56 P. Ball, E. Thompson, S. Anderson, V. Gwenin and C. Gwenin, *Eur. J. Pharm. Sci.*, 2019, **127**, 217–224.

57 G. F. Paciotti, L. Myer, D. Weinreich, D. Goia, N. Pavel, R. E. McLaughlin and L. Tamarkin, *Drug Deliv. J. Deliv. Target. Ther. Agents*, 2004, **11**, 169–183.

58 I. Fratoddi, I. Venditti, C. Cametti and M. V. Russo, *J. Mater. Chem. B*, 2014, **2**, 4204–4220.

59 N. L. Rosi, D. A. Giljohann, C. S. Thaxton, K. R. Abigail, Lytton-Jean., M. S. Han and C. A. Mirkin, *Science*, 2006, **312**, 1027–1030.

60 Y. Ding, Z. Jiang, K. Saha, C. S. Kim, S. T. Kim, R. F. Landis and V. M. Rotello, *Mol. Ther.*, 2014, **22**, 1075–1083.

61 P. Ghosh, G. Han, M. De, C. K. Kim and V. M. Rotello, *Adv. Drug Deliv. Rev.*, 2008, **60**, 1307–1315.

62 J. R. Nicol, E. Harrison, S. M. O'Neill, D. Dixon, H. O. McCarthy and J. A. Coulter, *Nanomedicine Nanotechnology, Biol. Med.*, 2018, **14**, 439–449.

Chapter 6:

Appendix

6.1 NfnB-Cys

Ddunnet critical value: 17.71105 (values highlighted in green are individually statisitically significant points).

Groups	*Count*	*Sum*	*Average*	*Variance*	*Ddunnet*
Control	3	300	100	0	
25 nM	3	243.1913978	81.06379928	18.42121074	18.93620072
50 nM	3	247.3210417	82.44034723	21.14881561	17.55965277
75 nM	3	249.7246508	83.24155028	3.457153586	16.75844972
100 nM	3	259.6474733	86.54915777	4.222927334	13.45084223
125 nM	3	284.8473702	94.94912339	26.63898452	5.050876607
150 nM	3	252.3588561	84.1196187	22.04051221	15.8803813
175 nM	3	263.1460988	87.71536627	3.875601179	12.28463373
200 nM	3	246.2616753	82.0872251	72.75259255	17.9127749

Source of Variation	*SS*	*df*	*MS*	*F*	*P-value*	*F crit*
Between Groups	1006.239	8	125.7799243	6.560232	0.0004656	2.510157895
Within Groups	345.115	18	19.17308864			

6.2 NfnB-Cys:HR9

Ddunnet critical value: 36.45492

Groups	*Count*	*Sum*	*Average*	*Variance*	*Ddunnet*
Control	3	300	100	0	
25 nM	3	177.5859	59.19531	73.36849	40.80469
50 nM	3	173.0583	57.68611	119.7039	42.31389
75 nM	3	233.9987	77.99956	62.91052	22.00044
100 nM	3	211.0136	70.33787	2.928494	29.66213
125 nM	3	209.32	69.77334	6.828988	30.22666
150 nM	3	226.9002	75.63338	26.70435	24.36662
175 nM	3	197.2458	65.7486	166.5157	34.2514
200 nM	3	174.3841	58.12805	0.374847	41.87195

Source of Variation	*SS*	*df*	*MS*	*F*	*P-value*	*F crit*
Between Groups	4263.096	8	532.8871	10.44114	2.26E-05	2.510158
Within Groups	918.6705	18	51.03725			

6.3 NfnB-Cys:Pep-1
Ddunnet critical value: 21.93373

Groups	*Count*	*Sum*	*Average*	*Variance*	*Ddunnet*
Control	3	300	100	0	
25 nM	3	243.2237	81.07457	90.32083	18.92543
50 nM	3	247.9613	82.65377	3.371787	17.34623
75 nM	3	245.8808	81.96025	16.1419	18.03975
100 nM	3	244.5302	81.51005	6.835578	18.48995
125 nM	3	256.7362	85.57875	70.24892	14.42125
150 nM	3	247.2377	82.41256	2.560579	17.58744
175 nM	3	243.6446	81.21485	10.95141	18.78515
200 nM	3	205.6742	68.55805	37.61449	31.44195

Source of Variation	*SS*	*df*	*MS*	*F*	*P-value*	*F crit*
Between Groups	1543.256	8	192.907	7.293408	0.000243	2.510158
Within Groups	476.091	18	26.4495			

6.4 YfkO-Cys
Ddunnet critical value: 25.64078

Groups	*Count*	*Sum*	*Average*	*Variance*	*Ddunnet*
Control	3	300	100	0	
25 nM	3	228.9542	76.31806	7.682889	23.68194
50 nM	3	238.887	79.629	17.69679	20.371
75 nM	3	248.093	82.69766	8.360731	17.30234
100 nM	3	236.1433	78.71443	53.25972	21.28557
125 nM	3	227.7982	75.93273	31.685	24.06727
150 nM	3	228.2878	76.09592	21.21424	23.90408
175 nM	3	247.6356	82.54518	48.4691	17.45482
200 nM	3	193.1758	64.39193	82.19418	35.60807

Source of Variation	*SS*	*df*	*MS*	*F*	*P-value*	*F crit*
Between Groups	2108.994	8	263.6242	8.7692	7.39E-05	2.510158
Within Groups	541.1253	18	30.06252			

6.5 YfkO-Cys:HR9
Ddunnet critical value: 35.37663

Groups	*Count*	*Sum*	*Average*	*Variance*	*Ddunnet*
Control	3	300	100	0	
25 nM	3	180.5446	60.18153	76.04447	39.81847
50 nM	3	190.0056	63.33519	80.60588	36.66481
75 nM	3	183.5099	61.16995	20.08791	38.83005
100 nM	3	193.1517	64.3839	53.32479	35.6161
125 nM	3	201.87	67.29001	60.68265	32.70999
150 nM	3	188.1368	62.71225	22.44526	37.28775
175 nM	3	207.8888	69.29626	18.5528	30.70374
200 nM	3	167.4792	55.82641	38.14699	44.17359

Source of Variation	*SS*	*df*	*MS*	*F*	*P-value*	*F crit*
Between Groups	4014.564	8	501.8205	12.21005	7.49E-06	2.510158
Within Groups	739.7815	18	41.09897			

6.6 YfkO-Cys:Pep-1
Ddunnet critical value: 27.23717

Groups	*Count*	*Sum*	*Average*	*Variance*	*Ddunnet*
Control	3	300	100	0	
25 nM	3	186.3891	62.12972	99.61655	37.87028
50 nM	3	189.1314	63.04379	12.52916	36.95621
75 nM	3	187.8567	62.61889	27.6606	37.38111
100 nM	3	183.6297	61.2099	2.64469	38.7901
125 nM	3	192.1744	64.05813	23.35572	35.94187
150 nM	3	196.286	65.42867	7.271059	34.57133
175 nM	3	177.8962	59.29873	6.904179	40.70127
200 nM	3	153.2512	51.08375	74.32325	48.91625

Source of Variation	*SS*	*df*	*MS*	*F*	*P-value*	*F crit*
Between Groups	4448.016	8	556.0019	19.67721	2.08E-07	2.510158
Within Groups	508.6104	18	28.25613			

6.7 AuNP NfnB-Cys

Groups	*Count*	*Sum*	*Average*	*Variance*
Control	3	300	100	0
25 nM	3	240.4865	80.16217	35.80367
50 nM	3	259.9025	86.63418	0.22577
100 nM	3	260.4997	86.83322	35.1631
200 nM	3	244.4228	81.47427	16.5727

Source of Variation	*SS*	*df*	*MS*	*F*	*P-value*	*F crit*
Between Groups	739.3472	4	184.8368	10.53018	0.001311	3.47805
Within Groups	175.5305	10	17.55305			

6.8 AuNP NfnB-Cys:HR9

Groups	*Count*	*Sum*	*Average*	*Variance*
Control	3	300	100	0
25 nM	3	270.7402	90.24672	2.601644
50nM	3	264.2661	88.0887	3.427574
100 nM	3	254.8861	84.96204	7.648822
200 nM	3	226.5995	75.53318	11.29132

Source of Variation	*SS*	*df*	*MS*	*F*	*P-value*	*F crit*
Between Groups	940.2992	4	235.0748	47.07265	1.87E-06	3.47805
Within Groups	49.93872	10	4.993872			

6.9 AuMNP NfnB-Cys

Groups	*Count*	*Sum*	*Average*	*Variance*
Control	3	300	100	0
25 nM	3	296.1898	98.72992	17.12075
50 nM	3	263.6912	87.89708	41.13312
100 nM	3	235.0575	78.3525	72.79006
200 nM	3	234.7278	78.24259	12.40218

Source of Variation	*SS*	*df*	*MS*	*F*	*P-value*	*F crit*
Between Groups	1336.04	4	334.01	11.64235	0.000883	3.47805
Within Groups	286.8922	10	28.68922			

6.10 AuMNP NfnB-Cys:HR9

Groups	*Count*	*Sum*	*Average*	*Variance*
Control	3	300	100	0
25 nM	3	251.5537	83.85122	132.0112
50 nM	3	239.3294	79.77648	81.02851
100 nM	3	212.6603	70.88675	103.3253
200 nM	3	208.7643	69.58809	41.8097

Source of Variation	*SS*	*df*	*MS*	*F*	*P-value*	*F crit*
Between Groups	1808.924	4	452.2311	6.312996	0.008416	3.47805
Within Groups	716.3493	10	71.63493			

6.11 Dunnett critical value table

n	α	Number of Groups, Including Control Group								
		2	3	4	5	6	7	8	9	10
5	.05	2.57	3.03	3.29	3.48	3.62	3.73	3.82	3.90	3.97
	.01	4.03	4.63	4.98	5.22	5.41	5.56	5.69	5.80	5.89
6	.05	2.45	2.86	3.10	3.26	3.39	3.49	3.57	3.64	3.71
	.01	3.71	4.21	4.51	4.71	4.87	5.00	5.10	5.20	5.28
7	.05	2.36	2.75	2.97	3.12	3.24	3.33	3.41	3.47	3.53
	.01	3.50	3.95	4.21	4.39	4.53	4.64	4.74	4.82	4.89
8	.05	2.31	2.67	2.88	3.02	3.13	3.22	3.29	3.35	3.41
	.01	3.36	3.77	4.00	4.17	4.29	4.40	4.48	4.56	4.62
9	.05	2.26	2.61	2.81	2.95	3.05	3.14	3.20	3.26	3.32
	.01	3.25	3.63	3.85	4.01	4.12	4.22	4.30	4.37	4.43
10	.05	2.23	2.57	2.76	2.89	2.99	3.07	3.14	3.19	3.24
	.01	3.17	3.53	3.74	3.88	3.99	4.08	4.16	4.22	4.28
11	.05	2.20	2.53	2.72	2.84	2.94	3.02	3.08	3.14	3.19
	.01	3.11	3.45	3.65	3.79	3.89	3.98	4.05	4.11	4.16
12	.05	2.18	2.50	2.68	2.81	2.90	2.98	3.04	3.09	3.14
	.01	3.05	3.39	3.58	3.71	3.81	3.89	3.96	4.02	4.07
13	.05	2.16	2.48	2.65	2.78	2.87	2.94	3.00	3.06	3.10
	.01	3.01	3.33	3.52	3.65	3.74	3.82	3.89	3.94	3.99
14	.05	2.14	2.46	2.63	2.75	2.84	2.91	2.97	3.02	3.07
	.01	2.98	3.29	3.47	3.59	3.69	3.76	3.83	3.88	3.93
15	.05	2.13	2.44	2.61	2.73	2.82	2.89	2.95	3.00	3.04
	.01	2.95	3.25	3.43	3.55	3.64	3.71	3.78	3.83	3.88
16	.05	2.12	2.42	2.59	2.71	2.80	2.87	2.92	2.97	3.02
	.01	2.92	3.22	3.39	3.51	3.60	3.67	3.73	3.78	3.83
17	.05	2.11	2.41	2.58	2.69	2.78	2.85	2.90	2.95	3.00
	.01	2.90	3.19	3.36	3.47	3.56	3.63	3.69	3.74	3.79
18	.05	2.10	2.40	2.56	2.68	2.76	2.83	2.89	2.94	2.98
	.0l	2.88	3.17	3.33	3.44	3.53	3.60	3.66	3.71	3.75
19	.05	2.09	2.39	2.55	2.66	2.75	2.81	2.87	2.92	2.96
	.01	2.86	3.15	3.31	3.42	3.50	3.57	3.63	3.68	3.72
20	.05	2.09	2.38	2.54	2.65	2.73	2.80	2.86	2.90	2.95
	.01	2.85	3.13	3.29	3.40	3.48	3.55	3.60	3.65	3.69
24	.05	2.06	2.35	2.51	2.61	2.70	2.76	2.81	2.86	2.90
	.0l	2.80	3.07	3.22	3.32	3.40	3.47	3.52	3.57	3.61
30	.05	2.04	2.32	2.47	2.58	2.66	2.72	2.77	2.82	2.86
	.0l	2.75	3.01	3.15	3.25	3.33	3.39	3.44	3.49	3.52
40	.05	2.02	2.29	2.44	2.54	2.62	2.68	2.73	2.77	2.81
	.01	2.70	2.95	3.09	3.19	3.26	3.32	3.37	3.41	3.44
60	.05	2.00	2.27	2.41	2.51	2.58	2.64	2.69	2.73	2.77
	.01	2.66	2.90	3.03	3.12	3.19	3.25	3.29	3.33	3.37